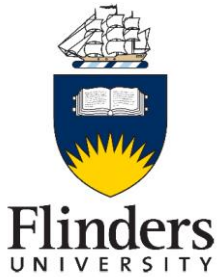

AN INVESTIGATION ON THE DAILY ACTIVITY FORCES AND FRICTIONAL MOMENTS AND THEIR CONTRIBUTION TO THE FRETTING CORROSION FAILURE OF MODULAR HIP JOINT IMPLANTS

by

Hamidreza Farhoudi

Thesis

Submitted to Flinders University

for Degree of

Doctor of Philosophy

College of Science and Engineering

January 2021

Table of contents

List of Figures

list of Tables

Abstract

The contemporary design of hip implants for Total Hip Arthroplasty (THA) comes with modular components to provide flexibility for the surgeons during the operation. This modularity increases the number of material interfaces, each of can become a source of failure. Fretting-corrosion at the metallic components of the femoral head- stem neck (head-neck) interface can lead to THA failure due to adverse local tissue reaction to the emitted ions and debris from the interface. Literature review suggests loads on the interface, the geometry of the interface, and corrosivity of the ambient as the main effective parameters on fretting-corrosion of an interface. Loads acting on the head-neck interface of THA comprise body forces and frictional moments caused by sliding of the femoral head inside the pelvic cup. Body forces of daily activities have been well studied and are available in the literature. However, frictional moments of these activities, especially for metal on metal head-cup bearing, is poorly studied and is currently not available. Given the importance of load components on fretting-corrosion, the frictional moment of daily activities needs to be provided as an effective parameter of the study on fretting-corrosion.

An analytical method is developed to provide the currently not available frictional moments for metal-on-metal bearing couples for different patient weights and wide range daily activities. For the nine investigated activities, the maximum magnitude of the frictional moment ranged from 2.6 to 7.1 Nm. The maximum magnitude of the torque acting on the head-neck interface ranged from 2.3 to 5.7 Nm. These induced torques on the head-neck interface were close or even higher than the pure torques previously reported for depassivation of the head-neck interface. Interruption of this oxide layer by fretting initiates corrosion of active metal underneath. Forces and frictional moments of level gait walking found to be in a range inclusive of most of the other daily activity and considering its high daily frequency, it was selected as the loading scenario of this study.

A Finite Element Analysis, which was developed by another PhD student in the research group, was implemented to investigate mechanical responses of the head-neck interface to the frictional moments and forces of walking activity. Loading scenarios were frictional moment only, forces only and simultaneous frictional moments and forces. In the walking forces only loading scenario mechanical response of the head-neck interface had a

considerable change as 8.43% initially separated surface nodes came into contact. The stress-field of the press-fitted area also changed temporarily. The frictional moments only did not cause considerable changes in the mechanical response of the interface (only 0.27% of the non-contacting surface nodes temporarily came into contact). The effect of frictional moments was considerable in superposition on forces in simultaneous frictional moments and forces case where the micro-motions and contact stresses changed compared to forces only case. The normal contact stresses and micro-motions obtained from this realistic load-controlled study were typically in the range of 0–275 MPa and 0–38 μm, respectively.

In vitro investigation on fretting-corrosion of the head-neck interface was conducted on two different head-neck material combinations of Ti6Al4V-CoCr and CoCr-CoCr. To keep the stress field, induced micromotion and crevice geometry of the head-neck interface as of its service condition, a full-scale implant was studied under frictional moments and forces profile of walking activity. A range of frictional moment varying from 0Nm to 7.5Nm was combined by a range of forces from 900N to 1800N. It observed that Ti6Al4V-CoCr head-neck combination was more susceptible than CoCr-CoCr material combination. The non-loaded control value of Open Circuit Potential (OCP) of Ti6Al4V-CoCr was -0.311V against -0.116V of CoCr-CoCr material combination, and at the highest drop of OCP, their OCP reached to -0.615V and -0.506V, respectively. Frictional moments effects on fretting-corrosion damage were more considerable in the lower vertical forces (for example, walking force with a maximum magnitude of 900N). In the presence of higher vertical forces equal to 1800N, the variation of moments from zero to 7.5Nm had a smaller effect on the OCP and the fretting-corrosion response of the interface. The general outcome suggests that increase of the forces had a more intensifying effect on fretting-corrosion while frictional moments, is more effective on fretting-corrosion damage when is combined with lower contact forces.

The outcome of this research suggests that frictional moments play a considerable role in both mechanical responses of the head-neck interface and fretting-corrosion of the head-neck interface. Considering the accumulative nature of fretting-corrosion damage in the interface, simplification of loading to forces only scenarios in FEA studies and *in vitro* studies need to at least come with a justified increase in the force magnitude.

List of Publications from Thesis

1. **Farhoudi, H.**; Oskouei, R.H.; Jones, CF; Taylor, M. A novel analytical approach for determining the frictional moments and torques acting on modular femoral components in total hip replacements. *Journal of Biomechanics* **2015**, *48, 6*, 976-983.

2. **Farhoudi, H.**; Oskouei, R. H.; Pasha Zanoosi, A.A.; Jones, C.F.; Taylor, M. An analytical calculation of frictional and bending moments at the head-neck interface of hip joint implants during different physiological activities, **2016** *Materials*,*9,12*,982.

3. **Farhoudi, H.**; Fallahnezhad, K.; Oskouei, R.H.; Taylor, M. A finite element study on the mechanical response of the head-neck interface of hip implants under realistic forces and moments of daily activities: Part 1, level walking", *Journal of the Mechanical Behavior of Biomedical Materials* ***2017***,75, 470-476.

4. **Farhoudi, H.**; Oskouei, R.H.; Taylor, M. *In Vitro Independent Multi-Axial Load Control Fretting-Corrosion Investigation on the Head Neck Junction of Hip Joint Implants under Walking Gait Loading*. XXVI Congress of the International Society of Biomechanics, Brisbane, Australia, July 2017.

5. **Farhoudi, H.**; Oskouei, R.H.; Jones, CF.; Taylor, M. *Three-dimensional frictional moment induced from head-cup bearings of hip joint implants,* Australian and New Zealand Orthopaedic Research Society (ANZORS), 20th Annual Scientific Meeting, Adelaide, Australia, Sep 2014; p 138.

6. Fallahnezhad, K.; **Farhoudi, H.**; Oskouei, R.H.; Taylor, M. *A three-dimensional finite element model of the head-neck junction of a modular total hip arthroplasty,* Australian and New Zealand Orthopaedic Research Society (ANZORS), 20th Annual Scientific Meeting, Adelaide, Australia, Sep 2014; p 139.

Declaration

I certify that this thesis does not incorporate without acknowledgment any material previously submitted for a degree or diploma in any university; and that to the best of my knowledge and belief it does not contain any material previously published or written by another person except where due reference is made in the text.

Full Name: Hamidreza Farhoudi

Acknowledgment

I would like to express the deepest appreciation to my primary supervisor Dr. Reza Oskouei, who has been supportive to me beyond expectations during the course of this PhD, and before all the help and assists he had to me, I should acknowledge his respectful and humble attitude to me and all the other students and colleagues. He has been a role model to me on being supportive to the entire community around. Without his guidance and persistent help, this dissertation would not have been possible.

I would like also to thank my associate supervisor, Professor Mark Taylor and my adjunct supervisor, Dr. Claire Jones, whose inputs and supports during the course of this PhD have improved my research significantly.

To also be acknowledged are:

- Australian Government Research Training Program Scholarship which supported me during this PhD,
- The Premier's Research and Industry Fund (Oskouei R.H., Catalyst Research Grant, Government of South Australia, 2014) which supported me to develop the testing System, and
- Flinders node of Australian Microscopy and Microanalysis Research Facility (AMMRF).

My deep and sincere gratitude goes to my family and friends for their continuous and unparalleled love, help and support. I am forever indebted to my parents for giving me the opportunities and experiences that have made me who I am. Last but not least, I am greatly thankful to my beloved wife, Samin. Thank you for your kindness, tremendous patience and for giving me the strength to endure the PhD journey.

Introduction

Total hip replacement (THR) is widely used for the treatment of the end-stage osteoarthritis of the hip. Many contemporary designs include tapered junctions between the modular neck and stem and modular head and neck (Campbell, Ebramzadeh et al. 2010), providing surgeons flexibility to adapt the geometry of the artificial joint to the patient's anatomy in an inoperative manner. This can be provided by choosing suitable modular head components, allowing modifications of the diameter of the head and the offset of the prosthesis. Modularity between the femoral stem and the ball head also enables the use of different materials for the bearing components.

Despite the many advantages of modularity in hip joint implants, the stem-head taper connection of modular hip implant is at the risk of fretting-corrosion and mechanically-assisted crevice corrosion (Gilbert, Buckley et al. 1993) due to the mechanical interruption layerof used biometals at the interface from the cyclic loading of daily activities and in the presence of corrosive body fluid. In recent years, an increasing number of postoperative complications have been observed in modular hip prostheses in clinical applications (Bobyn, Tanzer et al. 1994, Jacobs, Gilbert et al. 1998). Macroscopic and microscopic inspection of retrieval implants have shown surface damage, such as scratches, discolouration, fretting (Urban, Gilbert et al. 2006), wear and corrosion at the taper interfaces (Collier, Surprenant et al. 1992). The cause of the failure is complex, but it seems that it has both mechanical and electrochemical causes.

The reported surface damage appears to be a result of oscillating relative motion between the adjacent implant components, leading to a cycle of removal of the passive layer (fretting) and subsequent repassivation. Along with a corrosive fluid environment, this might lead to corrosion (Atwood, Patten et al. 2010). A mismatch in a small conical taper angle between the adjacent components could result in crevices, and this could allow fluid stagnation. These effects could potentially accelerate the overall corrosive damaging process (Gilbert, Mali et al. 2012). As a further consequence of the interface motions, metal ions (Jacobs, Gilbert et al. 1998) and wear debris (Mohrbacher, Celis et al. 1995, Schramm, Wirtz et al. 2000) are released, which remain in the periprosthetic tissue or migrate to other parts of the body.

Previous studies have indicated a link between wear debris and adverse tissue reactions, such as the generation of pseudotumor, allergic reactions and metallosis (Korovessis, Petsinis et al. 2006, Pandit, Glyn-Jones et al. 2008). Postoperative complications induced by fretting appear to be more prevalent in large diameters of metal-on-metal (MoM) bearings. These bearings exhibit the highest revision risk of all frequently used bearing surfaces. With an increase in the head diameter, the incidence of revision rises even more (Smith, Dieppe et al. 2012); this is speculated to be a consequence of higher frictional moments applied to the modular junction due to a larger head diameter, especially in case of inadequate lubrication (Bishop, Hothan et al. 2013).

High moments acting at modular junctions might accelerate fretting and corrosion, explaining why this issue is predominantly observed for these implants. However, MoM bearings with a head diameter of 32 mm or less are usually successful in patients with low revision rates as compared to other bearings. Many case reports regarding damage of large diameter MoM bearings are available in the literature. Some of these *in vivo* failures can be traced back to issues at the bearing interface between the ball head and acetabular cup. However, many clinically observed problems might be initiated by postoperative complications at the conical taper interface (Cooper, Della Valle et al. 2012, Nassif, Nawabi et al. 2013).

There have been relatively few studies examining the mechanical aspects of taper junction failure; thus, there is a paucity of knowledge regarding the interface micromotions at taper junctions. Some studies reported micromotions from 8 to 25 µm between the stem and ball head of standard modular implants (fixed neck stems) (Gilbert, Mehta et al. 2009). Hip joints allow the transfer of forces and moments from the upper to the lower body during daily activities, leading to high bending loads at the hip joint. *In vivo* average peak loads range between 1100N (knee bend) and 2000N (going down stairs) for a bodyweight of 750N depending on the performed activity (Bergmann, Graichen et al. 2010). Considering the possible contribution of different components of daily activity loads (forces and frictional moments) on the fretting-corrosion of the head-neck interface, these components need to be determined, and their contribution on the degradation should be examined. This leads this thesis to firstly determine the currently unknown components of frictional moment for the vulnerable metal-on-metal bearing couples. This then will be followed by numerical and experimental study of fretting-corrosion at the head-neck interface to investigate

interrelation of service condition load components in fretting-corrosion of the head-neck interface. This thesis comprises chapters below:

Chapter 1: A review on the history and related studies on the subject is presented. In the first part of this chapter, the history of the Total Hip Arthroplasty (THA) is provided. In the second part, contemporary THA and its disorders and failures are mentioned. Failures pertinent to the modular interface design are discussed in further detail. In the third part, fretting-corrosion, as a cause of ion and particle emission to the surrounding tissues and failure at the head-neck interface, is discussed in detail. For this, each of the phenomena of fretting, corrosion and their effective parameters are reviewed separately to gain an understanding of main effective parameters in the study of fretting-corrosion. This understanding was then implemented to design realistic study on fretting-corrosion by keeping the effective parameters as they are in the service condition. Fretting crevice corrosion at the head-neck interface is discussed to provide the perspective behind the study design. The brief conclusion made in this part is the necessity to have a realistic and quantitative *in vitro* study on fretting-corrosion of head-neck interface; in fact, similar loads to service condition in the presence of similar corrosive ambient need to be applied on a full-scale interface. Further, studies based on a load of daily activities on the hip joint implant and consequently head-neck interface is reviewed. This part of the literature review concludes that literature on the frictional moment for MoM hip joint implant is limited for three-dimensional forces and kinematics of daily activities. In part five, current studies on the mechanical response (stress-field and local micromotions) of the head-neck interface to daily activities are discussed. This part suggests that further study regarding the contribution of frictional moments in mechanical responses of head-neck interface is required. In part six, *in vitro* studies on fretting-corrosion of head-neck interface is provided. This part suggests the need for *in vitro* study regarding the contribution of the frictional moment in fretting-corrosion of head-neck interface.

In Chapter 2, an analytical method for the calculation of the currently unavailable frictional moments of hard-on-hard bearing couples in service condition is developed. This method can calculate the frictional moment under 3D varying force along with 3D rotational dynamics of bearing couple in the presence of friction. It was validated against currently available *in vitro* frictional moments reported for simplified testing conditions and its capabilities demonstrated by calculating frictional moments of walking activity through currently

available kinematics and forces. This method was developed to provide inputs for the next steps of Finite Element Analysis of the mechanical response of the head-neck interface as well as *in vitro* study on fretting-corrosion of the interface.

In Chapter 3, the developed analytical method is implemented to study the variation in the frictional moment during daily activities. This provides a good vision of the currently unavailable magnitude and variation of the frictional moment at the hip joint implant during its service condition. The results in this chapter will help to decide on the load profile to be used for the Finite Element Analysis of the mechanical response of the interface and *in vitro* study of fretting-corrosion of the head-neck interface.

In Chapter 4, With the current state of the art, it is not feasible to experimentally monitor the mechanical responses of the head-neck interface. Therefore, a collaborative numerical study between the author and members of the research team developed. Author provided loads for daily activities extracted from the as an input to another PhD student (Mr. Khosro Fallahnezhad) who developed an explicit Finite Element Model of the head-neck junction in the service conditions. Outcome data of simulations were then investigated and interpreted by a MATLAB code developed by the author. To have a good perspective of contribution and interrelation of the frictional moment and bearing forces, three different loading scenarios: 1) frictional moment only (M only), 2) bearing forces only (F only) and 3) combined frictional moment and bearing forces (F&M) are investigated. The results of this chapter are categorised as stress field, induced micromotions and fretting work occurred during these different scenarios. Its outcomes can provide a good view of what mechanically occurs inside the studied head-neck junction because of applied loads.

In Chapter 5, different aspects of design, manufacturing, commissioning and implementing of an *in vitro* testing system are provided. This system is aimed to study the interrelation between the load component of daily activities that affects fretting-corrosion of the head-neck interface. It comprises state machine design, structural design, data acquisition system design, cooling system selection and integration, corrosion monitoring system integration and feedforward/feedback control design and integration. The details of each of these sections and method of integration are described in this chapter. This system provides the required

substrate to control the input parameters of the load while monitoring the output parameter of fretting-corrosion of head-neck interface.

In Chapter 6, using the testing system as described in Chapter 5, an *in vitro* study is conducted on a common head-neck geometry with two different combinations from the commonly used materials. For this, a test protocol is developed to investigate interrelation and superposition of high and low magnitudes of the frictional moment and bearing forces on fretting-corrosion of the head-neck interface. Extracting daily activity's load components in Chapter 2 and 3 provided inputs for finite element analysis (FEA) on mechanical responses of the head-neck interface under walking activity. This followed by experimental investigations of fretting-corrosion at the head-neck interface under combinations of walking activity loads components (different scales of frictional moments and activity loads) in this chapter. Having the mechanical responses of the interface from FEA along with fretting-corrosion responses of the interfaces from the experimental study provides a clear picture of service condition of the implant and level of contribution of frictional moments in fretting-corrosion degradation of head-neck interface.

In Chapter 7, a general discussion of this thesis is provided to organise this research for an overall understanding.

In Chapter 8, Based on the developed knowledge during this thesis, a conclusion and suggestions for future works is provided

Chapter 1. Literature review

1.1 Total Hip Replacement History

Osteoarthritis of the hip joint is a recognised disease, and many studies and methods about its treatment have been conducted. These treatments have progressed from a solution with significant long-term drawbacks, in most infirm patients, to an elective surgery that provides frequent and high success rates (Pivec, Johnson et al. 2012).

Before 1800, amputation was the treatment considered for the leg affected by hip osteoarthritis. To find less aggressive alternatives, Henry Park introduced total extirpation of the joint as a method to cure the disease through callus formation (Park 1783, Gomez and Morcuende 2005). In 1821, Anthony White introduced excision arthroplasty in which the head, neck and trochanters of the femur are removed. A less invasive treatment by using osteotomies was introduced in 1826 (Barton 1827). The first experiments with interpositional materials were performed by Vitezlav Chlumsky in the late 19th century. He examined different materials, such as muscle, celluloid, silver plates, rubber struts, magnesium, zinc, glass, pyres, decalcified bones, wax and celluloid (Gomez and Morcuende 2005). The interposition idea was continued by Sir Robert Jones in 1912 by resurfacing the shape of the bone and applying a gold layer to articulate it more smoothly. This method had good following reports after a period of 20 years, the longest follow-up in the history of arthroplasty during that time (Jones and Lovett 1929).

In 1930, Wiles introduced the first Total Hip Arthroplasty (THA). In THA, femur and acetabulum were replaced by metallic components (Wiles 1958). This method was further improved by McKee and Watson-Farrar in the 1950s who substituted the stainless steel with a cobalt-chrome-molybdenum alloy (McKee and Watson-Farrar 1966). In 1953, Sir John Charnley introduced the now “traditional” metal-on-polyethylene THA in which he used bone cement for fixing the implant and considered using polyethylene instead of an MoM bearing. In the 1970s, after the success of Charnley’s high-density polyethylene low friction arthroplasty and acrylic bone cement, MoM implants had almost been removed from the market (Charnley 1961). In the early 1990s, the MoM bearing was revived using a new design accompanied by the introduction of resurfacing prosthesis. The benefits of the introduced MoM bearing over the “traditional” arthroplasty was that it preserved bone better on the

femoral side and increased the range of motion and stability which was suitable for the young and more active patient group.

THA is only 80-years old, but in this short period, it has evolved to one of the most successful and most performed procedures in the history of medicine (Learmonth, Young et al. 2007). However, this success does not necessarily indicate that there are no shortcomings in the method. Several complications still occur and can significantly influence the survival of the implant and the patient's illness.

1.2 Total Hip Arthroplasty and its failures

Current THA implants benefit from modular components, such as taper and trunnion design for head-neck connection. Figure 1.1 illustrates a common type of metal-on-polyethylene hip implant and its modular components.

Removed due to copyright restriction

Figure 1.1 Modular components of a common metal-on-polyethylene THA implant[1].

Modularity allows the adjustment of inferior-superior and lateral-medial offsets, length of leg, and neck version/anteversion, as shown in Figure 1.2. This flexibility in component selection can serve a wide range of patients with different complications.

1 http://www.exac.com

Removed due to copyright restriction

Figure 1.2 modular implants with different positions for head to provide varying leg length and mediolateral offset for patients with different anatomies[2]

Modularity also provides options in replacing only the damaged component in revision surgery (Krishnan, Krishnan et al. 2013).To provide flexibility for surgeons, two different types of single tapered and dual tapered designs of the stem's neck have been developed (Figure 1.3). Single tapered design provides options in head size and material selection for the surgeons. Dual tapered design offers changes in the geometry of the neck as they can vary in version/anti-version and offset of the neck. The dual tapered design has shortcomings, such as the early failure of the distal taper, which are not as common in single tapered design (Moore and Lachiewicz 2017).

[2] http://www.zgreatlakes.com/

Removed due to copyright restriction

Figure 1.3 Different designs of the femoral neck in Total Hip Arthroplasty implant. a) Single tapered neck b) dual tapered neck [3]

In MoM hip joint implants, a metal alloy head, usually made from cobalt and chromium, slides inside a metal acetabular cup or cup liner component.

There are two major types of MoM hip arthroplasty. The first one is THA in which the bone of the femoral head is replaced with a modular metallic head, assembled on as stem fixed in the femur. This metallic head articulates with a metallic cup fixed in the acetabular (Ansari, Matharu et al. 2018) (Figure 1.4).

The other MoM hip joint arrangement is named resurfacing in which the surface of the existing hip joint head is slightly removed and replaced with a metallic surface which articulates against a metallic cup in the pelvic. This type is mostly called hip joint resurfacing (Resende, Kirkwood et al. 2017) (Figure 1.4).

[3] www.zimmerbiomet.com

Removed due to copyright restriction

Figure 1.4 Schematic view of metal-on-metal total hip arthroplasty (left) and metal-on-metal hip resurfacing (right)[4]

1.3 Common THA failures and disorders

Although THA offers several advantages, recent studies report an increase in the number of early failures and retrieval surgeries. In this context, failure indicates any reason causing the implant to fail, provided the considered functionality. Some of these failures are dislocation (Figure 1.5-a), periprosthetic femoral fractures (Figure 1.5-b), fracture of the implant (Figure 1.5-c), thrombosis, leg length discrepancy (Figure 1.5-d) and fretting-corrosion of interfaces followed by adverse local tissue reaction (Figure 1.5-e and f).

[4] www.fda.gov

*Figure 1.5 a) Dislocation of implant failure (Adam, Philippe et al. 2012) b) periprosthetic femoral fractures failure (Rayan, Dodd et al. 2008) c) fracture of implant (Mencière, Amouyel et al. 2014) d) Leg length discrepancy (Mahmood, Mukka et al. 2015) e) adverse local tissue reaction (*mark in the photo) to fretting-corrosion products from head-neck interface (Cooper, Della Valle et al. 2012) f) adverse local tissue reaction to wear and fretting-corrosion products of the implant (Canham, Muradov et al. 2017)*

Ulrich et al. (Ulrich, Seyler et al. 2008) reported that 95% of the initial THA has been successful for longer than 10-years of follow-up. They also declared that with an increase in the number of younger patients and patients with a high level of activity, a greater number of revisions of THA had been reported. About 25% of THA surgeries conducted in the USA are revision THA which imposes a high financial load on the healthcare system, and its outcome is not as favourable as the initial THA.

Ulrich et al. reviewed 225 patients who underwent 237 surgeries after THA had been conducted on them at two centres during a 6-year time period (Ulrich, Seyler et al. 2008). The range of the time required for revision surgery was 0–360 months with an overall mean time of 83 months. In 51.9% (123 hips) of the cases, aseptic loosening was reported as the cause of failure, followed by 16.9% (40 hips) failures caused by instability in 40 hips. In 5.5% (37 hips) of the cases, failures were diagnosed because of infection in the hip. About 50% of the

revisions surgeries had been conducted in five years or less with 33% caused by instability and 24% resulting from infection.

As will be discussed later, cyclic loading on metallic interfaces of the hip joint implant in the presence of corrosive body fluids can mechanically and chemically degrade the passive protective oxide layer of the interfaces and the metal underneath. Body tissues and bones, as an interacting counterpart of the implant, can be affected by undesired products of degradation of the passive layer of the implants.

1.3.1 THA failures related to taper interface

(Morlock 2015) has provided a very useful review on ,the taper junction problems and their consequences on the clinical performance of THR prior to the introduction of large head MOM implants to the market. At its introduction, large head MOMs faced high level of acceptancefrom the community focusing on the outstanding wear performance and decrease of dislocation. These advantages, however, overshadowed by the poor fretting-corrosion performance of the large MOM design, especially at the taper junction of the head-neck interface as will be discussed in the section.

Clinical indications of the reaction of the body to fretting and corrosion productsfrom biometal implants go back to 1956 when McDougall (McDougall 1956) reported malignant tumour at the site of bone plating. Failure of hip joint implants prior to the introduction of large MOM had been reported in range of cases such as osteosarcoma after THR (Penman and Ring 1984), soft tissue tumour after THR (Swann 1984), (Ryu, Bovill et al. 1987, Ingram 1988), bone tumour near to THR area (Brien, Salvati et al. 1990), osteolysis as a consequence of metal wear near modular junctions (Salvati, Lieberman et al. 1995), pseudotumor resulted from metallosis after implantation(Picard, Montbarbon et al. 1997). 4 out of 240 malignant soft tissue tumours analysed from Bristol tumour register had occurred after a hip joint replacement (Langkamer, Case et al. 1997).

Jacobs et al. (Jacobs, Skipor et al. 1998) in their prospective controlled longitudinal study on metal release in patients with primary THR concluded that the taper junction between the head and stem is responsible for the significant increase in titanium and cobalt concentrations

in the patients, even when the prostheses are functioning well. They had warned that this in the long-term could lead to local and systematic consequences.

Jacob et al. (Jacobs, Gilbert et al. 1998) in a study on corrosion of metal orthopaedic implants investigated three groups of patients with different stems (cemented modular Co-head, uncemented porous-coated Co stem and uncemented proximally porous-coated Ti) all with a Co-head and uncemented Ti socket. Increase in the Ti and Co levels in urine and serum were observed in all the patients after three years. They had concluded that fretting corrosion at the head-neck is a major source of metal release which can lead to concentration of chromium in the serum.

Savarino et al. (Savarino, Granchi et al. 2002) in a research on two groups of patients with the same prosthesis and different bearings of MOM and MOP concluded that MOM group showed a significantly higher systematic release of Co and Cr compared to MOP.

From the aforementioned clinical studies, Morlock (Morlock 2015) in his review summarises that “None of the authors really did ring the bell” that there might be a major problem. Furthermore, none of these papers investigated extra large size MoM heads. The studies investigate patients with small metal heads or resurfacings, which are continued to be used today. since the registry results of small metal heads are up to 12 years after implantation which is similar to other bearings (Annual report of the National Joint Registry, AOA, 2014).”

Morlock (Morlock 2015) extends his review on the state of knowledge on the failure of head-neck interface to before the introduction of large head size MoM implants to retrieval THR studies. In the retrieval THR review, he points studies such as Collier et al. (Collier, Surprenant et al. 1991) which raises the presence of corrosion in 57% of analysed revision with CoCr head and Ti stem.

Collier et al. (Collier, Mayor et al. 1992) in another study titled mechanisms of failure of modular prostheses analysed 250 explants. They found fretting-corrosion as an issue that needs to be addressed through and by improvement in design and low tolerances in modular interfaces. In another study, (Collier, Surprenant et al. 1992) They obsereved corrosion in 50% of different material combination in taper junction and no corrosion with the same material combination.They reported that galvanic corrosion is of the causes of the failure. Mathiesen

et al. (Mathiesen, Lindgren et al. 1991) suspected crevice corrosion on the taper of the head and stem as the cause of necrosis in surrounding tissues.

Collier et al. in another study (Collier, Mayor et al. 1995) analysed 731 modular head junctions and observed corrosion as the principal problem of the junction. Depending on the material combination, they had observed corrosion in 7% to more than 30% of the retrieved implants.

Goldberg et al. (Goldberg, Gilbert et al. 2002) in a multicentre retrieval study of the taper interface analysed 231 modular head-neck and observed greater corrosion in mixed metals and on the head of the prosthesis increasing with mechanical stress. They suggested larger taper diameters as a possible solution while not restricting the range of the motion .

As reflected by Morlock (Morlock 2015) in retrieval studies on implant designs prior to large head metal-on-metal, the relation between corrosion and failure of the implants has been underlined, and influence on material pairing on the failure has been identified.

Local tissue reaction has been reported as one of the major complications and causes of retrieval surgeries in different studies (Campbell, Ebramzadeh et al. 2010, Cooper, Urban et al. 2013, Canham, Muradov et al. 2017, Moore and Lachiewicz 2017). This syndrome can cause localised pain and lead to early revision surgery.

In a study on adverse local tissue reaction in THA, Campbell et al. (Campbell, Ebramzadeh et al. 2010) investigated the histological features of pseudotumor-like periprosthetic tissue reactions around MoM hip replacements. They couldn’t diagnose these reactions completely but reported that the reactions are in relation to excessive wear, hypersensitivity to metallic debris or a currently unknown cause. This study hypothesised that tissue features indicate and distinguish between adverse tissue reaction to high wear (Figure 1.6) from those suspected to high sensitivity to metal (Figure 1.7).

Removed due to copyright restriction

Figure 1.6 Light Microscopic photo of atypical histologic feature occurs for high wear debris, including large organised Fibrin (Campbell, Ebramzadeh et al. 2010)

To this aim, they examined the synovial lining integrity, inflammatory cell infiltrates, tissue organisation, necrosis and metal wear particles in 32 MoM retrieval hip replacement with pseudotumor-like tissues.

They concluded that pseudotumor-like reactions can be caused by high wear, but could also occur around implants with low wear most likely because of a metal hypersensitivity reaction. Metal hypersensitivity could be a reaction of the surrounding tissues to fretting-corrosion products of the head-neck interface. Their results suggest that histologic features might help differentiate the causes.

Removed due to copyright restriction

Figure 1.7 Light microscopic photo of a local tissue adversely reacted suspect case to metal hypersensitivity with low wear particles. The character F arrow refers to organised fibrin usually shaped around a wounded area. (Campbell, Ebramzadeh et al. 2010)

Cooper et al. (Cooper, Urban et al. 2013) conducted a study on adverse local tissue reaction (ALTR) caused by metallic ions and debris emitted from corrosion at stem-neck junction in a dual tapered stem with a cobalt-chromium modular neck. Their study was a multi-centred retrieval series for twelve hips from eleven patients (eight women and three men- one of the patients with two retrievals) with ALTR. All studied implants were dual tapered neck-type with titanium-alloy stem and cobalt-chromium-alloy neck. The cohort suffered from new-onset and increasing pain in a mean of 7.9 months with retrieval surgery in a mean time of 15.2 months. They examined tissues histologically and investigated retrieved implants using light and scanning electron microscopy (SEM). Their energy-dispersive x-ray spectrum results revealed an increase in the serum metal level of cobalt, chromium and titanium (Cooper, Urban et al. 2013). Metal artefact reduction sequence (MARS) and magnetic resonance imaging (MRI) demonstrated ALTR in eight of the nine patients. All the hips that were studied had large masses of soft-tissue and surrounding tissue damage with visible corrosion product at the distal taper interface of the dual tapered implant. Damaged tissues and necrosis were found in seven out of ten cases. Their microscopic analysis was consistent with fretting and crevice corrosion marks. From these results, they concluded that corrosion of distal interface of dual tapered modular neck made from cobalt-chromium-alloy leads to the release of metal ions and debris causing local soft tissue damage.

In another study conducted on two cases of retrieval surgeries, Cook et al. (Cook, Bolland et al. 2013) conducted case investigation of the failure of two large-diameter Metal-on-Polymer bearing THA which suffered from pseudotumor formation. Their study focussed more on the features of implants degradation in retrieval cases with pseudotumor formation. In their failure analysis, they observed a discrete pattern of material loss from the distal end of the head taper-stem interface (Figure 1.9).

Figure 1.8 Energy-dispersive x-ray spectrum shows chromium (CR), cobalt (Co) and titanium (Ti) presence in histological specimen collected during the THA revision surgery. The spectrum is constant with chromium phosphate shows the particles by corrosion at the junction. O = oxygen, Mg = magnesium, P = phosphorus, S = sulphur, and Ca = calcium (Cooper, Urban et al. 2013).

They suggested that the use of a proximal contacting taper design led to insufficient mechanical press-fit between the head and the stem, enabling the head to rock on the trunnion. They also concluded that the angular mismatch of the trunnion femur and the taper shaped a crevice between the two components. Through a combination of crevice environment, mechanically assisted corrosion, mechanical wear and erosion debris and metal-ions have been released resulting in the ALTR.

Figure 1.9 Observed discrete pattern of material loss in the distal side of a proximal press-fitted hip joint implant for two retrieval cases (Cook, Bolland et al. 2013)

Ulrich et al. (Ulrich, Seyler et al. 2008) identified the infection as the reason for 24% of retrieval surgeries. This significant portion of infection which might have been caused by fretting-corrosion, alongside the literature review on implant degradation and histology of damaged tissues around retrieved implant, intensifies the need to profound investigation on the mechanism of mechanically assisted crevice corrosion as a suspected cause of not yet well-diagnosed retrieval surgeries. Fretting crevice corrosion has not been introduced as the leading cause of the 24% infection caused retrieval surgeries; however, many of the scrutinising case studies emphasised on it as the main reason (Gill, Alfaro-Adrian et al. 2002, Campbell, Ebramzadeh et al. 2010, Cook, Bolland et al. 2013, Cooper, Urban et al. 2013, Cooper 2014).

Larger head size MoM bearings were introduced to the market to increase the range of motion and reduce the chance of dislocation of the head from its position in the cup. However, this design was followed by a high rate of immature retrieval surgeries (Bishop, Hothan et al. 2013, Del Balso, Teeter et al. 2016, Gascoyne, Turgeon et al. 2018).

Higgs et al. (Higgs, Hanzlik et al. 2013) have discussed that larger head sizes and non-similar alloys of head and neck junction cause increase in damage at the head taper. They have also mentioned that from a biomechanical perspective, an increase in mediolateral offset induces larger neck moment and leads to more significant damage at the head-neck interface. In a retrieval study on 126 failed large-diameter MoM THA, Langton et al. (Langton, Sidaginamale et al. 2012) have reported that larger head diameters and laterally engaged head-neck taper junction are effective parameters on THA failure from ALTR to fretting-corrosion larger head-sized design.

Removed due to copyright restriction

Figure 1.10 A large cyst containing chalky fluid consistent with pseudotumor and adverse local tissue reaction to the fretting-corrosion product of a large size hip joint implant (Canham, Muradov et al. 2017)

These head cup designs come with considerable drawbacks including an increase in volumetric wear, dictating a thinner liner geometry in metal-on-polyethylene head cup interfaces, and adverse local tissue reaction to fretting-corrosion products emitted from MoM head-neck (Canham, Muradov et al. 2017, Moore and Lachiewicz 2017).

In a clinical case study, Terreault et al. (Tetreault, Jacobs et al. 2018) reported a male patient (70-years old) with several revision of MoM THA. They have reported large periprosthetic fluid unexpectedly found during tomography. The patient had a painless growing swelling on the

lateral side of his hip. In these studies, the result of the examination of serum and metal-lymphocyte transformation was negative regarding the presence of the fretting-corrosion product. However, during the revision surgery, they came across a large fluid collection and corrosion at the head-neck junction of the implant. The examination during post-surgery pathology showed ALTR. This was a previously undescribed ALTR in which the level of metal ions hadn't elevated in the serum. At the same time, ALTR to corrosion product was happening in the surrounding tissues of the head-neck interface. They emphasised on considering different parts of the patient's clinical reports, such as imaging and laboratory testing, to diagnose symptomatic MoM THAs.

Overall, the histological studies indicated that fretting-corrosion and mechanically assisted crevice corrosion could be the primary sources of metallic ion and debris which cause local tissue reaction. This ALTR leads to severe damages to surrounding tissues of the head-neck modular interface and obliges the surgeons to conduct retrieval surgeries. To this end, understanding the mechanism of fretting-corrosion at the head-neck interface and possible compromises in the evaluation of implant designs concerning fretting-corrosion can help in improving the performance and outcome of the method of THA.

1.4 Overview on fretting-corrosion and mechanically assisted crevice corrosion

To study the aspects of examination required for realistic testing of implants, fretting-corrosion and effective parameters need to be understood. Fretting-corrosion is a degradation of material which occurs because of the small relative motion of two contacting surfaces that are under compressive load, exposed to a corrosive medium. In case of corrosion-resistant materials whose resistance relies on their passive adhesive oxide film, initially, fretting degrades their passive layer and the fretting wear along with chemical corrosion of underlying metals. They start to degrade the material in a cyclic manner (Figure 1.11). For a better understanding, each of the composing parts of fretting and corrosion needs to be understood separately.

Removed due to copyright restriction

Figure 1.11 Schematic of the interrelation of fretting and corrosion in the degradation of materials with a passive oxide layer [5]

1.4.1 Fretting

The American Society for Metals Handbook on Fatigue and Fracture (1996) defines fretting as: "A special wear process that occurs at the contact area between two materials under load and subject to a minute relative motion by vibration or some other force."

Fridrici et al. (Fridrici, Fouvry et al. 2001), in their definition for fretting mentioned that: "When two contacting surfaces are submitted to tangential loading due either to vibrations or to a fatigue loading in one of the contacting component, small amplitude displacements (from one tenth of a micron to hundreds of microns) are induced at the interface. Depending on the materials properties and the normal and tangential loadings, this phenomenon, known as fretting, can lead to crack nucleation (and possible propagation if one of the components is subjected to a fatigue loading) or to wear by debris formation."

More than 50 parameters are listed as effective on fretting. However, the interdependency between these parameters reduces them to seven major parameters: amplitude, number of cycles to fretting, materials, contact temperature, frequency, stress field and environment (Berthier, Vincent et al. 1989).

[5] www.connectorsupplier.com

Two different fretting regimes can be defined with respect to tangential displacement control:

1) Elliptical fretting loop (tangential force Q versus displacement δ: Figure 1.12(a)): This is also called partial slip regime. In this regime, contact is divided into a central stick domain and an external domain with sliding).

2) Gross slip regime: In this regime, higher displacement amplitudes happen while the central stick domain disappears (Figure 1.12(b)).

Removed due to copyright restriction

Figure 1.12 Fretting regimes: (a) Elliptical fretting regime; (b): Gross slip regime (Fridrici, Fouvry et al. 2001)..

Considering three parameters of tangential force (Q), tangential displacement (δ), number of cycles and three regimes of partial, mixed and gross slipping, fretting is a complex system that needs multi-disciplinary (mechanical, structural and physicochemical) approach since, as mentioned, numerous parameters affect this behaviour of materials.

Removed due to copyright restriction

Figure 1.13 Friction logs for the (a) partial, (b) mixed and (c) gross slip regimes.(Fridrici, Fouvry et al. 2001)

To consider all of material characteristic as well as contact loading factors of running condition map, fretting maps is a practical approach (Neu 2011). Figure 1.14 illustrates fretting maps that show the relationship of fretting regimes with the fretting fatigue test configurations. As can be found from this figure, the regime of fretting depends on normal force (contact's normal stress) and relative displacement. As shown in this graph, contact geometry has

significant contribution in the fretting mode of material as it is effective in the stress field that is imposed on materials (Han, Pillon et al. 2006).

Removed due to copyright restriction

Figure 1.14 Fretting maps showing relationship to fretting fatigue test configurations (PSR= partial slip regime, MFR= Mixed fretting regime, GSR=Gross slip regime) (Neu 2011).

From a different perspective, material response to fretting needs to be determined. Three main responses of bulk materials (first bodies) are identified by studying contact area of fretting degradation (Zhou, Fayeulle et al. 1992). The three categories of material response are: low damage surface (no degradation), formation of cracks and particle detachment. The two modes of cracking and particle detachment (degradation) modes happen simultaneously.

Low damage surface generally exists for stick regime friction (regime with no sliding at the interface). In this contact area, small plastic deformation of some asperities might occur. Few wear particles might also be found in this regime and are supposed to be produced in initial stages and micro-displacement of the edge of the contact area in the fretting test.

On the other hand, debris is always found in the slip regime. These particles are made from mixed metallic, oxidised and can shape other compounds and form thick or thin layers on first bodies. Thus, the parallelepipedic Q-δ cycles correspond to sliding accommodation inside the third body (Zhou, Fayeulle et al. 1992).

Brittle materials generate debris in very first strokes while more ductile materials suffer cyclic plastic deformation which results in phase transformation and decreases ductility to such low values that cracks, and the debris then form (Figure 1.16).

Figure 1.15 Material response of the fretting map (Neu 2011).

Characteristics which show the appearance of damage vary during fretting testing. Cracking mechanisms are very complex. Two main evolutions of cracks can be considered:

In first evolution, the fretting crack stops, and a large particle can detach due to the joining of the two cracks nucleated at each side of the contact (in the moving direction-Figure 1.17). In second evolution, the fretting crack is propagated, but the direction strongly changes.

Figure 1.16 Optical micrograph of crack formed in fretting test on 2091 alloy (normal force=1000N, spherical sample R=100mm, δ=±33μm, number of cycles=10^6cycles)(Zhou, Fayeulle et al. 1992).

From numerous fretting tests performed on different types of materials, the mixed regime is shown to be the most detrimental regime for cracking. The mixed regime of running-

condition-fretting-map (Figure 1.14) is made up of initial gross slip followed by partial slip conditions after a hundred cycles. Obviously, the partial slip transition develops the highest stress levels, which can induce fatigue crack nucleation depending on the fatigue properties of contacting first bodies (Fouvry, Kapsa et al. 1995).

Removed due to copyright restriction

Figure 1.17 Forming of a large particle due to the joining of two cracks nucleated at each side of the contact (Zhou, Fayeulle et al. 1992)

Overall, it can be found the fretting phenomenon can considerably change based on the parameters of stress field, lateral force, number of cycles and surface characteristics. Fretting at the head-neck interface of the hip joint implant has a more force control nature than a displacement control fretting that occurs due to vibration. In the force control fretting, the amount of normal force and tangential force is almost repeated (the forces and frictional moment induced by an activity, such as walking is almost cyclically repeated) while the displacement responses to this cyclic load could vary because of geometry and the number of cycles. To this end, the service condition of the implant can be best replicated by applying as similar loads as possible to as similar material and geometry as possible to induce normal and tangential forces, such as the service condition of the fretted interface.

1.4.2 Corrosion

Corrosion is defined as the destructive attack of metal by chemical or electrochemical reaction with its environment. Deterioration of the metal due to physical or mechanical actions is not referred to as corrosion, it is described as erosion, galling or wear. In some instances, chemical attack accompanies physical deterioration. Many biomaterials owe their resistance against corrosion to an oxide or passive layer; however, materials with a strong passive layer still experience ion transfer and dissolution of the passive layer itself is possible (Bryant 2013).

The types of corrosion are usually distinguished based on their forms. The major types of corrosion include: general attack also named as uniform attack, galvanic corrosion, crevice corrosion, pitting corrosion, intergranular corrosion, selective leaching corrosion, tribo-corrosion and stress cracking corrosion (Bryant 2013). Most of the corrosion degradation of biocompatible metals that occur inside the human body is due to crevice corrosion (Hussenbocus, Kosuge et al. 2015).

Crevice Corrosion

Crevice corrosion usually occurs in metals that their corrosion residency relies on for the formation of a passive adhesive layer from their oxide. According to Fontano (Fontana 2005), for the initiation of crevice corrosion, the following conditions must be satisfied. First, the metallic sample must be electrically connected to the outside of crevice. Stagnation of fluid within the crevice is the second requisite as it prevents migration of the ionic components. As the third condition, the outside material must remain passive due to the transportation of ions.

Oldfield et al. (Oldfield and Sutton 1978, Oldfield and Sutton 1980) explain how crevice corrosion occurs because of the concentration of oxygen-starved electrolyte in the crevice. The measure of starving oxygen is the bulk electrolyte of the outside of the crevice, where plenty of oxygen is available. To keep the potential energy inside the crevice minimum and maintain charge conservation, ions from bulk electrolyte transfer to the crevice. By ions transferring complex ions, metal dissolution and corrosion product forms inside the crevice. Crevice corrosion is an autocatalytic reaction and continues autonomously.

Passive Dissolution Model for Crevice Corrosion Initiation

In 1978, Oldfield and Sutton (Oldfield and Sutton 1978) defined passive dissolution model as a theory of quantifying crevice corrosion. This model proposes a decrease in pH and development of aggressive localised solution-initiated crevice corrosion. This is due to the slow transportation of metal ions out of the crevice by diffusion or migration, and hydrolysis of these ions leads to a gradual pH decrease (Oldfield and Sutton 1978).

This model considers four stages for crevice corrosion. At the first stage, normal corrosion occurs inside and outside the crevice with the following cathodic and anodic reactions:

$$2H^+ + 2e^- \rightarrow H_2 \text{ (Cathodic)}$$

Equation 1-1

$$O_2 + 4H^+ + 4e \rightarrow H_2O$$

Equation 1-2

$$O_2 + 2H_2O + 4e \rightarrow 4OH^-$$

Equation 1-3

At the second stage, as a result of cathodic reaction inside the crevice, most of the oxygen ions are consumed. To maintain the minimum potential energy across the electrolyte and crevice, Cl^- and OH^- diffuse into the crevice. Metal chloride forms as a result of this migration of ions. Hydrolysis of metal chloride lowers the pH within the crevice causing the production of metal hydroxides and hydrochloric acid. (Equation 1-4).

$$MCl_n + nH_2O \rightarrow M(OH)_n + nHCl$$

Equation 1-4

In the third stage, metal ions reduce Cl^-, leading to further hydrolysis and decrease in the pH within the crevice. This process of dissolution of metal accelerates, and more ions are formed which lowers pH (fourth stage).

Crevice Geometry Effects

Crevice geometry can affect the crevice corrosion dramatically as tight crevices result in an initiation of differential aeration cells. According to Oldfield et al. (Oldfield and Sutton 1978), by an increase in crevice size from 0.1 µm to 1 µm, the initiation time of the crevice corrosion in seawater also increases. Mathematical models also agree that decreasing the gap dimension can decrease the crevice corrosion initiation time. This could be because of the reduction in the volume of crevice solution that needs to be deoxygenated and become sufficiently acidified for the breakdown of the passive layer (Oldfield and Sutton 1978, White, Weir et al. 2000). The surface roughness of crevice forming bodies could also contribute to the level of crevice corrosion (Shan and Payer 2007).

1.4.3 Effect of geometry on fretting-corrosion and crevice corrosion

Geometry affects both fretting-corrosion and crevice corrosion. In case of fretting-corrosion, the stress-field determines the material response and the fretting regime. The stress-field itself is a function of loading condition and geometry. It can be mimicked by a surrogate geometry calculated from Hertz contact theory as many studies have done (Duisabeau, Combrade et al. 2004, Heredia and Fouvry 2010, Mathew, Uth et al. 2011, Swaminathan and Gilbert 2012, Baxmann, Jauch et al. 2013, Zhang, Harrison et al. 2013). However, this will be accompanied by dramatic compromises in the multiaxial nature of the stress-field, which could lead to an underestimating of the damages, and its simplification would need to be well justified.

In case of crevice corrosion, it highly depends on geometry as a requisite of stagnation of the corrosive medium in a volume with low contact with its surrounding electrolytes. To this end, to have a quantitative and realistic understanding of mechanically assisted crevice corrosion, full-scale geometry of taper junction of hip implants should be used. This illustrates a realistically stressed geometry for fretting-corrosion as well as a realistic crevice in contact of the head-neck interface.

1.4.4 Mechanically assisted crevice corrosion in hip joint implants

Although modularity offers many advantages in THA, some *in vivo* and *in vitro* studies have shown problems in this interface, such as the corrosion which can lead to the failure of the implant (Kretzer, Jakubowitz et al. 2009, Rodrigues, Urban et al. 2009). The emitted products

of corrosion and mechanical degradation could be distinguished as the cause of local tissue reaction, pseudotumor formation and finally retrieval surgery due to pain and body infection (Campbell, Ebramzadeh et al. 2010, Cook, Bolland et al. 2013, Cooper, Urban et al. 2013, Cooper 2014).

Studies conducted on the degradation mechanisms of metallic components report that high cyclic stresses of physiological activities cause repeated fractures of passive oxide films in the taper (Pillar 2009). This leads to an unstable electrochemical environment inside the contact crevice of the modular interfaces for the metallic components whose corrosion resistance relies on their passive oxide layer. As a result of the disturbance in this resistance mechanism, active attack occurs on the depassivated metallic surface. In fact, modularity leads to large crevice environment under continuous relative micromotions. This cyclic micromotion in the presence of corrosive body medium provides fretting-corrosion of metallic components (Figure 1.18) (Gilbert, Buckley et al. 1993, Rodrigues, Urban et al. 2009).

Removed due to copyright restriction

Figure 1.18 Digital images of retrieval implants suffering from severe fretting crevice corrosion at the modular junction (Rodrigues, Urban et al. 2009)

In addition to fretting-corrosion, crevice corrosion has also been detected as a significant contributing phenomenon in interfacial degradation of contacting metals (Gilbert, Mehta et al. 2009). Crevice corrosion is a form of attack that is localised and within crevices, followed by stagnating corrosive medium inside with low or no circulation with the bulk solution (Corlett, Eiselstein et al. 2010). The crevice corrosion can be an autonomous phenomenon which continues inside the crevice in the absence of fretting and mechanical disturbance. This is mainly because of the low pH of the crevice ambient, which continuously dissolves the passive layer and the active metal underneath.

1.5 Dynamics of hip joint and head-neck interface during daily activities

It was concluded that to replicate service condition of the head-neck interface of the hip joint implant, realistic loads needed to be applied on a full-scale interface geometry to induce similar stress-fields which would result in the desired micromotions. Head-neck interface experiences complex six degrees of freedom loading because of the combination of the joint contact force and frictional moments generated at the head-cup bearing surface. The mechanical loads resulting from activities of daily activities induce contact forces and frictional moments at the articulation which in turn induce forces, frictional torques and bending moments at head-neck interface (Figure 1.19) (Bergmann, Deuretzbacher et al. 2001, Bergmann, Graichen et al. 2010, Damm, Dymke et al. 2013).

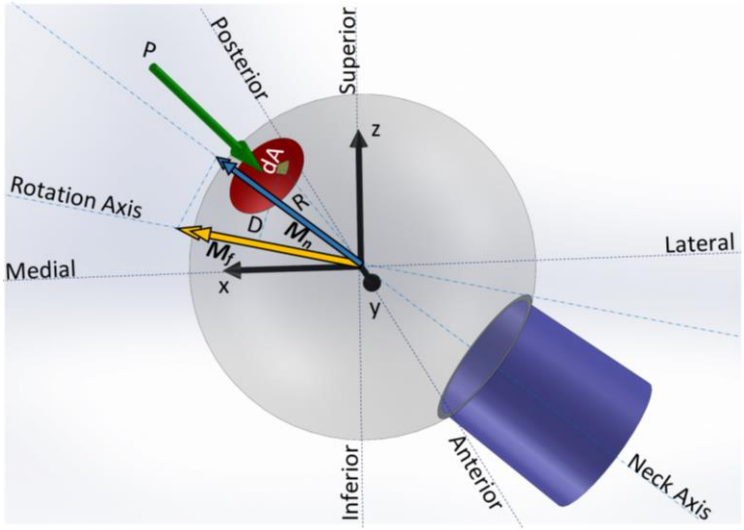

Figure 1.19 Motion of head inside the cup in the presence of force (p) and friction between head and cup induces forces and moments (Mf) with projection on all three axes. The frictional moment (Mf) has torque on head-neck interface (Mn)

Hip joint kinematic has an important role in the frictional moment of the hip joint; the direction of the frictional force is opposite to the direction of relative displacement; similarly, the direction of the frictional moment is opposite to the direction of the relative rotation. The hip joint can be considered as a ball-and-socket joint with three degrees of freedom and almost no translation between the components. (Bowman, Fox et al. 2010).

Kinematics of the hip joint is described with three rotational degrees of freedom of flexion-extension, abduction-adduction and internal-external rotation. Flexion is the movement of the hip joint at the lateromedial axis (in the sagittal plane – not shown in Figure 1.19) in which the angle between the joint and the body decreases, and the extension increases this angle.

Abduction increases the angle between the leg and the body at the anteroposterior axis (in the coronal plane) and adduction decreases this angle. Finally, internal rotation of the hip is the rotation of the hip at the inferosuperior axis (transverse plane), which moves the toe inward while external rotation moves the toe outward from the body.

Johnston et al. (Johnston and Smidt 1969) were the pioneers of recording hip joint kinematics. They used an electrogoniometer to measure hip-joint motion for walking. Electrogoniometer is a device which is attached to the body to measure the angle of the joint and send a proportional electrical output. The data recorded by Johnston et al. was collected from 33 normal cases of walking and showed 52 degrees in flexion-extension, 12 degrees of abduction-adduction and 13 degrees of internal-external rotation. This method used by Johnston et al. in 1969 is still prevalent (Fabry, Herrmann et al. 2013) due to its simplicity, low cost and accuracy.

Bergmann et al. (Bergmann, Graichen et al. 2010) provided a valuable database for the hip joint and gait analysis and loads for a range of daily activities. In this extensive research, Dr. G. Deuretzbacher oversaw gait analysis through inverse dynamics. For this, a Vicon system equipped with six infrared cameras was used. This system uses 3D data analysis to extract the kinematics of the hip joint.

Removed due to copyright restriction

Figure 1.20 Set-up for gait analysis, laboratory and local coordinate systems (Bergmann, Graichen et al. 2010)

The mechanical loads resulting from daily activities induce contact forces, frictional moments and bending moments on the implant and its interfaces (Damm, Dymke et al. 2013, Panagiotidou, Meswania et al. 2015). Head-cup contact forces are induced by body weight and muscle contraction forces. The bending moments resulting from the offset of forces and the contact area of the implant. The frictional moments are induced by the rotation of the head inside the cup (bearing couple) in the presence of friction (Bishop, Waldow et al. 2008, Bishop, Hothan et al. 2013). Fretting-corrosion at the head-neck interface, especially in larger diameter MoM bearings, are hypothesised to be influenced by frictional moments. Fretting wear is driven by relative micromotion at the head-neck interface, which is significantly influenced by the mechanical loading environment (Swaminathan and Gilbert 2012).

To determine head-cup contact forces, *in vivo* telemetry measurements have been conducted in several studies. English and Kilvington (English and Kilvington 1979) employed a prosthesis equipped with strain gauges to determine load magnitude but not the orientation. Bergmann et al. (Bergmann, Graichen et al. 1993) used the same method of telemetering forces to measure hip joint force magnitudes, orientations and moments at the femoral stem axis during walking and running gaits. They implemented three semiconductor strain gauges along with the inductive loop-powered telemetry system in a hollow neck sealed by a laser-welded plate that contained the antenna inside the ceramic head to collect and transfer the strain gauges signal with a frequency of 250Hz to an external receiver. Before implantation, they checked the safety of the implant through analytical calculations – 10 million cycles of fatigue test at a maximum load of 9300N – three times greater than ISO-7206-7:1993 – endurance performance of stemmed femoral components without torsion. The implant was checked through microscopic weld examination, corrosion response of the neck and biocompatibility and electrical devices reliability through intensive tests and examination. They observed two patients for 18 and 30 months. Their results revealed orders and directions of the forces in the hip joint implant for ranges of walking speed and other activities. Bergmann et al. (Bergmann, Graichen et al. 2010) expanded their previous work (Bergmann, Graichen et al. 1993) by investigating four patients during various daily activities; the outcomes of these two studies provide invaluable data of forces in hip joint implant for the research society and are freely available on the Orthoload website (orthoload.com). It should be mentioned that this data has been provided after spending immense time and money.

To determine the frictional moments induced in the head-cup interface, Damm et al. (Damm, Graichen et al. 2010) instrumented a hip joint prosthesis to provide measuring three forces and three moments components (Figure 1.21). They measured deformation of a hollow neck via six semiconductor strain gauges. They also integrated a small coil inside the neck cavity for inductive power supply. They closed the neck cavity by electron beam welding. They implemented a 120 Hz sampling rate of pulse interval modulate for sensor signals and transmitted the pulses at radio frequencies. For radio transmit, they used a small antenna loop placed inside the ceramic head connected to the electronics circuit by two-pin feedthrough. The external unit provided the inductive power supply, load calculation from neck deformation and real-time display of loads.

Removed due to copyright restriction

Figure 1.21 Cut-model of the instrumented cementless tapered femur with a ceramic head (Damm, Graichen et al. 2010)

Damm et al. (Damm, Dymke et al. 2013) used the instrumented implant to measure forces and frictional moments and derived friction coefficients, during walking for a 32 mm ceramic-on-polyethylene bearing couple *in vivo* for eight patients over a course of three months. They reported the average peak contact forces as 248% of the body weight and peak frictional moment as 0.26% of body weight times metre. This study reported varying coefficient of friction of the joint but hasn't provided any analytical models for it as a function of effective parameters. Frictional moment depends on the friction coefficient of the bearing couple, the

size of the implant, and the geometry of the bearing couple (Bishop, Waldow et al. 2008, Bishop, Hothan et al. 2013, Farhoudi, Oskouei et al. 2015)). Hence, frictional moments measured for a specific head-cup bearing couple configuration cannot be generalised to other bearing geometries and/or materials. Thus, the state space, including all material combinations, geometries (head-cup sizes, neck offset and version/anti-version) and daily activities, is too large to be studied by *in-vivo* experimental methods to provide the frictional moment of all different combinations of hip joint design.

1.6 Friction at the head-cup interface of the hip joint implant

In this section, friction at the head-cup interface will be reviewed as it is of the effective parameters on the magnitude of the frictional moment on the head-neck interface.

Scholes et al. (Scholes, Unsworth et al. 2000) investigated the friction performance of 28-mm diameter head-cup interfaces with material combinations as: metal-on-metal (CoCrMo-CoCrMo), ceramic-on-ceramic (Alumina-Alumina) and metal-on-polyethylene (CoCrMo-Ultra High Molecular Weight Polyethylene (UHMWPE)) inside lubricants as: carboxy methyl cellulose-(CMC) at viscosities of 0.001, 0.005, 0.012, 0.033 and 0.155 Pa s, and 100% single batch, newborn calf serum with a viscosity of 0.007 Pa s. The CMC was chosen due to similar rheological properties to synovial fluid. Ceramic-on-ceramic joints inside CMC showed full fluid film lubrication (friction factor range of 0.0002 to 0.0055). In contrast, with bovine serum as the lubricant, the full fluid film lubrication was inhibited due to adsorbed proteins (friction factor range of 0.0025 to 0.075). Metal-on-metal and metal-on-Polyethylene prostheses operated under a mixed lubrication regime when examined with CMC as the lubricant (friction factor range of 0.18 to 0.32 and 0.008 to 0.043, respectively). For the metal-on-metal joints inside the bovine serum as the lubricant, the adsorbed protein layer reduced the friction (friction factor range of 0.13 to 0.18). The use of bovine serum as the lubricant significantly increased the friction in the metal-on-polyethylene joint (friction factor range of 0.03 to 0.04).

In another study, Scholes et al. (Scholes and Unsworth 2000) investigated the friction of the same head-cup material combination of the previous study in different lubricants of CMC fluids, silicone fluids, synovial fluid and different concentrations of bovine serum. The outcomes suggest that The metal-on-metal joints have friction factors one order of magnitude higher than ceramic-on-ceramic and metal-on-polyethylene, except when they

are lubricated with high viscosity silicone fluid. When lubricated by CMC, ceramic-on-ceramic had friction factors of at least one order of magnitude smaller than metal-on-metal and metal-on-polyethylene. However, in case of lubrication with the bovine serum of any concentration, the friction factor of ceramic-on-ceramic was in the same order of magnitude of the metal-on-polyethylene. Outcomes of these two studies by Scholes et al. suggest to avoid using of non-biologilcal lubricants during design and evaluation of orthopaedic bearing surfaces and rather use a standard lubricant during measurement of wear and friction of artificial joints.

In some studies, the friction coefficient at the hip joint bearing couple is considered as a function of contact stress. In a study on the effect of contact pressure on the wear and friction behaviour of Ultra-High Molecular Weight Polyethylene (UHMWP), Saikko (Saikko 2006)suggested a power-law fitting to define friction factor as a function of contact stress. Wang et al. (Wang, Essner et al. 2001) suggested a similar fitting to calculate the friction factor of (Saikko 2006). Both these studies conducted the fitting on experimental points calculated during simplified unidirectional loading and motion. They selected experimental data points from uniform parts of motion of the experiment and did not include points with a change in the direction of rotation which exhibits complicated behaviour.

In an MoM head-cup interface, a metallic head from the femoral component articulates with a cup from acetabular component; this happens in the presence of synovial fluid (a viscous non-Newtonian fluid, existing in cavities of synovial joints). Film lubrication from the synovial fluid is the most effective parameter in the frictional behaviour of the bearing couple (head and cup). An investigation on the head-cup tribology shows that its lubrication comprises fluid film lubrication along with boundary asperity contact regions (Wang, Brockett et al. 2008). This is called a mixed lubrication regime. The friction of the head-cup interface is mainly caused by contact pressure in the boundary asperities. High friction could lead to excessive heat, change in the adsorbed protein layer on the bearing surface and consequent change in lubrication regime.

Understanding the friction behaviour of the implant can significantly improve assessing the success of the hip implant from the aspects related to the friction, e.g. head-cup interface wear, head-neck interface fretting-corrosion and acetabular cup loosening. Unfortunately, studies on the lubrication regime of the head-cup implant are mainly theoretical and cannot

be projected to experimental verification due to the simplifications required to change the underdetermined system of equations to a determined system of equations. To this end, the theoretical prediction of tribological behaviour of the implant in-service condition could be a significant development.

The hydrodynamic pressure in spherical geometry is calculated by Reynolds for the transient condition:

$$sin\theta\frac{\partial}{\partial\theta}\left(h^3 sin\theta\frac{\partial p}{\partial\theta}\right)+\frac{\partial}{\partial\theta}\left(h^3\frac{\partial p}{\partial\theta}\right)=6\eta R_C^2 sin\theta\begin{bmatrix}-\omega_x(sin\varphi\ sin\theta\ \frac{\partial h}{\partial\theta}+cos\varphi\ cos\theta\ \frac{\partial h}{\partial\varphi})\\+\omega_y(cos\varphi\ sin\theta\ \frac{\partial h}{\partial\theta}+sin\varphi\ cos\theta\ \frac{\partial h}{\partial\varphi})+\\+\omega_z sin\theta\frac{\partial h}{\partial\varphi}\end{bmatrix}$$

$$12\eta R_C^2 sin^2\theta\frac{\partial h}{\partial t}$$

Equation 1-5

(Wang, Brockett et al. 2008)

In Equation 1-5, φ and θ are the spherical coordinates, h is total film thickness, η is the viscosity of the synovial fluid, R_c is the cup radius, p is pressure, t is time and ω_x, ω_y and ω_z are the relative Euler angular velocities of the head and cup about the corresponding axis. Assuming the kinematic (ω_x, ω_y and ω_z) and material and geometrical characteristics (R_c and η)as known, this equation results in unknowns of $\frac{\partial}{\partial\theta}\left(h^3 sin\theta\frac{\partial p}{\partial\theta}\right)$, $\frac{\partial p}{\partial\theta}$, $\frac{\partial}{\partial\theta}\left(h^3\frac{\partial p}{\partial\theta}\right)$, $\frac{\partial h}{\partial\theta}$, $\frac{\partial h}{\partial\varphi}$ and $\frac{\partial p}{\partial\theta}$. To solve this underdetermined system of equations of the assumptions $\omega_y = 0$ and $\omega_z = 0$ so, the number unknowns in the partial differential will decrease (Liu, Jin et al. 2006, Wang, Brockett et al. 2008, Meng, Liu et al. 2011). This assumption is usually justified by the dominance of flexion-extension while walking. The system of equations is usually solved over the surface of the head-cup interface by numerical methods by implementing boundary conditions of the unknown pressures, adding load balance equations in three axes of the coordinate system, calculating the h by the relation between radial clearance and equivalent discrete spherical convolution model and the corresponding Fast Fourier Transform technique to solve elastic deformation (Liu, Jin et al. 2006, Wang, Brockett et al. 2008, Meng, Liu et al. 2011). This sophisticated method has improved by a cluster that focusses on the analytical calculation of friction and its torques at the head-cup interface. This method is usually called the electrohydrodynamic simulation of the hip joint. In one of the studies

(Wang, Brockett et al. 2008), the outcomes of this method were compared by experimentally measuring the frictional torques of 28 mm MoM hip implant under dynamic load and one degree of freedom (flexion-extension) motion. The inputs of this evaluation are shown in Figure 1.22.

Removed due to copyright restriction

Figure 1.22 Input of the experimental evaluation of the electrohydrodynamic numerical method. a) time-dependant motion and velocity in flexion-extension-applied load perpendicular to the motion axis (Wang, Brockett et al. 2008).

This evaluation was conducted by comparing the real frictional torque measured using an experimental device shown in Figure 1.23.

Removed due to copyright restriction

Figure 1.23 Testing setup used to measure the frictional torque to evaluate the method (Wang, Brockett et al. 2008).

The theoretical results for frictional torque are compared to real torques from experiments. As seen in Figure 1.24, there is a considerable lack of accuracy in predicting the calculation of torque for a 0–0.5(s) time interval of the cycle period.

Removed due to copyright restriction

Figure 1.24 Comparison of the theoretical calculation of frictional torque calculated by the electrohydrodynamic method with real experimental torques(Wang, Brockett et al. 2008).

In low angular velocities, the frictional torque from the theoretical method is reported as zero while there are non-zero magnitudes of torque at this velocity. There is also a considerable difference in the theoretical outcome in the rising side of the frictional torque. The study of Wang et al. (Wang, Brockett et al. 2008) is the only electrohydrodynamic study in which its outcomes are evaluated against the real experimental frictional moments. The assumption is that no motion in abduction-adduction and internal-external rotations of the joint could prevent the electrohydrodynamic method to be extended to the dynamics of the daily activities to calculate the friction and the frictional torque.

To use another approach to calculate the friction factor at the head-cup interface of the hip implant, Flanagan et al. (Flanagan, Jones et al. 2010) developed the Stribeck plots for ceramic-on-ceramic and conventional metal-on-UHMWP implants. The Stribeck plot shows the relation of the friction factor in fluid-lubricated contacts to the Sommerfeld number (Equation 1-6)

$$z = \frac{\eta u r}{L}$$

Equation 1-6

where z is the Sommerfeld number, η is the viscosity of the lubricant, u is the entraining velocity, and L is the applied load. The Stribeck plot is developed for the lubrication cases with one degree of freedom (one direction of relative motion/rotation). Flanagan et al. (Flanagan, Jones et al. 2010) studied the friction of the bearing couples via a Phoenix Tribology equipment. They had the head-cup assembly in an inverted position from the real *in vivo* service condition. During a stroke of ±24° flexion-extension, they measured the friction factor of the component in a fully lubricated regime. The results of their study are shown in Figure 1.25. The developed Stribeck plot cannot be used in the analytical calculation of frictional moment of daily activities with their three-dimensional rotation because 1) it is derived for one degree of rotation 2) it is calculated under a fully lubricated regime, while the real service condition of the head-cup interfaces occurs in mixed lubricated regime with boundary asperities' dry contacts (Wang, Brockett et al. 2008).

Removed due to copyright restriction

Figure 1.25 Stribeck plot of ceramic-on-ceramic and metal-on-UHMWP hip implants with 28 mm diameter (Flanagan, Jones et al. 2010)

In a different approach to investigating friction at the head-cup interface of hip joint implant, Wang et al. (Wang, Essner et al. 2001) studied the relation of contact stress and friction at the head-cup interface, focussing on metal-on-polyethylene bearing couples. They investigated friction of UHMWP cups with internal diameters varying from 32.05 to 36.05 mm-minimum thickness of 12 mm against a 32 mm (+0/-0.05 mm) cobalt-chromium head. A minimum thickness of 12 mm was maintained to ensure that the thickness of the cup is higher than the critical magnitude of 6 mm and will not affect the contact stress. A varying range of cup diameter under the same load caused variations in the stress-field of the contact and

corresponding friction response. The study was conducted using an eight-station hip joint simulator (MTS, Eden Prairie, Minnesota – Figure 1.26).

The heads and cups were installed in an inverted manner. As shown in Figure 1.26, the head was attached to the actuator head, which moved in axial and torsional directions. The test was conducted in the presence of a lubricant – a double-filtered α-calf serum that had been thinned with 50% deionised water. This dilution brought the protein concentration to 20 mg/ml, similar to that of a normal synovial fluid. The cup was mounted on the horizontal table. While sequential loads of 50, 100, 200, 500, 1000 and 2000N were applied, the head rotated to +/-10° at 33°/s magnitude of torque collected at -2.5° and +2.5° for each load case.

Figure 1.26 The MTS, Eden Prairie, Minnesota hip simulator device used by Wang et al. (Wang, Essner et al. 2001) to study the relation between friction and wear of UHMWP to contact stress

The measurements were repeated for each of the loading cases, and after 500 cycles of +/-10° rotation under a constant load of 2000N. They calculated the friction coefficient by dividing the measured torque to the statically applied load and the head radius. As seen in

Figure 1.27, with an increase in the radial clearance of the bearing couple, the contact stress increases. This is due to the geometry of the contact area, which decreases with increasing nonconformity (radial clearance) of the bodies, which leads to higher stress under the same amount of load.

Removed due to copyright restriction

Figure 1.27 Increase in contact stress by increase in radial clearance at metal-on-polyethylene head-cup interface (Wang, Essner et al. 2001).

As seen in Figure 1.28, for a metal-on-polyethylene bearing couple, an increase in radial clearance causes a decrease in the friction factor. Given that increase of radial clearance increases the contact stress, from Figure 1.27 and Figure 1.28, it can be concluded that in metal-on-polyethylene bearing couples, increase in contact stress causes a decrease in the friction coefficient.

Removed due to copyright restriction

Figure 1.28 Decrease in friction coefficient of metal-on-polyethylene (UHMWP) bearing couple because of an increase in the radial clearance (Wang, Essner et al. 2001)

The decrease in the friction coefficient by increase in the contact stress in metal-on-polyethylene bearing couples is better depicted in Figure 1.29. The friction coefficient has a significant correlation to maximum contact stress. The best fit correlation to friction coefficient to maximum contact stress was as follows:

$$\mu = 0.18\sigma_0^{-0.33}$$

Equation 1-7

Removed due to copyright restriction

Figure 1.29 Decrease in friction coefficient by an increase in contact stress in a metal-on-polyethylene head-cup interface (Wang, Essner et al. 2001)

The outcome of this study can be used for the analytical calculation of frictional moment for metal-on-polyethylene bearing couples. To the best of the author's knowledge, there is no such investigation for MoM bearing couples which correlates friction coefficient to contact stress.

St. John et al. (St. John, Zardiackas et al. 2004) evaluated the MoM THRs which expected to have a better wear resistance performance due to having a higher carbon content(0.25%) in a CoCrMo. They conducted an *in vitro* simulation of wear of this alloy by examining a 28 mm MoM bearing couples and compared its performance with a metal-on-polyethylene bearing couple. On a course of five million cycles, volumetric wear of the metal-on-polyethylene bearing couple was 110 to 180 times of the MoM bearing couple which had a higher carbon content in their CoCrMo alloy. They have found a good agreement between this research and other studies on periprosthetic tissues concerning volume and combination of retrieved particles.

In a study on MoM THRs, William et al. (Williams, Jalali-Vahid et al. 2006) hypothesised that THR by MoM changes the soft tissue tensioning and alters loading on the THRs during the swing phase of gait and consequently changes fluid film lubrication, friction and wear. In their study, they investigated ten 28mm diameter cobalt-chromium alloy (ASTM F1537) femoral heads and acetabular cups (DePuy International, Leeds, UK). After measuring the bearing couple dimensions and the existing radial clearance, they conducted a theoretical lubrication modelling by numerically solving EHL theory for the given geometry in bovine serum. From the theoretical calculations, they found that lower swing phase load comes with higher fluid film thickness Figure 1.30.

Removed due to copyright restriction

Figure 1.30 Transient lubrication film thickness vs time for low (100N) and high (280N) swing phase load. (Williams, Jalali-Vahid et al. 2006)

They also conducted experimental tests with low swing phase load (100N) as shown in Figure 1.31 for five million cycles on five couples and high swing phase load (280N, as per ISO 14242-1) for the other five couples.

Removed due to copyright restriction

Figure 1.31 Frictional torque measured during experimental simulation cycles wit a low (100N) swing phase load

The mean coefficient of friction of the MoM bearings at the peak load of 2kN was 0.129 and 0.173 for the loading scenarios of 280N and 100N swing phase loads, respectively. By measuring the wear particles during the test, they observed that this increase in friction coefficient increases the steady-state wear by 10-fold.

(Haider, Weisenburger et al. 2016) measured three-dimensional taper moments due to friction and contact load in THR tapers. Using a six DOF load cell during three-dimensional kinematics of walking (including internal-external rotation and abduction- adduction), they investigated various bearing couples including metal on polyethylene, metal on ceramic and metal on metal bearing couples. They also studied the effect of scratches over the polyethylene surface on the friction of highly cross-linked polyethylene coupled with a 40mm diameter femoral head. Presence of scratch increased the friction from 0.056 and 0.062 to 0.088 and 0.082 for highly cross-linked and highly cross-linked with vitamin E version, respectively.

In their study on 44mm metal on polyethylene earing couples, conventional UHMWPE showed the lowest friction at 0.045, followed by 0.046 for highly cross-linked. Ceramic on UHMWPE showed higher friction of 0.079 likely due to the ceramic surface is rougher than usual. Comparing metal-on-metal without and with TiN coating showed 0.049 and 0.097 friction factors respectively. The coating layer of all of the bearing couples was worn away for all the cases. The outcomes of this study present the wide range of effective parameters on frictional behaviour of bearing couples. Contribution of friction factor on the wear of the bearing couple is significant as reflected by studies such as (Williams, Jalali-Vahid et al. 2006).

Kaddick et al. (C. Kaddick 2015) conducted a study on the measurement of taper moments induced by contact loads and friction in 28mm and 48mm ceramic-on-ceramic and metal-on-ceramic bearing couples. By introducing a new testing rig equipped with spherical air bearing and several load sensors, they were able to measure three-dimensional frictional moments under realistic complex articulation of the joint bearing couple. They reported a highly dynamic moments under ISO walking cycles increasing by an increase of the head size. Their study reported a torque of 1.4Nm and a bending moment of 2.0Nm for 28mm head size. For the 48mm head size, these values were increased to 2.5Nm and 4Nm, respectively.

Sonntag et al. (Sonntag, Braun et al. 2017) conducted a three-dimensional friction measurement on three different sizes (28, 36 and 40mm) ceramic-on-polyethylene bearing couples. For this aim, they modified a standard hip simulator (Minibionix 852 incl. 4 DOF Hip, MTS Systems Corporation, USA) for high precision measurements of small frictional effects (Figure 1.32).

Figure 1.32 Heidelberg friction simulator. Modification of a single-station simulator to allow for low friction measurements in the hip joint. (Sonntag, Braun et al. 2017)

They verified the accuracy and performance of their setup by comparing its measurements with a pendulum model which measured the frictional effect on the damping behaviour of the oscillation (no need for any force/moment transducer).

Figure 1.33 Physical pendulum. (A) Pendulum setup with 2000 N arm weight. (B) Detail view on fulcrum. (C) Theoretical model of the physical pendulum (clockwise rotation).

Their results suggested that moments recorded from the physical pendulum experiment (36mm ceramic-on-crossed linked polyethylene) were in agreement with results of flexion-extension of the modified simulator. Of the observation was that maximal frictional moment remained constant against decreasing oscillation amplitude of the pendulum (Figure 1.34).

Figure 1.34 Pendulum results. (A) Comparison of friction results from the physical pendulum and the extension-flexion oscillation using the hip simulator (36 mm ceramic-on-XPE). (B) Extension-flexion (hip simulator) and best-fit torque amplitudes for different head sizes. (C) Oscillation angles from experimental (Pendulum) and calculated data (Best-fit, 36 mm ceramic-on-XPE).

In an *in-vitro* study on moments of friction of large MoM head-cups and other modern head-cups, Bishop et al. (Bishop, Waldow et al. 2008) simulated physiological joint condition under different service scenarios. They systematically studied tribology of the joint in a variation of frequency of load cycle (Hamrock and Dowson 1978), duration of resting (Nassutt, Wimmer et al. 2003), the effect of load at the swing (Williams, Stewart et al. 2004) and lubricant performance.

They conducted the tests using a custom-developed setup, as shown in Figure 1.35. The setup was designed to apply the unidirectional force isolated from the measured moment (Bishop, Waldow et al. 2008). As shown in Figure 1.35, the implant is positioned in an inverted manner from *in-vivo* service condition.

Removed due to copyright restriction

Figure 1.35 Gait loading simulation device used by Bishop et al. (Bishop, Waldow et al. 2008) to measure frictional moment in hip joint implant. As shown on the right, axial force F and rotation angle Ø were applied as inputs and M was measured as output (Bishop, Waldow et al. 2008)

They investigated a range of bearing couples of MoM, metal-on-polyethylene, metal-on-ceramic and ceramic-on-ceramic. Geometric details of the investigated implants are given in Table 1-1.

Table 1-1 Implant materials and dimensions investigated by Bishop et al. (Bishop, Waldow et al. 2008) for in vitro frictional moment (Bishop, Waldow et al. 2008)

An example of the force profile applied by the machine is shown in Figure 1.36. The parameters studied regarding to load profile were frequency (0.5, 1, 2 Hz) and swing-phase force magnitude (100, 250, 500N).

Removed due to copyright restriction

Figure 1.36 Vertical component normal walking force and flexion-extension angle applied to samples (Bishop, Waldow et al. 2008)

The experiments were conducted with 17% foetal calf serum as the lubricant. To study the effect of lubrication, they tested the implants N0.1 (metal-on-metal), No.2 (metal-on-polyethylene) and #7 (ceramic-on-ceramic) in water as well.

They also studied the effect of resting period on a frictional moment by applying different resting periods between the dynamic loadings. An example of this loading procedure is given in Figure 1.37. More details about the testing procedure and data collection are available in their publication (Bishop, Waldow et al. 2008).

Removed due to copyright restriction

Figure 1.37 Example of applying different rest periods between the loadings to study rest period effect on frictional moment of the implant (Bishop, Waldow et al. 2008)

In the findings of their research, they have reported the frictional moment under peak load. They also have extracted the friction coefficient by dividing the moment at the peak force to the peak load and radius of the head. This result is presented in Table 1-2.

Table 1-2 The results of variation in swing load, frequency, lubrication and rest period in the frictional moment and reported friction coefficient for norm testing

Removed due to copyright restriction

Their study also reported valuable outputs of variation of frictional moment under the norm loading case (swing load=250N, Frequency=1Hz and lubricant of serum) as shown in Figure 1.38.

Removed due to copyright restriction

Figure 1.38 Frictional moment profile of different bearing couples under the norm loading case (swing load=250N, Frequency=1Hz and lubricant of serum) (Bishop, Waldow et al. 2008)

This study is one of the most comprehensive studies on friction coefficient of different implant interfaces and its reported friction coefficient could be used to evaluate the analytical or numerical models accurately in predicting frictional moments of different material combinations.

1.7 Mechanical response of the head-neck interface to daily activity loads

Mechanical responses of the head-neck interface to daily activity loads include micromotions, stress-field and resulted fretting work. These are of interest because fretting is identified as the initiator of the fretting-corrosion phenomenon at the head-neck interface and is also termed as mechanically assisted crevice corrosion in modular junctions (Gilbert, Mehta et al. 2009). This needs to be well understood to comprehend the concept of fretting-corrosion completely. Fretting itself is a function of a variety of parameters, in particular stress field, micromotion amplitude, frequency and number of cycles (Berthier, Vincent et al. 1989).

The mechanical environment at the head-neck junction is complex and is subjected to forces and frictional moments. These vary with time, type of physical activity, characteristics of the patient and the geometric and material properties of the implant (Bishop, Waldow et al. 2008, Bergmann, Graichen et al. 2010, Farhoudi, Oskouei et al. 2015).

To better understand fretting at the head-neck junction, the mechanical environment of the junction needs to be studied in terms of contact pressure, contact length and relative micromotions. Finite element analysis (FEA) is found to be a cost-effective method for this purpose (Donaldson, Coburn et al. 2014, English, Ashkanfar et al. 2015). Fallahnezhad et al. (Fallahnezhad, Farhoudi et al. 2016) developed a three-dimensional finite element (FE) model to investigate the torsional strength of a head-neck taper junction with different material combinations. As an example of the application of FE for revealing complex mechanical responses of taper junction, this study unveiled that due to conical geometry and complex 3D stress-field of the contact of head and neck, the femoral neck bulges during a twist-off moment which causes the neck to tighten inside the head and require higher torque to twist-off.

Figure 1.39 a) Radial deformation of head due to assembly force of 3700N b) radial bulging of the under the twist-off torque (19.8Nm) (Fallahnezhad, Farhoudi et al. 2016)

They reported that under the same assembly force, a higher contact length occurred between a CoCr head and a titanium neck as compared to a CoCr head and a CoCr neck and consequently, the CoCr/Ti combination had higher torsional strength. In another study, Donaldson et al. (Donaldson, Coburn et al. 2014) developed a stochastic FEA to evaluate the effective parameters on the frictional work over a cycle (fretting work) in a head-neck taper junction based on the forces of level gait. They concluded that the major parameters that effectively contribute to the value of fretting work are taper angle mismatch, centre offset and body weight. It was also reported that every 0.1˚ increase in the mismatch angle can increase the contact pressure by 85 MPa. To verify their model, they applied an assembly force at 45˚ off-axis to two sets of head-neck junctions made of Al 6061 at a 3:1 size scale. As stated in their paper, for a single case study (not stochastic) a more accurate validation is required for a more realistic prediction.

Removed due to copyright restriction

Figure 1.40 Left: Design variables studied by Donaldson et al. (Donaldson, Coburn et al. 2014) including taper angle, trunnion angle, angular mismatch, neck angle, centre offset, trunnion length, trunnion diameter and taper thickness. Right: Section cut of FE mesh of a typical simulation (Donaldson, Coburn et al. 2014)

Dyrkacz et al. (Dyrkacz, Brandt et al. 2015) developed a 3D FE model to seek the parameters that could affect relative micromotions in the taper junction. They applied an assembly force, 3300N compression force and 100N of tension to the simulated head. Their study revealed that assembly force, taper size and materials combination play an important role in changing the micromotion values. They reported a greater increase of micromotion in mixed material combination (CoCr head on Ti alloy neck) as compared to same material combination of all CoCr alloys. However, in their model, the angular mismatch between the head and neck components was neglected despite it having a significant effect on the contact pressure and micro-motions (Donaldson, Coburn et al. 2014). This simplification in their study was not justified.

Thom et al. (Thom, Imran et al. 2017) developed a FE model consistent with their fretting experiments of assembling, disassembling (Figure 1.41) and fretting wear of head-neck junction. In their FE model, wear equation was implemented for wear scoring comparison. They concluded that the FE models that do not incorporate geometry updates are not appropriate for prediction of the degradation of the material. This comes to the edges of

complication of FE modelling which successfully reveals the mechanics of the junction for short period of time, but its modelling of the entire service condition of the part would be time-consuming due to a wide range of required inputs from experiments.

Removed due to copyright restriction

Figure 1.41 Demographic of FE boundary condition and initial condition of push-on and pull off (Thom, Imran et al. 2017)

Elkins et al. (Elkins, Callaghan et al. 2014) investigated the extend of the head size effect on stability of THA while monitored, the changes in wear at the taper junction due to changes of the head size. In their study, they also investigated the effect of the head size and the assembly impaction on the potential wear in the bearing. Based on its results, this research refers to the utilisation of large head THA as an example of "choices and compromises" between reduction in the impingement, improvement of the stability and enhancement of elastohydrodynamic of the joint lubrication against significant increase in fretting-corrosion of the subsequent failures. They investigated the range of head size of 32 to 56mm (Figure 1.42). Their result suggests that the increase of the head size increases the stability of the joint. However, this benefit considerably diminishes in head sizes greater than 40mm. In sizes larger than 40mm modest improvement in joint stability comes with the considerable cost of increased wear potential in the head-neck junction. The authors have raised limitations of

their study as simplifying the damage to monitoring only fretting and not the electrochemical effect of corrosion. They also raise limitations in considering identical liner thickness and liner edge profile for all the head-sizes.

Removed due to copyright restriction

Figure 1.42 A) cumulative linear wear at the end of the motion, B) cumulative linear wear for sit to stand. For all motions linear wear increased with increased femoral head diameter.(Elkins, Callaghan et al. 2014)

Overall, FEA is a cost-effective method to understand the mechanical responses of head-neck geometry under a cyclic load. Additionally, there is no experimental method yet to comprehensively and accurately investigate the stress-field, micromotions and fretting work of the close geometry of the head-neck interface.

1.8 *In vitro* studies on Fretting-corrosion and mechanically assisted crevice corrosion of THA

The interrelation between effective parameters of fretting-corrosion, such as material, geometry and loads and their complications, concludes experimental study to be the most suitable method of research for this phenomenon. Literature review of fretting, corrosion, fretting-corrosion and mechanically assisted crevice corrosion, especially in head-neck interface of the implant, shows that for a realistic *in vitro* study of head-neck interface, a real geometry needs to be examined under realistic loads of daily activities. This study needs to be conducted in a fluid with similar corrosivity of body ambient, such as Ringer's solution or Bovine serum, as a representative of joint synovial fluid. This will lead to investigating fretting-corrosion and mechanically assisted crevice corrosion in similar stress-field, micromotion response of interface, crevice geometry and corrosivity of the environment. Realistic loads of hip joint implant comprise a force vector caused from body forces and muscle contraction (Bergmann, Graichen et al. 2010) alongside frictional moment vector induced by relative slip of head-cup interface in the presence of friction (Damm, Dymke et al. 2013, Farhoudi, Hashemi Oskouei et al. 2014, Damm, Bender et al. 2017).

Some *in vitro* studies have conducted displacement-control pin/cylinder on disk experiments in combinations of relative displacement and normal forces (running condition fretting map) to depict material response varying from no degradation to cracking and wear induced by debris formation. Dusabeau et al. (Duisabeau, Combrade et al. 2004) aimed to describe damage mechanism at the head-neck interface for a material combination of Ti-6Al-4V, as the neck, in contact with stainless steel (AISI 316L SS), as the head. The geometry of the test comprised a cylindrical stainless steel (radius=20mm and length=10mm) fretting against a flat surface of Ti-6Al-4V; they applied a force per length of 4.3-12.6N/mm on the length (10mm) of the contact rectangle (Figure 1.43) to replicate stress field as compared to the head-neck interface for an 80 Kg person.

Removed due to copyright restriction

Figure 1.43 Schematic view of TRIBOMINES® fretting-corrosion setup (Duisabeau, Combrade et al. 2004)

They conducted the fretting test in air and fretting-corrosion tests in Ringer's solution and continuously recorded friction coefficient, tangential force-displacement (F_t-D cycles in Figure 1.44) and free corrosion potential. These experiments show that at the beginning of the test in both ambients, the fretting regime lied in gross slip gradually changed to a partial slip (Figure 1.44).

Removed due to copyright restriction

Figure 1.44 Interdependency of fretting regime, dissipated energy and open circuit potential during fretting-corrosion test in Ringer's solution (Duisabeau, Combrade et al. 2004)

They reported that the Ringer's solution modifies the transition of the fretting regime to lesser fretting related damages but adds corrosion degradation to the interface. The results of this study provide a qualitative understanding of the resulted damages of fretting-corrosion. These results cannot be projected to real service condition of the head-neck interface due to significant simplifications, such as conducting the tests in displacement-control while the real service condition of the implant is dominated by the applied body loads and displacements are not necessarily repeated with the same range in every single cycle as in displacement control tests.

In another study based solely on fretting at the head-neck interface, Zhang et al. (Zhang, Harrison et al. 2013) conducted pin-on-disk tribological and wear tests in a pin-on-disk arrangement for material combinations of Co–28Cr–6Mo/forged Ti–6Al–4V and Co–28Cr–6Mo/DMLS Ti–6Al–4V. They implement a dead weight on the CoCr pin in contact with the Ti alloy disk. The Ti alloy disk reciprocated, leading to the required relative motion of the surfaces.

Removed due to copyright restriction

Figure 1.45 a) Pin-on disk testing setup, b) Schematic view of the pin-on-disk arrangement (Zhang, Harrison et al. 2013)

The geometry and amount of load were set to induce Hertz stress at the interface within the range of the stresses that could be calculated by FE model of a head-neck interface in its service condition. By conducting the fretting wear tests in a varying range of material combinations, normal load, surface roughness and number of fretting cycles, the wear

volume was formulated to form inputs of the FE model of fretting wear for a high number of cycles. The results of this study suggest that DMLS Ti64 alloy showed better wear resistance characteristics and lower frictions in the range of stresses occurring in the head-neck junction. From the simulated solely fretting wear for 10 years of service condition, the wear depth was predicted to be about 1µm.

Removed due to copyright restriction

Figure 1.46 The FE model used for the prediction of fretting wear at the head-neck junction (Zhang, Harrison et al. 2013)

This study is one of the first to develop a numerical method to evaluate degradation at the head-neck interface. This study assumes that fretting is the dominant phenomenon of degrading the interface and the taper-lock contact environment doesn't let any moisture to enter the interface. This is a significant and non-justifiable simplification in monitoring the service condition of the head-neck interface. Furthermore, they neglected corrosion phenomenon while corrosion at the head-neck has been reported as the main cause of

exposing metal ions and debris to the surrounding tissue and cause ALTR (Campbell, Ebramzadeh et al. 2010, Cooper, Urban et al. 2013, Tetreault, Jacobs et al. 2018).

To provide an in-depth theoretical fretting-corrosion study, Swaminathan et al. (Swaminathan and Gilbert 2012) have developed a fretting-corrosion test which incorporates both mechanical and electrochemical aspects of fretting-corrosion. Their theoretical model suggests that the rate of volume degradation of an oxide film is a function of passive film formation current, the density of oxide film and effective valence of the oxide. Passive film formation current is a function of the stress-field, material characteristics and varying surface characteristics, including the density of asperities. In their experimental tests, they investigated the effect of applied normal load in fretting-corrosion performance with Ti6Al4V/Ti6Al4V, CoCrMo/Ti6Al4V and CoCrMo/CoCrMo material couples under potentiation condition with a determined roughness of the surfaces. Their observation showed that Ti6Al4V/Ti6Al4V has the highest corrosion current in potentiation condition along with a higher coefficient of friction and dissipated energy, all suggesting a higher amount of material degradation. Expanding this method to complicated geometries, such as head-neck interface, would involve a wide range of difficulties and is hardly repeatable due to manufacturing tolerances which cause deviation in stress-field and density of surface asperities both effective on passive layer formation current.

Figure 1.47 Schematic view of fretting-corrosion setup used for data collection by Swaminathan et al. to investigate fretting-corrosion and to collect required input parameters of their theoretical fretting-corrosion model. (Swaminathan and Gilbert 2012)

In an innovative approach in this research cluster, Royhman et al. (Royhman, Patel et al. 2017) studied fretting-corrosion on a double-sided pad contacting with a middle specimen in the fretting arrangement. This arrangement is called single clamp type of fretting fatigue tests which have been reported as a more suitable fretting fatigue test arrangement for low-stress-high-displacement ranges and high stresses with high displacement ranges (Neu 2011). These cases of fretting-corrosion could be projectable to loosen Morse tapers of hip joint implants. In this study, Bovine calf serum with 30g/L protein content was used as the corrosive medium representative of body corrosive ambient. In the examined material combinations of Ti6Al4V-Ti6Al4V-Ti6Al4V, Ti6Al4V-Ti6Al4V-CoCrMo, and CoCrMo-Ti6Al4V-CoCrMo, they reported the Ti6Al4V-Ti6Al4V-Ti6Al4V exhibited superior electrochemical behaviour and earliest forming of the passive film. This research also provided a qualitative outcome reporting dependency of degradation mechanisms at the junction to material and mechanical ambient.

Figure 1.48 A) Fretting-corrosion testing chamber of a rod fretting against two pads in presence of Bovine solution. B) Top view of the mechanism displaying the pressing mechanism of pads (Royhman, Patel et al. 2017)

These studies provide a qualitative evaluation of the effect of materials and loading condition on fretting-corrosion. However, due to considerable simplification in testing conditions, these results cannot be directly expanded to the service condition of the implant.

For a better understanding of the real service condition of the implant, some studies have applied simplified loads on a real scale implant. Jauch et al. (Jauch, Coles et al. 2014) have assembled a titanium stem and a cobalt-chromium head with 4.5kN and 6kN assembly forces (Figure 1.49).

Removed due to copyright restriction

Figure 1.49 Drop rig implemented to impact implant head on rigidly fixed stem with limited friction loss in sliders (Jauch, Coles et al. 2014)

Following this assembly, they examined the threshold of depassivation of the passive oxide layer by monitoring galvanic potential (Open Circuit Potential (OCP)) of the interface inside Ringer's solution while applying a torque ramp of 0 to 15Nm. Their study suggests that 6kN assembly force required higher torque (7.23 ± 0.55 Nm) for depassivation as compared to the torque required for depassivation head-neck assembled by 4.5kN (3.92 ± 0.97 Nm).

These results are limited in terms of applied load to the interface and cannot be expanded to real service condition. This is because the test was conducted in the absence of vertical forces,

which affects the mechanical response of the interface in-service condition, including the stress-field and range of micromotions.

Removed due to copyright restriction

Figure 1.50 Testing setup of Jauch et al.: Manual force applied to an instrumented bar to monitor the amount of torque applied to the head-neck interface while monitoring the OCP for corrosion initiation. (Jauch, Coles et al. 2014)

Gilbert et al. (Gilbert, Mehta et al. 2009) have experimentally studied CoCr and stainless steel (SS) stems assembled with CoCr head to investigate the effect of corrosive fluid prior to assembly in the head-neck junction on fretting-corrosion degradation of the implant over one million cycles of loading. In their experimental test, they assembled the head on the neck in a 2000N ramp-hold-unload manner. They embedded the hip stem in PMMA and exposed the head-neck interface to a phosphate-buffered saline solution (pH nominally 7.4) along with a second electrode from the same material of the stem for the corresponding reduction reaction and an Ag/AgCl reference electrode (Figure 1.51). They applied a simplified uniaxial load as a short-term variable force for a range of 0 to 3300N in steps of 100 to 1000N and steps of 200N from 1000N to 3300N force (~500 cycles for each load case) and long term (one million cycles) cyclic loading under 3300N load.

They investigated the effect of material combination and wet versus dry assembly in SS/CoCr combination. It was found that dry assembly condition improves the interface response in-service condition as it raises the corrosion onset load. They also reported that the SS/CoCr combination suffered more severely from fretting-corrosion than the CoCr/CoCr combination.

Removed due to copyright restriction

Figure 1.51 Test setup used by Gilbert et al. to investigate short and long-term fretting-corrosion response of the head-neck interface in presence and absence of initial fluid in the junction. (Gilbert, Mehta et al. 2009)

This study has a well-designed systematic approach to the targets however the implemented load is simplified to a sinusoidal vertical force and the frictional moment at the interface is neglected.

Panagiotidou et al. (Panagiotidou, Meswania et al. 2015) investigated the effect of frictional torque and bending moment on fretting-corrosion of real scale head-neck interface assembled with force of 4000N. Accordingly, they applied a vertical force with a peak magnitude of 2300N (ASTM F1875-98) in an out of the taper axis manner (Figure 1.52). They varied the out of axis offset distance to change the magnitude of applied torque as 0Nm, 9Nm, 14 Nm and 18 Nm.

Removed due to copyright restriction

Figure 1.52 The method of applying a torque coupled to the axial force via off entering the force. (Panagiotidou, Meswania et al. 2015)

To monitor fretting-corrosion at the interface, in their experimental test, they implemented the three-electrode arrangement (Figure 1.53), similar to experimental setup of Gilbert et al. (Gilbert, Mehta et al. 2009), and investigated material combinations of CoCr/CoCr, CoCr/titanium alloy and ceramic/ CoCr as head/stem.

Removed due to copyright restriction

Figure 1.53 Schematic view of the test setup to investigate fretting-corrosion of a head-neck under force and coupled moment inside a corrosive solution (Panagiotidou, Meswania et al. 2015)

The corrosive medium of phosphate-buffered saline was used to represent the corrosive ambient of the body. They reported a significantly higher corrosion current for increased torque magnitudes. As described, in this study, the profile of the torque was coupled with the force through a lever arm distance, and the torque profile was depended to the force profile while these two components of load independently varied in-service condition. This study applied the frictional moment and force as coupled load component whose variation was in phase together. Considering that the frictional moment could lead to shear stresses applying it in phase with maximum contact, stresses might change the fretting response of the interface. To this end, the simplification of coupling frictional moment and vertical forces, rather than applying them in an out of phase manner, must be justified.

1.9 Microscopic studies on fretting-corrosion damage of modular interfaces

Microscopic investigation of the fretting-corrosion damage of the modular interfaces has been conducted in some studies, especially on the retrieval samples. Lanting et al. (Lanting, Teeter et al. 2015) investigated 19 retrieval samples of a single design of the dual tapered design head-neck which was facing a significant number of retrieval surgeries (Figure 1.54). Metallosis was observed in twelve of the patients who underwent retrieval surgeries; three of the patients suffered from infection and two from subsidence.

Removed due to copyright restriction

Figure 1.54 a)The dual tapered design which 19 of its retrieval cases studied by Lanting et al. (Lanting, Teeter et al. 2015) b) Visible corrosion damages on the distal end of the retrieved neck c) Corresponding fretting and corrosion damages of the neck in the cross-section of the femoral stem's female taper

Their visual investigation on the damaged distal taper suggests that superior and inferior zones of the distal end of the taper were damaged more than the anterior and posterior. The SEM and Energy-dispersive X-ray spectroscopy (EDX) studies on the samples showed chromium phosphate as a bi-product of the corrosion body ambient existing in the corroded black regions. To have a better vision of mechanical service condition of this interface, they have conducted FEA on the distal taper of a dual tapered design. They concluded that corrosion in the crevice of the neck-stem interface provided the conducive conditions for fretting-corrosion at the interface, leading to a low pH level.

Figure 1.55 FEA on the mechanical ambient of the dual tapered design, suffering from fretting-corrosion and early retrieval surgeries (Lanting, Teeter et al. 2015).

Gilbert et al. (Gilbert, Mali et al. 2012) studied the distal taper of a single retrieval case which was six-years long in which dual tapered interface (Wright Medical-Profemur^{TM}) of a Ti6Al4V/ Ti6Al4V neck-stem interface (Figure 1.56) had been implanted.

Figure 1.56 The retrieved dual tapered neck studied through SEM imaging for oxide-induced stress corrosion (Gilbert, Mali et al. 2012)

They conducted SEM imaging on a cross-section of the damaged interface cut by a slow-speed diamond sectioning saw. The SEM imaging on the pitting attack (Figure 1.57) shows the propagation of the pitting corrosion and formation of new oxide-induced stress corrosion cracking at the damaged interface.

This study suggests that even in the same material interfacing of Ti6Al4V, due to formation of a fretting crevice corrosion environment at the modular interface, crevice-corrosion dissolution of the alloy might occur. This crevice corrosion dissolution then is followed by selective beta phases pitting corrosion at the interface. Formation of crack-shaped pitting corrosion alongside hydrogen embrittlement and tensile stress can cause oxide-induced stress corrosion cracking at the material. Channels shape in the oxide which brings the corrosive fluid to the yet intact alloy at the tip of the crack.

Figure 1.57 SEM investigation on the cross-section of the retrieved implant a) Low magnification backscattered SEM image of the pitting corrosion (grey area) b) Higher magnification image of corrosive fluid transferring channel c) Higher magnification of the distinct interface between the alloy and the pitting oxide products d) Higher magnification at the tip of the deepest crack e) Propagation of the crack at the tip of the deepest crack which could be followed by corrosion.

Martino et al. (De Martino, Assini et al. 2015) also investigated a dual tapered design (Rejuvenate) where out of 199 implanted cases, 30% retrieval surgeries were required (Figure 1.58). From a cohort of 60 retrieved implants with visible tracks of corrosion on them, five implants were studied using SEM imaging EDX to identify the elements present in the corrosion debris.

Removed due to copyright restriction

Figure 1.58 Rejuvenate design dual tapered implant with 30% retrieval rate in 199 implanted cases (De Martino, Assini et al. 2015)

Comparing the EDX results from non-damaged areas, and damaged areas of the implant showed the presence of Ti, O, Mo and Cr in the corroded area. Although chromium was the constituent element of the fabricated neck, it was either completely absent or present as a minimal peak in the corrosion debris area (Figure 1.59) (De Martino, Assini et al. 2015). The results of this research align with other research conducted on dual tapered design.

Studies suggest that due to lower surface hardness, Ti6Al4V alloy is vulnerable for fretting-corrosion even in the same material combination. CoCrMo alloys also significantly suffered from fretting-corrosion at the interface despite their higher surface hardness and wear characteristics as compared to Ti6Al4V. Some studies (Gilbert, Mali et al. 2012) shed light on the nature of crevice/pitting corrosion at the modular interfaces in which initiation of fretting-corrosion occurs with disruption of the passive adhesive layer due to breakage of the passive layer in contact stress in the modular interface; this will be followed by corrosion of the active metal underneath due to the lack of enough oxygen in the stagnated fluid in the crevice gap and the low pH due moving corrosive ions, such as chlorine, toward the gap. After lowering

the pH corrosion and oxide-induced stress, corrosion cracking can continue at the interface even in the absence of initial fretting loads.

Removed due to copyright restriction

Figure 1.59 EDX results on a) Not damaged b) Corrosion damaged areas of Rejuvenate design of dual taper THA(De Martino, Assini et al. 2015)

1.10 Research gap

The outcomes of many retrieval studies and *in vitro* tests on fretting-corrosion and mechanically assisted crevice corrosion of the head-neck interface of hip joint implants were sceptical to be affected of daily activities' frictional moment in intensifying the mechanical environment of the modular interface. This was more of a concern in larger MoM bearing couples which discontinued from the market due to high rate of immature retrieval surgeries.

As mentioned earlier, to conduct a realistic study regarding the mechanically assisted crevice corrosion at the head-neck junction, realistic loads of the bearing need to be applied on a real-scale head-neck interface to induce stress-field and micromotions in a crevice geometry

as it would be in the service condition of the implant. To investigate the level of contribution of components of loads of daily activities in the degradation of the head-neck interface, first, these loads need to be experimentally measured or analytically/numerically calculated. A review of the literature confirms that the contact forces and kinematics of hip joint implants are well-understood (Bergmann, Graichen et al. 1993, Bergmann, Deuretzbacher et al. 2001, Bergmann, Graichen et al. 2010). Some studies have reported frictional moment of metal-on-ceramic bearing couples. However, as the frictional moment of different material combinations and geometries vary, further research is essential first to determine the frictional moments induced in sceptical MoM bearing couples.

Additionally, mechanical ambient of the head-neck interface, including a range of micromotions and their corresponding contact stresses during fretting-corrosion under realistic loads, have not been well investigated. With the current state of the art of stress-strain field monitoring, experimental monitoring of the micromotions and corresponding stress over the surface of a closed geometry, such as in head-neck interface, is not possible. Hence, FEA is the best tool to simulate the stress and micromotion conditions inside the head-neck interface under daily activity loads. To this end, upon the availability of data regarding daily activity forces and moments, the FEA should be conducted to gain a complete understanding of the workings of the geometry during fretting-corrosion and mechanically assisted crevice corrosion at the head-neck interfaces.

As stated earlier, fretting-corrosion is sensitive to the geometry of the clamping interface, stress-field and the resulting micromotions. Studies about fretting-corrosion and mechanically assisted crevice corrosion have been conducted in a wide variety of arrangements from pin-on-disk to simplified coupled forces and moments. However, the isolated effect of frictional moments and forces in an out-phase manner as occurs during realistic daily activities at the interface has not been investigated yet. For a realistic evaluation, the best method is to apply a load of daily activities on a full-scale sample with the same geometry of the head-neck interface as it would be inside Ringer's solution to investigate the interrelation of load components and evaluate whether the load simplification is justifiable.

1.11 Research objectives

- Developing an analytical method to calculate frictional moments of metal on metal (MoM) hip implants in three dimensions for daily activities using the currently available joint forces and kinematics
- Investigating the variations of frictional moments of an MoM hip joint bearing couple under currently available activities, kinematics and forces
- Using a previously developed FEA simulation by another PhD student in the team to understand mechanical ambient of the head-neck interface under the available activities, forces and the frictional moments calculated using the analytical method
- Designing, manufacturing and commissioning an *in vitro* test setup capable of replicating realistic conditions of the implant on a real-scale head-neck interface
- Investigating interrelation of frictional moments and forces in mechanically assisted crevice corrosion at head-neck junction of the modular hip joint implant using the commissioned setup

Chapter 2. Analytical calculation of frictional moment of a hip joint bearing couple

This chapter is based on the following publication:

Farhoudi, H.; Oskouei, R.H.; Jones, CF; Taylor, M. A novel analytical approach for determining the frictional moments and torques acting on modular femoral components in total hip replacements. *Journal of Biomechanics* **2015**, *48, 6*, 976-983.

2.1 Overview

In this chapter, to determine the frictional moment vector of the hip joint implant, a three-dimensional analytical approach, which utilises joint kinematics, body loads, THR material and geometric characteristics, has been developed. This approach will provide a mean to calculate the currently unavailable frictional moments at MoM hip joint implants; the more sceptical design for from fretting-corrosion. This will provide a method to calculate frictional moments for further investigation on the effect of forces and moments acting on the bearing couple and the head-neck junction and to better understand the mechanical environment at the head-neck junction during physical activities.

Table 2-1 Nomenclature (list of symbols for this chapter):

$\overrightarrow{M_f}$	Frictional moment vector in bearing couple
$\overrightarrow{V_r}$	Rotation vector of the head relative to the cup
μ_k	Coefficient of kinetic friction
A	Contact area (Hertz theory)
D	Lever arm (perpendicular distance between the under pressure differential area and the rotation axis)
r	Radial distance from the centre of under pressure contact area (Hertz theory)
p_0	Maximum contact pressure (Hertz theory)
p	Contact pressure of a point at distance r from the centre of contact area (Hertz theory)
P	Bearing contact force
R^*	Equivalent radius (Hertz theory)
E^*	Equivalent Young's modulus (Hertz theory)
R_i, E_i and ν_i	Radius, Young's modulus and Poisson's ratio, respectively. $i = 1$ refers to head and $i = 2$ refers to cup
R_{zxy}	Euler rotation matrix for zxy sequence

$R_i(\omega)$	Rotation matrix about axis $i = x, y \; or \; z$ by angle of ω
$c\alpha$ and $s\alpha$	$\cos(\alpha)$ and $\sin(\alpha)$, respectively
C_H^n , C_H^i and C_P	Neutral head coordinate system, head coordinate system at instant i and spherical coordinate system with a z-axis in direction of P, respectively
$x_{C_H^i/C_H^n}$ (or $y_{C_H^i/C_H^n}$ or $z_{C_H^i/C_H^n}$)	x (or y or z) axis of the head coordinate system at instant i with respect to the neutral head coordinate system
$R\left(C_H^{i+1}/C_H^i\right)$	Rotation matrix from C_H^i to C_H^{i+1}
$\vec{L}$	Position vector of the under pressure points
β	Angle between $\vec{V_r}$ and $\vec{L}$
R, θ and φ	Radial distance, polar angle, and azimuthal angle, respectively in spherical coordinate system
M_n	Projection of the frictional moment vector on the neck axis
$\vec{V_n}$	Unit vector of the neck axis

2.2 Materials and methods

An analytical method was developed to find bending moments ($\overrightarrow{M_b}$), frictional moments ($\overrightarrow{M_f}$) and frictional torque about the head-neck interface ($\overrightarrow{M_n}$) under contact forces. The aim of this method was to analytically calculate frictional and bending moments of different implants during different activities through currently available inputs regarding activities and implants.

Friction is an effective parameter to be considered and further discussed regarding the frictional moment. Additionally, the friction coefficient is a function of contact forces, kinematics and material properties which in the presence of a lubricant (i.e. synovial fluid of hip joint), results in different regimes of lubrication (Liu, Jin et al. 2006). Currently, the elastohydrodynamic lubrication (EHL) theory is the most comprehensive analytical model to simulate lubrication regimes and frictional moments at the bearing interface of hip joint implants. As stated in the literature review, in EHL method, the elastic deformation of the contact area, the equilibrium equations and generalised Reynolds equations of the lubricant film are solved simultaneously to figure out the lubrication film thickness, the shear stress in the film due to relative motion of the surfaces and the resulting friction and frictional moment from the shear stresses in the liquid. To decrease the number of unknowns to equations (determined system), EHL uses the contact force only in the vertical direction and considers the rotational motion in the flexion-extension direction only (two degrees of freedom (DOF)); and assumes the other two components of the force and rotational motion as zero (Meng, Liu et al. 2011, Meng, Wang et al. 2015). This simplification cannot be expanded to a quantitative 6 DOF study because the system of equations will become indeterminant. Furthermore, this method is based on the assumption of a fully lubricated film which is not well justifiable for real tribology conditions of the implant with mixed lubrication regime (Wang, Brockett et al. 2008) and loss of lubrication film in large hard-on-hard bearing couples suffering from film pressure drop (Bishop, Hothan et al. 2013).

In this chapter, assumption of a constant friction coefficient for hard-on-hard couples (combinations of metals and/or ceramics) in a 6 DOF problem will be justified for the purpose of finding maximum values, changes of direction and an overall trend of variation in frictional moments. This assumption was successfully validated in and published in a peer-reviewed journal (Farhoudi, Oskouei et al. 2015) where the experimental and analytical frictional

moment results for hard-on-hard bearing couples corresponded with each other. Validation of this assumption against the accuracy in predicting these parameters is given in section2.3.

Regarding the developed analytical approach for frictional moments, as shown in Figure 2.1, due to the relative rotation of the head and cup, the frictional moment of $\overrightarrow{M_f}$ is induced in the relative direction of rotation of the head to the cup ($\overrightarrow{V_r}$). This relative rotation in the presence of friction at the interface of head-cup causes frictional moment. The magnitude of the frictional moment is a function of the frictional force and its distance from the relative rotation axis ($\overrightarrow{V_r}$). With reference to Figure 2.1, to calculate the frictional moment of $\overrightarrow{M_f}$, one can integrate the product of the differential frictional force and its perpendicular distance to the rotation vector (lever arm D) over the contact area (A). The differential friction moment will be $\mu_k.p.dA$ where μ_k is the coefficient of kinetic friction and p is the normal contact pressure at the differential area, calculated according to Hertz contact theory Thus, M_f is defined as follows:

$$M_f = \int D.\mu_k.p.dA$$

Equation 2-1

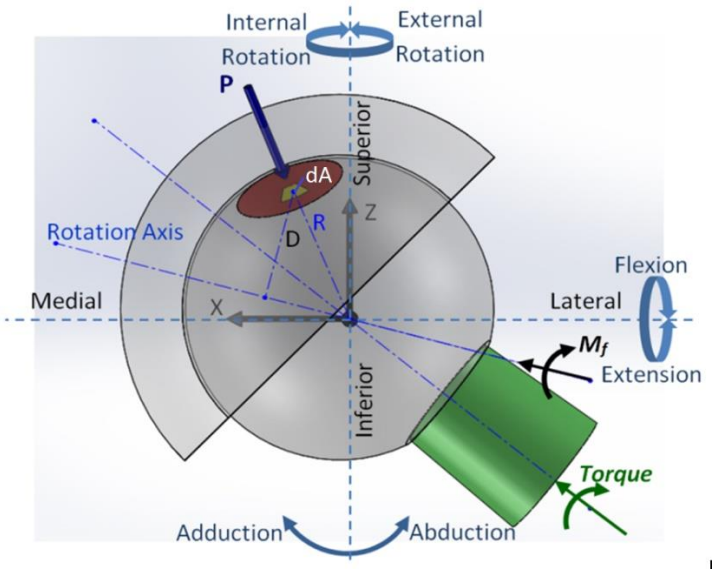

Figure 2.1. An antero-posterior view of THR implant with directions of angular motions (left hip, coronal plane).

To calculate this integral, the Hertz pressure distribution, direction of rotation and lever arm of the differential friction force should be determined. It is also important to possess a working knowledge of the friction factor.

2.2.1 Calculation of Hertz contact pressure distribution (p)

The Hertz pressure distribution theory is used to calculate the contact pressure on the differential area. According to the Hertz contact pressure distribution theory, which is suitable for determining the contact pressure between two non-conforming elastically deformed surfaces (Johnson 1987) such as hard-on-hard bearing couples, the normal pressure (p) at a distance r from the concentrated force (P) is defined as:

$$p = p_0 \times \{1 - (r/a)^2\}^{1/2}$$

Equation 2-2

where a is the radius of the contact area, r is the radial distance of the point from the centre of the contact area and p_0 is the maximum normal pressure.

$$a = \left(\frac{3PR^*}{4E^*}\right)^{1/3}$$

Equation 2-3

$$p_0 = \frac{3P}{2\pi a^2}$$

Equation 2-4

The variables P, R^* and E^* are contact force, equivalent radius and equivalent Young's modulus, respectively:

$$1/R^* = 1/R_1 + 1/R_2$$

Equation 2-5

$$\frac{1}{E^*} = \frac{1-\nu_1^2}{E_1} + \frac{1-\nu_2^2}{E_2}$$

Equation 2-6

where R_1, E_1 and ν_1, and R_2, E_2 and ν_2, are the radius, Young's modulus and Poisson's ratio for the head and cup, respectively. As the cup is concave, its radius must be considered negative. The radial distance r is defined in Equation 2-22.

2.2.2 Calculation of instantaneous direction of rotation

The instantaneous direction of rotation of the head relative to the cup (equivalent to the instantaneous direction of the frictional moment) is required to determine normal distance of the differential frictional force to the rotation axis. This distance is named as the lever arm (D). In the currently available activities kinematics data, the position of the head (at each instant of an activity cycle) is usually described by rotation from the hip neutral position similar to an origin for rotational motion (with corresponding time of $t = 0$) based on the Euler's rotation theorem (Saikko and Calonius 2002). For example, as illustrated in Figure 2.2 and Figure 2.3, the orientation of the head coordinate system at $t = i$ is defined with respect to the head coordinate system at $t = 0$ by a zxy Euler sequence rotation. The instantaneous rotations α, β and γ (about the z, x, and y axes, respectively) are determined as shown in Figure 2.2 and are applied to the head as Figure 2.3. The neutral head coordinate system (C_H^n) is fixed at the mutual centre of the head and cup.

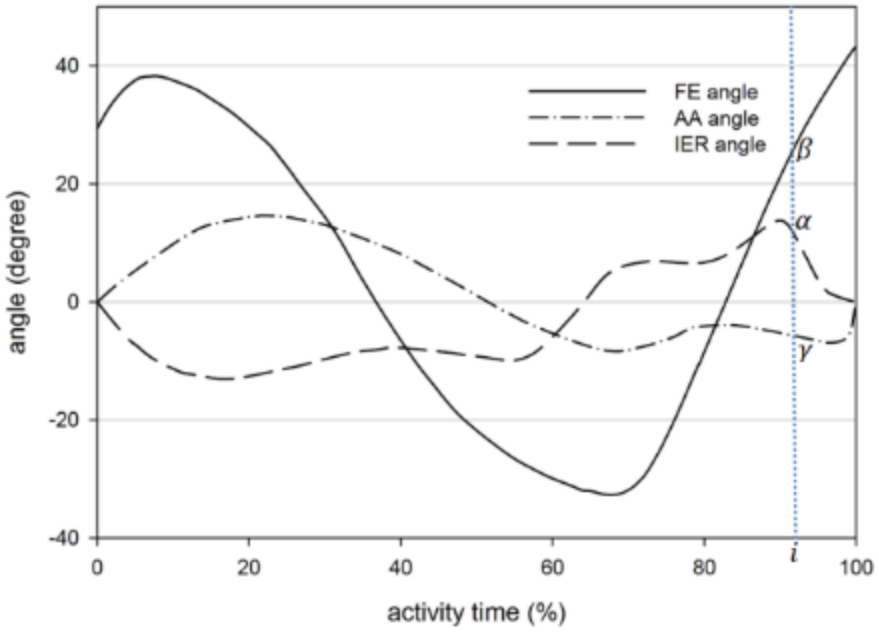

Figure 2.2 Euler angles in a zxy sequence (Internal-External rotation (IER) – Flexion- Extension (FE)– Abduction-Adduction (AA)) for hip kinematics of an activity to define C_H^i with respect to C_H^n (position at time =0).

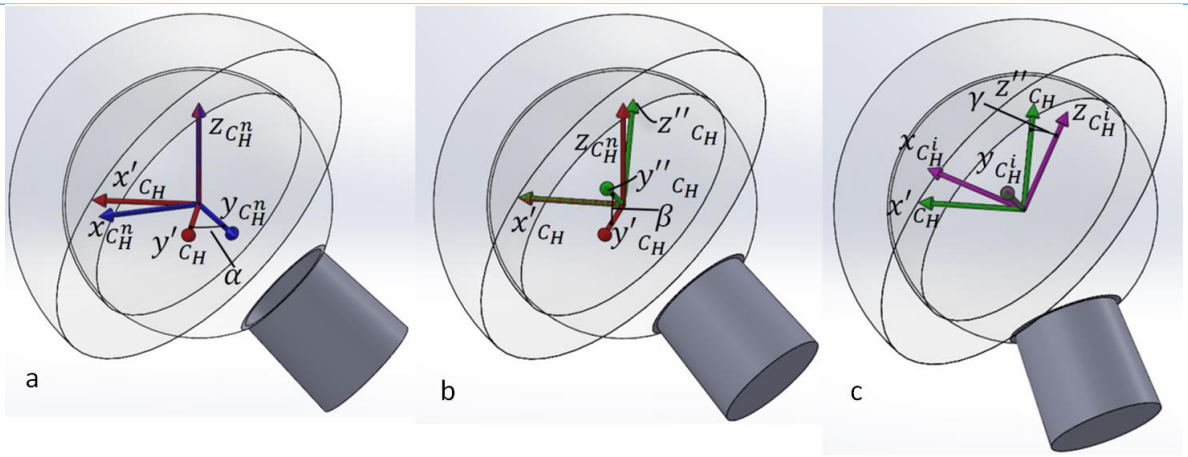

Figure 2.3. zxy Euler rotation sequence to describe the change in (left) head orientation from $t = 0$ to $t = i$. (a) α: rotation of C_H^n (blue) about $z_{C_H^n}$ to make C'_H (red), (b) β: rotation of C'_H (red) about x'_{C_H} to make C_H''(green); and, (c) γ: rotation of C_H'' about y''_{C_H} to make final C_H^i (purple). Flexion, abduction, and external rotations are in positive direction of x, y and z, respectively.

The Euler rotation matrix for zxy sequence is as follows (Equation 2-7 to Equation 2-9 (O'Reilly 2008)):

$$R_{zxy} = R_z(\alpha)R_x(\beta)R_y(\gamma)$$

Equation 2-7

$$= \begin{bmatrix} \mathrm{c}\,\alpha & -\mathrm{s}\,\alpha & 0 \\ \mathrm{s}\,\alpha & \mathrm{c}\,\alpha & 0 \\ 0 & 0 & 1 \end{bmatrix} \begin{bmatrix} 1 & 0 & 0 \\ 0 & \mathrm{c}\,\beta & -\mathrm{s}\,\beta \\ 0 & \mathrm{s}\,\beta & \mathrm{c}\,\beta \end{bmatrix} \begin{bmatrix} \mathrm{c}\,\gamma & 0 & \mathrm{s}\,\gamma \\ 0 & 1 & 0 \\ -\mathrm{s}\,\gamma & 0 & \mathrm{c}\,\gamma \end{bmatrix}$$

Equation 2-8

$$= \begin{bmatrix} c\gamma.c\alpha - s\gamma.s\beta.s\alpha & -c\beta.s\alpha & c\alpha.s\gamma + c\gamma.s\beta.s\alpha \\ c\gamma.s\alpha + c\alpha.s\beta.s\gamma & c\alpha.c\beta & s\gamma.s\alpha - c\gamma.c\alpha.s\beta \\ -c\beta.s\gamma & s\beta & c\gamma.c\beta \end{bmatrix}$$

Equation 2-9

where $c\alpha = \cos(\alpha)$, $s\alpha = \sin(\alpha)$ and so on. The instantaneous direction of rotation of the head depends on the rotation between two consecutive points in time, $t = i$ and $t = i + 1$. For calculating the instantaneous direction of rotation, the rotation matrix from $t = i$ to $t = i + 1$ was determined as follows.

Using the Euler angles and corresponding Euler rotation matrix of the i^{th} instant, the position of the head at each time step (i^{th}) was defined with respect to the neutral head coordinate system (C_H^n), as illustrated in Figure 2.4. Using Equation 2-10 to Equation 2-12, the coordinate

system axes at all instants (C_H^i) were defined with respect to C_H^n such that $x_{C_H^i/C_H^n}$ defines the x axis of the head coordinate system at instant i ($x_{C_H^i}$) with respect to the neutral head coordinate system (C_H^n) and so on.

$$x_{C_H^i/C_H^n} = R_{(C_H^i/C_H^n)} \times \begin{bmatrix} 1 \\ 0 \\ 0 \end{bmatrix}$$

Equation 2-10

$$y_{C_H^i/C_H^n} = R_{(C_H^i/C_H^n)} \times \begin{bmatrix} 0 \\ 1 \\ 0 \end{bmatrix}$$

Equation 2-11

$$z_{C_H^i/C_H^n} = R_{(C_H^i/C_H^n)} \times \begin{bmatrix} 0 \\ 0 \\ 1 \end{bmatrix}$$

Equation 2-12

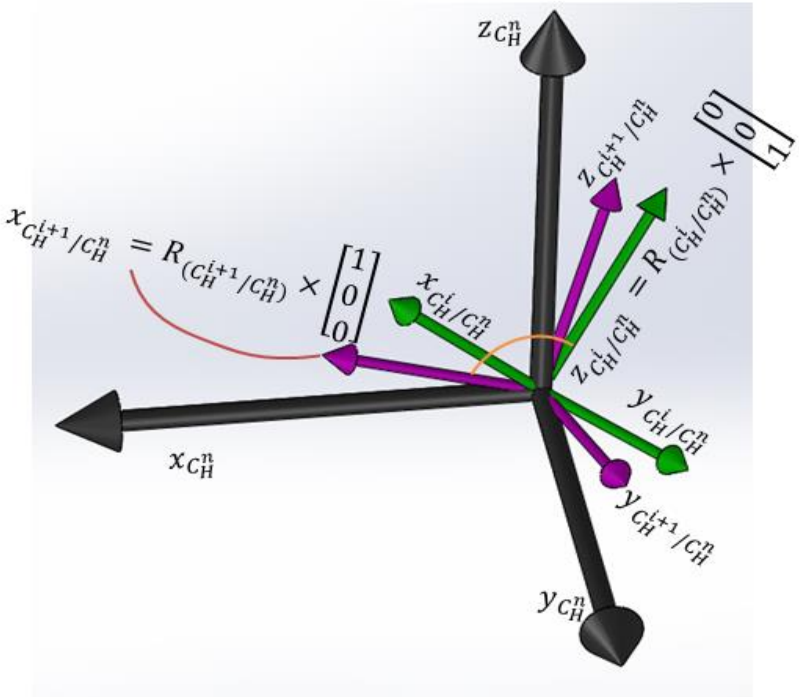

Figure 2.4. C_H^i and C_H^{i+1} coordinate systems described with respect to the neutral head coordinate system (C_H^n) to determine the instantaneous rotation matrix and instantaneous rotation direction.

The rotation between each consecutive instant (i.e. i and $i+1$) was defined using the direction cosine rotation matrix. By definition, the direction of rotation of the head from instant i to instant $i+1$ is the eigenvector of the rotation matrix from C_H^i to C_H^{i+1} (Figure 2.4). The rotation matrix from C_H^i to C_H^{i+1} can be defined by the cosines of the angles between the consecutive axes:

$$R\left(C_H^{i+1}/C_H^i\right) = \begin{bmatrix} \mathrm{c}\left(x_{C_H^i}, x_{C_H^{i+1}}\right) & \mathrm{c}\left(x_{C_H^i}, y_{C_H^{i+1}}\right) & \mathrm{c}\left(x_{C_H^i}, z_{C_H^{i+1}}\right) \\ \mathrm{c}\left(y_{C_H^i}, x_{C_H^{i+1}}\right) & \mathrm{c}\left(y_{C_H^i}, y_{C_H^{i+1}}\right) & \mathrm{c}\left(y_{C_H^i}, z_{C_H^{i+1}}\right) \\ \mathrm{c}\left(z_{C_H^i}, x_{C_H^{i+1}}\right) & \mathrm{c}\left(z_{C_H^i}, y_{C_H^{i+1}}\right) & \mathrm{c}\left(z_{C_H^i}, z_{C_H^{i+1}}\right) \end{bmatrix}$$

Equation 2-13

where, for example, $\mathrm{c}\left(z_{C_H^i}, x_{C_H^{i+1}}\right)$ is the cosine of the angle between axes $z_{C_H^i}$ and $x_{C_H^{i+1}}$ (illustrated in Figure 2.4). The components of Equation 2-13 are defined using the dot product of two vectors. Thus:

$$\cos\left(\vec{u}_i.\vec{v}_j\right) = \frac{\vec{u}_i.\vec{v}_j}{|\vec{u}_i|.|\vec{v}_j|}$$

Equation 2-14

Defining the denominator terms as unit vectors ($|\vec{u}_i|$=1 and $|\vec{v}_j|$=1):

$$R\left(C_H^{i+1}/C_H^i\right) = \begin{bmatrix} x_{C_H^i/C_H^n}.x_{C_H^{i+1}/C_H^n} & x_{C_H^i/C_H^n}.y_{C_H^{i+1}/C_H^n} & x_{C_H^i/C_H^n}.z_{C_H^{i+1}/C_H^n} \\ y_{C_H^i/C_H^n}.x_{C_H^{i+1}/C_H^n} & y_{C_H^i/C_H^n}.y_{C_H^{i+1}/C_H^n} & y_{C_H^i/C_H^n}.z_{C_H^{i+1}/C_H^n} \\ z_{C_H^i/C_H^n}.x_{C_H^{i+1}/C_H^n} & z_{C_H^i/C_H^n}.y_{C_H^{i+1}/C_H^n} & z_{C_H^i/C_H^n}.z_{C_H^{i+1}/C_H^n} \end{bmatrix}$$

Equation 2-15

Consequently, the instantaneous rotation vector of the head coordinate system from instant i to instant $i+1$ is determined from the eigenvector equation:

$$\left|R\left(C_H^{i+1}/C_H^i\right) - \lambda I\right| \times \overrightarrow{V_r} = 0$$

Equation 2-16

2.2.3 Determining the lever arm

Lever arm D, from the axis of the frictional moment (M_f) to the differential area of pressure application (dA) is given by:

$$D = |\vec{L}|.sin\beta$$

Equation 2-17

where $\vec{L}$ is the position vector of dA and β is the angle between the rotation vector $\overrightarrow{V_r}$ and $\vec{L}$.

The lever arm is defined using the cross product between $\vec{L}$ and $\overrightarrow{V_r}$:

$$|\vec{L}||\overrightarrow{V_r}|sin\beta = |\vec{L} \times \overrightarrow{V_r}|$$

Equation 2-18

$$sin\beta = \frac{|\vec{L}\times\overrightarrow{V_r}|}{|\overrightarrow{V_r}||\vec{L}|}$$

Equation 2-19

$$D = |\vec{L}| \times \frac{|\vec{L}\times\overrightarrow{V_r}|}{|\overrightarrow{V_r}||\vec{L}|} = |\vec{L} \times \overrightarrow{V_r}|$$

Equation 2-20

$\vec{L}$ = ($R.sin\,\theta\,.cos\varphi, R.sin\,\theta\,.sin\varphi, R.cos\,\theta$)^T and $\overrightarrow{V_r}$ is unit vector calculated from Eq. 7 and Eq. 8 and transmitted to the coordinate system of the contact force line of action (C_P).

2.2.4 Friction factor in head-cup interface

The developed method can implement a varying friction factor for each instance of a simulated activity but requires either experimental data or an analytical prediction of the friction factor to be provided/ calculated based on general inputs such as contact stress, kinematics and geometry of the bearing. However, there is only limited data available for magnitude and variation of the friction factor. *In vitro* studies have measured the frictional moment from which the friction factor can be calculated, typically for one instance in a simplified load case. This offers a qualitative evaluation of friction factor for different bearing geometries, material combinations and lubrication conditions (Bishop, Waldow et al. 2008, Bishop, Hothan et al. 2013). Based on *in vivo* measurements of frictional moment, the variation of friction factor during various activities for hard-on-soft (ceramic-on-polyethylene) bearings has been reported (Damm, Dymke et al. 2013). However, their results cannot be generalised to other bearings, specially hard-on-hard bearing couples as in ceramic/metal-on-polyethylene by increase of the contact stress the friction coefficient decreases (Wang, Essner

et al. 2001), while in hard-on-hard bearing couples this is not the case. Although the friction factor has been shown to a function of contact stress for metal-on-polyethylene bearings (Wang, Essner et al. 2001, Saikko 2006), no such data exists for hard-on-hard bearings. An analytical approach has been developed to predict the friction factor based on electrohydrodynamic lubrication (EHL) equations. However, the existing analytical solution can only be solved for simplified loading conditions with a uniaxial load and flexion/extension. The EHL studies have also simplified positioning of the implant cup from anatomically inclined to horizontal (Meng, Liu et al. 2011, Meng, Liu et al. 2013). Wang et al predicted the frictional moment and verified it against *in vitro* results (Wang, Brockett et al. 2008); however, there were considerable discrepancies between the predictions and measured moments. Although these studies are based on the EHL theory, the required simplifications cannot be implemented in three dimensional motions under multi-axial loading of the bearing to predict the frictional behaviour.

None of the studies is generalisable to simulate friction in a three-dimensional motion under multi-axial loading because of their simplifications; the simplifications of considering two of the angular velocities equal to zero was required to change the underdetermined system of equations to a determined system of equations (Chapter1, page 32). This will reduce the degree of freedom of the kinetics from three to one. The simplifications in unidimensional kinematics and loads are discussed in section 1.6 which reflect that in a real three dimensional kinetics and three-dimensional force, number of equations would be smaller than the number of unknowns which would lead to an underdetermined system of equations. Therefore, in this study, a constant value of friction factor derived experimentally at the highest contact force will be assumed for each bearing couple, and the consequences of this assumption will be assessed.

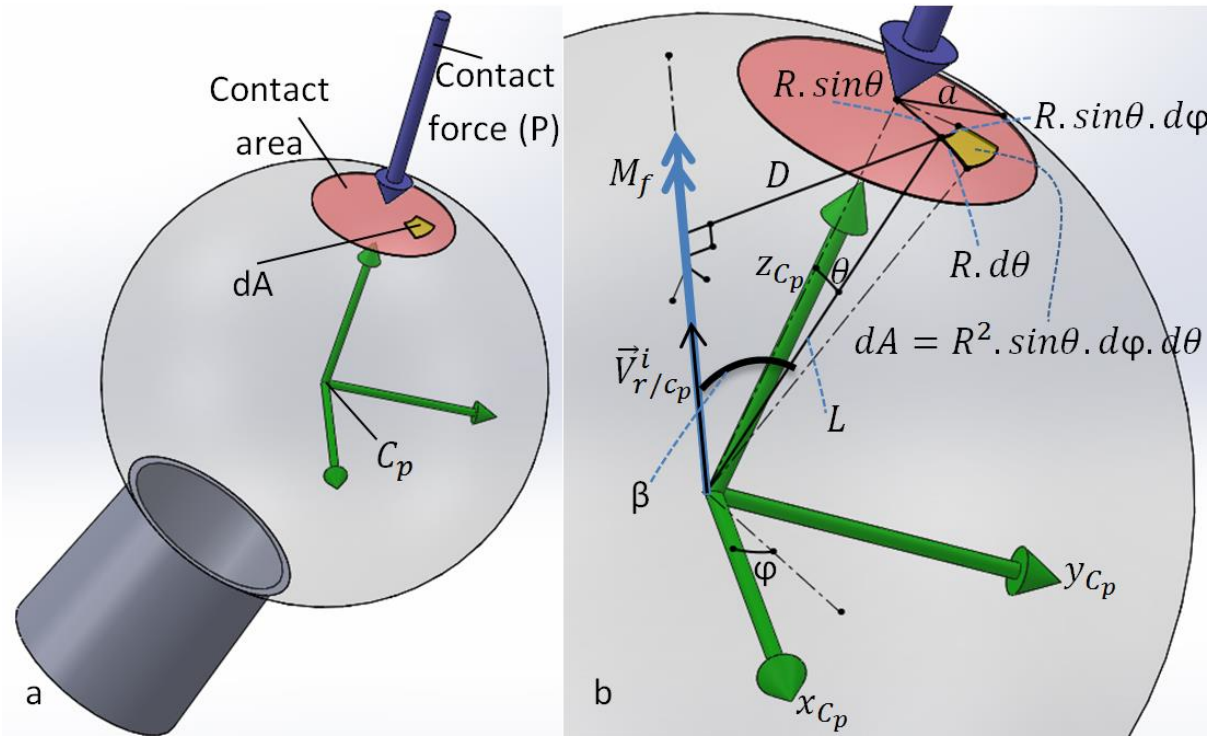

Figure 2.5 (a) Hertz contact area and coordinate system (C_P) with z axis in line of action of P and (b) integral parameters for determining frictional moment.

2.2.5 Resultant frictional moment at head-cup interface

The instantaneous frictional moment (M_f), at each instant, is determined using Equation 2-1. Since the contact area is a circle around the point of contact force, the integral is calculated in a spherical coordinate system with the z-axis aligned with the line of action of P (C_P in Figure 2.5). Thus, the differential area is defined as:

$$dA = R^2.\sin(\theta)\, d\theta d\varphi$$

Equation 2-21

where r in Equation 2-2 in C_P spherical coordinate is:

$$r = R.\sin(\theta)$$

Equation 2-22

The resultant frictional moment is determined at each instant as follows:

$$M_f = \int_{\varphi=0}^{\varphi=2\pi}\int_{\theta=0}^{\theta=\sin^{-1}a/R} p_0 \times \left\{1 - \left({}^{R.\sin(\theta)}/_{a}\right)^2\right\}^{1/2} \times \mu_k \times \left|\vec{L} \times \vec{V_r}\right| \times R^2.\sin(\theta)\, d\theta d\varphi$$

Equation 2-23

From the projection of a vector on an axis, the frictional torque about the neck axis can be determined as:

$$M_n = M_f . \left| \vec{V}_n . \vec{V_r} \right|$$

Equation 2-24

where $\vec{V}_n$ is the unit vector of the neck axis defined in the head coordinate system (C_H).

The analytical method was implemented using a custom MATLAB code (2013a, The Mathworks, Mattick, MA) to calculate the frictional moment acting on the femoral head during different physical activities with given bearing contact loads, bearing characteristics and hip joint kinematics. The activity input data was resampled to *n* data points (*n*=100) across the activity time cycle using linear interpolation and then corresponding frictional moment vector and torque on the neck axis were calculated. The method was verified against experimental results of an *in vitro* study conducted by Bishop et al. (Bishop, Waldow et al. 2008). The details of validation are given in Appendix.

To calculate the bending moments induced at the head-neck interface, the instantaneous distance vector of the contact force from the clamping region of the head and neck was formed from the available kinematics of the head with respect to the cup. The offset of the contact region of the head and neck from the force was assumed to be 10 mm which is near the common geometry of a neutral 12/14 taper design. The cross product of the instantaneous distance vector and the corresponding contact force (the bending moment induced at the head-neck clamping interface) was determined for the entire activity cycle.

2.3 Validation of the analytical method

The analytical approach was validated against *in vitro* experimental data reported by Bishop et al. (Bishop, Waldow et al. 2008). The experiment measured the frictional moment between the head and cup for different THR material and size combinations (Table 2-2) under loading conditions simulating a simplified walking cycle. The reported values for the friction coefficient are for the instance of the maximum load of the cycle. Considering that the friction coefficient may vary by the contact stress and kinematics of the surfaces, implementing a constant value for the friction coefficient from the peak force for may lead to error in calculated moments and overestimate the frictional moment. The method is capable of implementing a variable friction coefficient as a function of other parameters; however, data for this purpose for three-dimensional kinetics is not available in the literature.

Table 2-2. Implant head and cup materials, dimensions and coefficient of kinetic friction (M-M=metal on metal, M-P= metal on polyethylene M-C= metal on ceramic and C-C=ceramic on ceramic) used by Bishop et al. (Bishop, Waldow et al. 2008).

#	1	2	3	4	5	6	7	8	9
Material	M-M	M-M	M-M	M-M	M-M	M-M	M-P	M-C	C-C
Nominal ø (mm)	55	55	50	48	46	36	28	28	28
Head ø (mm)	54.437	54.500	49.785	47.981	45.964	36.002	27.938	27.980	28.001
Cup ø (mm)	54.601	54.601	50.020	48.055	46.018	36.107	28.123	28.074	28.064
Friction coefficient μ(-)	0.16	0.10	0.13	0.12	0.12	0.15	0.15	0.09	0.09

Since the simulator applied only a uniaxial load in flexion-extension rotations, in the custom analytical code, the adduction-abduction and internal-external rotations were inserted as zero over the entire cycle. The radius of the head and cup, and the friction factors for the bearing couples were inserted as per Table 2-2. The analytical predictions were linearly regressed against the *in vitro* results to evaluate the performance of the developed approach.

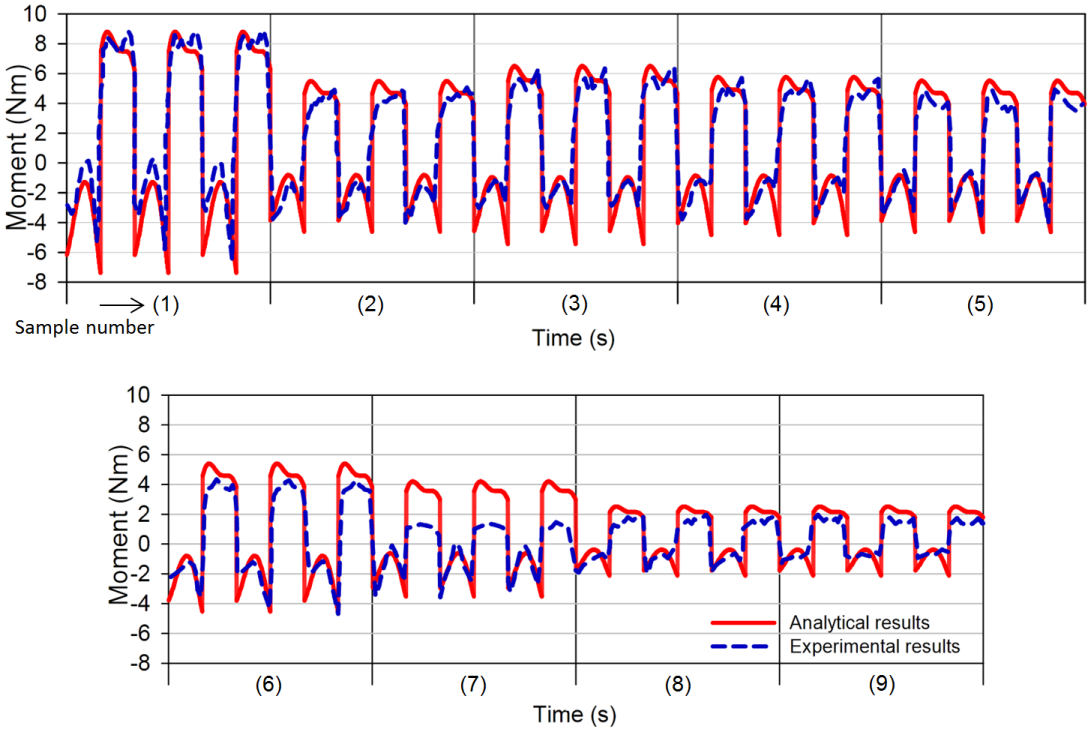

Figure 2.6 Comparison of the experimental results (Bishop, Waldow et al. 2008)) and the predictions by the analytical approach for each bearing couple, as described in Table 2-2

For each implant specification (totally 9 head-cup bearing samples), the analytical calculation was determined for three cycles to produce a plot of frictional moment versus time, in a similar fashion to that provided for the experimental results (Figure 2.6) by Bishop et al. (Bishop, Waldow et al. 2008).

Table 2-3. Linear regression parameters of analytical results versus experimental results for bearing couples.

#	1	2	3	4	5	6	7	8	9
Slope	1.109	1.033	1.102	1.042	1.140	1.121	1.454	1.113	1.237
Intercept	-0.116	0.234	-0.302	-0.048	-0.055	0.146	0.642	0.233	0.017
R- squared	0.996	0.978	0.984	0.969	0.996	0.989	0.972	0.962	0.976
RMSE (Nm)	0.382	0.548	0.548	0.668	0.215	0.373	0.463	0.324	0.256

For linear regression and quantitative evaluation of level of agreement between experiments and analytical method, the *in vitro* results were averaged over three repeats for each bearing

(Table 2-3). In the Table 2-3, *in-vitro* frictional moment and analytically calculated frictional moment for each instant shapes a point of (x, y) in a 2D plot. The near to one slope and the near to zero intercept of the linear regression of these points reflects the agreement of the analytical results to the corresponding frictional moment. The analytical approach was found to be predictive of the frictional moment for different head-cup bearing couples, especially metal on metal bearings in terms of anticipating the valleys, peaks, instants of change of directions and maximum and minimum magnitudes. According to Table Table 2-3, with slopes close to unity, high R-squared values and small RMS (root-mean-square) errors obtained from the linear regression support the good predictions by the analytical method. However, the predictions for the metal on polyethylene bearing (number 7) are not as good as other bearings. It is believed that the Hertz contact theory could not predict the metal on polyethylene behavior correctly since the assumption of negligible material strain for Hertz theory is not satisfied for this type of bearing. Moreover, the friction constant in reported by (Bishop, Waldow et al. 2008) is reported under the max contact stress moment, while the friction factor of hard-on-polyethylene bearing couples is minimum under the maximum contract force. This can become a source p error for the analytical method to predict the frictional moment of metal-on-polyethylene using the minimum friction factor for entire course of the activity.

2.4 Implementation of method

After development and validation of the analytical method, to understand the nature of the frictional moment at the head-cup interface, the method was implemented on three of the currently available activity scenarios (hip-joint dynamics and characteristics). The activity scenarios were as below:

A) Simplified gait scenario

1 rotational degree of freedom (flexion-extension) under

1 dimensional activity force (vertical force)

B) ISO12424-1:2012 standard gait

3 degrees of rotational freedom (flexion-extension, abduction-adduction, internal-external rotation) under

1 dimensional activity force (vertical force)

C) Physiological level gait

3 degrees of rotational freedom (flexion-extension, abduction-adduction, internal-external rotation) under

3-dimensional activity force (vertical, lateral and transversal forces)

2.4.1 Simplified gait scenario (1 rotational degree of freedom, 1 dimensional activity forces)

Inputs for the analytical method for this analytical simulation was from Bishop et al. study (Bishop, Hothan et al. 2013) on hip friction moments of large hard-on-hard hip replacement bearings in poor lubrication condition (Bishop, Hothan et al. 2013). This study has investigated different sizes of metal-on-metal and ceramic-on-ceramic bearing couples in presence and absence of 25% fetal bovine serum as the lubricant. The analytical simulation used the inputs of implant characteristics and friction factors shown in the Table 2-4.

is extracted at the instant of maximum contact force. Figure 2.7-a shows the dynamics applied on the implant during the experimental test. As can be seen, A sinusoidal uniaxial rotation of [±20^o] (flexion-extension around y Figure 2.7.a) and uniaxial cyclic loading of Figure 2.7.b (in $-z$ direction) were applied. Figure 2.7-b gives a better understanding of how these dynamics is applied on the implants by the experimental setup.

In the analytical calculation of frictional moment for this activity scenario, the same dynamics of the experimental study was applied on the implants and variation of frictional moment was extracted. The experimental study (Bishop, Hothan et al. 2013) has not reported variation of the frictional moment under the given dynamics but has reported the maximum value of the frictional moment from which they have extracted friction coefficient.

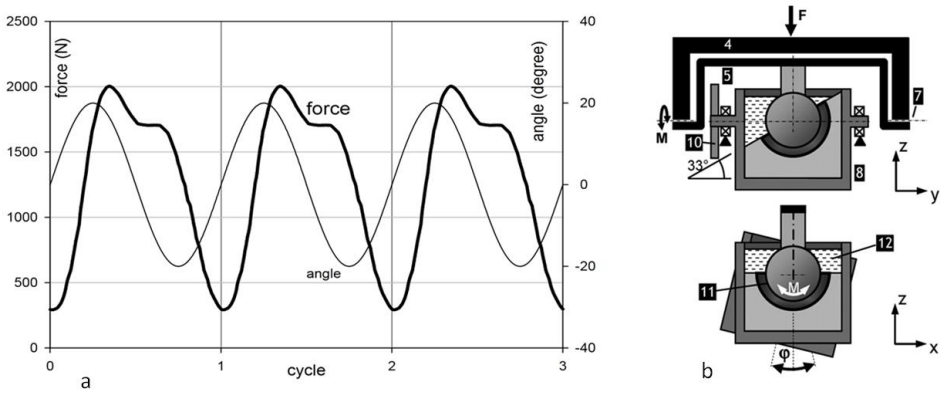

Figure 2.7 (a) Cyclic axial loads and corresponding angles as a simplified gait; and (b) experimental set-up used by Bishop et al. (Bishop, Waldow et al. 2008, Bishop, Hothan et al. 2013).

2.4.2 ISO 12424-1:2012 gait scenario (3 rotational degree of freedom, 1 dimensional activity force)

ISO 12424-1:2012 is a standard developed to define loading and displacement parameters for wear-testing machines of polyethylene linen and corresponding conditions. The dynamic of this gait scenario consists of a 3 rotational degree of freedom for the relative motion of head-cup (flexion-extension, abduction-adduction, internal-external rotation) in presence of 1 directional force (in vertical direction). The profile of the force and angular rotations are shown in Figure 2.9-a. The rotational degree of freedoms is a simplified case of Physiological level walking gait (Figure 2.9-b). the applied force in this gait scenario is a simplified and

magnified case of the vertical forces in Physiological level walking gait with neglecting the other two components of lateral and transversal forces of physiological level walking gait. As a measure of vertical force magnification, maximum force in ISO1242-1:2012 is 400% of the body weight (%BW) against 233BW% for Physiological level gait (3136 N for an 80 kg patient against 1828 N for an 80 kg patient).

In the analytical calculation of frictional moment for this activity scenario, the same dynamics of the ISO12424-1:2012 is considered. Considering that the forces are determined in BW% unit, the calculated frictional moment was in BW%.m unit. For example, a 0.5%BW.m frictional moment meant that for an 80 kg patient meant 0.5% x 80 (kg) x 9.81 (m/s^2).m=3.924 $kg.m/s^2$.m=3.924Nm. Regarding the inputs for geometry, material and friction coefficient of the implant for ISO12424-1:2012 gait scenario, the sample number 5 of Bishop et al. study (Bishop, Waldow et al. 2008) for which the method had a high-level of agreement was found. The nominal head diameter of this metal-on-metal bearing couple was 46mm and its friction coefficient under maximum contact force of 2000N was reported as 0.12.

2.4.3 Physiological level gait scenario (3 rotational degree of freedom, 3-dimensional activity force)

As mentioned in the previous section, ISO12424-1:2012 has differences from the physiological level gait. The magnitude of the vertical load in ISO 400BW% (3136 N for an 80 kg patient) against 233BW% (1828 N for an 80 kg patient) of physiological level gait. In ISO12424-1:2012 the lateral and transversal forces are neglected, and rotational motions of the head-cup are simplified. To study the effect of these assumptions of ISO12424-1:2012 on the frictional moment induced at the head-cup interface, frictional moments of physiological level gait is also studied.

For modelling the physiological level gait, inputs for kinematics was from Johnston et al. (Johnston and Smidt 1969) who had extracted the joints kinematic by electrogoniometers. This study is of the most cited studies reporting hip joint kinematic. For the activity forces, inputs were from Orthoload.com (Bergmann, Graichen et al. 2010) which has used *in-vivo* telemetry force transducers placed inside a hollow implant. The same to the ISO12424-1:2012 gait scenario, the implant characteristics were from the sample number 5 of Bishop et al.

study (Bishop, Waldow et al. 2008) so the results of these two scenarios would be comparable.

As in both the ISO12424-1:2012 and physiological level gait the frictional moment had a projection on the neck axis, in addition to the total frictional moment, its projection on the neck axis was calculated.

Table 2-4. Bearing specifications and maximum moment predicted by the analytical method and measured in the experimental tests for simplified gait (Bishop, Hothan et al. 2013)

			Serum				Dry			
#	Material	Bearing ø (mm)	Experimental friction factor (-)	Max moment in experiment (Nm)	Max calculated moment (Nm)	Difference	Experimental friction factor (-)	Max moment in experiment (Nm)	Max calculated moment (Nm)	Difference
1	MoM	40	0.146	5.6	5.8	4%	0.283	9.9	11.3	14%
2	MoM	50	0.162	11	10.7	-3%	0.280	12.1	14	16%
3	CoC	32	0.096	3.4	3.1	-9%	0.491	16	15.7	-1%
4	CoC	48	0.051	3.7	3.4	-8%	0.580	26.5	27.9	5%

2.5 Results

2.5.1 Simplified gait

Maximum values of frictional moments were extracted and compared to the experimental results of Bishop et al. (Bishop, Waldow et al. 2008) (Table 2-4). Differences between analytical and experimental results were -9% to 16%. Because of the loading profile simplicity (perpendicular load on rotation axis), the frictional moment followed the trend of the applied force. As can be seen in Figure 2.8 and Table 2-4 the frictional moment in dry condition can be increased by up to 8 times compared to the lubricated condition. The worst case of 8 times

increase in frictional moment happened for 48 mm ceramic on ceramic implant with presence of ceramic chips in the interface. This 48 mm ceramic on ceramic initially had a good frictional behaviour in lubricated conditions. The dry condition friction factor and resulted frictional moment is representative of poor lubrication condition of the modelled bearing couples in real service condition. This poor lubrication can happen in the large head implants because of poor cup placement or loss of lubrication film due to large contact area. This means that frictional behaviour of large size hard-on-hard bearings is significantly affected by their lubrication regime.

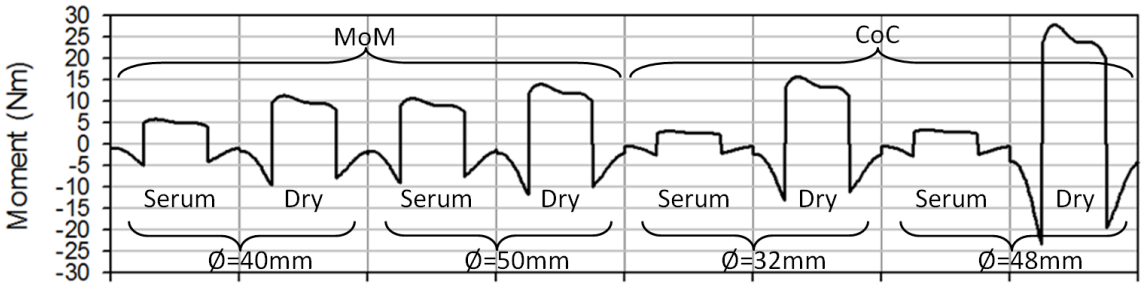

Figure 2.8. Frictional moment calculated for bearings of Physiological level gait scenario (3 rotational degree of freedom, 3-dimensional activity force)

2.5.2 Physiological level gait scenario (3 rotational degree of freedom, 3-dimensional activity force)

As mentioned in the previous section, ISO12424-1:2012 has differences from the physiological level gait. The magnitude of the vertical load in ISO 400BW% (3136 N for an 80 kg patient) against 233BW% (1828 N for an 80 kg patient) of physiological level gait. In ISO12424-1:2012 the lateral and transversal forces are neglected, and rotational motions of the head-cup are simplified. To study the effect of these assumptions of ISO12424-1:2012 on the frictional moment induced at the head-cup interface, frictional moments of physiological level gait is also studied.

For modelling the physiological level gait, inputs for kinematics was from Johnston et al. (Johnston and Smidt 1969) who had extracted the joints kinematic by electrogoniometers. This study is of the most cited studies reporting hip joint kinematic. For the activity forces, inputs were from Orthoload.com (Bergmann, Graichen et al. 2010) which has used *in-vivo* telemetry force transducers placed inside a hollow implant. The same to the ISO12424-1:2012 gait scenario, the implant characteristics were from the sample number 5 of Bishop et al.

study (Bishop, Waldow et al. 2008) so the results of these two scenarios would be comparable.

As in both the ISO12424-1:2012 and physiological level gait the frictional moment had a projection on the neck axis, in addition to the total frictional moment, its projection on the neck axis was calculated.

2.5.3 Table 2-4 under loading profile and configuration of Figure 2.7.

Looking at Figure 2.7, change of rotation direction happens at the change of the flexion-extension angle's slope coinciding at 0.25 and 0.75 of cycle normalized time (Figure 2.7) result in sudden changes of direction of the frictional moment. The magnitudes of these slopes are given in Table 2-5. As can be seen, the frictional moment slope at 0.25 of the activity cycle is higher than 0.75 because the force corresponding to the 0.25 of the activity cycle is higher than of 0.75. Also, by comparing the results, the higher the frictional the friction moment, the higher the change of direction's frictional moment slope would be. The effect of this change of direction in the frictional moment can be considered as a rotational impact on the modular interface, which may affect the fretting-corrosion at them.

Table 2-5 magnitude of slope frictional resulted from change between flexion and extension

			Serum		Dry	
#	Material	Bearing ø (mm)	Slope at 0.25 of activity cycle(Nm/s)	Slope at 0.75 of activity cycle(Nm/s)	Slope at 0.25 of activity cycle(Nm/s)	Slope at 0.75 of activity cycle(Nm/s)
1	MoM	40	1489.5	-1260.7	2887.3	-2443.7
2	MoM	50	2721.9	-2303.8	3570.8	-3022.3
3	CoC	32	783.5	-663.1	4007.4	-3391.8
4	CoC	48	864.9	-732.1	7100.8	-6010.0

2.5.4 ISO12424-1:2012 standard gait

The maximum magnitude of frictional moment for this profile was 1.46×BW%.m (11.4 Nm for 80 kg patient) which occurred at the instance of the peak contact force (Figure 2.9.c). Frictional torque about the neck axis varied from -0.86×BW%.m (-6.74 Nm for 80 kg patient) to 0.88×BW%.m (6.89 Nm for 80 kg patient) and its maximum magnitude occurred simultaneous with the maximum frictional moment and maximum contact force. Maximum frictional moment does not necessarily occur with maximum load as it is also a function of angle between contact force and direction of rotation. Averaged over one cycle, the x axis (medial direction of the head coordinate system in neutral position) received 94% of the frictional moment which was the highest projection compared to the y and z axes (anterior and superior directions of neutral head, respectively).This highest projection in x axis direction is a result of combination of dominant force component (vertical force) and dominant rotational motion (flexion-extension) frictional moment. At the moment of change in the direction of flexion-extension, there was a sharp change of direction in the neck torque. Change of direction in abduction-adduction and internal-external rotation did not alter the direction of the neck torque.

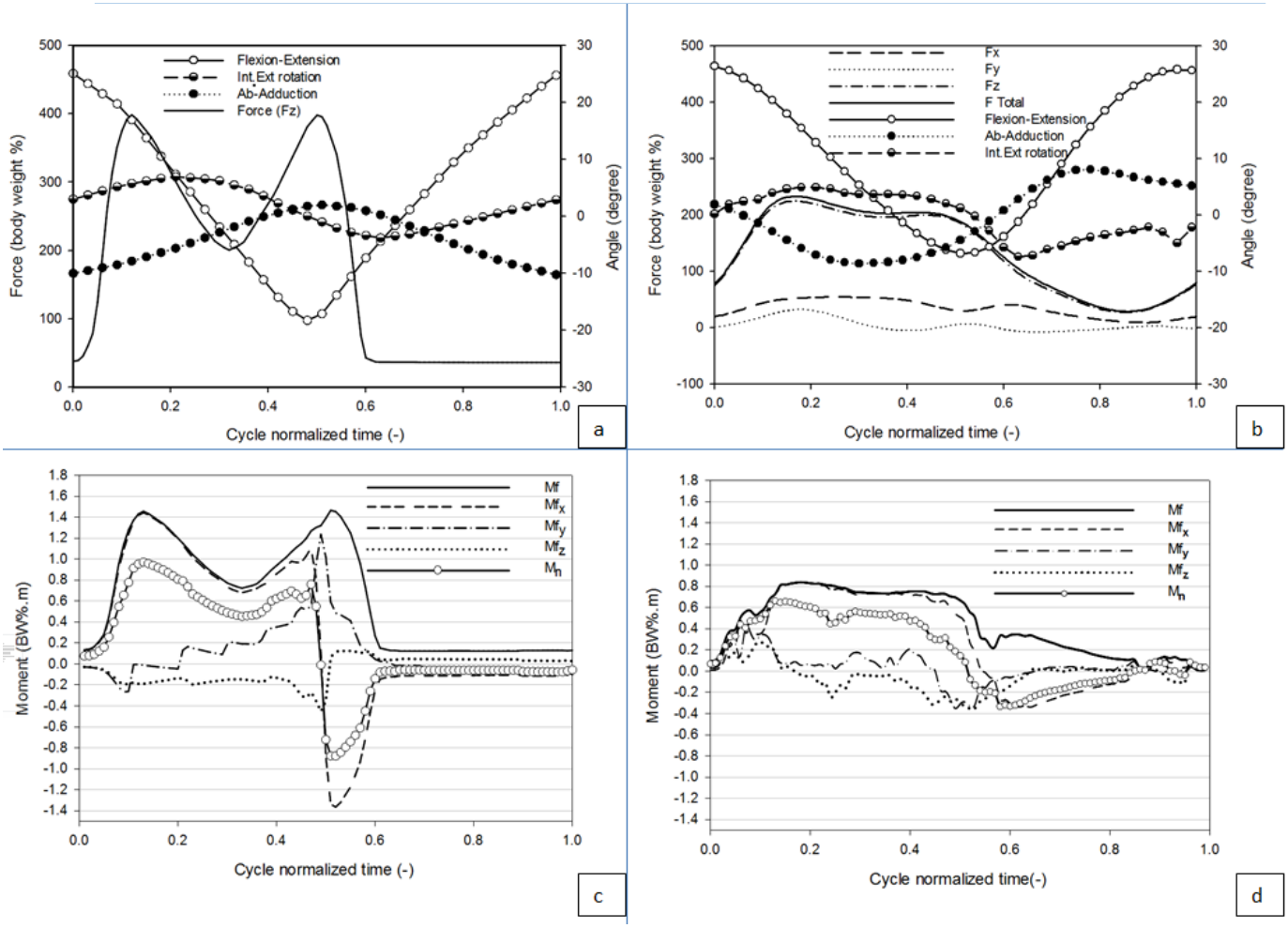

Figure 2.9. (a) Loading and kinematics of gait cycle of ISO standard gait; (b) Physiological walking profile, loading from ortholad.com for real walking activity applied with kinematics from Johnston and Smidt (Johnston and Smidt 1969) for real walking; (c) and (d) Frictional moment and its projections on the neck direction and head coordinate axes for a 46 mm metal on metal bearing simulated under ISO standard gait and physiological level gait, respectively. (x, y and z are medial, anterior and superior directions of the head coordinate system, respectively).

2.5.5 Physiological level gait

The maximum magnitude of frictional moment for this profile was 0.84×BW%.m (6.58 Nm for an 80 kg patient). (Figure 2.9.d) which occurred at the instance of the highest contact force (400BW% - 3136 N for a 80 kg patient). Similar to the ISO standard, the x axis experienced the highest projection of the frictional moment by receiving 92% of the total moment on average. The neck torque varied from -0.38xBW%.m to 0.66×BW%.m (-2.97 Nm to 5.17 Nm for an 80 kg patient) with its maximum magnitude occurring at a different instance to the maximum frictional moment and maximum contact force. This indicates that the neck torque does not necessarily follow the contact force or even total frictional moment as it is also a function of angle between the direction of neck and frictional moment. The neck torque had its main change of direction at 0.58 of cycle normalized time while this change was not as sharp as the

ISO standard gait. The complex kinematics and loadings of this profile led to small fluctuations on overall trend of frictional moment and its components on different axes.

2.6 Discussion

The analytical method was validated by comparing predictions of the frictional moment against experimental data for a simplified loading condition. The method had a good prediction of frictional behaviour of metal-on-metal and metal-on-ceramic bearing couples. Also, the method was applied on different loading profiles and the variation in the frictional moment was extracted. By utilising the available kinematics and loading data from other studies (Johnston and Smidt 1969, Bergmann, Deuretzbacher et al. 2001, Saikko and Calonius 2002, Bishop, Waldow et al. 2008), the method was capable of predicting complex behaviour of frictional moment in bearing couples and the torque acting on the head-neck interface. The method was applied on both the ISO12424-1:2012 and physiological gait to have a better view of differences in frictional behavior of a bearing couple its examination under ISO12424-1:2012 standard instead of physiological loads.

The role of fretting and fretting assisted corrosion in the failure of total hip replacement has become of significant interest, particularly with larger diameter and hard-on-hard bearing combinations. The current ASTM standard (ASTM F1875:2014) is the standard practice for fretting-corrosion testing of modular implant interfaces. This only applies a 1 degree of freedom loading (a uniaxial load with no rotational motion) and neglect the two forces and three frictional moment components of the load. *In vitro* studies (Preuss, Lars Haeussler et al. 2012, Jauch, Coles et al. 2014) tend to apply 2 degree of freedom load cases, combining a rotational motion with a time varying uniaxial load. However, these load cases do not replicate the complex multi-axial loads and rotations which result in axial and torsional loads on the head-neck interface. The frictional moment as a load component can affect the mechanical response of the interface by changing the stress field and resulted micro motion on the interface. The role of the frictional moment on fretting at head-neck interface is poorly understood while may contribute to accelerate the failure process. The frictional moment generated by two load cases was investigated: ISO standard gait and a physiological gait. The ISO standard is a 4 degree of freedom load case applying varying axial load with a peak of 400%BW and three rotations. The physiological gait was similar, but applied a peak axial load

of 233%BW, and two additional forces (anterior-posterior and medial lateral loads). The ISO standard was found to generate higher neck torques (0.88×BW%.m) compared to the physiological gait (0.66×BW%.m). This difference was expected, as the maximum contact force in the ISO standard was higher. However, proportional to the axial load, the neck torques were higher in the physiological gait. The variation of the neck torque during the load cases was also significantly different. For ISO, there was a change in the sign of the neck torque, which corresponded with the hip moving from flexion to extension. This change was more gradual in the physiological load case. The ISO standard generates more aggressive loads at the head-neck junction, both in terms of the frictional torque magnitudes and change in direction of the frictional torque.

The variation of frictional torque about neck axis is not a function of the contact force solely and the bearing moment, since the peak frictional torque does not necessarily occur at the same instance as the maximum contact force or bearing moment. The frictional torque about neck axis is also related to the distance from rotation direction to contact area (lever arm) and angle of the neck axis with the instantaneous frictional moment. These contributing parameters vary during activity cycle and from one activity to another. Simplified load cases do not capture the complexity of the interactions of the six degree of freedom loads and this may have consequences for the local mechanical environment and fretting at the head-neck junction.

There are two limitations: at present, the method is only suitable for hard-on-hard bearings. Further work is required to extend this approach to hard-on-soft bearings. This may be because of the significant strain occurring in the polyethylene cup, which does not satisfy the Hertz theory assumptions and/or different frictional behaviours from hard-on-hard bearings. Secondly, the model assumes that the friction factor is constant over the entire activity cycle. The friction factor may vary during the activity by changing the lubrication regime from dry to fluid film lubrication (Wang, Brockett et al. 2008, Meng, Liu et al. 2011, Meng, Liu et al. 2013). The developed method has the capability of using a varying friction factor; however, the analytical/numerical solutions for the behaviour of lubrication and friction regime are restricted to their simplifications and cannot be expanded to the presented 3D method. The simplifications, which include considering two of the angular velocities equal to zero, was required to change the underdetermined system of equations to a determined system of

equations (Chapter1, page 32 and chapter 2.2.4). Despite assuming a constant friction factor, good agreement was achieved compared to the experimental data for MoM and CoC bearings.

Compared with the numerical, *in vivo* and *in vitro* experimental studies on frictional moment (SchÄfer, SoltÉsz et al. 1998, Bishop, Waldow et al. 2008, Wang, Brockett et al. 2008, Bergmann, Graichen et al. 2010, Flanagan, Jones et al. 2010, Meng, Liu et al. 2011, Bishop, Hothan et al. 2013, Damm, Dymke et al. 2013, Meng, Liu et al. 2013), the method has the advantage of investigating a wide range of variables including bearing diameter, implanting angles, friction factor, loads and kinematics associated with different activities with insignificant cost. The method can be also expanded to investigate the variation of moment on the other implant interfaces such as cup-acetabulum and stem-femur. The outputs are useful for assessing the contribution of frictional moments to THR failure, particularly in fretting-corrosion at the head-neck junction, by providing the necessary localized loading conditions at the head-neck junction.

2.7 Limitations of the method

As mentioned in the literature review, friction at the head-cup interface is a function of kinematics, surface characteristics of the interfaces and lubrication regime at the interface. The interrelation of these parameters causes a complex variation of friction factor during cycles of daily activities. There is not a model in the literature for friction in three-dimensional rotation space which takes the aforementioned into account. To this end, the presented model simplifies the friction factor of the interface to a constant value, extracted under the peak load. The friction factor of metal-on-metal interfaces is maximum under peak load(Damm, Dymke et al. 2013). However, for metal-on-polyethylene material combination, by increase of the contact stress the friction factor decreases (chapter 1, page 38). Hence, compared to *in-vitro* results (Figure 2.6), assumption of a constant friction factor extracted from peak load of a cycle overestimates the frictional moment value for all the cases within marginally and conservatively higher magnitudes for metal-on-metal bearing couples and significantly higher magnitudes for metal-on-polyethylene .

2.8 Summary

In this chapter, an analytical method was developed to calculate three-dimensional frictional moments in MoM bearing couples under loading of daily activities. This method was validated against currently available frictional moments reported from *in vitro* studies on different bearing combinations and its reliability for calculating the demonstrated MoM frictional moments. Furthermore, the uses of this method for calculating frictional moments from available kinematics and forces of walking were established, the ISO standard of this method was demonstrated. The differences in the frictional moment behaviour between these two were discussed. In the next chapter, this method will be implemented to demonstrate frictional moment variation during a range of daily activities to depict the complete kinematic of the head-neck junction in its service condition.

Chapter 3. Variation of frictional moments and bending moments at the head-neck interface during daily activities

This chapter is based on the following publication:

7. **Farhoudi, H.**; Oskouei, R. H.; Pasha Zanoosi, A.A.; Jones, C.F.; Taylor, M. An analytical calculation of frictional and bending moments at the head-neck interface of hip joint implants during different physiological activities, **2016** *Materials*,*9,12*,982.

3.1 Overview

In the previous chapter, a new methodology was developed to analytically determine frictional moments at the head-cup bearing couple of THR. This method can calculate bending moment induced on the head-neck interface due the offset of the force from its contact region. The theoretical frictional moment resulted from a variety of bearing couples being successfully verified against the experimental results for a simplified gait cycle. Mechanical loading data were required for common physical daily activities of patients so that realistic loading situations could be determined for a better understanding of the failures and the identification of activities which are potentially more damaging than others in terms of the frictional torques and moments. Moreover, the existing literature confirms that there is not enough information about the bending moments at the head-neck taper junction, especially for MoM bearing couples; hence, these moments should be also determined and quantified.

In this chapter, frictional moments and bending moments, at the head-cup interface, and frictional torques acting on the head-neck junction are determined for MoM bearings during nine activities performed on a daily basis. This study provides useful data on the magnitude and direction of frictional and bending moments generated by different head sizes and body weights. These mechanical loads of various physical activities are essential for understanding of the mechanical behaviour and failure of the taper junction *in vivo* without which computational and *in vitro* testing methods cannot be projected to service condition of the implant.

3.2 Methods

The analytical method was implemented to find bending moments vector ($\overrightarrow{M_{\mathrm{b}}}$), frictional moments vector ($\overrightarrow{M_{\mathrm{f}}}$), and frictional torque about the head-neck interface vector ($\overrightarrow{M_{\mathrm{n}}}$) under contact forces during nine different activity cycles. To calculate the bending moments induced at the head-neck interface, the instantaneous distance vector of the contact force from the clamping region of the head and neck was formed from the available kinematics of the head with respect to the cup. The offset of the contact region of the head and neck from the force was assumed to be 10 mm which is near the common geometry of a neutral 12/14 taper design. The cross product of the instantaneous distance vector and the corresponding contact

force (the bending moment induced at the head-neck clamping interface) was determined for the entire activity cycle.

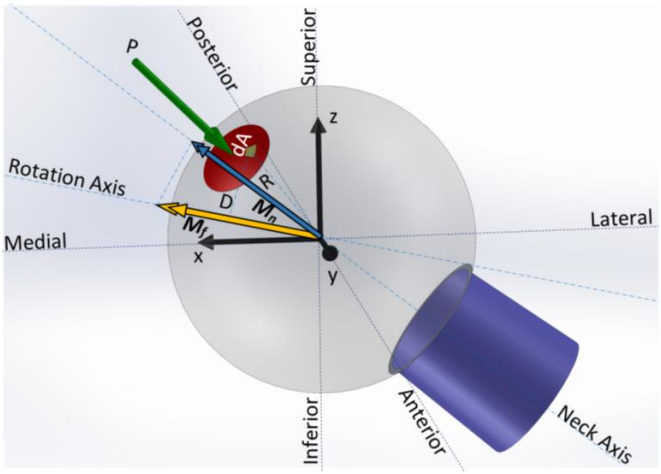

Figure 3.1. Head-neck taper junction of a left hip implant and femur coordinate system. The contact force P distributed over the Hertz contact area induces a tangential frictional force during the relative motion of the head and cup. The tangential force and lever arm D produce the frictional moment Mf and its projection onto the neck direction which is the frictional torque Mn.

In this manner, the bending moments, frictional moments, and torque at the head-neck interface were determined for one cycle of nine activities taken from the Orthoload website: slow, normal, and fast walking, stair up and stair down (ipsilateral foot contacting ground), sit-to-stand and stand-to-sit (two legged), one-leg-standing (ipsilateral), and knee bending (two legged). Patient dynamics data were obtained from the Hip98 software available in the Orthoload database (Bergmann, Graichen et al. 2010) for three cases: lightest patient (702 N), heaviest patient (980 N), and an average patient (836–920 N, as defined in Hip98). Dynamics of the average patient are illustrated Figure 3.2. For all cases, the investigations were carried out for a CoCr/CoCr bearing couple with a nominal diameter of 46 mm and clearance of 54 µm (cup diameter: 46.018 mm and head diameter: 45.964 mm) and a friction coefficient of 0.12 (Bishop, Waldow et al. 2008). This friction coefficient corresponded to the maximum contact load instance. To determine the effect of implant head diameter on the frictional moments and torque at the head-neck interface, the normal walking activity of the average patient was simulated for three bearing diameters (28, 46, and 70 mm) representative of commonly used heads in total hip replacement and hip resurfacing.

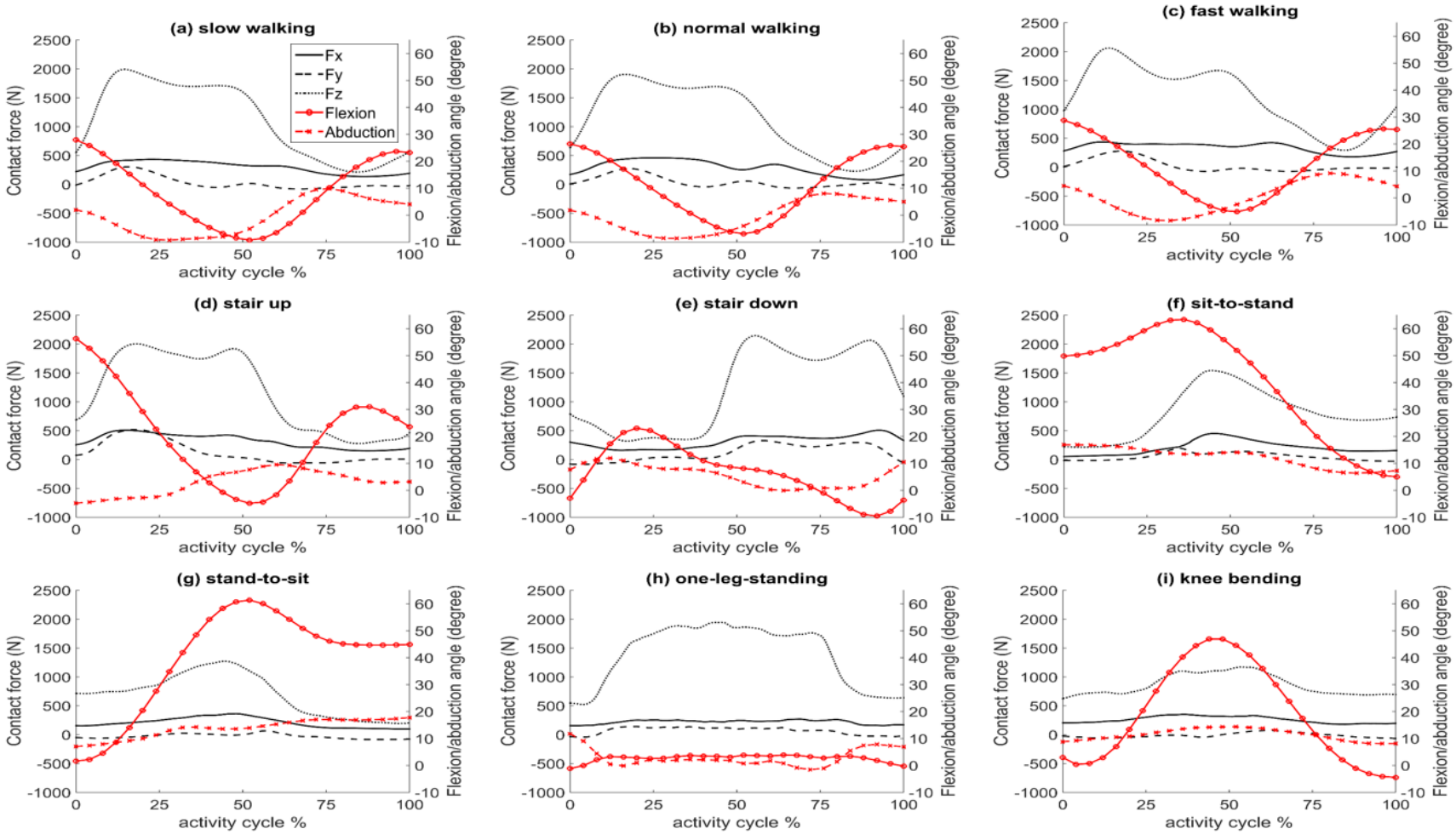

Figure 3.2 Contact forces in the x, y, and z axes along with flexion and abduction angles for one cycle of each activity for the average patient, data from Hip98 and Orthoload. (a) slow walking (b) normal walking (c) fast walking (d) stair up (e) stair down (f) sit-to-stand (g) stand-to-sit (h)one leg standing (i)knee bending

3.3 Results

Frictional and bending moments of the average patient were plotted as vector components in the neck coordinate system of a left hip implant (Figure 3.3). The data are extracted in a head-neck coordinate system to be suitable as inputs if future finite element studies on head-neck mechanical responses to daily activity loads. Slow and fast walking activities had components almost identical to normal walking and therefore were excluded for a clearer presentation of the graphs Figure 3.3. The results of the walking activities are separately presented in Figure 3.4 for a clearer presentation. The one-leg-standing activity was also excluded from the graphs of Figure 3.3 for a better presentation of the other graphs as its numerous irregular fluctuations would deface the other graphs. Results for one leg standing activity is also presented in Figure 3.4.

3.3.1 Frictional moment on the head-neck interface

Considering all the activities (Figure 3.3, Figure 3.4) no single component of the frictional moments dominated the other two; and thus, ignoring any of these components for simplification should be justified. The frictional moment components of sit-to-stand, stand-to-sit and knee bending activities had sharper changes of direction in comparison with normal walking, stair up and stair down activities. Variations in the total magnitude of the frictional moment vector (M_f) were plotted against the activity cycle for the lightest, heaviest and average patient for each physical activity (Figure 3.5). Both the magnitude and sign (direction) of the torque component of the frictional moment about the neck axis ($\overrightarrow{M_n}$) are shown in Figure 3.5 to illustrate the change of direction and variations in magnitude. To provide insight into fretting-corrosion initiation at the head-neck interface as a consequence of frictional torque, a lower threshold torque (L.T=4.97 Nm) and an upper threshold torque (U.T=7.78 Nm) for depassivation of the material surface from Jauch et al. study (Jauch, Coles et al. 2014) are presented in Figure 3.5. These thresholds are the upper bounds of torques initiating corrosion at the head-neck interface, reported by Jauch et al. (Jauch, Coles et al. 2014) for 4.5 kN and 6 kN assembled implants, respectively (Chapter1, page 60). It can be seen from Figure 3.5 that, in most simulated activities, the maximum and/or minimum torque values were near the L.T threshold. Looking at Figure 3.6, frictional moment showed a linear relation with the head size. If the bearing diameter is increased to 70 mm, the torque exceeded the U.T threshold for walking. Recent studies have reported a direct relationship between increased bending

moment at the head neck junction and increased oxide layer depassivation current (Panagiotidou, Meswania et al. 2015). However, threshold bending moments for depassivation have not been reported.

3.3.2 Bending moment on the head-neck interface

All activities had a three-dimensional dynamic behaviour. The x' component of the bending moments dominated the y' component and was positive during all activity cycles (i.e. no change in direction, Figure 3.3.d, Figure 3.3.e, Figure 3.4d and Figure 3.4e). There was no z' component for the bending moment because the contact force passes through the centre point of the head located on z' axis of the neck coordinate system. In case of the walking activity Figure 3.4.d and Figure 3.4.e) the faster the walking was, the higher the bending moment components were happening. The stair down activity has the highest bending moment imposed on the head-neck interface because during this activity the gravity forces of descending from stairs was more gravity forces occurring in the other activities in an in-level manner.

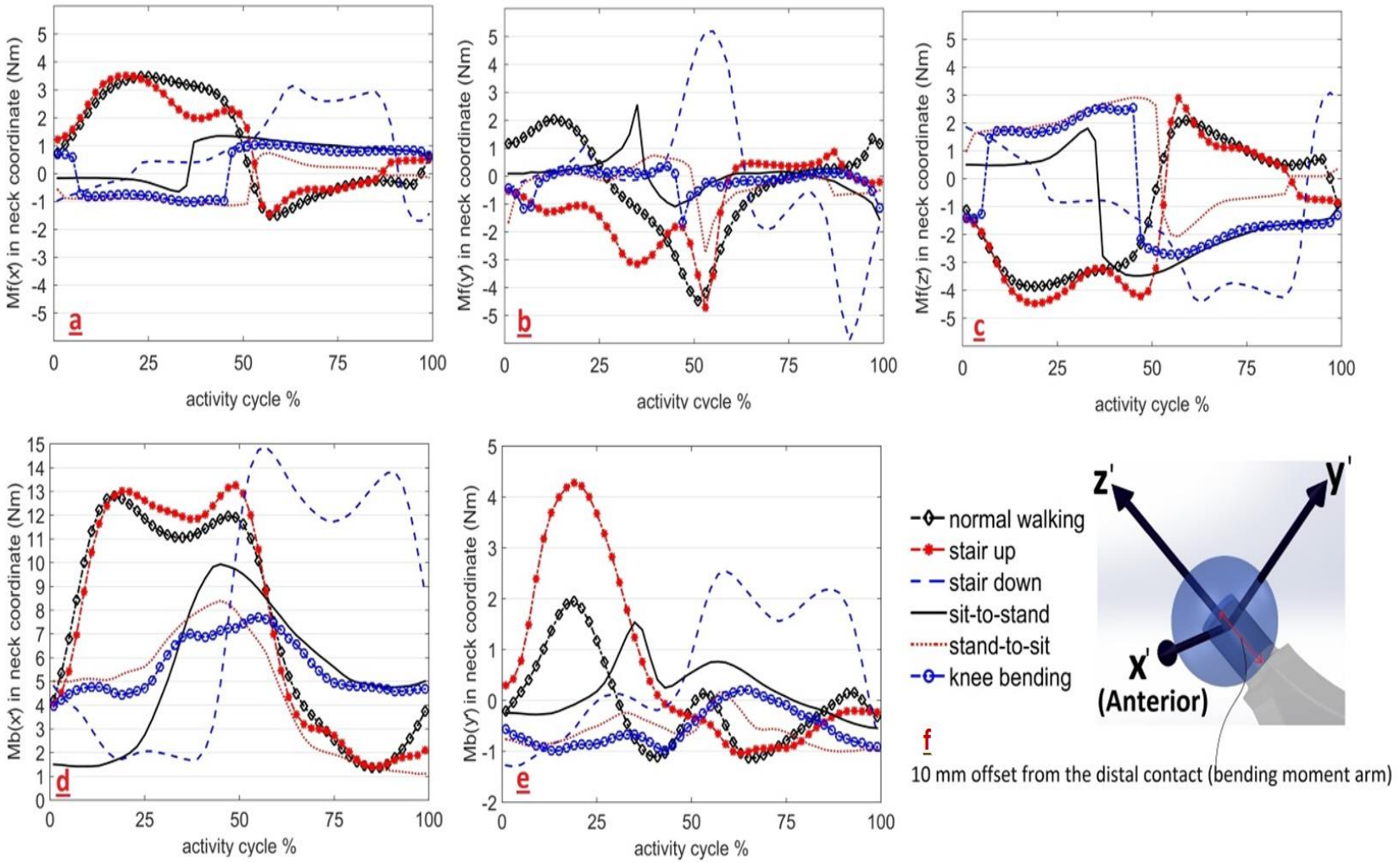

*Figure 3.3 Components of frictional moments and bending moments for six daily activities in the neck coordinate system (x'y'z'): (**a**) Frictional moments about the x' axis; (**b**) Frictional moments about the y' axis; (**c**) Frictional moments about the z' axis; (**d**) Bending moments about the x' axis; (**e**) Bending moments about the y' axis; and (**f**) Coordinate system definition.*

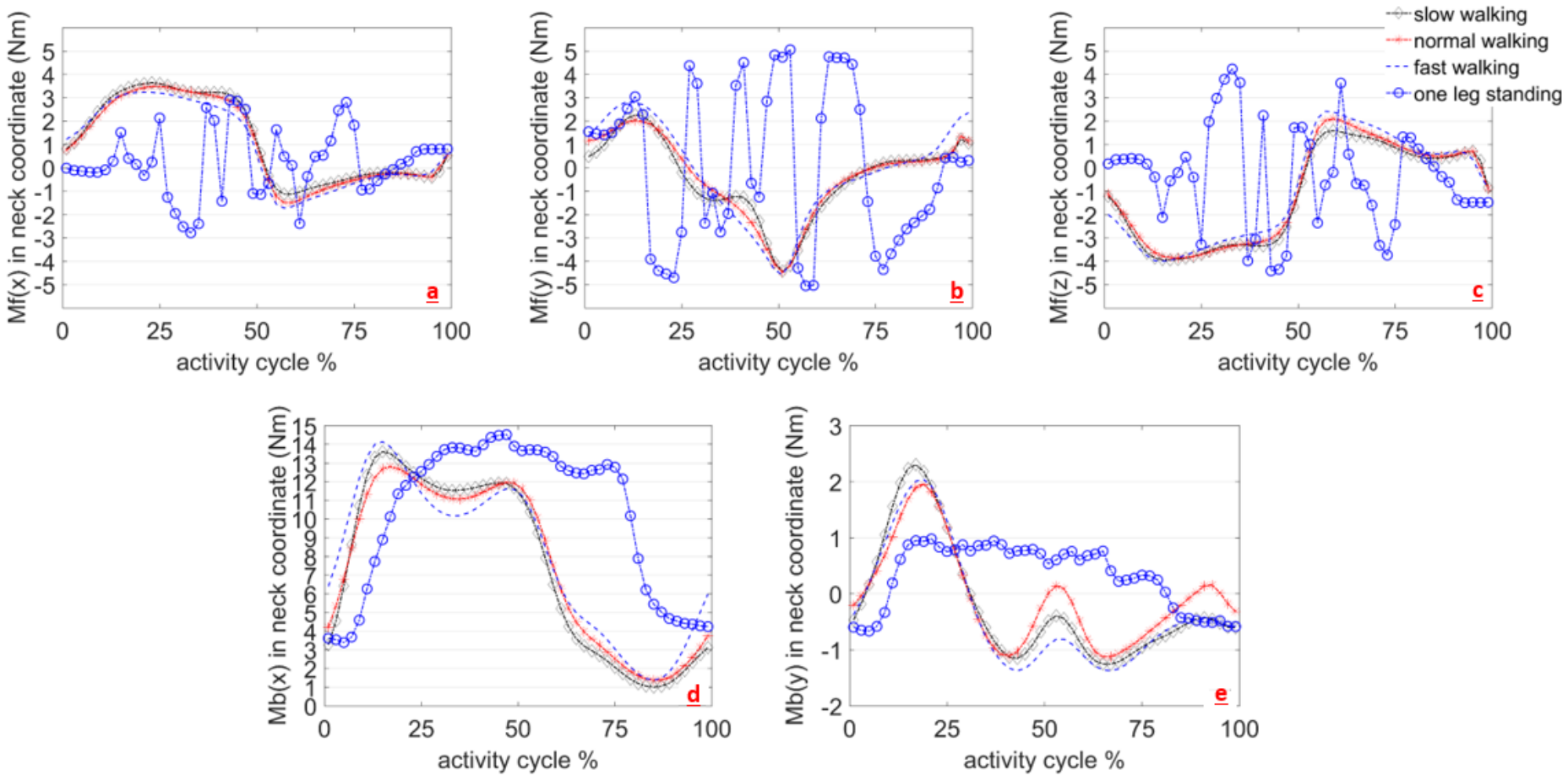

*Figure 3.4 Components of frictional moments and bending moments for slow walking, normal walking, fast walking and one leg standing in the neck coordinate system (x'y'z'): (**a**) Frictional moments about the x' axis; (**b**) Frictional moments about the y' axis; (**c**) Frictional moments about the z' axis; (**d**) Bending moments about the x' axis; (**e**) Bending moments about the y' axis; and (**f**) Coordinate system definition.*

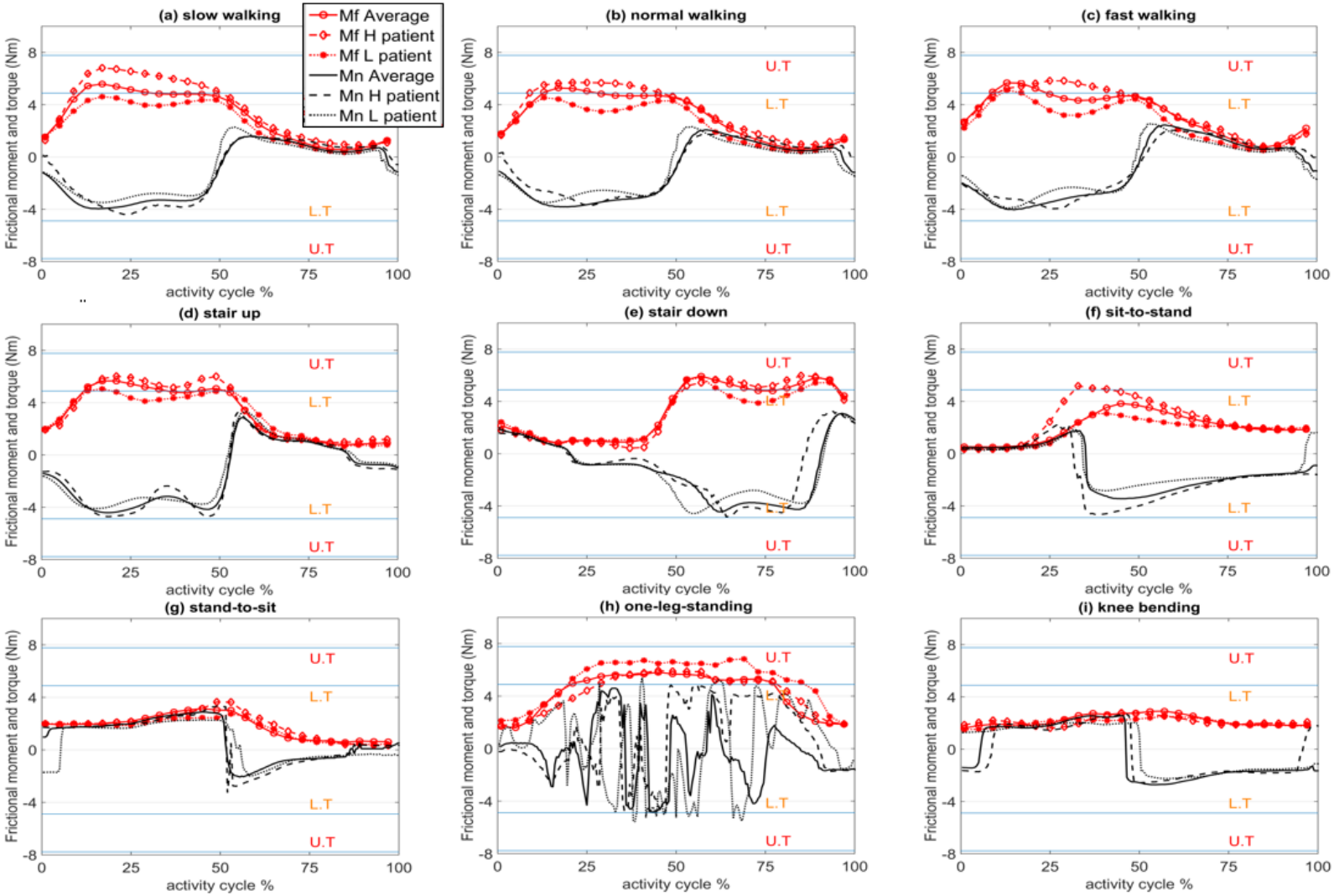

Figure 3.5. Frictional moment (M_f) and torque at the head-neck interface (M_n) for one cycle of each activity, for the average, heaviest (H), and lightest (L) patients. In the graphs, U.T and L.T indicate the upper and lower thresholds for depassivation, respectively. (a) slow walking (b) normal walking (c) fast walking (d) stair up (e) stair down (f) sit-to-stand (g) stand-to-sit (h)one leg standing (i)knee bending

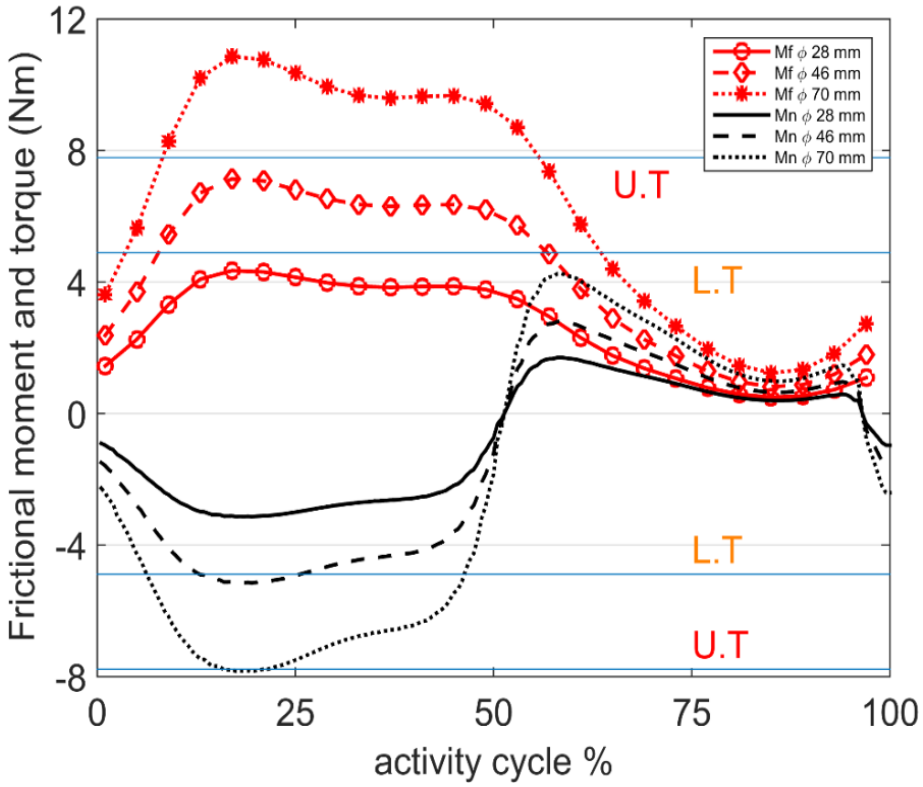

Figure 3.6. Frictional moment (M_f) and torque at the head–neck interface (M_n) for one cycle of normal walking, for the average patient, for different head diameters of 28, 46, and 70 mm. U.T = upper threshold for depassivation and L.T = lower threshold for depassivation.

The maximum magnitude of the bending moments, frictional moments and torques over the cycle of each activity is listed in Table 3-1 for the lightest, heaviest and average patients. These maximum magnitudes ranged from 7 to 21.6 Nm for the bending moment, 2.6 to 7.1 Nm for the frictional moment and 2.3 to 5.7 Nm for the torque acting on the head-neck interface. Generally, knee bending, and stand-to-sit activities had the lowest maximum magnitudes and one-leg-standing caused the highest magnitudes of bending moment, frictional moment and torque. The almost simultaneous occurrence of the maximum magnitude of M_b, M_f, M_n and contact force P can be seen in Table 3-1 where the times of maximum moments, torque and contact force (t_{Mb}, t_{Mf}, t_{Mn} and t_p) in different patients and activities are approximately the same in 14 out of the 27 simulated cases. t_{Mb} was found to be more coincide with t_p which is due to the direct relationship between the bending moment and contact force, regardless of the presence or absence of relative rotation. This was not true for the frictional moment due to the dependency

of the frictional moment on the occurrence and direction of the relative rotation. Depending on the activity, the torque at the head-neck interface had several changes in its direction. The number of changes of direction ranged from 1 to 4, with most cases changing direction twice over the activity cycle. However, one-leg-standing experienced 12-15 changes in the direction of the torque. In most cases, frictional torque appeared in both the positive and negative direction of the neck axis.

Table 3-1 Maximum magnitude of bending moment (M_b, Nm), frictional moment (M_f, Nm), torque at the head-neck interface (M_n, Nm), contact force (P, N) and their corresponding times (percent of activity cycle), number of changes in direction of the torque at the head-neck interface (#CD); for the lightest (L), heaviest (H), and average (Avg) patient

Activity		M_b	M_f (Nm)	M_n (Nm)	P (N)	t_{M_b} (%)	t_{M_f} (%)	t_{M_n} (%)	t_P (%)	#CD
Slow Walking	**L**	12.6	4.6	3.5	2066	17.0	17.0	17.0	17.0	2
	H	15.5	6.8	4.4	2133	17.0	17.0	23.5	16.5	3
	Avg	13.8	5.6	4.0	2057	16.0	15.5	16.0	15.0	2
Normal Walking	**L**	12.7	5.7	3.5	2030	13.5	14.0	14.0	14.0	2
	H	12.8	5.7	3.7	1769	21.0	22.5	25.5	19.0	3
	Avg	12.9	5.3	3.8	2285	17.5	17.5	19.5	17.5	2
Fast Walking	**L**	14.5	5.2	3.9	2330	13.0	13.0	13.0	13.0	2
	H	13.0	5.9	4.0	1998	26.5	26.5	26.0	26.5	3
	Avg	14.3	5.7	4.0	2456	14.0	14.5	15.0	14.0	2
Stair Up	**L**	14.6	5.1	4.1	2278	16.0	16.5	15.5	16.0	2
	H	14.1	6.0	4.1	1927	47.0	47.5	47.0	47.5	2
	Avg	13.7	5.7	4.7	2466	18.5	18.5	18.5	18.5	2
Stair Down	**L**	16.2	5.9	4.4	2626	54.5	55.0	55.0	54.5	2
	H	13.9	6.0	4.6	2212	89.0	85.0	64.0	89.5	2
	Avg	15.1	3.0	4.8	2553	56.0	56.0	62.0	56.0	2
Sit-to-Stand	**L**	9.5	3.1	2.8	1678	41.0	41.0	41.0	41.0	2
	H	11.7	5.3	4.7	2036	37.5	34.0	38.0	38.0	1
	Avg	9.9	3.8	3.4	1866	45.0	45.0	45.0	45.0	1
Stand-to-Sit	**L**	7.6	2.8	2.3	1266	45.5	55.5	44.0	45.0	2
	H	8.9	3.7	3.3	1504	49.5	53.0	50.0	49.5	4
	Avg	8.4	3.2	2.9	1529	45.0	51.5	45.0	45.5	4
One-Leg-Standing	**L**	21.6	7.1	5.7	3616	39.0	39.0	38.5	39.0	13
	H	14.5	6.0	4.9	2185	46.5	46.0	46.5	46.5	12
	Avg	14.5	5.8	4.8	2270	46.5	46.5	43.5	46.5	15
Knee Bending	**L**	7.6	2.6	2.3	1445	58.0	50.0	58.0	58.0	1
	H	7.1	3.0	2.7	1150	46.0	48.0	45.0	46.0	3
	Avg	7.7	3.0	2.7	1406	55.5	46.0	54.5	57.0	2

3.4 Discussion

This study determined the variations in the bending moment, frictional moment and torque at the head-neck interface of a metal-on-metal bearing couple for different activities of daily living.

The obtained moment and torque profiles can be employed in *in vitro* tests and computer simulations.

As can be seen in Figure 3.5, stair up and normal walking activities had similar trends of variation in their frictional moment components especially in x' and z'. This could be because of similarities in their dynamics, as presented in Figure 3.2(b) and Figure 3.2(d). Moment components of the normal walking activity were almost in a range that covers the other activities. This suggests that *in vitro* tests based on a realistic walking cycle, (the most frequent daily activity (Morlock, Schneider et al. 2001)), may be an acceptable representation of the other daily activities in terms of the range of frictional moments.

The flexion/extension degree of freedom (Figure 3.2) was dominant in determining the direction of frictional moment vector ($\overrightarrow{M_f}$), especially the x' and z' components. The instants of switching between flexion and extension (peaks of the flexion graph in Figure 3.2) coincide with the change of direction of $M_{fx'}$ and $M_{fz'}$ (intersecting with 0 Nm in Figure 3.3(a) and Figure 3.3(c)). Considering the small version/anti-version angle (usually in the range of ±10 degrees), the neck axis (z'-Figure 3.3) receives a larger projection from the flexion-extension frictional moment (Figure 3.1). Consequently, changes in direction of the frictional torque (intersecting with 0 Nm in Figure 3.5) coincide also with peak of flexion and extension angle.

Among the studied activities, normal walking resulted in the smallest range (minimum to maximum peak) of frictional torque about the neck axis (6.1 Nm). An overall consistency can be seen in both the frictional moment and torque trends and, to some extent, their magnitudes during three activities of slow, normal and fast walking for all the studied patients. One-leg-standing caused the largest range (11 Nm) of frictional torque about the neck axis. This could result from un-interrupted contact force due to the body weight and muscle contraction forces on one leg combined with small flexion and extension "stabilising" movements leading to high positive and negative torques. Several changes in flexion and extension for stabilising could explain the high number of changes of the frictional moment direction and its torque component (12-15 times) during one-leg-standing.

Based on the reported thresholds for critical torques initiating fretting-corrosion at the head-neck interface (Figure 3.5), frictional torques in most activities were near the lower threshold. Disruption of the passive protective layer formed on the metal surface at the head-neck interface (due to the repetitively applied contact forces) may be intensified when assisted by the frictional moments. Given that frictional moments are thought to contribute to fretting-corrosion at the head-neck interface (Jauch, Coles et al. 2014, Panagiotidou, Meswania et al. 2015), experimental and numerical studies should be performed to better understand if simplified uni-axial force testing protocols represent realistic, six degree of freedom fretting-corrosion conditions.

Frictional moments and torques were proportional to the head diameter of the implant. The relationship was linear; thus, one may scale the results of this study by the ratio of head diameters to estimate the moment and torque trends for other head sizes during the studied activities. For the 46 mm head, the torque about the head-neck interface exceeded the lower threshold for depassivation during the stance phase of walking. In the case of the 70 mm head, the torque exceeded the upper threshold for depassivation during the stance phase and the lower threshold during the swing phase. This would be expected as, under a constant friction coefficient considered in the method, an increase in the head size would increase the frictional moment. In a perfect condition, it would be expected that due to the low abrasion of hard-on-hard bearings and promoting the hydrodynamic lubrication by a smooth surface and low clearance at the bearing, the friction coefficient of the large head metal-on-metal bearings decreases. However, in the real condition, poor positioning of the cup can considerably demote the lubrication film pressure and cause partial lubrication and consequently increase the friction coefficient (Bishop, Hothan et al. 2013). This suggests that increase in the head diameter increased the torsional loads at the head-neck interface, which may also increase the potential for fretting-corrosion failure in the taper junction (Panagiotidou, Bolland et al. 2013).

Bending moments conformed to the contact forces in all the activities to a great extent. The unidirectional bending moment about x’ contributes to both the normal and tangential forces of the contact area. The fretting regime of a contact area is a function of normal and tangential forces and may vary from elastic region to partial slip and gross slip regions (Neu 2011).

Panagiotidou et al. (Panagiotidou, Meswania et al. 2015) reported that with increasing bending moment, the maximum fretting current (an indicator of the oxide layer depassivation) increases and then decreases for a CoCr/Ti combination. For CoCr/CoCr and ceramic/CoCr head-neck combinations, the maximum fretting current increases with increasing bending moment. Donaldson et al. (Donaldson, Coburn et al. 2014) reported that for one cycle of walking activity, a 10 mm increase in the head offset (which results in a linearly proportional increase in the bending moment), increases the micro-motions by 5 µm. The predicted moments in this study may be scaled with respect to the offset and bearing radius to calculate the bending moments and frictional moments, respectively.

Overall, the results suggest that six degrees of freedom loading may be required to adequately simulate the mechanical environment of total hip replacement implants. The observed synchronicity of the maximum values of the frictional moment ($\overrightarrow{M_f}$), torque at the head-neck interface ($\overrightarrow{M_n}$) and contact force ($\vec{P}$) suggests that applying a uni-directional contact force in its dominant direction (z axis), together with a bi-directional moment, maybe an acceptable simplification of the *in vivo* mechanical environment of the implant. Given the significance of the frictional moment and torque in terms of both magnitude and direction, simplified mechanical tests of fretting-corrosion at the head-neck interface which apply only uni-directional contact forces (Goldberg and Gilbert 2003, Gilbert, Mehta et al. 2009) may considerably underestimate the severity of the mechanical environment by neglecting the depassivation effect of frictional torque on the contacting materials of the head and neck. Panagiotidou (Panagiotidou, Meswania et al. 2015) recently reported an experimental method of applying coupled uni-directional torque and uni-directional contact force at the head-neck interface. This approach is a more reasonable testing method with two degrees of freedom in loading. However, it still neglects the multi-directional oscillatory nature of the frictional moment and may underestimate the severity of the *in vivo* mechanical environment; and consequently, overestimate the service longevity of the implant taper junction.

3.5 Summary

Bending and frictional moments induced at the head-cup bearing, and frictional torques at the head-neck interface were determined for an MoM bearing couple during nine different daily activities. Frictional moments had a three-dimensional nature varying in both magnitude (maximum values ranging 2.6 to 7.1Nm) and orientation (up to 15 changes in directions) over the activity cycles. The range of frictional moment components for walking covers the range of frictional moments in most activities, except knee bending. However, the pattern of variation in frictional moment components for walking did not resemble the other activities. The calculation of frictional moments for different head sizes showed that frictional moment is linearly proportional to the head's radius. In most cases, frictional moment components in the lateromedial direction had the highest magnitude.

Chapter 4. Effect of frictional moments in stress field and micro-motions in head-neck interface

This chapter is based on the following publication. It is declared that the finite element model was developed and implemented by another PhD student in the team (K. Fallahnezhad) for this study.

Farhoudi, H.; Fallahnezhad, K.; Oskouei, R.H.; Taylor, M. A finite element study on the mechanical response of the head-neck interface of hip implants under realistic forces and moments of daily activities: Part 1, level walking", Journal of the *Mechanical Behavior of Biomedical Materials* ***2017***,75, 470-476.

4.1 Overview

Physiological loads on modular junctions include 3-axis cyclic forces along with 3-axis cyclic frictional moments, resulting from sliding at the bearing couple interface. The projection of the frictional moment onto the axis of the head-neck junction (neck axis) produces a torque on the neck which is transferred to the taper junction. This torque can induce torsional micromotion at the head-neck interface, which can then lead to multiaxial fretting when combined with the hip contact force. The simplified loading conditions used in the previous studies could significantly influence the outputs of the fretting and corrosion observed in such experiments.

In addition to the previously available contact forces (English and Kilvington 1979, Bergmann, Graichen et al. 1993, Bergmann, Graichen et al. 2010), the data on head-cup frictional moments are now available for the activity of walking (Damm, Dymke et al. 2013, Farhoudi, Oskouei et al. 2016). This provides 6 DoF load inputs which include three force components and three-moment components. However, the contribution of the frictional moments to the stress-field, relative displacements between the contacting surfaces and consequently, the fretting wear behaviour has not been reported yet.

Using the available 6 DoF load inputs, in this chapter, a FEA of a head-neck taper junction of an implant was conducted (using a previously developed FE model by another PhD student in the team) in three different loading conditions which included level walking gait forces only (F only), level walking frictional moments only (M only) and combined gait forces and frictional moments (F&M). This analysis aimed at carefully evaluating the contribution of frictional moments to the fretting-wear-related parameters at the head-neck interface. The results of this study present a perspective of dynamic stress-field and micromotion at the head-neck interface of the modelled geometry and materials during level gait walking.

4.2 Methods

The previously established and verified three dimensional (3D) finite element model of an isolated head-neck interface ((Fallahnezhad, Farhoudi et al. 2016)) was developed by another PhD student in the team (K. Fallahnezhad) to simulate and apply currently available 6 DoF load inputs of level gait normal walking for this chapter of thesis. The model consisted of a 12/14 taper CoCr head and a CoCr neck with a proximal angular mismatch (head taper angle = 2.858˚, neck taper angle = 2.834˚, angular mismatch = 0.024˚ (Rehmer, Bishop et al. 2012)). The nodes located at the external surface of the head were constrained in all directions. The assembly force and the load components of level gait were applied to the bottom face of the neck. The forces were obtained from Hip98 software (Bergmann, Graichen et al. 2010) and the frictional moments were calculated from a previous chapter metal-on-metal bearing couple (Farhoudi, Oskouei et al. 2016), as shown in Figure 4.1.a.

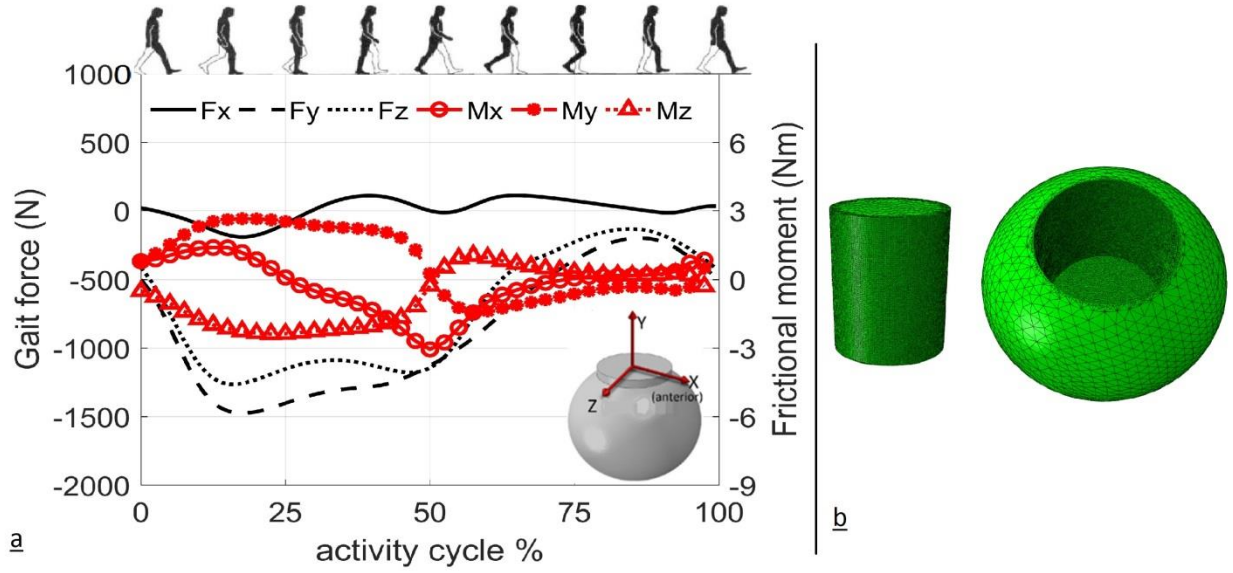

Figure 4.1. (a) Input gait forces and frictional moments for a normalized walking gait cycle presented in a coordinate system at the bottom face of the neck (end-of-neck coordinate system) for right hip, and (b) finite element models of head and neck with a meshing structure gradually refined towards the contact interface.

These load components were sampled over 100% of a normalized gate cycle (0 for initial contact and 100 for terminal swing) and were applied to the end-of-neck coordinate system. The selection of a metal-on-metal bearing for this study was because of their high failure rates together with wear debris and metal ions generation at the head-neck interface (Bolland,

Culliford et al. 2011, Cook, Bolland et al. 2013), and higher frictional moments in comparison with common metal-on-polyethylene bearings (Bishop, Waldow et al. 2008, Flanagan, Jones et al. 2010).

Using ABAQUS/Explicit, an explicit (dynamic) FE analysis was used in this study. A fixed mass-scaling method was applied to reduce the computational time, and the kinetic-energy/total-energy ratio was monitored to be less than 10% during the entire simulations. This assures that inertia forces do not influence the results due to mass-scaling. To simulate mechanical interactions at the head-neck interface, a surface-to-surface discretization contact method with a finite sliding formulation was used. Contact pressures (Cp) were monitored using a Lagrange multiplier formulation. A friction coefficient of 0.3, which was verified previously for the same junction (Fallahnezhad, Farhoudi et al. 2016), was used in the penalty method for the contact model.

Quadratic tetrahedral elements (C3D10M in ABAQUS) were used to mesh the head and neck models (Figure 4.1b). The elements were refined in successive steps to achieve mesh-independent results. The size of elements at the contacting interface was 0.15 mm. The head and neck models were meshed with 177,573 and 114,761 elements, respectively. The CoCr alloy (ISO 5238–12) was modelled with an elastic-linear plastic material model with properties of: Young's modulus=210 GPa, Poisson's ratio=0.30, yield strength = 910 GPa, linear-plastic-slope/elastic-modulus = 1.4%, ultimate tensile strength = 1,350 MPa and elongation = 15%.

In the first step, the assembly process of the head-neck junction was replicated for which a force of 4 kN was applied with a rate of 500 N/s. In the second step, the load components of a full gait cycle of normal walking were applied to the bottom face of the neck in three different loading scenarios of: F only (only gait forces), M only (only frictional moments) and F&M (gait forces and frictional moments). Contact pressures (Cps) and micro-motions (δ) were monitored before and after applying the activity gait loads and the time step at which the maximum of contact pressure and micro-motion occurred was determined. It was found that the maximum contact pressure and maximum micro-motion occur simultaneously under the peak force (resultant of F_x, F_y and F_z) for F only and peak frictional moment (resultant of M_x, M_y and M_z) for M only loading

scenarios. In the F&M loading case, the maximum contact pressure and maximum micro-motion occurred under the peak force, indicating that the force components were more dominant than the moment components in inducing maximum contact pressure and micro-motion. This instance of peak load was considered as the critical instance for further investigation of the interface's mechanical responses.

Using a custom-written Python code, the results of contact pressures, shear stresses and displacements were extracted for each loading scenario for all the nodes of the head and neck contacting surfaces at the maximum force and moment instance which resulted in maximum stresses and micro-motions over the gait cycle. A MATLAB code was then implemented to determine micro-motions (relative displacements), and fretting work at the contacting nodes of the head-neck interface for this instance of time. For a better presentation of results, the neck circumference was projected onto a plane, and the extracted parameters were presented as the normal axis (z). In this configuration, as shown in Figure 4.2, the proximal end of the neck was considered as the origin (zero) for the neck length axis. The second axis presents the angular position starting from the middle line of the inferomedial sector (zero radians).

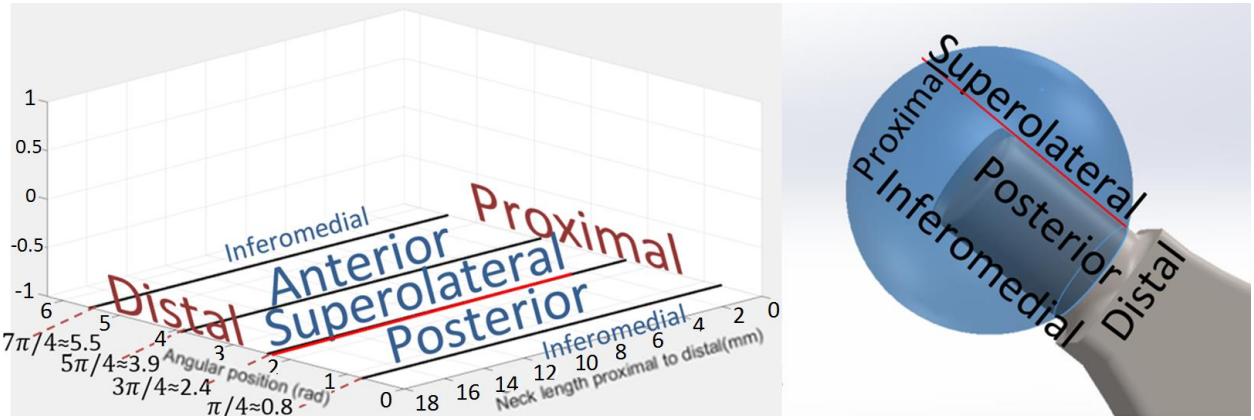

Figure 4.2. 3D configuration used for results presentation.

4.3 Results and discussion

The results of the mechanical response of the head-neck interface in the form of contact pressure, micro-motions, shear stresses and fretting work are presented and discussed in the

following sections. It is then followed by the possible implications of the results for *in vitro* testing.

4.4 Contact pressure

Contact pressures (Cp) are plotted over the neck surface for the three loading scenarios Figure 4.3. The contact pressure contours distinguish contacting nodes from non-contacting ones over the neck surface (i.e. non-contacting nodes have zero contact pressure). The assembly force results in a press-fit connection in the proximal side of the junction inducing large local contact pressures (900 MPa at the circular edge). In the M only loading case, the contact area was similar to the initial press-fit area in the proximal region (after applying the moment only 0.27% of the initially non-contacting surface nodes temporarily came into contact). When subjected to the level gait forces in both the F only and F&M loading cases, the contacting region was extended over the superolateral sector where 8.43% and 9.57% of the initially non-contacting surface nodes were in contact, respectively. This caused a reduction in the peak Cp in the proximal contact region. The extended contact region in the superolateral sector under the F only and F&M loading cases was due to the bending effect of the force components which suggests that the vertical component of the force was dominant in bending the neck towards the head surface and causing them to contact each other. This occurred while the torsional components of the frictional moment and tangential components of the force with respect to the neck axis lead to relative displacements in the tangential direction of the contacting surface. On the proximal side, the maximum Cps (red circles in Figure 4.3a-c) were distributed over the initial press-fit area for all the three cases. In the temporary contact region of F only and F&M, the maximum Cps occurred mostly along the middle-line of the superolateral sector. Comparing the maximum magnitudes of contact pressure over the length of the neck (*Figure 4.3*d), M only induced the lowest values of Cp in the initial press-fit area (proximal) and negligible contact extension occurred in the remaining length of the neck. Whereas, F only and F&M had similar values of maximum Cp over the neck length.

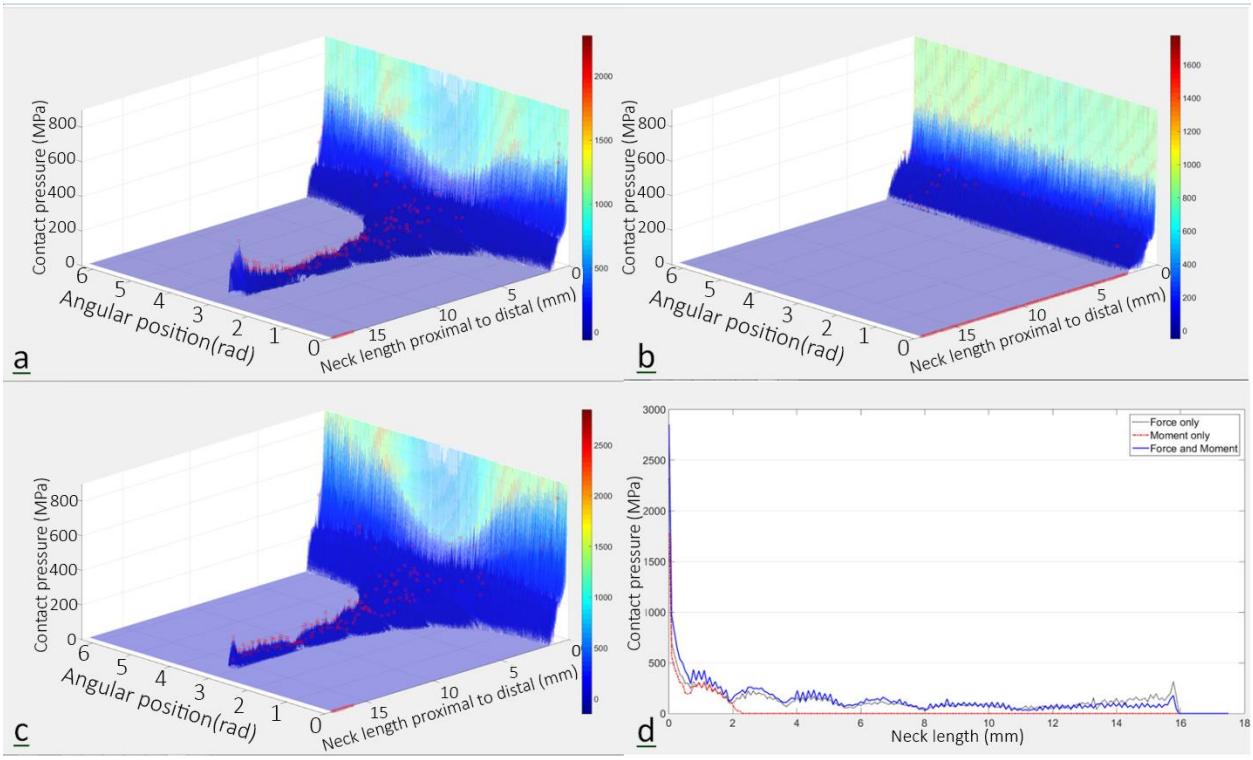

Figure 4.3. Distribution of contact pressure (Cp) in MPa over the neck surface for: (a) force only, (b) moment only, (c) force and moment loading scenarios. Small red circles in the contours indicate the maximum contact pressure in each division of the neck length over 360 degrees of the neck circumference, and (d) maximum magnitudes of contact pressure along the neck length.

At the proximal press-fit rim, the initial uniform distribution of Cp was disturbed and higher magnitudes occurred at the anterior, posterior and inferomedial sections in F only and F&M loading cases, while this did not significantly change for the M only loading.

4.5 Micro-motions

Figure 4.4 illustrates the distribution of micro-motion (δ) for the contacting nodes under three cases of loading. Magnitudes of micro-motion for M only were significantly (by order of 10^2) smaller than F only and F&M loading cases. However, the frictional moment increased the micro-motions of the F&M loading compared to the F only case, especially when approaching the distal side of the neck, increasing the most distal micro-motions from 31 to 38 µm. Considering Figure 4.4a and 4c, the entire contacting area in the F only and F&M loadings experienced similar

magnitudes of micro-motions. A similar pattern for the distribution of micro-motions in M only (with peaks in the proximal anterior and posterior sectors) was observed in F only and F&M but with higher magnitudes (by order of 10^2). Although the δ magnitudes for the M only case were negligible, by comparing the maximum values of micro-motion for F only and F&M (Figure 4.4d), one can find that the superposition of the frictional moments with the gait forces has increased the micro-motions along the neck length.

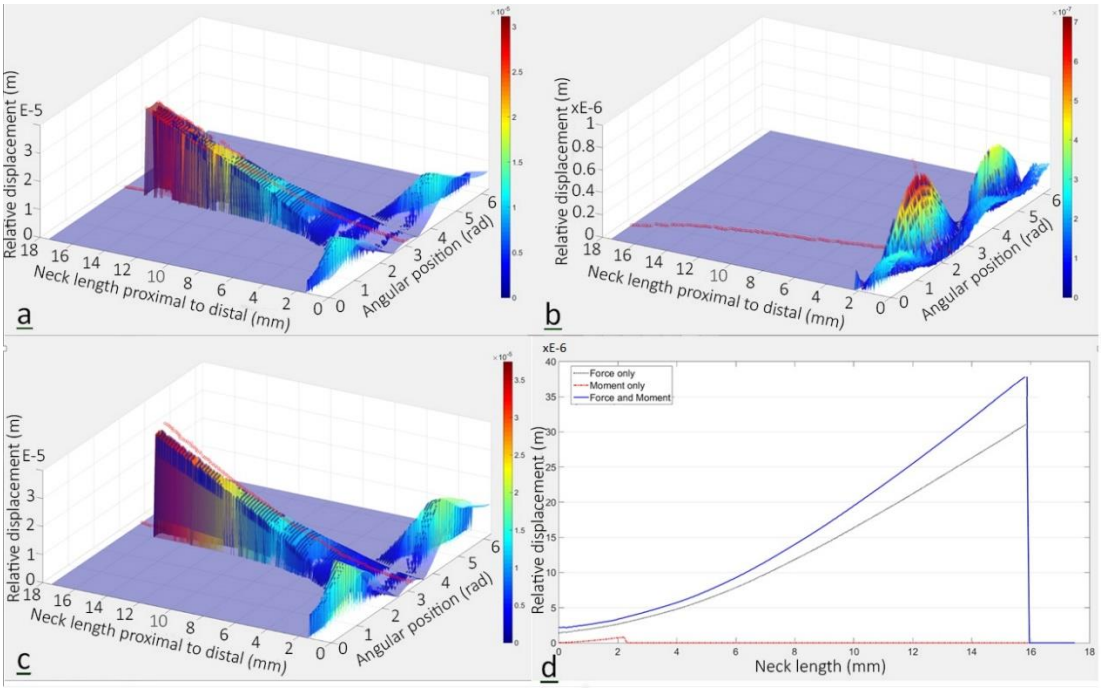

Figure 4.4. Distribution of relative micro-motions for contacting nodes for: (a) force only loading, (b) moment only loading, (c) force and moment loading, and (d) maximum magnitudes of micro-motion along the neck length.

4.6 Shear stresses

Biometals such as CoCr alloys and Ti alloys offer a good corrosion resistance by forming a thin passive oxide layer with an approximately 10 nm thickness (Bronzino 2006). These oxide layers have low shear strengths (Bronzino 2006); for instance, shear strength of the oxide layer in Ti alloys is less than 40 MPa (Liu, Chu et al. 2004). Maximum shear stresses along the neck length are plotted in Figure 4.5. Shear stresses in the proximal initial press-fit region for all the studied loading cases are found to be significantly higher than the shear strength of typical passive oxide

layers. Shear stresses of F only and F&M cases in the temporary contacting area were found to be about the reported disruptive shear stress levels for oxide layers. This may suggest that at each gait of walking activity, the oxide layer can experience depassivation. This is aligned with the results of simplified *in vitro* experiments of fretting-corrosion at the head-neck interface which showed depassivation/repassivation at each cycle of loading-unloading (Panagiotidou, Meswania et al. 2015).

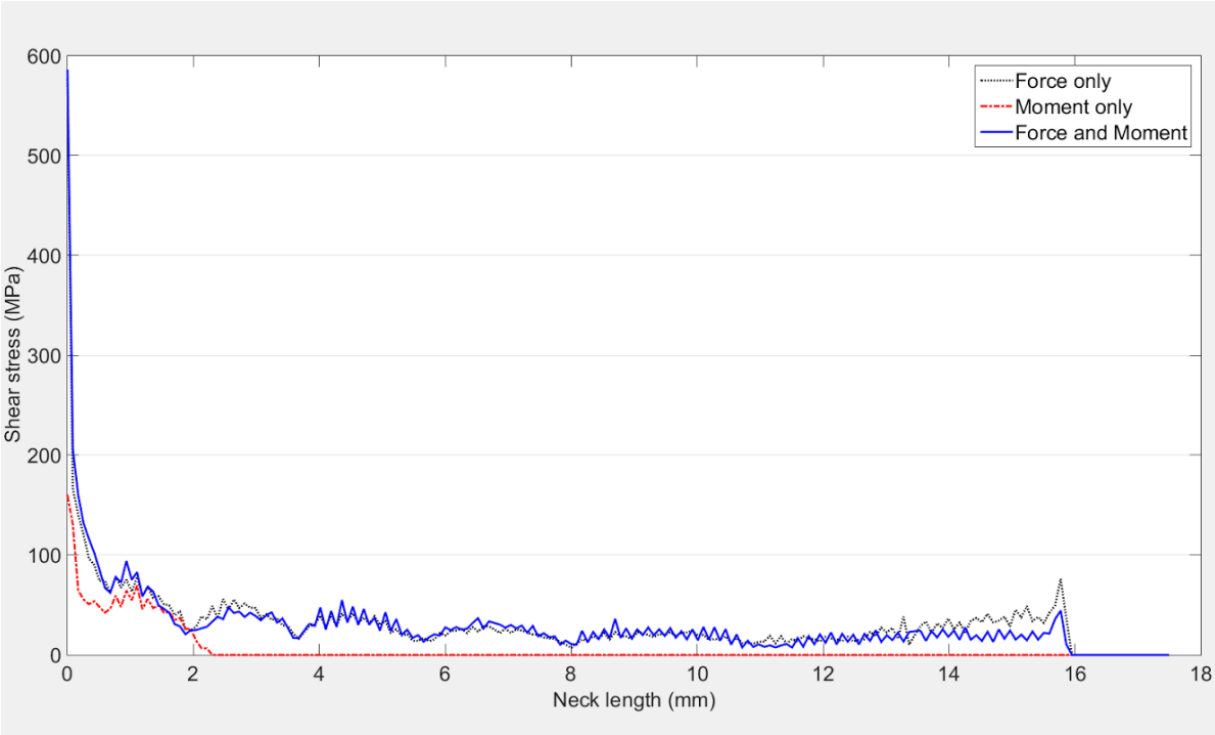

Figure 4.5. Maximum Shear stress distribution along the neck axis for three cases of loading.

4.7 Fretting work

Fretting work per unit of area (J/m^2) was determined as the product of shear stress and its corresponding micro-motion at each point (Figure 4.6). It can be found that the M only loading results in negligible fretting work compared to F only and F&M. F only had similar fretting work to F&M, but was more uniform. In the last three millimeters (13 mm - 16 mm) of the temporary extended contact area, the superposition of M with F in the F&M loading scenario almost doubled the maximum fretting work compared to the F only loading case. Maximum magnitudes of fretting work were concentrated around the middle line of the superolateral sector especially

in the proximal press-fit rim. It is therefore believed that this sector may be expected to experience a greater level of fretting wear and consequently more material removal. This is in good agreement with retrieval studies which have reported localised damage in superolateral surfaces and press-fit rims (Higgs, Hanzlik et al. 2013, Kurtz, Kocagöz et al. 2013).

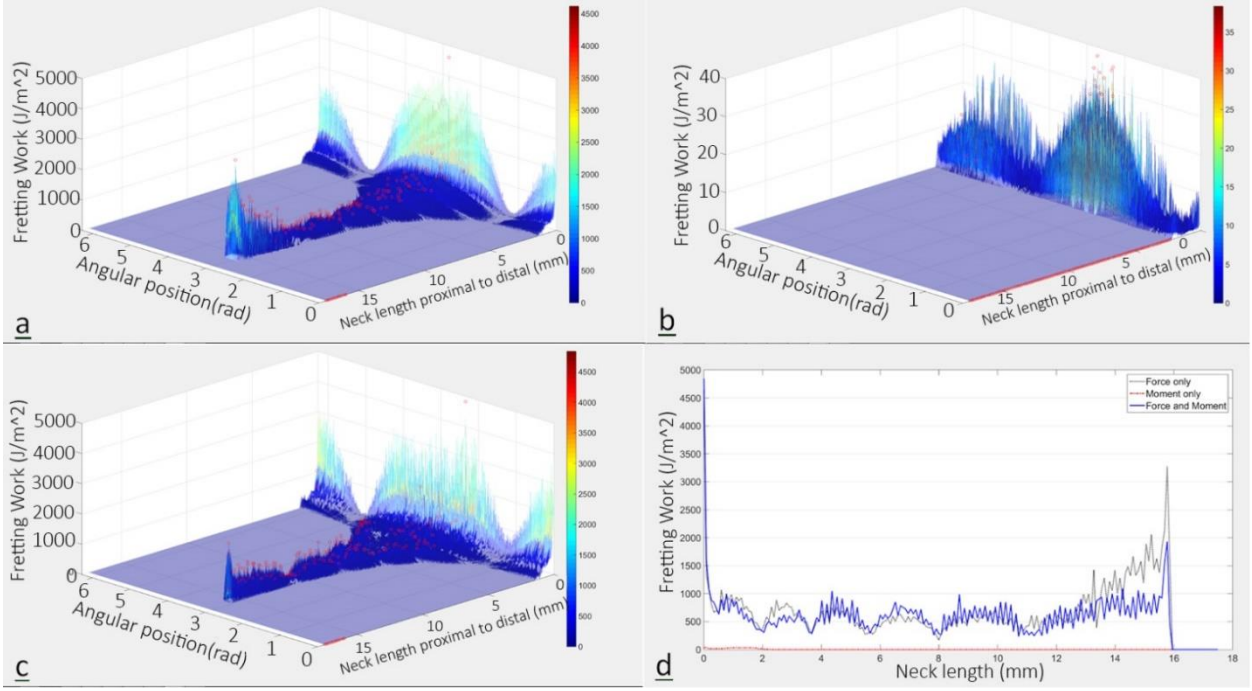

Figure 4.6. Fretting work per unit of area: (a) force only loading, (b) moment only loading, (c) force and moment loading, and (d) maximum magnitudes of fretting work along the neck axis.

4.8 Range of contact pressures and micro-motions

Maximum Cp and maximum δ were identified in various circumferential hoops around the neck with 1 mm incremental distances over the neck length. These maximum values were plotted versus their corresponding δ and Cp, respectively (Figure 4.7). The data points are mostly located in a region with an upper pressure of 275 MPa and an upper micro-motion of 38 µm. Also, for a specific Cp such as 100 MPa, there exists a range of corresponding δ from 0 µm to 35 µm. For a specific δ such as 13 µm, the corresponding contact pressure varies approximately from 20 MPa to 200 MPa.

Table 4-1 presents the maximum δ and its corresponding Cp; and also, maximum Cp and its corresponding δ along the neck length. In the proximal initial press-fit rim, there were zero micro-

motion areas, although their Cps were not higher than those of in the adjacent areas. In other words, higher Cps did not coincide with minimum δs as there were non-zero δs for maximum Cps (Table 4-1). Considering the influence of contact pressure and micro-motion on the phenomenon of fretting wear, the ranges presented in Figure 4.7 and Table 4-1 may provide an indicative guideline for future *in vitro* tests on CoCr/CoCr head-neck junctions (with the same geometry and dimensions reported in this work) to depict a realistic picture of the mechanical environment of these junctions during normal walking activity.

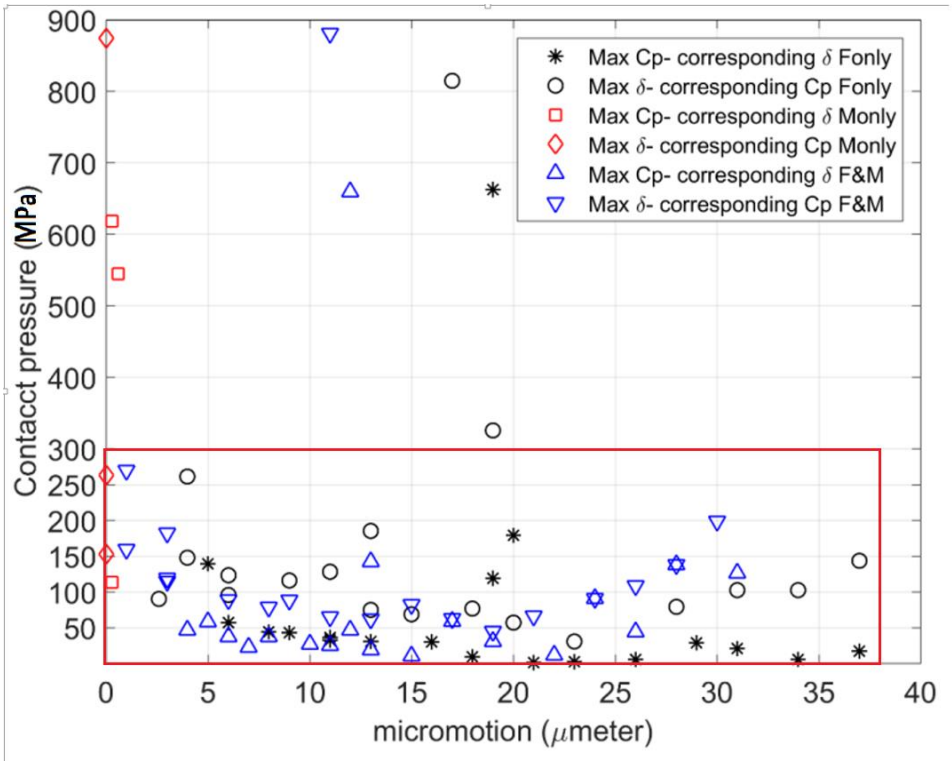

Figure 4.7. Maximum contact pressures and their corresponding micro-motions, and maximum micro-motions and their corresponding contact pressures over the neck circumference and in 1mm intervals for studied loading cases of F only, M only and F&M.

Table 4-1. Variaiton of contact pressure (Cp) – micromotion (δ) over the neck length for the studied loading cases of F only, M only and F&M. The location of Max Cp and Max δ are specified by "(A)" as anterior, "(P)" as posterior, "(S)" as superolateral and "(I)" as inferomedial sides of the neck.

	F&M				M only				F only			
Z (mm)	Max. δ (μm)	Cp (MPa)	Max. Cp. (MPa)	δ (μm)	Max. δ (μm)	Cp (MPa)	Max. Cp. (MPa)	δ (μm)	Max. δ (μm)	Cp (MPa)	Max. Cp. (MPa)	δ (μm)
0	19 (P)	662	814.2 (A)	17	0.3 (I)	618.3	874.0 (P)	0.01	12 (P)	659	880.4 (A)	11
1	20 (P)	179	325.6 (P)	19	0.3 (I)	113.2	262.8 (I)	0.01	13 (P)	142	269.5 (A)	1
2	19 (A)	119	185.2 (A)	13	0.6 (A)	544.7	152.5(P)	0.02	12 (P)	46.6	159.4 (A)	1
3	11 (A)	36.1	261.1 (S)	4	-	-	-	-	7 (P)	22.6	182.1 (S)	3
4	5 (S)	139	147.5 (S)	4	-	-	-	-	4 (S)	46.1	119 (A)	3
5	6 (S)	56.7	122.9 (S)	6	-	-	-	-	5 (S)	57.8	114.6 (A)	3
6	9 (S)	42.7	115.8 (S)	9	-	-	-	-	8 (S)	37.4	78.4 (S)	8
7	11 (S)	32.1	127.7 (S)	11	-	-	-	-	10 (S)	26.7	88.1 (S)	9
8	13 (S)	30.2	74.4 (S)	13	-	-	-	-	11 (S)	24.9	64.5 (S)	11
9	16 (S)	29.5	68.3 (S)	15	-	-	-	-	13 (S)	18.9	61.8 (S)	13
10	18 (S)	9	76.3 (S)	18	-	-	-	-	15 (S)	10.1	81.7 (S)	15
11	23 (S)	2.2	30.2 (S)	23	-	-	-	-	19 (S)	30.3	44.4 (S)	19
12	26 (S)	5.2	90.1 (S)	2.6	-	-	-	-	22 (S)	11.4	66.1 (S)	21
13	29 (S)	28.8	79.1 (S)	28	-	-	-	-	24 (S)	90.6	90.6 (S)	24
14	31 (S)	20.8	102.4 (S)	31	-	-	-	-	26 (S)	44	108.4 (S)	26
15	34 (S)	5.5	102.2 (S)	34	-	-	-	-	28 (S)	138	137.7 (S)	28
16	37 (S)	16.8	143.4 (S)	37	-	-	-	-	31 (S)	126	198.6 (S)	30

For the modelled geometry and materials, and under the loading of walking activity, this work demonstrates that the force components had a significant influence on the stress distribution, micro-motions and fretting work. Focusing more on the isolated role of frictional moments in the fretting related characteristics at the interface, the results of this study indicate a negligible effect purely from the frictional moments. However, when the frictional moments are superposed with the forces, they intensify the mechanical response of the interface, especially in terms of fretting work.

It is noted that this work is limited to fretting-wear related parameters (contact stresses and relative micro-motions) and does not study the electrochemical behaviour of the head and neck materials. However, as mentioned in the introduction, fretting wear is the initiator/assistant of corrosion within the crevice of the junction (mechanically assisted crevice corrosion). The fretting-wear related results of this finite element study can only indicatively assist the interpretation of implant retrieval studies, especially the ones with similar taper geometries and materials. Given that both fretting wear and corrosion are sensitive to the geometry of the interface (Neu 2011, Bryant, Ward et al. 2014), one should be cautious expanding the results of this work to the other geometries and materials. Instead, the finite element modelling approach used in this work can be applied to the other materials and taper geometries (e.g. various taper angle mismatches, and head diameters) in order to use their results more accurately for future relevant *in vitro* studies.

4.9 Summary

The effects of realistic loads (level gait forces and frictional moments - F&M) of walking activity on the mechanical response of the head-neck interface in hip implants were studied. For understanding the level of contribution of the frictional moments to the mechanical response of the interface, two additional loading scenarios of gait forces only (F only) and gait frictional moments only (M only) were also studied. A 3D finite element model which was developed by another PhD student in the team was used to analyse a CoCr/CoCr junction with a head size of 32 mm having a 12/14 taper design and a proximal mismatch angle of 0.024° which was initially assembled with a 4 kN force. The simulations were performed to obtain stress field, micro-motions and fretting work for this taper junction under a complex 6 degree of freedom loading during a gait cycle of walking. Normal contact stresses and micro-motions

at the interface were mostly found in the ranges of 0-275 MPa and 0-38 µm, respectively. The frictional moments alone had a negligible effect in increasing the contacting area as only 0.27% of the non-contacting surface nodes were engaged in contact. F only made 8.43% of the non-contacting surface nodes to get in contact. Frictional moments were effective in the F&M case as the contacting nodes increased to 9.57% when compared to 8.43% in the F only case. Superposition of the frictional moments and gait forces (F&M) in comparison with F only, also resulted in:

a) Up to an approximately 100% increase in the maximum value of fretting work per unit area in the last three millimetres of the temporary extended contacting area (14mm- 16mm).

b) Approximately 15% increase in the maximum magnitude of micro-motions.

The results suggest that gait forces dominate the mechanical environment of the interface; however frictional moments when combined with the gait forces can have some considerable effects on increasing the fretting work and gradually increasing micro-motions in the contacting area. This may suggest that simplifying mechanical loads of daily activities to gait forces only in both finite elements and *in vitro* studies needs acceptable justifications.

Chapter 5. Designing and manufacturing of a multi-axial cyclic fretting-corrosion testing system

The PhD student was in charge of software and hardware design, system integration, assembly and commissioning of this system. Great assistance from the Technical Services and Engineering Team at Flinders University in both the design and manufacturing of the testing machine is acknowledged. Also, The Premier's Research and Industry Fund (Oskouei R.H., Catalyst Research Grant, Government of South Australia, 2014) to develop the testing machine is acknowledged.

5.1 Overview

As provided in the literature review, fretting-corrosion and mechanically assisted crevie corrosion have a complex relation to the geometry and applied forces on the degraded interface (head-neck interface in this study). Any simplification to the geometry or loads applied to it could considerably alter the response of the interface in its service condition. To study the relationship between the frictional moment of head-cup bearing and the daily activities forces in fretting-corrosion of the head-neck interface, a custom testing system has been designed, manufactured and commissioned. The testing system comprises state machine design, structural design, component selection, data acquisition system design, cooling system selection and integration, corrosion monitoring system integration, feedforward/feedback control design and integration. This system is designed to replicates service condition of the head-neck interface under different loading scenarios to reveal the relation of fretting-corrosion and mechanically assisted corrosion with forces and moments on the head-neck interface.

To provide a general overview of the testing system and the integrated components interaction, an overall photo and schematic of the testing system is provided in Figure 5.1.

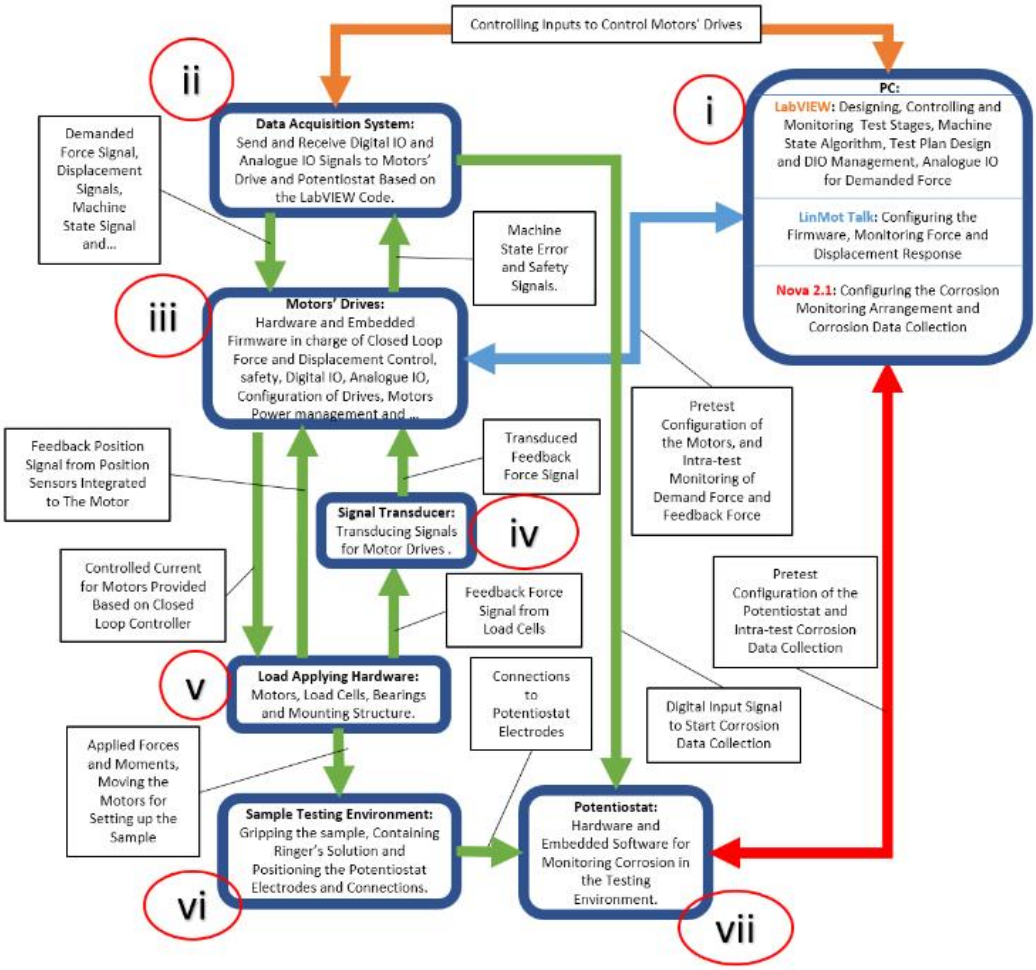

Figure 5.1 Schematic Diagram and overall picture of the testing system

5.2 Method of applying the load

To apply similar stress-field to the contact interface and replicate stress-field and micromotions in the head-neck interface during fretting-corrosion, similar forces and frictional moments were applied as they would be in real-life conditions. According to the calculated loads of daily activities in Chapter 1, it was concluded that walking gait activity, the most repetitive daily activity, has a load profile with a range and magnitude inclusive of other activities. It can also be concluded that superoinferior (vertical) force component and lateromedial frictional moment components are the main components in level gait walking load. This *in vitro* testing system can replicate these forces and moments of level gait walking activities.

The testing system has been designed to be applied to two independent but simultaneous load components.

a) A vertical independently varying force representing body forces in a superoinferior direction

b) An independently varying moment perpendicular to the force vector representing lateromedial frictional moment

5.2.1 Method of producing independent force and frictional moment

Two linear forces were implemented in a parallel arrangement to apply simultaneous, independent load components of the gait vertical forces and the lateromedial frictional moments to the implant (Figure 5.2-a and Figure 5.2-c). The summation of these forces at each instant is equal to the activity's superoinferior (vertical) force; meanwhile the resulting moment at the clamping point of the specimen due to differences in the motor forces equals to the lateromedial frictional moment. For example, considering the instant *t* of the level gait walking loads shown in Figure 5.2-c, to achieve F_t and M_t, summation of $F_1(t)$ and $F_2(t)$ should be equal to F_t while their moment on the implant needs to impose M_t (Figure 5.2-b and Figure 5.2-d).

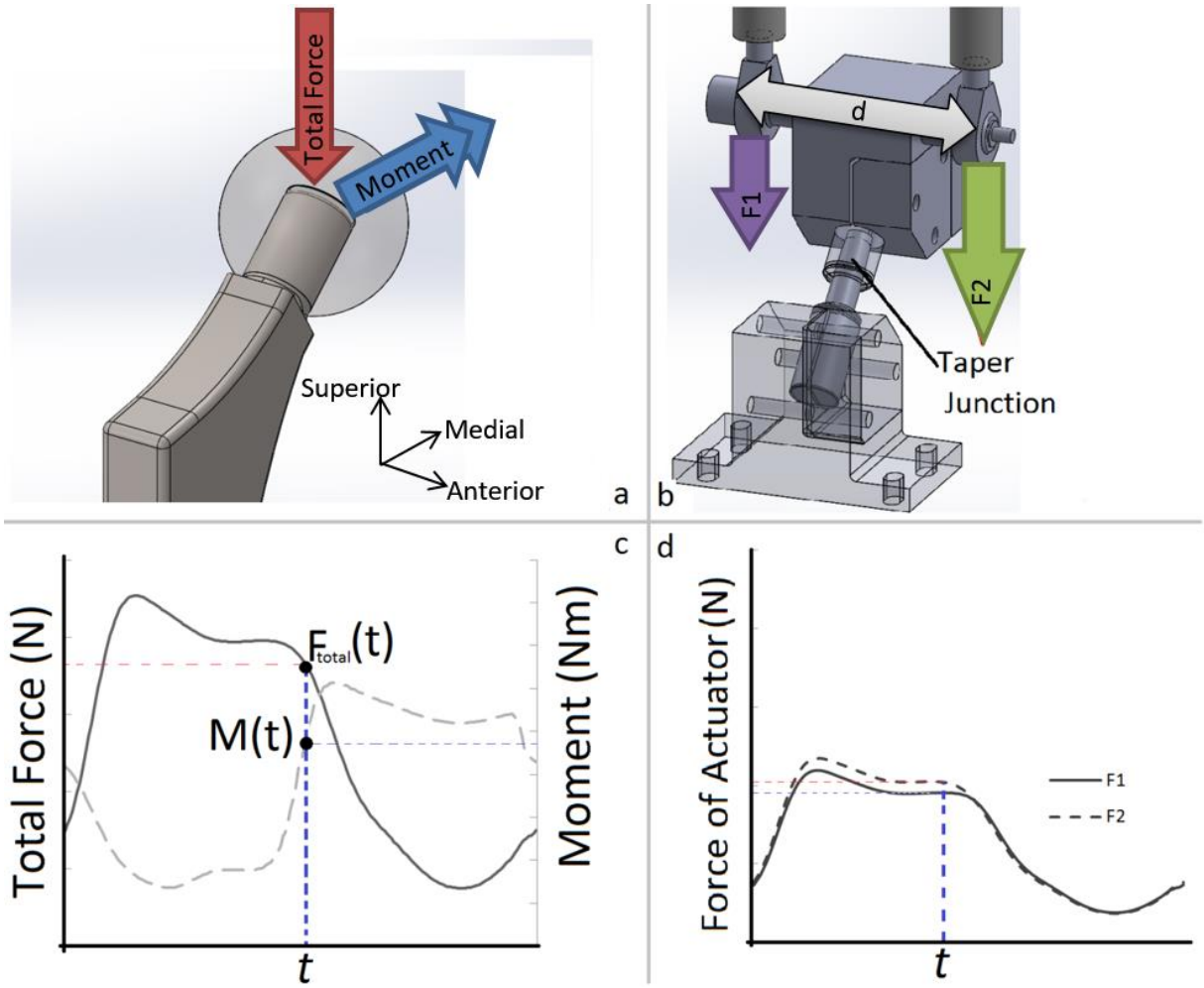

Figure 5.2-a) Demonstration of applied Superoinferior force component and the Lateromedial frictional moment b) Applying F1 and F2 at distance of "d" with the implant clamped in the middle to replicate superoinferior force and Lateromedial frictional moment c) Profile of the superoinferior force component and the Lateromedial frictional moment in walking activity d) Required F1 and F2 to simulate superoinferior force component and the Lateromedial frictional moment on the implant

Solving the two simultaneous equations (Equation 5-1) of the vertical activity force and activity frictional moment through entire the activity cycle provides the vertical forces and frictional moments of the activity.

$$\begin{cases} F_1(t) + F_2(t) = F_{total}(t) \\ F_1(t) \times d/2 - F_2(t) \times d/2 = M(t) \end{cases}$$

Equation 5-1

Rearranging Equation 5-1 gives the required force profile (Equation 2) from each of the linear forces.

$$\begin{cases} F_1(t) = \frac{F_{total}(t)}{2} + \frac{M(t)}{d} \\ F_2(t) = \frac{F_{total}(t)}{2} - \frac{M(t)}{d} \end{cases}$$

Equation 5-2

5.2.2 Hardware for applying force and the frictional moment

Different mechanisms of applying forces were evaluated for the loading arrangement. The range of options for the motors and their advantages and disadvantages are provided below:

a) Hydraulic linear actuators: These are of the common devices used for applying cyclic loading to in mechanical testing experiments.

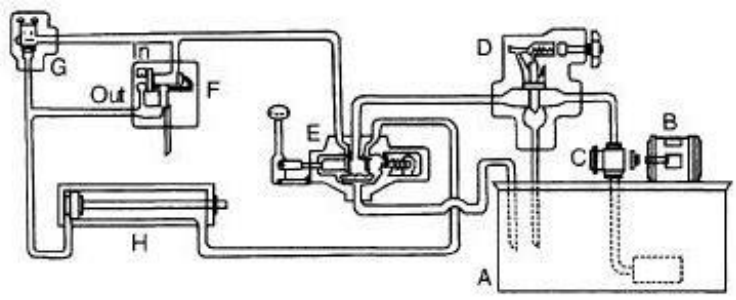

List of components

A – Reservoir
B – Electrical motor
C – Pump
D – Maximum pressure (relief) valve
E – Directional valve
F – Flow control valve
G – Right-angle check valve
H – Cylinder

Figure 5.3 schematic view of a linear hydraulic actuator system.[6]

[6] www.valvehydraulic.info

These devices comprise a linear actuator (H-cylinder in Figure 5.3), a pump coupled with an electrical motor reservoir and control valves (flow control and directional valves in Figure 5.3) and safety valves.

These systems can provide high level of accuracy and repeatability in cyclic loadings. Hydraulic systems couldn't be implemented in this setup because the costs were higher than the project's budget limits and a large area and infrastructure was required to set it up in the lab area.

b) Pneumatic linear actuators: These systems have a mechanism similar to hydraulic linear actuator systems (Figure 5.4). These two systems are different regarding the medium that they use to transfer and amplify the force. In pneumatic actuators, air is the pressurised medium used to transfer/amplify the force. Pneumatic systems are widely used in automation industries due to their ease of implementation and lower initial and maintenance costs as compared to hydraulic systems. They couldn't be implemented in this setup as it requires a large infrastructure. The pneumatic would not be a good option also because of high magnitudes of force (up to 1,000N) required in a small corresponding displacement of the implant and fixture sub-assembly with the frequency of the cycles being up to three with which the pneumatic systems are not well compatible.

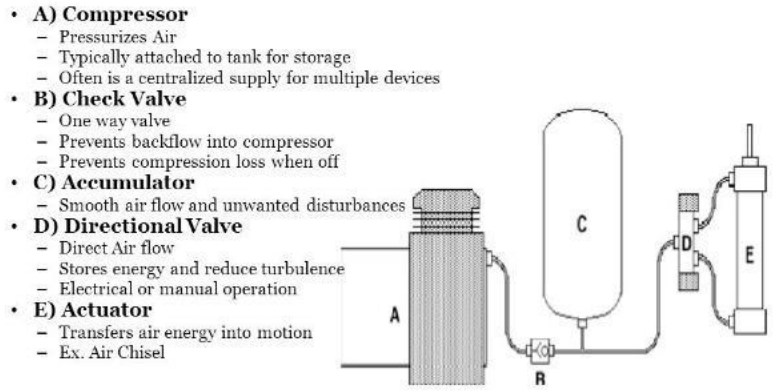

Figure 5.4 schematic view of a linear pneumatic actuator system [7]

[7] www.e-pneumatic.com

The selected mechanism for applying target forces was linear electrical direct drive motors. These motors comprise a linear motor and a drive controller which provides and controls the electrical linear current required for driving the motor. The direct drive motors were chosen against the regular electrical motors, such as DC-driven electrical linear motors. The main reason was that the regular electric motors come with high RPM and low torque rotary motors which requires mechanical power transmission, such as gears, pullies and ball screws along ball/roller bearing systems, to transmit low torque rotary motion to high magnitude linear forces and simultaneously cancel unwanted mechanical loads generated by power transmission system. These mechanical transmission systems come with clearances and gaps between the driving/driven components, such as gears teeth, which will themselves suffer from fretting and fatigue loading during cyclic loading applications. These clearances and gaps could also become a source of control system disturbance while applying the forces in small range of motion as was the case in this setup.

Linear direct drive motors can provide forces in short range of displacement and implement a magnetic contactless bearing (Figure 5.5) which eliminates the source of fatigue failures existing in mechanical ball/roller bearings.

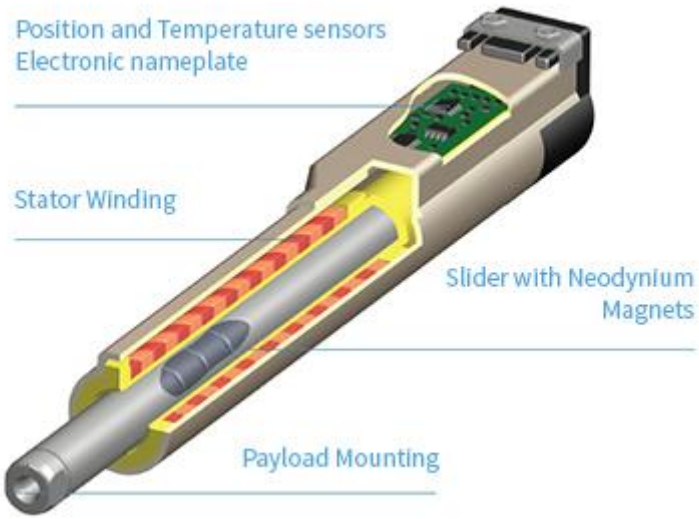

Figure 5.5 Linear Direct drive motor schematic view comprising stator and winding working against neodymium magnet inside the slider [8]

[8] www.linmot.com

They also don't need considerable lab area for power packs such as compressor and control valves, for pneumatic and hydraulic systems. These features made linear direct drive motors a suitable option for our selection.

LinMot direct drive motors were considered for this setup. The type of the stator, slider drive and cooling system were determined by simulating the motors service condition on the LinMot design software (Figure 5.6).

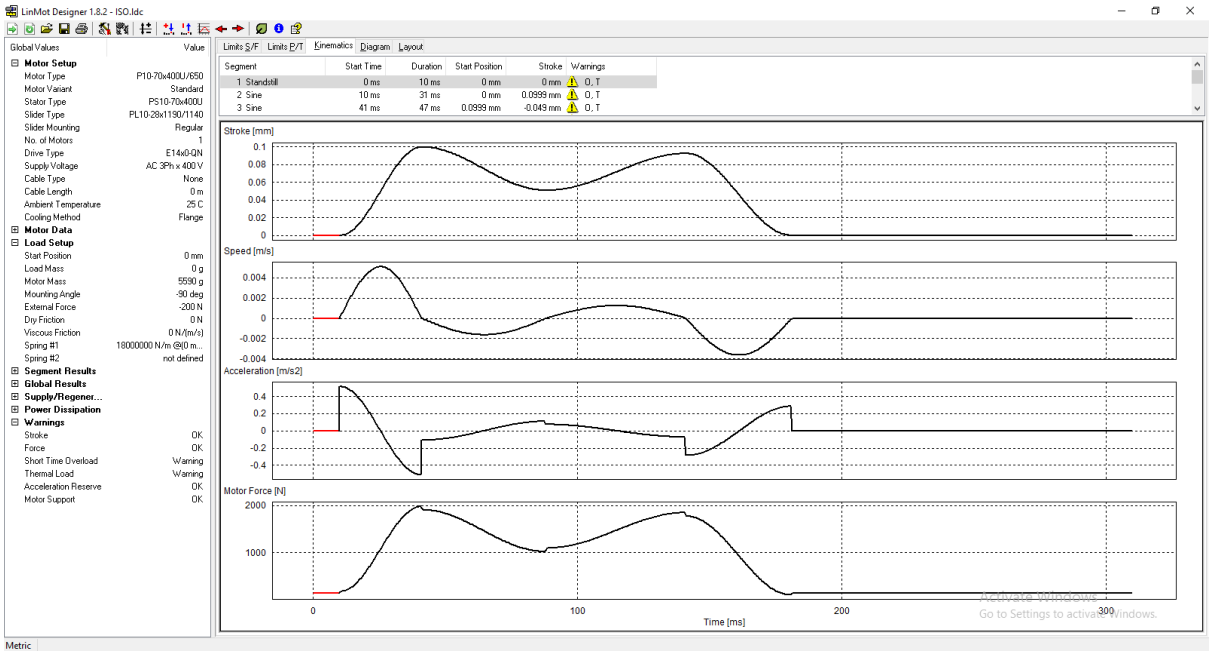

Figure 5.6 LinMot Designer software used for purpose of motor selection by simulating critical loading required from actuators

Two LinMot linear direct drive motors comprise stators of PS10-10x400U-BL-QJ, sliders of PL10-28x590/540 and drives of E1400-GP-QN-0S (NTI AG LinMot & MagSpring, Spreitenbach, Switzerland) were implemented to apply the required forces and moment. The sliders PL10-28x590/540 consist of a stainless-steel tube, which is filled with neodymium magnets. PF10-70x430-FC flanges were considered for water cooling and mounting of the motors.

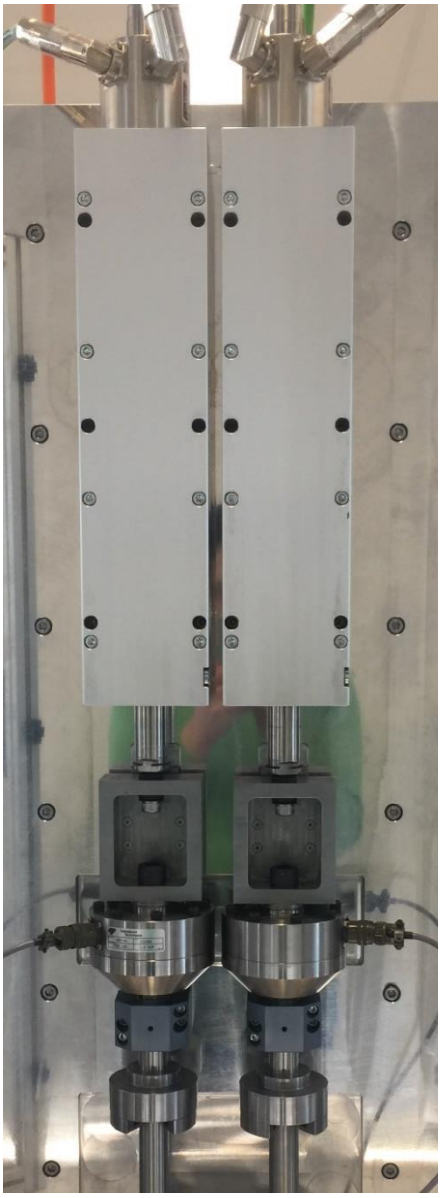

Figure 5.7 Two linear direct drive motors mounted in parallel inside cooling flanges for cooling of the motor through circulating chilled water through flanges

A S150 chiller unit from Aqua Cooler Pty Ltd, Australia was used to circulate and chill the water as the chilling medium. The maximum chilling capacity of the S150 is 1800W for supplied water temperature of 25°C water and heat dissipating to 20°C. The amount of 1800W heat dissipation of the chiller was enough to cover maximum capacity of heat transfer of the cooling flange which was 760W per flange and hence 2 x 760W=1520W for both flanges. Generally, in electrical motors, the lower the temperature is, the higher the force coefficient and efficiency of the motor will be. Therefore, the temperature of the chiller was set to 25°C.

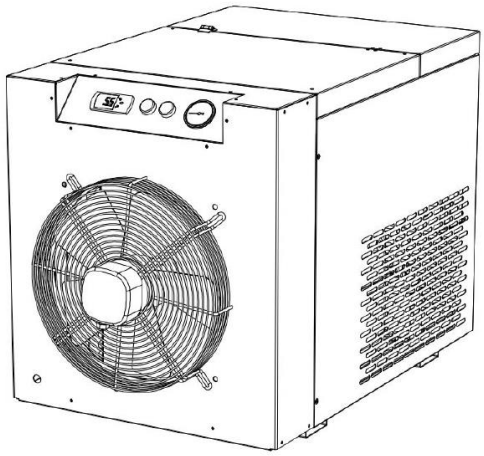

Figure 5.8 S150 chiller used for chilling the motor drive through its cooling flanges

As required by the manufacturer of the motors, any lateral force, torsion and moment on the stainless-steel tube of the slider must be prevented. Hence, a PAE15ARS linear bearing (NSK Ltd, Shinagawa, Tokyo, Japan) along with a custom manufactured box-like coupling was considered for each slider (Figure 5.9).

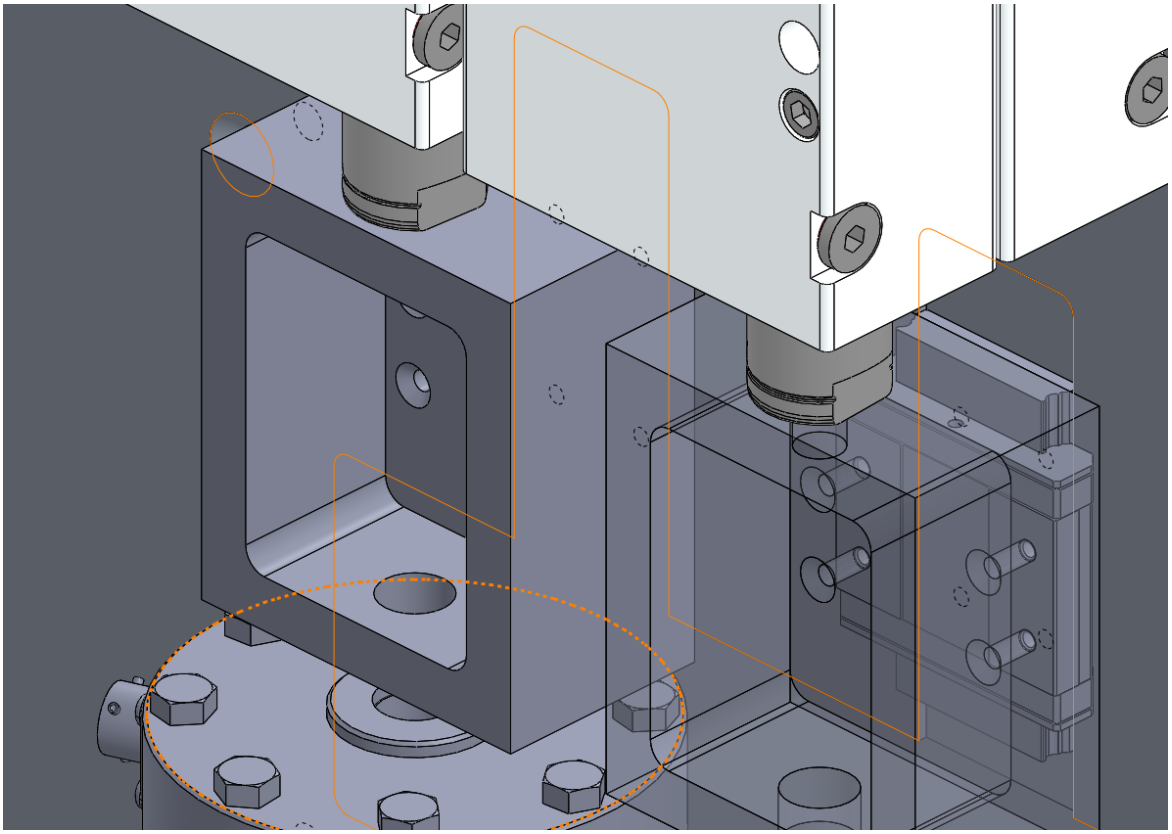

Figure 5.9 Required support for slider of the drive comprising a linear bearing and the coupling

Controlling the motors for force control function required the forces to be measured and fed back to the motor's drive. The generated forces of the motors were measured by two uniaxial SWP-1K fatigue resistant loadcells (Transducer Techniques-LLC, California, USA). The rated output of these loadcells was 2mV/V. This indicates that for an excitation voltage of 10V on ends of the bridge, the output voltage of the loadcell under maximum capacity of the loadcell (1000 pound-force=4448.22N) would be equal to 0.002Vx10V (excitation voltage) = 0.02V. This voltage needed to be amplified to suit the LinMot drive force feedback input range of 0-10V. Accordingly, an analogue signal amplifier was used from which output of each of the loadcells connected to one channel and amplified the voltage feedback to the control drive.

The structure of the setup comprises two 18mm thick perpendicular aluminium 6061 T4 plates supported by two gussets from rear. The criteria of design of this structure was to provide rigid and simple manufacturing support for the sample and the loading components. Stiffness of the structure in direction of load application was about 12.6 x 10^6 N/mm, hence the structure's deformation compared to the sample's deformation was negligible. For safety, the testing area of the setup needed protection in case the samples shattered during the test. Therefore, two customised hinged doors with transparent polyethylene screens was designed and manufactured. Polyethylene has a high impact resistance, is of a reasonable price and weighs lesser than other types of laminated glass. Two safety interlock switches were added to the setup to provide a safety freeze signal upon the opening of each door of the LinMot drives to stop any operation. Figure 5.10 shows the exploded view of the structure. Detailed drawings of the setup are available in Annex B.

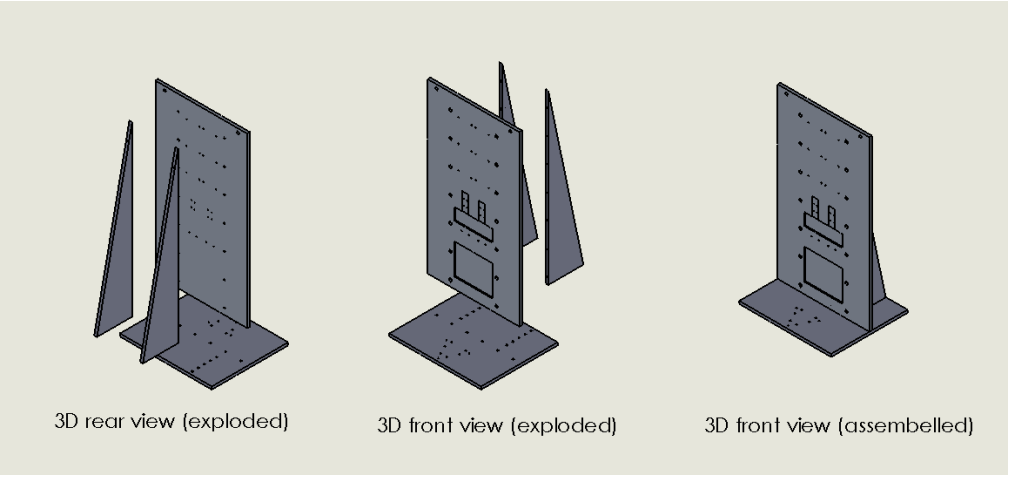

Figure 5.10 Exploded view of the loading structure of the testing setup

The input power of the LinMot drive could be provided through a DC power supply for lower range of force output (up to 1000N) or a 3-phase AC power for higher range of force output (2700N). Due considerable modifications required in the wiring infrastructure of the lab for the 3-phase AC power, a DC power input was considered. For each motor drive, one 60V power supply was used to provide the required power to run the motors. For the logic power input of the drive, a power supply of 24V was also used to provide input power as required for logic board of the motor drives.

To protect the loadcell from moments and lateral forces, a GX 20 F thrust spherical bearing (SKF, Gothenburg, Sweden) along with a linear polymeric sliding bearing of TJUM-05 (Igus-DryLin, Cologne, Germany) was used. Considering the small range of motion in load control mode ($\simeq$ 2mm), to prevent fatigue failure of ball/roller bearings because of a critical angle of oscillation, ball/roller bearings were avoided in this section.

5.2.3 Hardware for corrosion monitoring and Data Acquisition

The corrosion monitoring was conducted by a PGSTAT204 potentiostat/galvanostat (Metrohm AG, Herisau, Switzerland). The OCP of the working electrode (specimen) was measured against a reference electrode (Ag/AgCl Reference system with electrolyte-KCl = 3 mol/L, Metrohm AG, Herisau, Switzerland). Ringer's solution was used at ambient condition. The chemical composition of Ringer's solution has been shown in Table 5-1.

Table 5-1 Composition of Ringer's solution (g/l).

NaCl	8.5
KCl	0.25
$CaCl_2$	0.22
$NaHCO_3$	0.15
Purified H_2O	Balance

A data acquisition system required to collect, communicate and control the data from the motor control drives, loadcells and corrosion monitoring systems. The data acquisition hardware comprised the following:

- NI-cDAQ-9178 – 8 slot USB compact DAQ chassis

- NI-9263 – 4 channel Analogue Output signal range +/-10V
- NI-9375 – 16 channel Digital Input/ 16 Channel Digital Output

The pin assignment and wiring schematic diagram was as shown below:

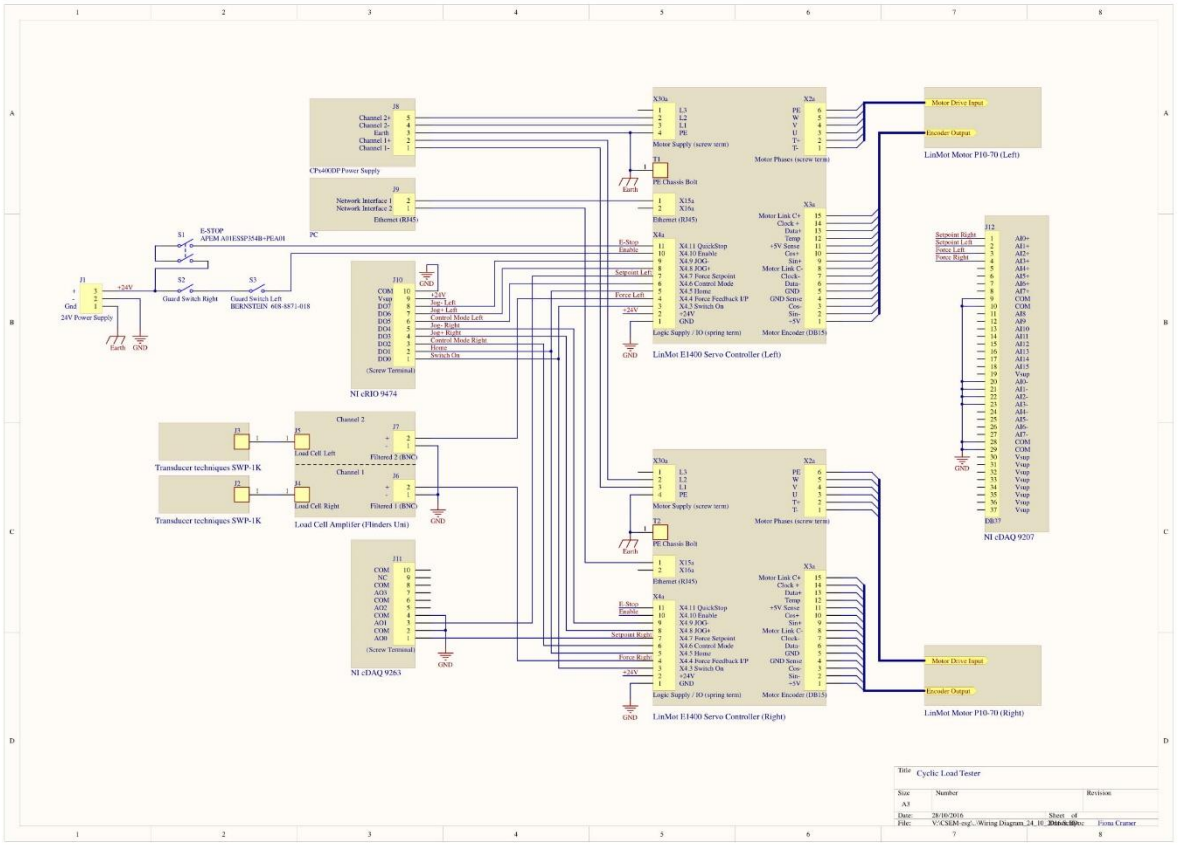

Figure 5.11 Wiring schematic diagram of the data acquisition system and system integration

5.3 Software and Data acquisition code

The motor drives and the potentiostat unit were communicated with using a custom-developed NI-LabVIEW code. This code read the loads of one cycle of the activity (level gait walking). It can scale the loads to the ranges determined by user and calculate required forces with respect to time from each motor to replicate the vertical force and frictional moment of the activity on the sample. It was also able to generate waveforms as sets of loads with different scales of magnitude of vertical forces/frictional moments and determine the rest times between the sets. These waveform outputs as analogue voltage waveforms of demanded forces sent to the motor drives using a NI-cDAQ9178 chassis and a NI-9263 analogue output module. Parallelly, the code also triggered data collection of potentiostat/galvanostat at configured time periods or at every specified intervals of cycles

of each set. The code also generated digital output signals for position control of the motors for pretest assembly steps. Digital I/O signals were sampled using a NI-9375 Digital I/O module. Front panel view of the LabVIEW code is shown in Figure 5.12. The LabVIEW block diagram code is available in Annex C.

Figure 5.12 Front panel of the custom developed LabVIEW code

LinMot Talk software was used to define the required setting and functions of the motor drives and its communication ports, e.g. digital input pins for machine state design, the analogue input of force feedback from loadcells and demand force from NI LabVIEW.

LinMot Talk was also used for force control mode, proportional–integral–derivative (PID) controller and its gain value setting. Calibration of the PID gains was conducted through Ziegler–Nichols heuristic PID tuning method. To have a smooth transition to final PID values of the test and prevent any overshooting and impact on the sample, the PID constants controlled by gradually increasing the gains at the initial stage of the test. As has been shown in Figure 5.13, The PID controller was successfully capable of applying the required forces. Author encourages readers to visit the video of testing system performance at https://goo.gl/fKttQE to have a better view of overall performance of the testing system.

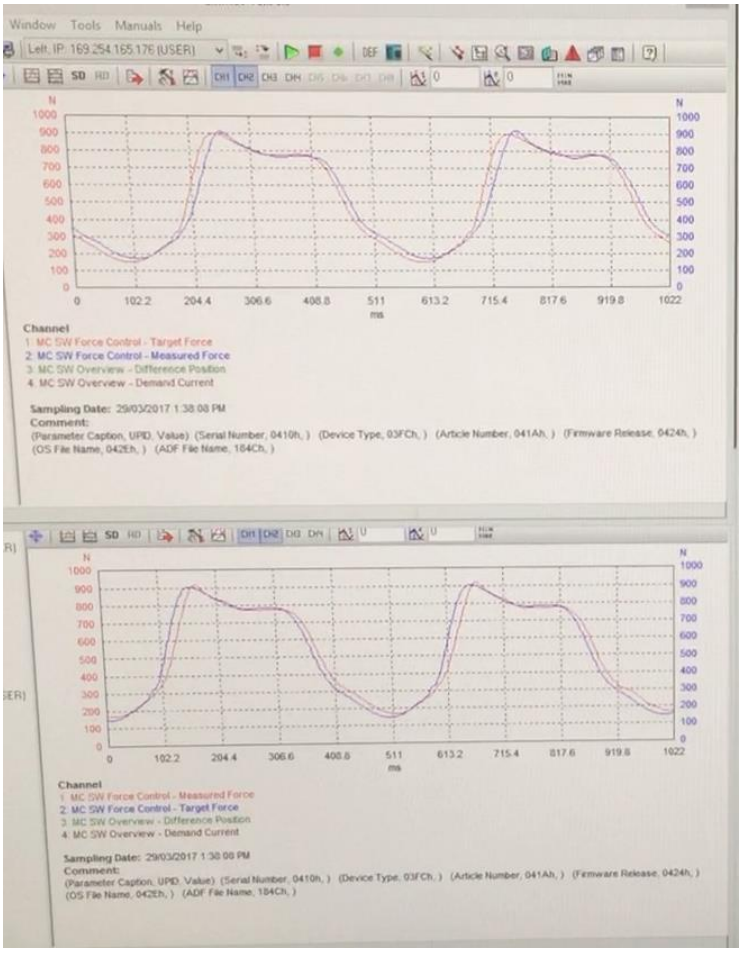

Figure 5.13 Performance of the PID controller is following the target force (demand force) during the test

Warnings, errors, safety feature logic and displacement control parameters, such as maximum range, maximum speed and maximum acceleration of the actuators in displacement control mode, were implemented using the LinMot Talk software. Feedback force of the loadcells was also monitored through the oscilloscope feature of the software. This feature could also report displacement, velocity, acceleration, temperature, current, voltage and many other parameters of the motor and the drive which were used to monitor and set up the tests.

The corrosion data collection of the test was conducted by NOVA2 software of the Metroohm PGSTAT204. This software can design wide range test scenarios by arranging different features and determining the different setting that should be available. For these experiments, the test was set to collect OCP (corrosion potential) after receiving a digital trigger signal generated by the LabVIEW DAQ system. At the trigger signal, the PGSTAT would

start collecting the data on the voltage difference of the working electrode (specimen) with respect to Ag/AgCl reference electrode during the given time set in the NOVA2 software and store the results while waiting for the next data acquisition trigger from LabVIEW DAQ system.

5.4 Summary

A testing system was integrated for studying fretting-corrosion at head-neck interface of hip joint implant. This system was developed around the research question regarding interrelation of forces and frictional moments in fretting-corrosion of head-neck interface of hip joint implants. The system comprises state machine design, structural design, linear motors and drives, data acquisition system design, cooling system selection and integration, corrosion monitoring system integration, feedforward/feedback control design and integration. It is now capable of applying varying combination of forces and frictional moments on the head-neck interface with a corrosive medium to resemble the service conditions of the interface. This system will be implemented to study the research question in next chapter. *In-vitro* Investigation on interrelation of forces and frictional moments of hip joint implant in mechanically assisted crevice corrosion at head-neck junction of its head-neck interface

Chapter 6. *In-vitro* investigation on the interrelation of forces and frictional moments of hip joint implants in mechanically assisted crevice corrosion at the head-neck interface

6.1 Overview

The testing system described in the previous chapter is used to run an *in vitro* investigation on the interrelation of vertical forces and frictional moments in mechanically assisted crevice corrosion at head-neck junction of modular hip joint implant. The test plan aimed to investigate the effect of different load combinations, by the outcome of the tests along with SEM studies on the interface will provide an understanding on of fretting-corrosion and crevice corrosion degradation of head-neck interface of hip joint implant.

6.2 Material and Method

6.2.1 Geometry, material and assembly of the sample

From the Chapter 1. Literature Review, it can be concluded that to realistically study the service conditions of the head-neck interface with a focus on fretting-corrosion and mechanically assisted crevice corrosion, the stress-field and micromotions should be the same as they would be in the service condition. For the *in vitro* study, the geometry of the contact was a common 12–14 mm head-neck tapered junction with a proximal press-fit (Figure 6.1 angular mismatch of 0.07°±0.01°). The head-neck junction material combination was considered as material combinations in commercial metallic head-neck. The parts representing the head component were made from CoCrMo (ASTM F-1537). The parts representing the neck components were made from two different materials: CoCrMo (ASTM F-1537) and Ti6Al4V (ASTM F136-12a). Hence the tests were conducted on to different material combinations of: three samples of CoCr/CoCr head-neck combination and three samples of CoCr/Ti alloy head-neck combination.

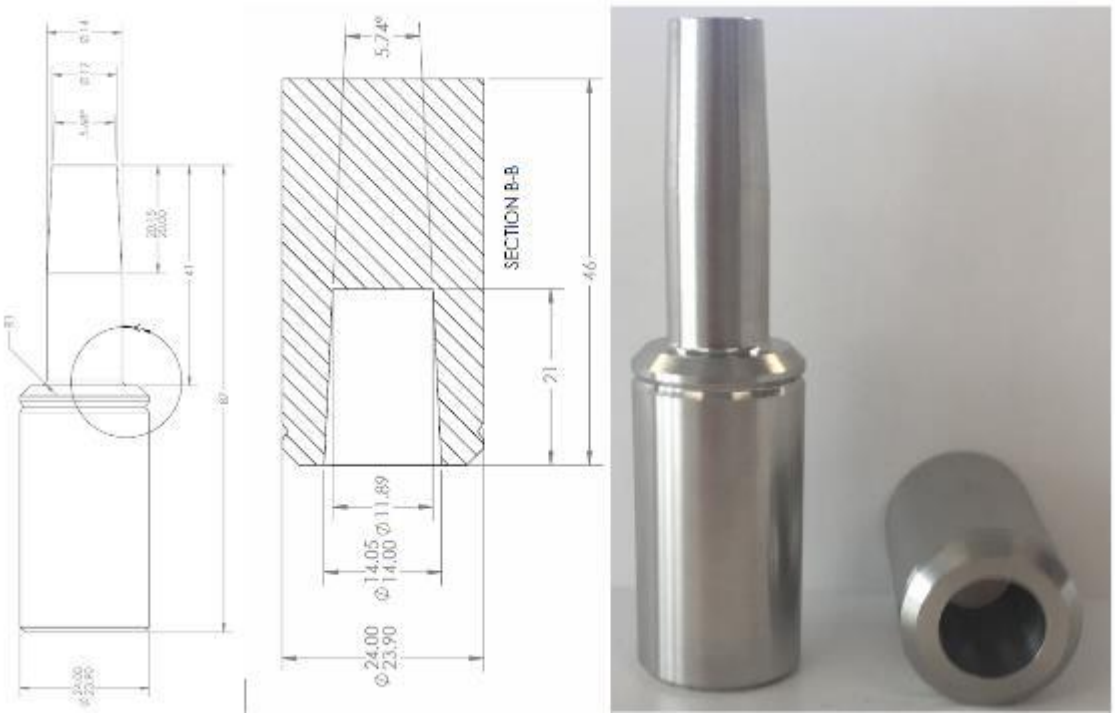

Figure 6.1. The geometry of the head-neck interface sample, more details provided in Annex AA

Figure 6.2-a shows one of the samples before assembly. Heads and necks were assembled by a single ramp preload applied (via Instron 5969 Dual Column Testing Systems) in axial direction of the sample up to 4000N to simulate impacting the head onto the stem with a hammer during the surgery. The load was applied in displacement control at a rate of 1mm/min with a stop limit of maximum force equal to 4000N. The magnitude of 4000N is reported as a suitable assembly force replicating assembly during the surgery (Panagiotidou, Meswania et al. 2015).

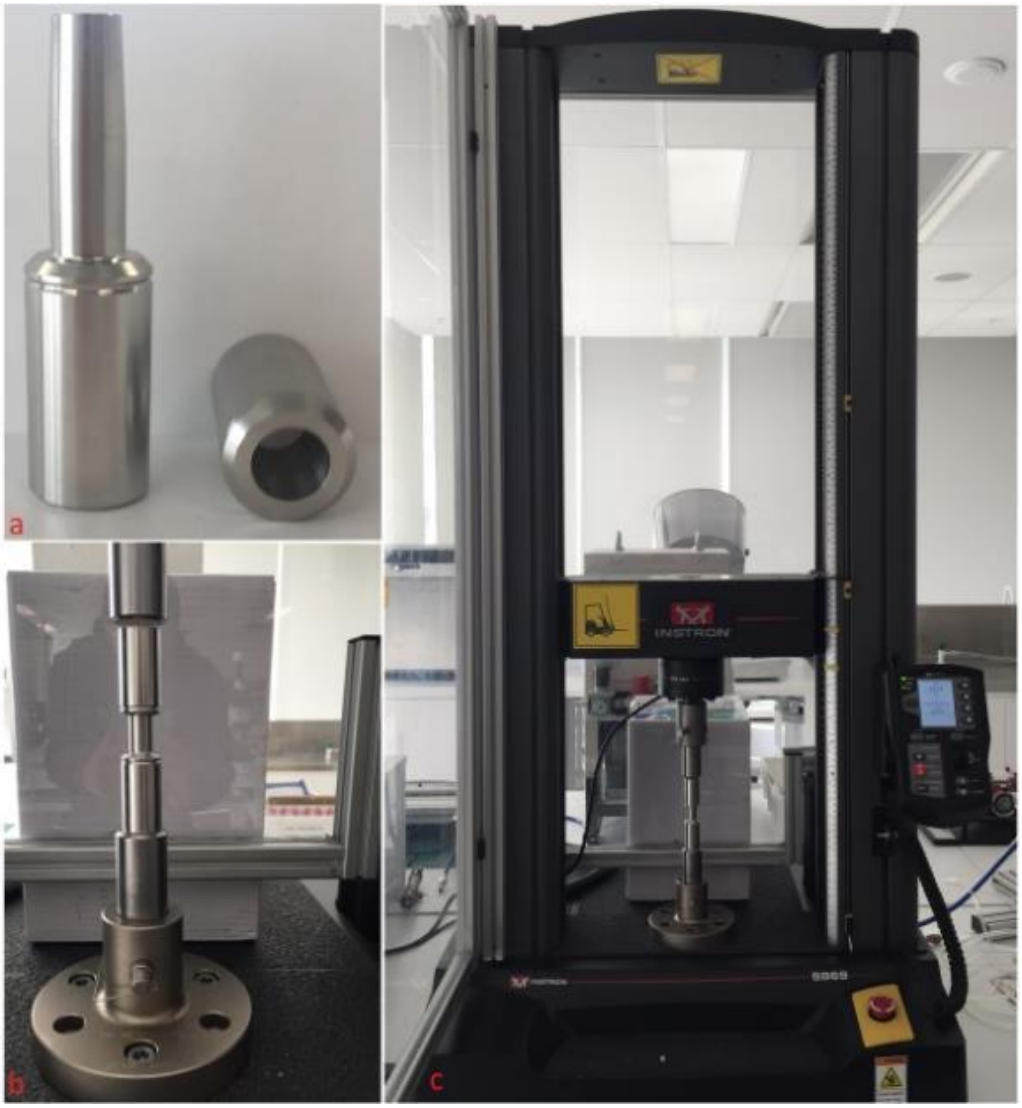

Figure 6.2-a) Geometry of the head-neck sample before assembly b) Assembly arrangement of the head-neck geometry for axial compressive ramp load up to 4000N to simulate impacting the head onto the stem with hammer c) Instron 5969 Dual Column Testing Systems used for assembly

6.2.2 Experimental device

The force control system was applied using the controllers embedded in the linear motor drives. A variable PID gains feedback algorithm was applied using the LinMot Technology Function Force Control. For position control, the control system comprised a feedforward controller with a PID feedback compensator. The position control system was mainly used for the pretest sample installation step.

A custom LabVIEW code was developed to integrate the control system of electrical components. OCP was measured with a three-electrode arrangement of the voltammeter system to monitor passivation and depassivation of the contacting surface.

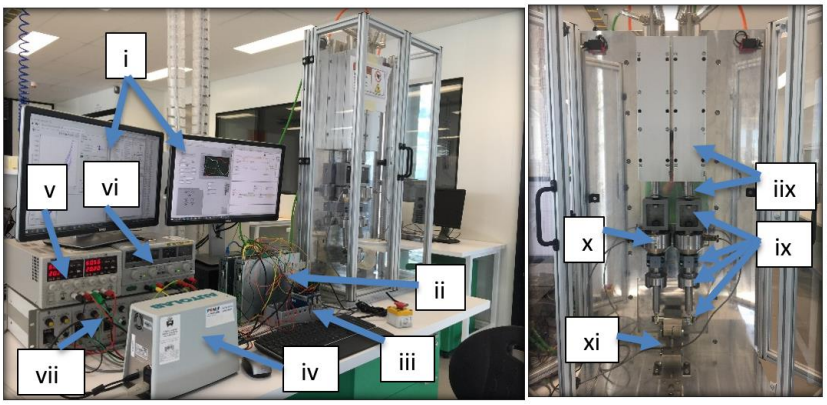

Figure 6.3) Custom designed and manufactured testing apparatus for fretting-corrosion testing on real scale head-neck interface of hip joint implant under realistic loading of daily activities. Ringer's solution chamber and three-electrode arrangements are detached for a better demonstration of samples mounting.

6.2.3 Test protocol

The aim of this study was to investigate the level of contribution of the main components of loads of level gait walking in severity of mechanically assisted crevice corrosion. Before starting the tests, each sample immersed in Ringer's solution in non-loaded condition for ten hours and the value of OCP at the end of the ten hours was recorded as the non-loaded control value of OCP. Different scales of the activity of level gait walking force and moment profile were applied to the sample. Frictional moment was applied in different scales such that its maximum magnitude varied at 0Nm (no moment applied), 1.25Nm, 2.5Nm, 3.75Nm, 5Nm, 6.25Nm and 7.5Nm (seven variations). These moments cover frictional moments up to 7.5Nm frictional moment calculated for normal walking activity of the average patient with a metal-on-metal bearing combination (Figure 3.5). These moment profiles were combined with force profiles scaled such that their maximum magnitudes varied at 900N, 1200N, 1500N and 1800N (4 variation) – the 1800N force covers the contact forces reported for average patient (Figure 3.2). Combining these forces and moments concludes to study of 28 combinations of moments and forces (seven scales of moment profile combined with four scales of force profile).

The OCP was monitored as the indicator of the depassivation of the oxide layer. As shown in Figure 6.4, each sample was examined on the first load combination of 900N-0Nm for three

sets of 700 cycles with two to three minutes rests between them. The 700 cycles were enough for the OCP to reach a steady mean magnitude. Mean OCP was recorded for last 10 cycles of each set. Then while keeping the force profile at the same scale (900N), the moment profile increased to next magnitude of 1.25 Nm and three sets of 700 cycles and recording of mean OCP was repeated for this 900N-1.25Nm load combination. This pattern continued to reach load combination of 900N-7.5Nm and then the next set of loading was 1200N-0Nm. The same pattern followed such that the moment scales increased on the same load to reach the last scale (7.5Nm) and then the force scales changed to next scale combined with the smallest moment scale up to the last combination of 1800N-7.5Nm. 2–3-minute rest between the 700 cycles and between sets was considered to let OCP settle to magnitudes that were close to its control set value.

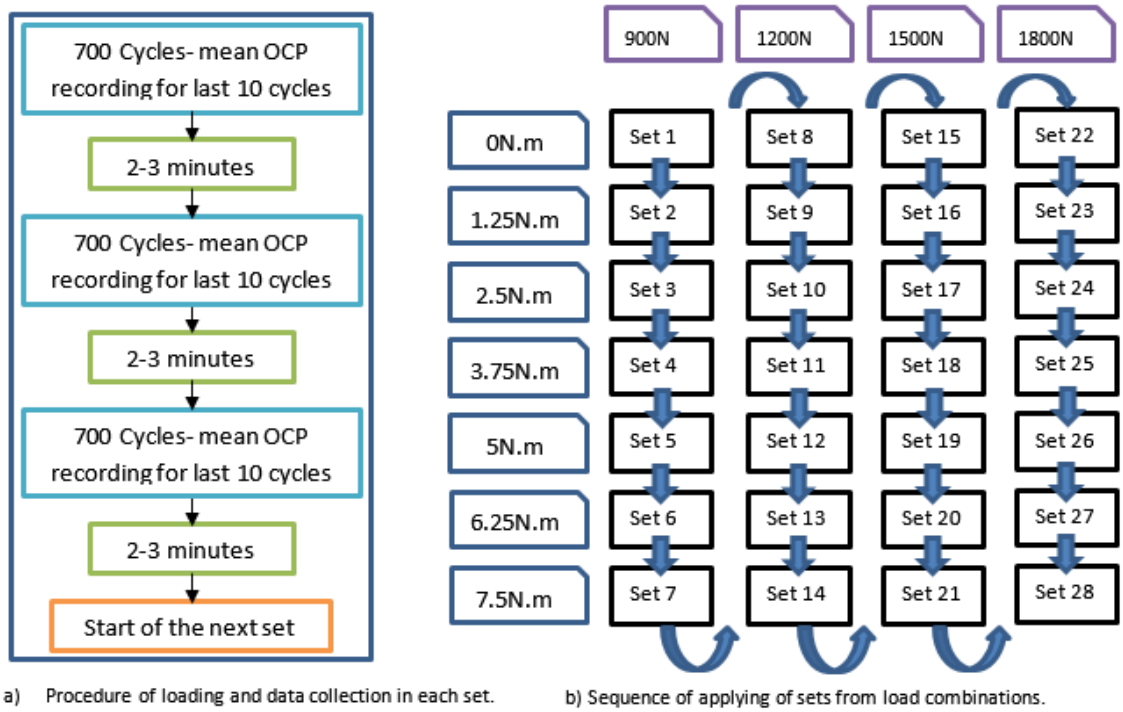

Figure 6.4-a) Details of each set in the test protocol: three steps of applying 700 cycles of load and mean OCP collection for last 10 cycles with 2–3 minutes rest between sets. b) Sequence of applying load combination sets by first increasing the maximum absolute moments then increasing the force.

The loading frequency was set to 3 gait cycles per second which provided enough time for repassivation and resembled the service condition from the aspect of fretting-corrosion (Goldberg and Gilbert 2003).

6.2.4 Post-test samples analysis

After conducting the tests, samples were disassembled by an MTS-Model 45 electro-servo machine at the University of Adelaide. The Instron machine of Flinders university couldn't be used for disassembly as the 24mm diameter of the testing samples were out of the range of commercially available jaws of the Instron machine. The safety settings and testing conditions of the disassembly were set by the MTS software and data acquisition from the system was conducted using a custom-developed LabVIEW code.

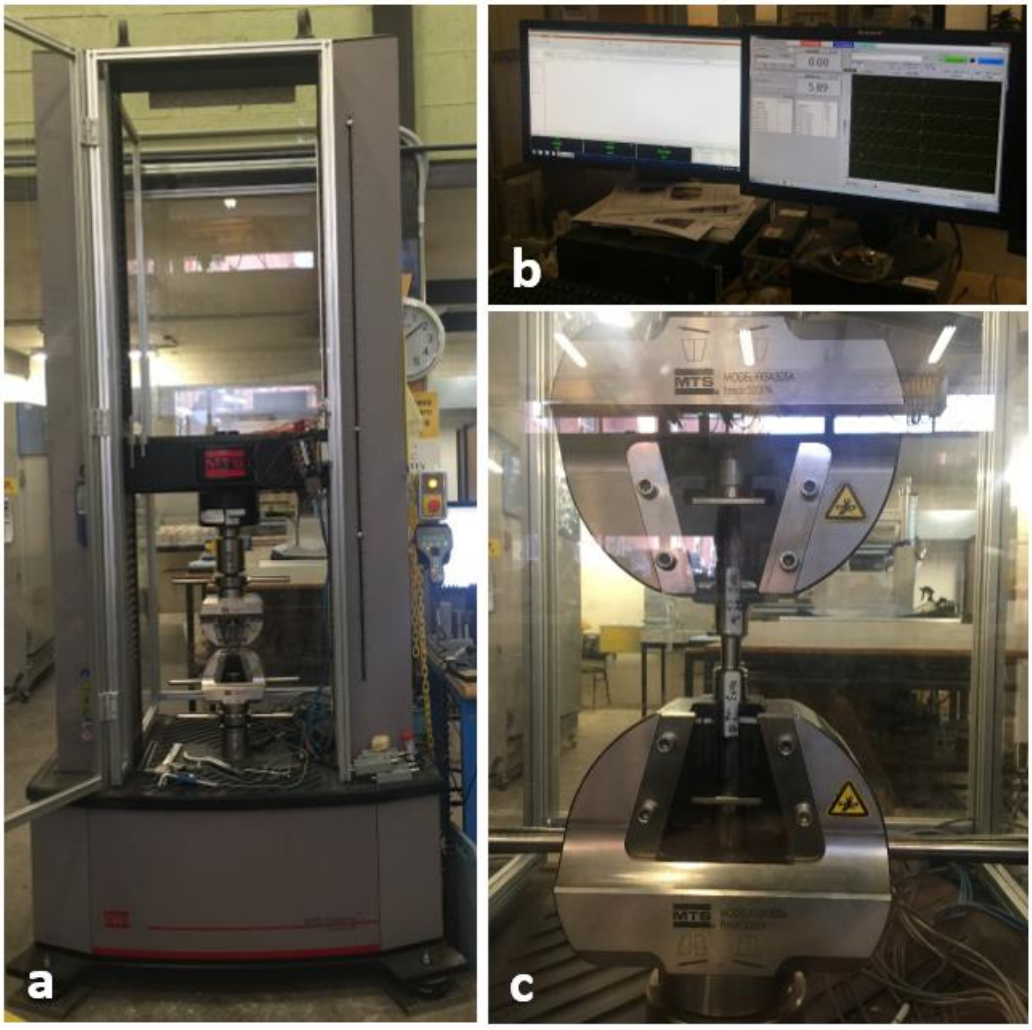

Figure 6.5 Post-test disassembly of the samples a) MTS-Model 45 Electro servo machine b) MTS software (left) used for setting safety limits of the test and LabVIEW custom code (right) used for the recording the disassembly loads. c) Sample mounted in the jaws during the disassembly process

To keep the disassembly loading in the quasi-static range, the samples were disassembled at a rate of 0.05 mm/min and the corresponding load-displacement was recorded. Additionally, due to the hardness of the materials in the samples (CoCrMo and Ti6Al4V), achieving a good drip in the samples from the tool steel jaws of the MTS machine was challenging.

The disassembled samples were then visually investigated to assess the damage induced on the samples during the fretting-corrosion tests. The visual assessment considered aspects of material combination, regions of visible mechanical damages (fretting damages) and regions of visible chemo-mechanical damages. The implants were investigated with respect to their superior, anterior, inferior and posterior positions.

One Ti alloy neck sample and one CoCr alloy neck sample was collected for further SEM and EDX investigation. The SEM and EDX was conducted by the Inspect_FEI_F50_SEM at Flinders node of the Australian Microscopy and Microanalysis Research Facility (AMMRF). To prevent any interruption in material composition and the degraded surface of the sample, no chemical cleaning medium was used on the samples during the sample preparations.

6.3 Results

6.3.1 Changes in corrosion current by changes in force and moment profile

Increase in absolute magnitude of OCP is an indicator of level of corrosion activities in the area. Instantiations corrosion current is in direct relation with amount of ions dissolution in every single moment in the corrosive environment. Figure 6.6 shows an example of the variation in corrosion current along with variations in force and moment profile through cycles of loading. There is a phase relation between current and loads. For the demonstrated case, current waveform reached its maximum value twice in one cycle of the activity load (biphasic): once at the minimum magnitude of force and frictional moment and once at the point of descending in force and moment from higher magnitudes to lower magnitudes. The current and loads waveform was correlated in different manners: biphasic for lower OCP magnitudes and transferred to monophasic (one pick value in one cycle of load) in higher OCP values. The transition from biphasic to monophasic response occurred in OCPs near to -0.35V and -0.5V for CoCr-CoCr and CoCr-Ti6Al4V material combinations, respectively.

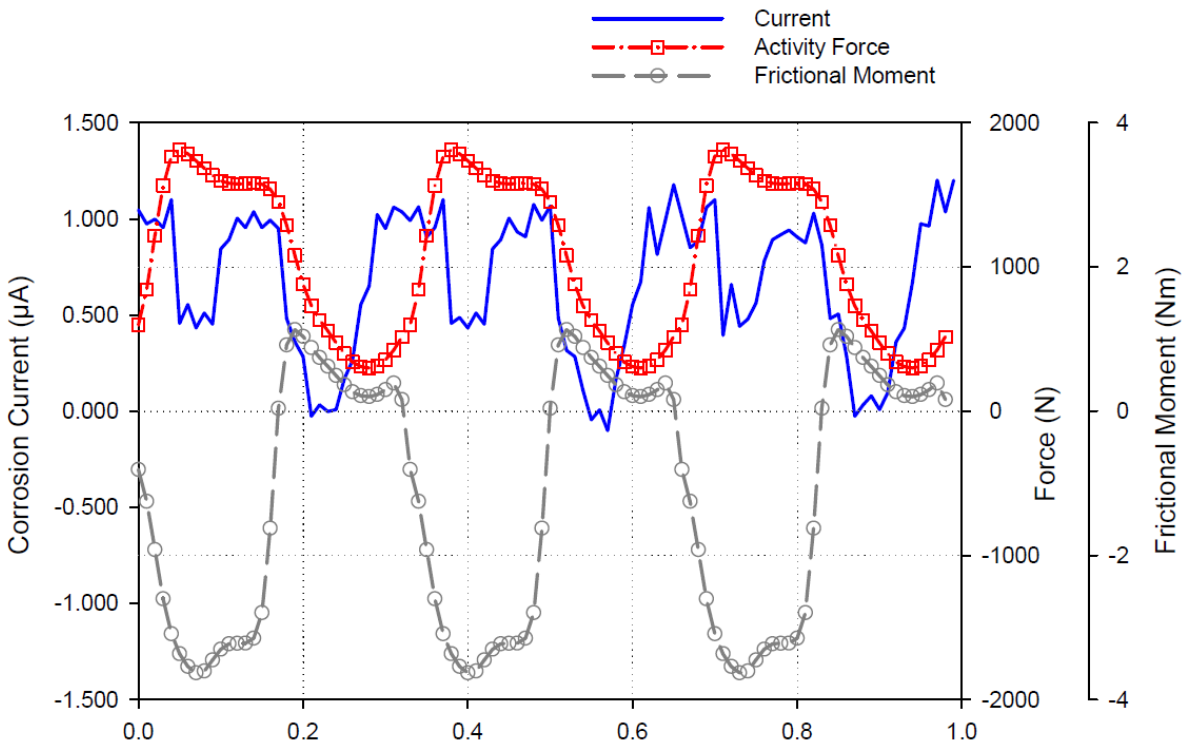

Figure 6.6) Example of Variation in Current by variation in the applied forces and frictional moments-Data extracted from 1800N-5Nm Load Combination for CoCr-CoCr material combination

6.3.2 Effect of load components and material combination

The non-loaded control value OCP was averaged between three samples of each material combination as -0.116V and -0.311V for CoCr-CoCr and CoCr-Ti6Al4V material combinations, respectively. each load combination was applied three times on the sample, each time for 700cycles and the OCP value was collected (Figure 6.4a). For each material combination, the test was conducted on three samples. The reported OCP value in Figure 6.7 is the average of all the value recorded for that material combination under the given load combination. For example, OCP value corresponding to load combination of 900N-1.25Nm for CoCr-CoCr material combination is average of nine OCP value collected for this material combination under this load combination (three samples with three OCP values collected from each sample as explained in Figure 6.4-a). The variation of OCP with change in maximum value of applied force and moment are presented in Figure 6.7 for both material combinations of CoCr-CoCr and CoCr-Ti6Al4V.

CoCr-CoCr material combination of head and neck

For the CoCr-CoCr material combination, in load combinations with lower vertical forces, increase in frictional moment leads to increase in OCP. For example, at 900N for CoCr-CoCr (Figure 6.7-a), increase in maximum value of frictional moment from 0Nm to 7.5Nm caused OCP to drop from -0.280V to -0.426V indicates -0.146V drop in OCP. The more negative the OCP be, the more corrosive the corrosion ambient had become to balance the dissolved metallic ions. This concludes that more negative OCP happens in occurrence of more metallic ions dissolution to the ambient. In load combinations with higher vertical forces, increase in frictional moment causes smaller change in OCP as compared to lower vertical forces cases. For example, at 1800N for CoCr-CoCr (Figure 6.7-a) with an increase in maximum value of frictional moment from 0Nm to 7.5Nm, OCP changes from -0.478 to -0.508V indicating -0.030V drop in OCP. This indicates that in higher magnitudes of force, increase in frictional moment doesn't affect as significantly as it does in lower magnitudes of force. In fact, it can be concluded that increase in vertical load has considerably intensified fretting-corrosion and increase in frictional moment from 0 to 7.5Nm cause only -0.030V change (from -0.478 to -0.508V). In summary, for CoCr-CoCr material combination, increase in the force consistently and almost linearly increased the fretting-corrosion. For this material combination, increase in the frictional moment also increases the fretting-corrosion more effectively when combined with lower vertical forces than higher vertical forces.

CoCr-Ti6Al4V material combination of head and neck

For the CoCr-Ti6Al4V material combination (Figure 6.7-b), response of the head-neck interface was slightly different from CoCr-CoCr material combination. Considering the lower vertical forces for this combination, increase in frictional moment from 0Nm to 7.5Nm cause -0.086V (from -0.390V to -0.476V) and -0.143V (from -0.450V to -0.593V) for 900N and 1200N vertical forces, respectively. This indicates that considering 900N and 1200N vertical forces, increase in frictional moment was more interruptive to the interface at the higher force than lower forces. From 1200N to 1800N, increase in frictional moment becomes less effective by increase in the force. Especially at 1800N, increase in frictional moment from 0 to 7.5 was almost the same for the fretting-corrosion of the interface. Looking from the perspective of increase of the force, two different groups should be considered: i) Increase of force combined with 0Nm, 1.25Nm and 2.5Nm (top three lines of Figure 6.7-b) and ii) Increase of

force combined with 3.75Nm, 5Nm, 6.25Nm and 7.5Nm (bottom four lines of Figure 6.7-b). For the first group (top three lines of Figure 6.7-b), increase of the force from 900N to 1800N increased fretting-corrosion in a linear manner. For the second group (bottom four lines of Figure 6.7-b), increase of force has most of its effect in 900N to 1200N step and changes from 1200N to 1800N were less effective in this group. In summary, increase in force was more dominant to intensify fretting-corrosion than to frictional moment.

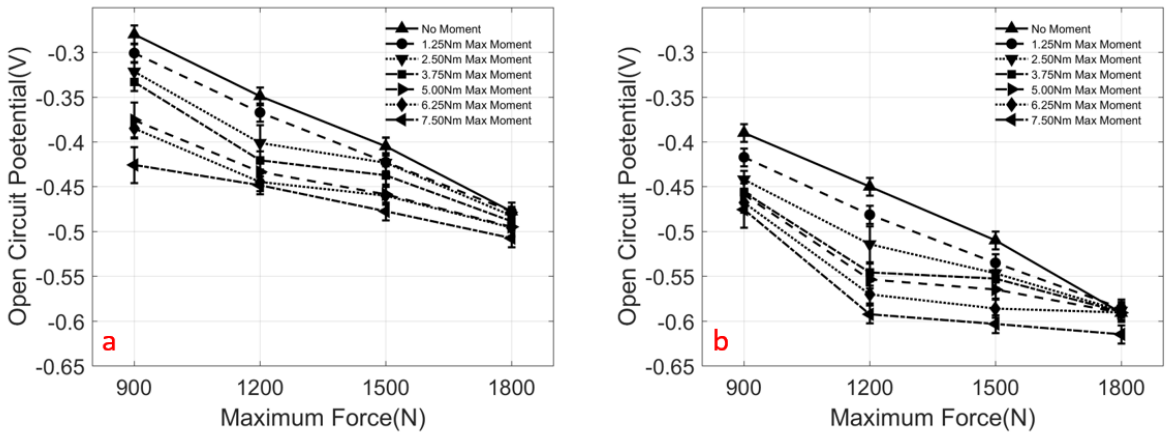

Figure 6.7) Variation of OCP with change of maximum value of walking activity's Force and Moment for a) CoCr-CoCr material combination of head and neck b) CoCr-Ti6Al4V material combination of head and neck

6.3.3 Variation of OCP by presence and absence of load

Figure 6.8 is an example of the variation of OCP from the non-loaded control value caused from the beginning of the loading. As observed, the initiation of the loading causes a sharp drop in the OCP. This indicates that the passive oxide layer has a low resistance to the daily activity loads and is damaged by the first initial load cycles. After a sharp initial drop, the OCP reached an almost constant value which didn't change even after experiencing a higher number of load cycles. This indicates that disturbance of the passive layer and fretting-corrosion at the interface was occurring in a more severe manner than non-loaded control value and a steady condition. After reaching 700 cycles, the loading stopped. It should be noted that the resettling of OCP value toward non-loaded control value occurs slowly.

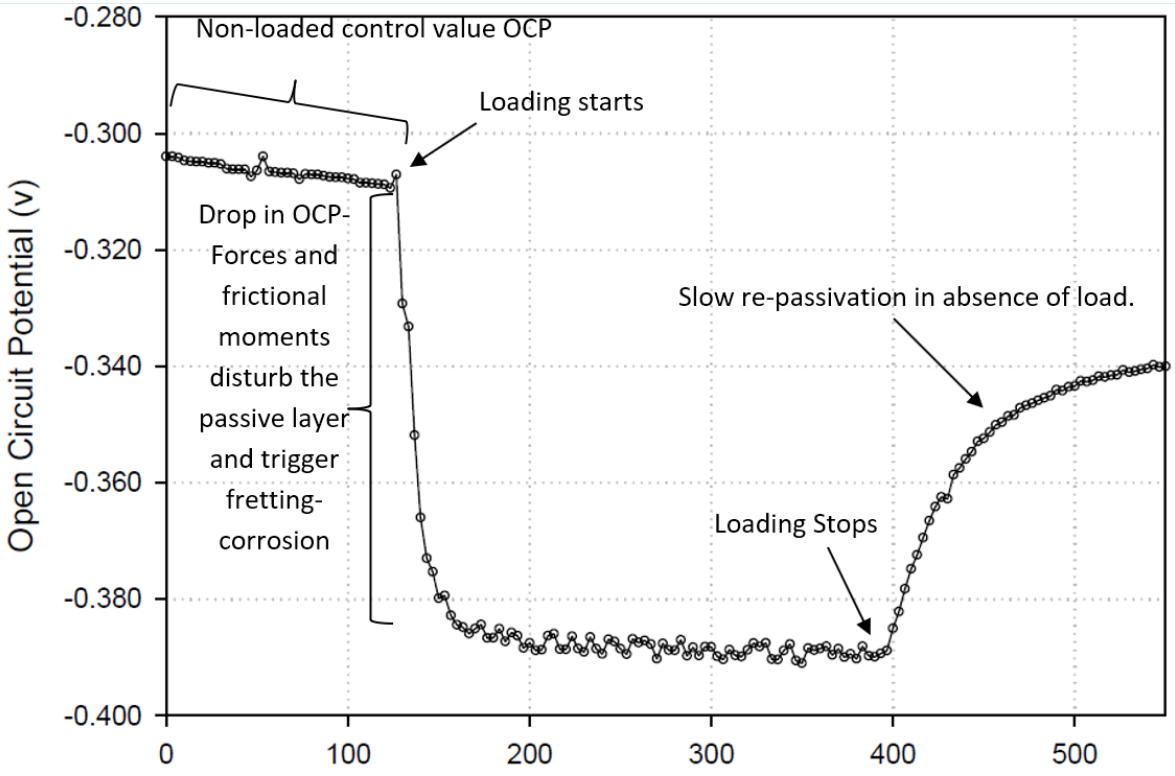

Figure 6.8) Example of changes in OCP from non-loaded control value due to start of loading indicates initiation of fretting-corrosion at the interface- slow re-passivation after stopping of loading - Data extracted from set 1 of CoCr-Ti6Al4V material combination

6.3.4 Post-test sample analysis results

After conducting the fretting-corrosion tests on the samples, the implants were disassembled using the MTS servo-electric machine at the University of Adelaide. For the Ti alloy/CoCr head/neck combination, the disassembly force was 1.61, 1.73 and 1.26kN which concluded an average pull-off force of 1.53kN. In the CoCr/CoCr head-neck combination, one of the samples' disassembly slipped inside the gripper during the first attempt because of the hardness of the material surface which prevented the steel tool jaws from biting into the sample. Disassembly force of this sample during the second attempt with a higher clamping force was 0.77kN. The other two CoCr/CoCr samples were disassembled with pull-off forces of 1.49 and 1.83kN with the average of 1.66kN. The slipped sample's disassembly results were considered invalid as it was an interrupted disassembly process.

After disassembly, the neck samples were visually inspected for fretting-corrosion damage at the head-neck interface. Figure 6.9 shows different sections of the disassembled samples. In all the samples, the machining pattern at the superior-proximal section of the samples was worn out under cyclic load on the interface and induced fretting. In the neck Sample 1 of the CoCr/Ti alloy head-neck combination, corrosion damage was present at the whole

circumference of the sample with more degradation at the anterior and posterior side of the sample. In the neck samples 2 and 3 of the CoCr/Ti alloy head/neck combination, corrosion damage was more concentrated on the anterior and posterior side of the implant and there was a small amount of visible corrosion damage on its superior and inferior side. Given that the applied moment is in the neck axis direction while the forces are in superior-inferior direction, the anterior and posterior area of the neck experienced lower contact forces than the superior side but still were in contact and had higher relative displacement due to lower compression and eventually experienced more damage than a more compressed superior side.

CoCr neck samples from CoCr/CoCr head-neck material combination were suffering from fretting damage at the superior proximal side of the implant, which was similar to the Ti alloy neck samples. Compared to the Ti alloy neck samples, there was considerably less visible damage caused by corrosion on the body of the CoCr neck samples. As reported in the intra-test, this is aligned with the results for different material combinations; compared to CoCr/CoCr the Ti/CoCr had higher magnitudes of OCPs which indicates higher corrosion activities in the head-neck interface.

Galvanic corrosion damages observed in the valleys of the damaged knurled. Beside the galvanic damage, localised corrosion damage nucleation was observed at several points on the surface.

Figure 6.9 Ti alloy and CoCr alloy neck samples fretting-corrosion damage after undergoing cyclic loading test in corrosive medium

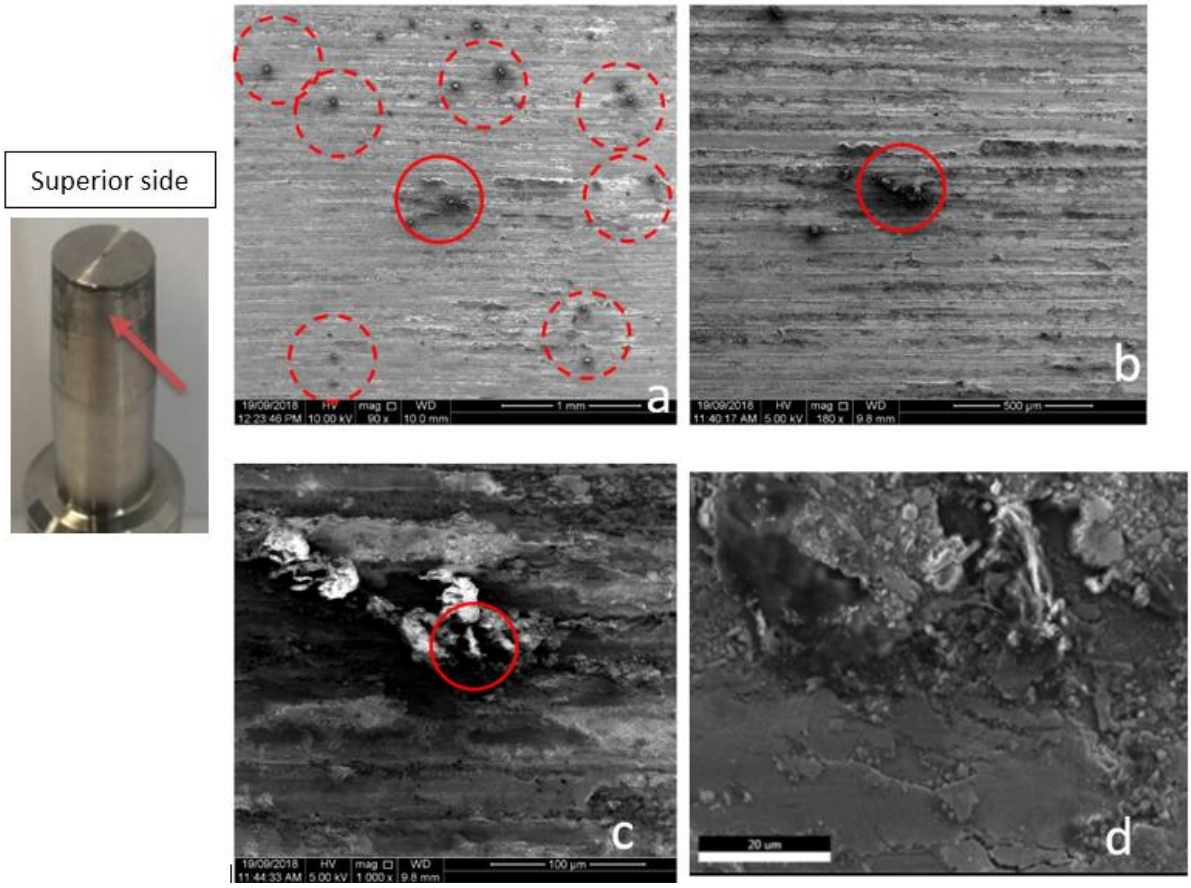

Figure 6.10 TI alloy sample under SEM imaging on localized damage on surface of the sample (Ti6Al4V – Sample 3)

After visual investigation of the neck samples, one neck sample of each Ti alloy (Ti6Al4V – Sample 3) and CoCr alloy (CoCrMo – Sample 2) were considered for further investigation by SEM imaging and EDX. SEM imaging was conducted using the FEI_F50_SEM at Flinders node of the AMMRF. To study the surface damages on the samples, acceleration voltage set as 5.00 KV for the Ti alloy sample and 10.00 KV for the CoCr alloy sample and sample's top surface located at working distance of 10mm. For the Ti alloy sample, the machining pattern from machining of the surface was considerably damaged due to fretting (Figure 6.10).

The localised corrosion damages on the surface were investigated by the EDX. It investigated region, live map and element overlay for the Ti alloy neck sample which is shown in Figure 6.11. Apart from Ti alloy elements, the presence of Co and Cr in this region suggests material transfer from the CoCr head to the Ti neck. The components of Ringer's solution salts, such as KCl and NaCl, were also present in this localised damaged region. The EDX spectrum of Ti, O, Co and Cr are shown together in Figure 6.12.

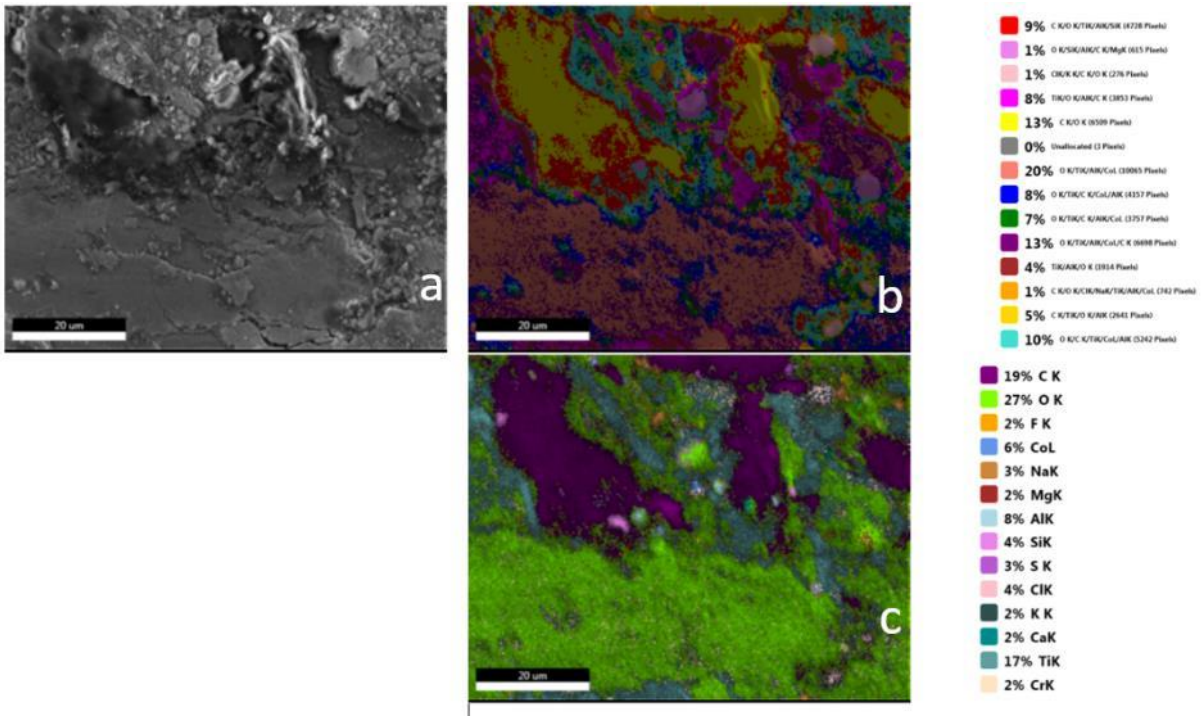

Figure 6.11 One of the localized damage regions on the Ti alloy neck sample (Ti6Al4V – Sample 3) a) SEM image, b) live map and c) elements overlay

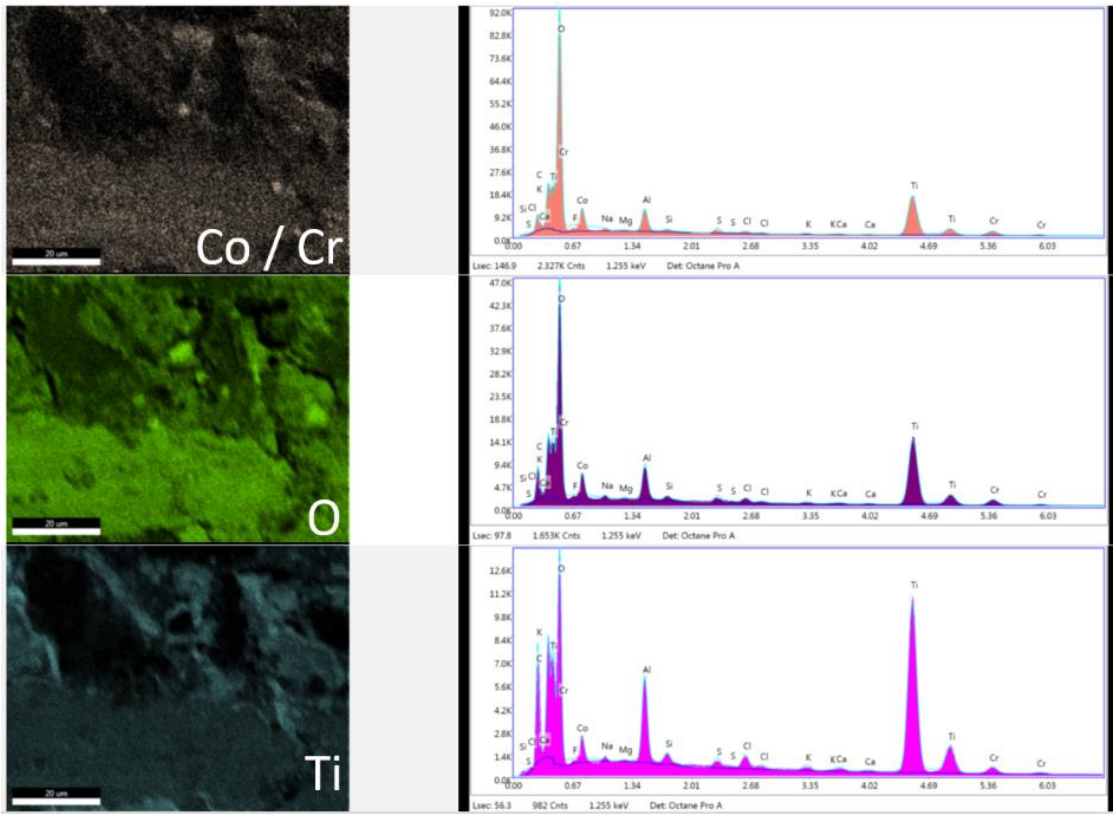

Figure 6.12 EDX spectrum of Cobalt/ Chromium, Oxygen, and Titanium for the Ti alloy neck sample (Ti6Al4V – Sample 3)

Similar to the Ti alloy neck sample, fretting wear and breakage of the passive oxide layer and the knurled machining tracks on the neck were observed during the SEM imaging. Localised corrosion damages were also visible in the SEM investigation of the CoCr neck sample in the form of dark areas on its surface. Figure 6.13 shows nucleation of severe corrosion damage on the CoCr neck sample. This localised corrosion damage was further studied through an EDX as shown in Figure 6.14 and Figure 6.15.

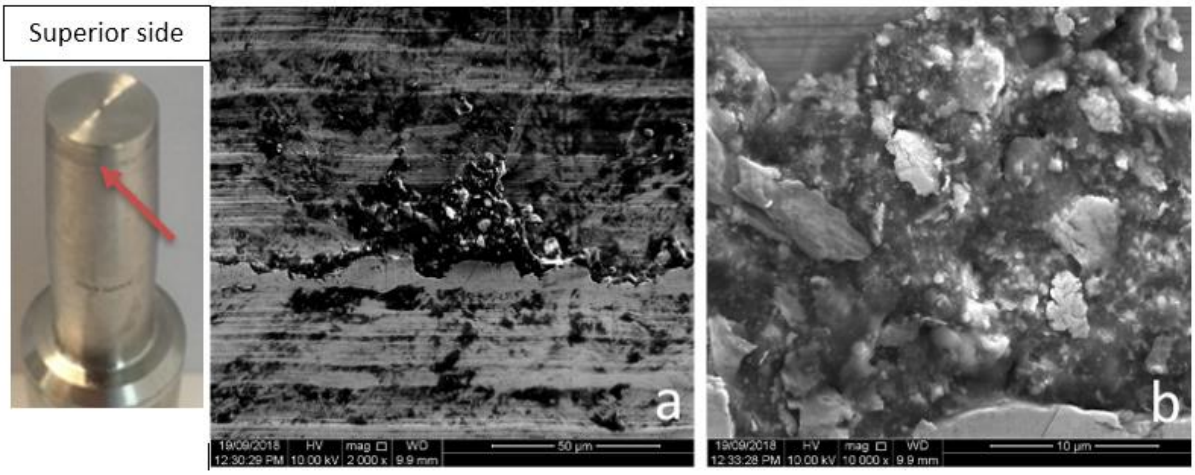

Figure 6.13 a) CoCr alloy neck sample SEM imaging, b) Nucleation of corrosion damage in CoCr neck sample (CoCrMo – Sample 2)

From Figure 6.14, it is observed that a large block of CoCr substrate material exists as broken and oxidised repassivated material forming from underneath the broken passive oxide layer. Presence of carbon found in the EDX analysis suggests that although it was tried to carry and prepare the samples with minimum contamination with the use of acetone to clean the clamping area of the samples, some contaminations moved to the samples surface.

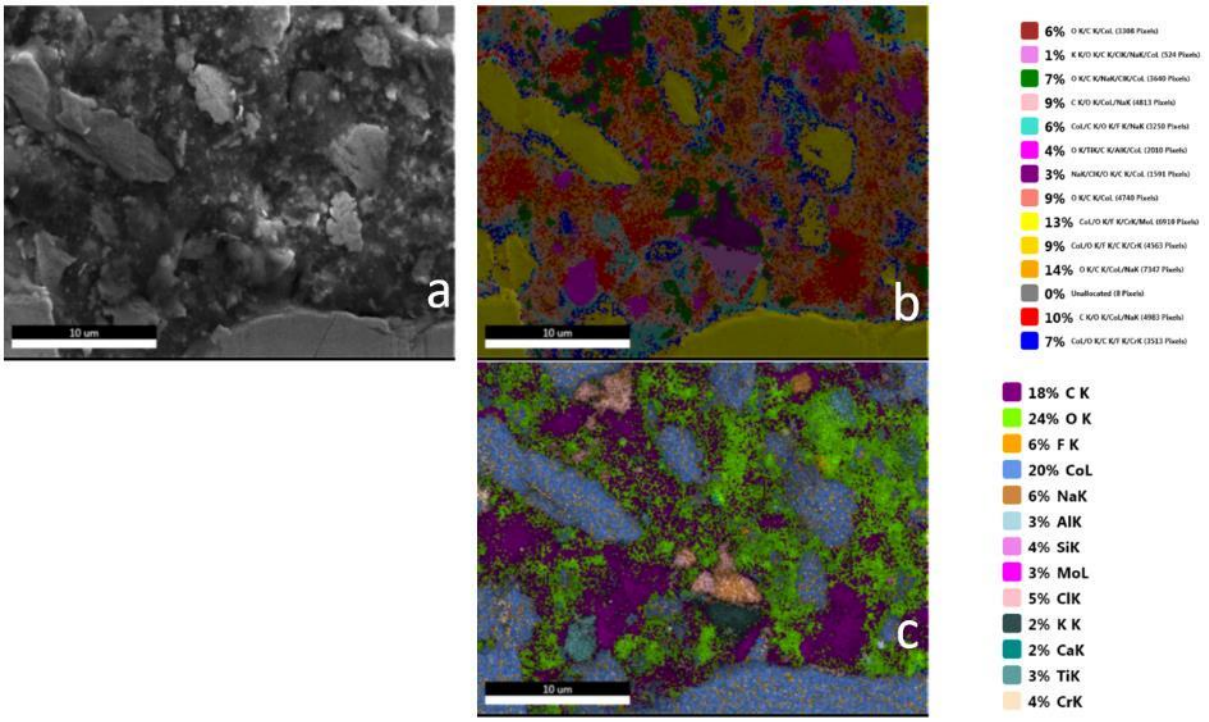

Figure 6.14 a) EDX investigated region of corrosion nucleation b) live map and c) elements overlay (CoCrMo – Sample 2)

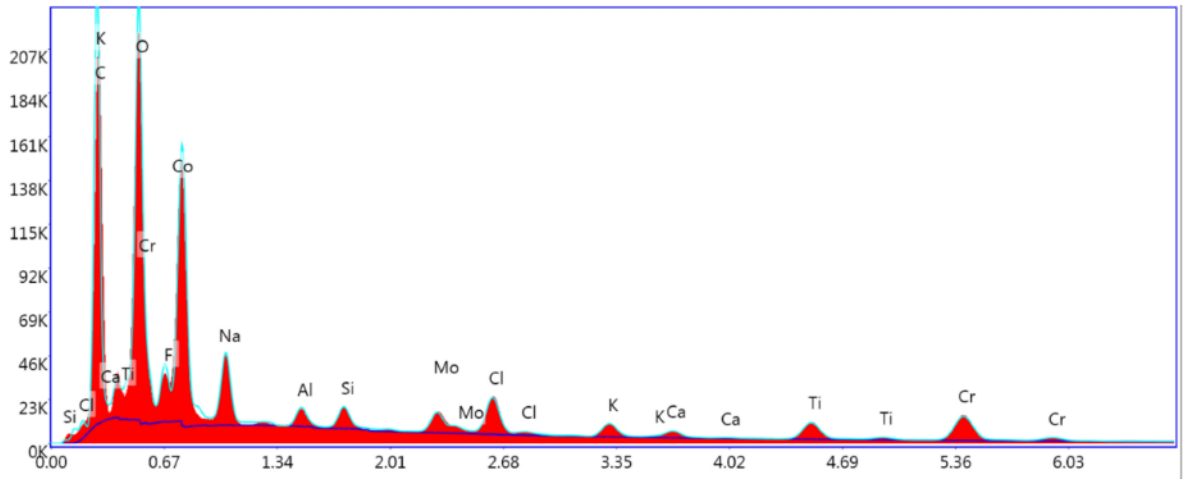

Figure 6.15 Sum spectrum of the EDX investigated section of the CoCr sample (CoCrMo – Sample 2)

6.4 Discussion

Qualitative pin/cylinder-on-disk fretting-corrosion studies along with tests on real scale head-neck interfaces under simplified load profiles have provided a good perspective on fretting-corrosion and mechanically assisted crevice corrosion of the head-neck interface. The outcomes of the current study can help to improve this understanding. Since the effect of the

forces of the realistic body and frictional moment on mechanically assisted crevice corrosion of head-neck interface of hip implant has not been investigated, the objective of this study was to determine the contribution of these loads in the degradation of the head-neck interface.

The effect of material combination of head and neck in fretting-corrosion at this interface has been studied in the simplified studies. Panagiotidou et al. (Panagiotidou, Meswania et al. 2015), in a study with applying forces and moment dependent to the forces, reported higher corrosion currents for CoCr-Ti, CoCr-CoCr and CoCr-ceramic material combination, respectively, under both bending and torque loads dependent to the axial forces. Gilbert et al. (Gilbert, Mehta et al. 2009), in their study on SS-CoCr and CoCr-CoCr head-neck combinations, have reported that SS-CoCr material combination was more susceptible to fretting crevice corrosion. In another study which investigated fretting-corrosion of common hip joint implant alloys in a pin-on-disk arrangement, Swaminathan et al. (Swaminathan and Gilbert 2013) have reported that Ti6Al4V-Ti6Al4V demonstrated the highest fretting-corrosion as compared to CoCr-Ti6Al4V and CoCr-CoCr. They suggest that in CoCr-Ti6Al4V material combination, CoCr dominates the response of the interface to fretting-corrosion and decreases fretting-corrosion as compared to TI6Al4V-Ti6Al4V.

In the current study, we have observed that Ti6Al4V-CoCr head-neck combination was more susceptible than CoCr-CoCr material combination. The non-loaded control value of OCP of Ti6Al4V-CoCr was -0.311V against -0.116V of CoCr-CoCr material combination and in the highest drop of OCP, their OCP reached to -0.615V and -0.506V, respectively. The higher susceptibility of Ti6Al4V-CoCr as compared to CoCr-CoCr combination is believed to be because of lower hardness of Ti6Al4V as compared to CoCr. This leads to faster interruption to the passive oxide layer. Regarding the non-loaded OCP value combination, the combination of two different materials (Ti6Al4V-CoCr) is more vulnerable for corrosion than the same material combination (CoCr-CoCr).

Studies have also investigated contribution of assembly force and simplified activity loads on fretting-corrosion of head-neck taper junction. Under a cyclic vertical load with maximum value of 2300N variation, a coupled torque with magnitudes 0Nm, 9Nm, 14Nm and 18Nm on a CoCr-CoCr head-neck combination caused mean maximal fretting currents 2µA, 3µA, 4µA

and 4.7 µA, respectively. These maximum fretting currents are indicators of instantaneous rate of dissolution of metallic ions to the ambient. This maximal fretting current was higher for CoCr- Ti material combination; it was 3µA, 5µA, 8µA and 25 µA, respectively (Panagiotidou, Meswania et al. 2015). After one million cycles, under 3300N pure vertical force and in absence of frictional moments, OCP of Stainless-steel-CoCr decreased from 150mV to 100 mV. This suggest that after 1 million cycles of loading, vulnerability of the interface to mechanically assisted crevice corrosion decreases (Gilbert, Mehta et al. 2009). Another study, with the assembly force as the variable parameter, reported that higher initial assembly force (6kN vs 4.5kN) increases the magnitude of pure torque required to initiate fretting-corrosion (from 3.92Nm to 7.23 Nm, respectively). Regarding the effect of loads on fretting-corrosion, the results of the current study demonstrated that independent realistic frictional moments of walking are effective when they are combined with lower vertical forces (cyclic force with maximum 900N for example). By increasing vertical forces, they had a more significant effect in intensifying the fretting-corrosion since in the presence of 1800N variation of moments from 0Nm to 7.5Nm, it did not significantly affect the OCP. This outcome is limited to the investigated head-neck geometry and isn't necessarily expandable to other head-neck designs. This limitation in these outcomes is mainly due to the variation of effective parameters of fretting and corrosion (stress-field, range of micromotion and contact condition) by change in interface geometry and surface finish.

Post-test analysis on the samples helped to gain a better understanding of fretting-corrosion damage on the examined head-neck interfaces. The average pull-off forces of the studied interfaces were 1.53kN and 1.66kN for CoCr/Ti alloy and CoCr/CoCr head-neck combination samples, respectively. For a similar push on force of 4000N, Rehmer et al. had reported (Rehmer, Bishop et al. 2012) average pull off forces of 2230N and 2100N for CoCr/Ti alloy and CoCr/CoCr head/neck combination; Their examined geometry was different of samples in our study which can be the possible source of difference in the value. Also, in Rehmer et al. study, samples didn't experience cyclic loading before disassembly while samples of our study disassembled after cyclic loading applied to them.

Visual investigation on the disassembled samples should be considered in parallel. With outcomes of finite element analysis from chapter 4. From chapter 4, it was concluded that maximum stresses happen in the press-fitted proximal ring with maximum stresses at the

superior part. This area is the same area of where highest fretting damage and deformation of the knurled machining pattern on the implant surface was observed for both the CoCr/CoCr and CoCr/Ti alloy material combination. This is the area which experienced the press-fit stress in the finite element modelling. Fretting-corrosion damages present more adjacent to the press-fit area, which experienced wear during the loading cycles. Regarding the black corrosion damage point, corrosion damages on the Ti alloy neck samples were more significant than of the CoCr neck samples. This outcome is aligned with the intra-test OCP results, which have shown that CoCr/Ti6Al4V more vulnerable than CoCr/CoCr.

SEM investigation of the tested samples showed considerable fretting wear on the interface for both the Ti alloy neck sample and CoCr neck samples. Nucleation of the local corrosion observed for both of the Ti alloy and the CoCr neck samples with more intensity in the Ti alloy samples. The breakage of the passive oxide layer and formation of oxide particle was observed in the local corrosion nucleation sites of the samples. In case of Ti alloy neck component, the presence of Co and Cr on the Ti alloy corrosion nucleation areas, especially in the same spot along with O, suggests the transfer of material from the head and possible formation of complex metallic oxide compounds.

Conclusively, fretting-corrosion has been reported as the cause of early retrieval surgeries for modular hip joint implants made from sceptical bio-metals of CoCr, Ti and stainless steel (Cooper, Della Valle et al. 2012). Although different designs and loading condition might vary in the intensity of the fretting-corrosion at head-neck junction, there has yet not been any solution to eliminate fretting-corrosion in the current modular arrangement and for the current CoCr and-or Ti alloy bio-metal combinations. Modularity provides a wide range of improvement to THR to overcome geometrical complexities and ease future retrieval surgeries of the damaged modules. To this end, changing the material to a less vulnerable one based on the nature of service condition (especially fretting-corrosion) could be one of the solutions to these problems. There are many ongoing studies working on the improvement of the characteristics of the currently used alloys (CoCr and Ti alloys) to address this issue. Magnesium (Mg) and its alloy are promising materials which are being researched to improve its biomedical performance and making it compatible for *in vivo* service condition (Radha and Sreekanth 2017). These materials don’t have the hardness and strength of the current

biometals such as Ti alloy and CoCr and need to be improved in these respects to become a viable solution for biomedical implants.

6.5 Limitations of this *in vitro* study

This *in vivo* comes with some limitations as below.

- Investigating one sample through a serries of loading: Testing of each of the loading cases was conducted after a settlement period (2-3minutes) before starting the next serries of loading. This settlement time provide enough time for repassivation of the damaged interface. However, due to changes in the geometry by the fretting-corrosion of the previous load cycle, results from the next step could be different as of results could obtained from a fresh sample experiencing only one regime of loading. Considering the large number of samples and amount of time required to test each loading regime on one sample, the testing scenario was designed aligned with previously researches (Gilbert, Mehta et al. 2009) with similar research target in which several loading scenarios were applied on one sample.

- Study on a single geometry of the interface and one assembly force: The geometry of the interface plays a role in the initial stress field after the assembly and mechanical response of the interface. Also, regarding the assembly force, in this study the recommended assembly force for the head-neck interface was considered. Initial assembly force has a role the initial contact stress of the interface. Considering the dependency of fretting response to the normal stress (resulted by initial assembly force) and fretting-corrosion to the interface geometry, results of this study are limited to the examined geometry and assembly force.

6.6 Summary

Interrelation of frictional moment and daily forces of level gait walking on fretting-corrosion and mechanically assisted crevice corrosion of the head-neck interface has been investigated. This study is conducted on two common material combinations that are currently used for the interface – CoCr-Ti6Al4V and CoCr-CoCr. Overall, the CoCr-CoCr interface had a better corrosion performance than CoCr-Ti6Al4V. This can be due to greater surface hardness of the material and similar electronegative material combination. Although the material

combinations had different detailed responses to combination of forces and moments, generally, it observed that frictional moments contributed more to intensity of the corrosion when they were combined with lower activity forces. Regarding interrelation of the of frictional moment and the forces, it observed that on lower amount of the force frictional moment can increase the fretting-corrosion on the interface. By increase of the forces, the fretting-corrosion also increases while frictional moments become less intensifying on the damage. The highest fretting-corrosion damages observed under the highest forces where increase of the frictional moments was less effective on the occurring fretting-corrosion. Considering observation of fretting-corrosion even under the low magnitude of loads, the degradation is inevitable for the considered material. This mainly comes from the nature of corrosion resistance of the studied material which relies on adhesive passive oxide layers that are susceptible to fretting wear in mechanically loaded interfaces.

Chapter 7. Discussion

7.1 Failure of the head-neck interface due to fretting-corrosion

THA is of the most successful methods among orthopaedic surgeries. THA implants' designs include modular components to address the complications in the geometry of the patient's body during the operation. The modular design has recently led to a range of new shortcomings and eventually decrease in implants' life expectancy due to premature failure. Rate of early failures of THA have been especially high for the larger head MoM bearing couples (Gascoyne, Turgeon et al. 2018) (Higgs, Hanzlik et al. 2013) (Bolland, Culliford et al. 2011).

Adding more modular interfaces which transfer loads while exposed to body corrosive ambient is of the causes of the failures. THA components are made of biocompatible metals, and their biocompatibility relies on a thin adhesive passive oxide layer which covers the active alloys (e.g. Ti6Al4V and CoCrMo) underneath. This passive layer has a low strength to mechanical disturbance and cyclic stresses of daily activities on the modular interfaces, which disrupt this passive layers repeatedly (Pillar 2009).

The metal underneath of the protective passive layer is chemically active. By degradation of the passive layer in presence of active ions in body fluids, such as chlorine in the synovial fluids, the active metal dissolve into the synovial fluids; a process which is known as corrosion. Tight geometry of the modular interfaces (crevice) also exacerbates the corrosion in the interface. The oxygen in the stagnated synovial fluid in the crevice is consumed to reshape the passive layer (repassivation) during early disruptions. By running out of oxygen, more metallic ions dissolve in the stagnated synovial fluid of the crevice and in absence of oxygen ions rather than reshaping a passive oxide layer over the active metal, metallic ions absorb corrosive ions such as chlorine to the crevice geometry. An increase in chlorine and other corrosive ions in the crevice drops its pH to 1 (Viceconti, Ruggeri et al. 1996). This level of acidity of the ambient could autonomously dissolve the remaining protective passive layer with no assist from fretting. This autonomous dissolving of passive layer and the metal underneath due to low pH in the stagnated electrolyte of a crevice geometry (here, synovial fluid) is called crevice corrosion. This means that after a while of applying daily activity loads to the modular interface, even by stopping the loading, degradation of the interface might continue due to crevice corrosion in the tight geometry of the modular interface. This

mechanism is described as fretting-corrosion and mechanically assisted crevice corrosion (Bryant 2013).

The ions from corrosion and crevice corrosion and the debris from fretting of the passive oxide layer and active metal underneath are toxic for surrounding tissues. These ions and debris lead to adverse local tissue reaction, severe pain and finally early retrieval surgery. The current standard for fretting-corrosion evaluation of the modular implants is ASTM F1875:2014 in which the implant experiences cyclic vertical forces in corrosive ambient of Ringer's solution.

As has been well discussed by Morlock (Morlock 2015)in a review paper on state of knowledge prior to introduction of large head MOM bearings, the biological existence of corrosion in modular hips and biological reactions to metallic debris were known at the introduction of large MOM bearings, however this issue hadn't been raised as a major concern. The reduction of the taper diameter (from the original 14/16 to 12/14 or V40) as well as the reduction of taper length (from 2 cm to below 1 cm) to expand the range of motion, was carried out without obvious new problems at the end of the 1990s, since smaller heads "load" the taper junction less than large heads that were introduced around this time (much larger than 36 mm in diameter; to emphasise: originally to allow to keep well-fixed acetabular cups in patients with femoral neck fractures after resurfacing NOT as an option for primary systems). It is hypothesised that the combined perturbation of the originally so successful THA implant system by the changes of 3 parameters (taper diameter, taper length, head diameter) together with the simultaneously occurring spread of MoM joint articulations, which can generate high friction in unfavourable situations, more or less "suddenly" jeopardised the strength and robustness of the taper junction. The extent to which deviations in the assembly process play a role (contamination and assembly force) has not been conclusively explained yet but is heavily suspected (Morlock 2015).

Cook et al. (Cook, Render et al. 2000) has raised valuable points of: Complex systems (modularity in this context) are intrinsically hazardous.

• Catastrophe requires multiple failures – single point failures are not enough;

• Catastrophe is always just around the corner;

• Post-accident attribution to a ‘root cause’ is fundamentally wrong;

• Hindsight biases post-accident assessments of human performance;

• Change introduces new forms of failure.

the risk of potential problems.

Morlock (Morlock 2015) in his review paper concludes: “The “taper disaster” has demonstrated, that the “operation of the century” cannot easily be improved further by changing implant design but rather the opposite can happen: solving a problem by introducing a new, larger problem. In the future, the main focus should be put on a controlled stepwise introduction of innovations, especially in areas – such as hip arthroplasty – where good solutions are already available. We have to continue to improve pre-clinical testing methods by including surgical variation, different patient activities, different biological environments and other factors.”

To have a better understanding on reasons of THA failure due to fretting-corrosion main effective parameters on each of the fretting and corrosion phenomena need to be identified and then the further simplification of these parameters in hip joint implant investigations needs to be justified. The minor dimension of taper problems observed until the beginning of the 21st century can probably be explained by the use of smaller head diameters until this point in time (up to a maximum of 36 mm).

7.2 Main effective parameters on fretting-corrosion

Fretting is indirectly a function of 50 parameters (such as geometry, roughness, lubrication, friction coefficient, material surface properties, and chemical composition) all of which directly affect the following three mechanical parameters:

- contact stress
- range of micromotions
- surface roughness (Neu 2011).

Literature (ASM-International-Handbook 2005, Neu 2011) strongly suggests that, to have a realistic understanding of fretting performance of an interface, one should apply a stress-field and micromotion similar to the service condition of the component on the same material combination and surface finish.

Corrosion and especially crevice corrosions is a function of electrolyte ions balance, material composition of the active electrode (dissolved material) and counter electrode (the part of the material which release electrons to the electrolyte). Literature (Bishop, Waldow et al. 2008, Baxmann, Jauch et al. 2013, Swaminathan and Gilbert 2013, Royhman, Patel et al. 2017) suggest that Ringer's solution and Bovine calf serum are good representatives of synovial fluid electrolyte balance. Corrosion and especially crevice corrosion are also a function of crevice geometry; the tighter the crevice geometry, the faster the autonomous degradation occurs because of crevice corrosion.

Given background concludes that, to investigate fretting-corrosion of head-neck interface in MoM bearing couples, realistic loads (contact forces along and frictional moments) should be applied on a full-scale modular head-neck interface manufactured from the same material combination. This will lead to a study of fretting-corrosion under similar contact stress, relative displacements, surface roughness and ambient corrosivity.

Following the target of applying service loads on a full scale geometry, through the literature review it has been understood that the contact forces of the hip joint implant has been extensively studied and is available on different databases, especially orthoload.com (English and Kilvington 1979, Bergmann, Deuretzbacher et al. 2001, Bergmann, Graichen et al. 2010). However, frictional moments caused from sliding of the head in the cup is reported for a 32mm ceramic-on-polyethylene bearing couple (Damm, Dymke et al. 2013, Damm, Bender et al. 2017). Frictional moments vary with changing the material combination and bearing couple diameter (Bishop, Waldow et al. 2008, Bishop, Hothan et al. 2013). Given the frictional moments of large MoM bearing couples under three dimensional daily activities were not fully available, the research aim of this doctoral study was setback to firstly determine the frictional moments at the head-neck interface of MoM bearing couples.

7.3 Magnitude and variation of frictional moment of a MoM bearing couple

An analytical method was developed to calculate frictional moment at the head-cup bearing couple of hip joint implant. Results of the developed analytical method verified against the reported frictional moments for simplified *in vitro* experiments and was in a good agreement for hard-on-hard bearing couples, especially for a 46 mm MoM case.

The analytical method was used to determine frictional moments of a 46 mm MoM bearing couple under different daily activities of slow walking, normal walking, fast walking, standing up, sitting down, ascending the stairs, descending the stairs, standing on one leg and bending of the knees.

As reported in the literature review, a head-neck interface assembled with 6kN assembly force required a torque equal to 7.23 ± 0.55 Nm for depassivation. This depassivation torque was reported as 3.92 ± 0.97 Nm for a head-neck assembled by 4.5kN (Jauch, Coles et al. 2014). The extracted frictional moments from the analytical method induced torques in range of these de-passivation torques. This concludes that effect of daily activities' frictional moments on fretting-corrosion of the head-neck interface should be investigated before being simplified or neglected in the Finite Element Analysis and *in vitro* studies of fretting and fretting-corrosion of the head-neck interface. Walking activity as the most frequent daily activity (Morlock, Schneider et al. 2001) had frictional moments and contact forces similar to other frequent daily activities such as fast walking, stair climbing and stair descending. To this end, walking activity's load profile was considered as a proper load scenario for the next steps of this study.

To have a comprehensive picture of fretting-corrosion of the head-neck in service condition, two parallel approaches considered:

- FEA investigation on mechanical responses of the head-neck interface to each and combined load components of daily activities: This needed to be addressed to have a perspective on internal motions and stress-field occurring at the head-neck interface during the daily activity of walking.
- *In vitro* investigation to find level of contribution of frictional moments and vertical loads in fretting-corrosion of head neck interface.

7.4 FEA analysis of Mechanical responses of the head-neck interface

FEA was considered as the method to investigate mechanical responses of the head-neck interface to load components of walking activity; this was the most efficient way to investigate mechanical responses of an embedded interface, such as the head-neck interface of hip joint implant to external loads. The study aimed at the effect of the frictional moment on mechanical parameters that affect fretting, such as contact stress, micromotions, shear stress and the resulted fretting work.

Three different loading scenarios were considered from walking activities loads:

- Only applying the forces of walking in absence of any frictional moment (F only).
- Only applying the frictional moment of walking in absence of any forces (M only).
- Applying both the forces and moments of walking (F&M).

The initial press-fit, resulting from the surgeon's assembly, was modelled by applying an assembly force on the head-neck interface. The initial contact geometry was a proximal rim-in-contact, resulted from press-fit of the head to the neck taper in a proximal mismatched geometry.

The M only case didn't affect the initial contact geometry as after applying the moment only 0.27% of the initially non-contacting surface nodes temporarily came into contact and stress-field of the press-fitted area remained almost same as preloaded condition.

The activity forces in both of F only and F&M loading scenarios caused a significant change in the contact region of the head-neck interface. F only loading scenario caused a bending in the neck and made 8.43% of the initially non-contacting nodes of the head and the neck to become in touch. This magnitude was 9.57% for F&M loading scenario. Extending the contact area in presence of the contact forces caused a decrease in contact stress in the press-fitted rim.

Regarding the induced micromotion at the interface, magnitudes of micromotion for M only were by order of 10^2 smaller than F only and F&M loading cases. However, the frictional moment increased the micromotions of the F&M loading compared to the F only case;

especially on the distal side of the neck, presence of frictional moment increased the most distal micromotions from 31 to 38 µm.

To conclude, although the micromotion magnitudes for the M only case were negligible, by comparing the maximum values of micromotion for F only and F&M, it was found that the superposition of the frictional moments with the gait forces increased the micromotions along the neck length.

Shear stresses of F only and F&M cases in the temporary contacting area were found to be about the reported disruptive shear stress levels for oxide layers. This suggests that with each gait cycle during walking, the oxide layer could experience depassivation. This is aligned with the results of simplified *in vitro* experiments of fretting-corrosion at the head-neck interface which showed depassivation/repassivation at each cycle of loading-unloading (Panagiotidou, Meswania et al. 2015).

Regarding the fretting work, it was found that the M only loading resulted in negligible fretting work in comparison to F only and F&M. F only had similar fretting work profile to F&M but was more uniform. In the last three millimetres (13 mm - 16 mm) of the temporary extended contact area, the superposition of M and F in the F&M loading scenario almost doubled the maximum fretting work as compared to the F only loading case. Maximum magnitudes of fretting work were concentrated around the middle line of the superolateral sector, especially in the proximal press-fit rim. It is believed that this sector might be expected to experience a significant level of fretting wear and consequently, more material removal. This agrees with retrieval studies which have reported localised damage in superolateral surfaces and press-fit rims (Higgs, Hanzlik et al. 2013, Kurtz, Kocagöz et al. 2013).

Finite Element Analysis on mechanical interface of the hip joint implant showed that the force components had a significant influence on the stress distribution, micromotions and fretting work. Focussing more on the role of frictional moments in fretting-related characteristics at the interface, the results of this study indicate a negligible effect purely from the frictional moments. However, when the frictional moments are superposed with the forces, they intensify the mechanical response of the interface, especially with respect to fretting work. Compared to F only loading scenario, higher fretting work was observed in the F&M loading

scenario. These partial slips and fretting works can contribute in degradation of the material and its accumulative effect may significantly contribute in material loss.

From outcomes of this section it is concluded that, Finite Element studies which aim to study only the stress field of the contact interface can simplify the loading scenario to F only scenario. However, for Finite Element studies in which the damage and material loss of the interface is the target, contribution of the frictional moments in material loss should be considered.

7.5 *In vitro* study on fretting-corrosion damage of the head-neck interface

The most current *in vitro* study on contribution of frictional moments on fretting-corrosion of the head-neck interface (Panagiotidou, Meswania et al. 2015) has applied forces and moments increasing in a coupled and in phase manner, meaning that forces and frictional moments have the same unidirectional profile and are varying in phase. However, as discussed, frictional moment of daily activities at the head-neck interface has a profile independent of the contact forces; It is a bidirectional varying vector (with changes in direction) during one corresponding cycle of the unidirectional contact forces. Also, due to variation of the frictional condition and patients' weight, these two different vectors may have varying magnitudes. As discussed before any change in the load conditions from what they are in the service condition may cause change of the stress-field, micromotions, fretting and fretting-corrosion condition and need to be justified.

In this PhD research, by developing a custom testing system, interrelation of forces and frictional moments of walking activity in fretting-corrosion degradation of the head-neck interface was investigated. A range of frictional moment varying from 0Nm to 7.5Nm (raising in 1.25Nm steps) was combined by a range of forces from 900N to 1800N raising in 300N steps). Due to technical limitation of designing the testing system, forces represented with a vertical contact forces of walking activity as the lateral and transversal components of force where negligible compared to it. Also, the medio-lateral frictional moments which had the highest projection from induced frictional moments were applied on the samples.

Results demonstrated that increase in the vertical forces intensified fretting-corrosion significantly in load combination with all the frictional moments profile. Frictional moments

were more effective on fretting-corrosion damage when they were combined with lower vertical forces (for example walking force with maximum magnitude of 900N). In presence of higher vertical forces equal to 1800N, variation of moments from 0Nm to 7.5Nm had smaller effect on the OCP and fretting-corrosion response of the interface. General outcome suggests that increase of the forces had a more intensifying effect on fretting-corrosion while frictional moments are more effective on fretting-corrosion damage when is happening with lower contact forces.

Our study applied the frictional moments as an independent bidirectional vector as they happen during walking activity. The closest study on effect of frictional moments on fretting-corrosion of the head-neck interface is from Panagiotidou et al. (Panagiotidou, Meswania et al. 2015), which applied the frictional moments in unidirectional manner coupled to a unidirectional vertical force vector. Panagiotidou et al. (Panagiotidou, Meswania et al. 2015) reported that increase of the frictional moments increases the fretting-corrosion at the head-neck interface which is aligned with the outcomes of this PhD research. The added finding of this PhD research is that frictional moments has a more significant role when occur along with the lower vertical forces. Considering the accumulative effect of fretting-corrosion damage, although frictional moments were less effective when combined with higher vertical forces, they still may change the final damage occurring to the interface after high number of cycles. This suggest that in case of simplifying the fretting-corrosion tests to vertical forces only, higher forces than of the service condition should be applied to the implant to induce similar amount of damage to the interface. Based on the outcomes of this study, OCP of 1500N-7.5Nm loading case was near to of 1800N-0Nm loading case; hence a 20% increase of the load the level of fretting-corrosion of force only were comparable with force and moments case. Determining the required realistic increase was out of the scope of this research and needs to be investigated with high number of cycles and comparison of several samples selected during course of the experiment.

The outcome of this study also suggests that Ti6Al4V-CoCr head-neck combination was more susceptible than CoCr-CoCr material combination even in non-loaded condition before tests initiation. Higher susceptibility of Ti6Al4V-CoCr is believed to be due to lower hardness of Ti6Al4V as compared to CoCr. This leads to faster interruption of the passive oxide layer. Additionally, regarding the non-loaded OCP value combination, the combination of two

different materials (Ti6Al4V-CoCr) is more vulnerable for corrosion than the same material combination (CoCr-CoCr).

Chapter 8. Conclusions and Suggestions for Future Works

Conclusions: To study the effects of the interrelation of frictional moment and forces on fretting-corrosion of hip-joint implant, first, the frictional moments induced from the friction of head-cup interface were required.

A three-dimensional analytical approach was developed to determine the frictional moment vector generated by the relative sliding of the head-cup bearing a couple of a total hip replacement. The projection of the frictional moment onto the femoral neck was also determined over the loading cycle. Predicted frictional moments for nine combinations of bearing materials and diameters corresponded with the existing *in vitro* data. It concluded that for hard-on-hard bearing couples, especially metal-on-metal, considering a constant friction coefficient extracted from *in-vitro* tests under peak load, provides reliable anticipation of the frictional moment. This was not the case for hard-on-soft (metal-on-polyethylene) bearing materials. Using friction coefficient of peak load for hard-on-soft result in large differences due to complicated frictional behaviour of these materials. In the hard-on-soft bearing couples, an increase of contact force results decrease in the friction coefficient.

The analytical method was then applied to simplified gait (lubrication conditions of dry and serum), ISO standard gait and physiological level gait loading cycles. ISO standard gait had a total contact force that was twice the physiological level gait, and there was a corresponding increase in the maximum frictional torque on the neck from 0.66×BW%.m to 0.88×BW%.m. For the ISO standard gait, the maximum frictional torque occurred at the same instance of the maximum frictional moment and the maximum contact force. In contrast, for the physiological level gait, the frictional torque did not occur at the same instance as the peak load. This suggests that the neck frictional torque is a function of other parameters, such as the angle between the neck axis and frictional moment vector as well as the magnitude of the contact force and frictional moment. The developed methodology was able to predict the maximum magnitude and change of directions of moments and the variation of torque at the head-neck interface. From this part, it can be concluded that ISO standard conservatively induces higher forces and frictional moments on the head-neck taper junctions while simplifies three-dimensional out of phase nature of these loadings by unidirectional in-phase loads.

Frictional moment of different daily activities was studied to provide a better understanding of the variation of the frictional moments in the hip joint implant. Using the developed and validated analytical method, the frictional moments at the head-cup interface and frictional torques and bending moments acting on the head-neck interface of a modular total hip replacement across a range of activities of daily living were predicted. The predicted moment and torque profiles were based on the kinematics of four patients and implant characteristics of a metal-on-metal implant. Depending on the body weight and type of activity, the moments and torques had significant variations in both magnitude and direction over the activity cycles. For the nine investigated activities, the maximum magnitude of the frictional moment ranged from 2.6 to 7.1 Nm. The maximum magnitude of the torque acting on the head-neck interface ranged from 2.3Nm to 5.7Nm. The bending moment acting on the head-neck interface varied from 7Nm to 21.6 Nm. The activity of standing on one leg had the widest range of frictional torque on the head-neck interface (11Nm) while normal walking had the smallest range (6.1Nm). The widest range, together with the maximum magnitude of torque, bending moment and frictional moment, occurred when the lightest patient stood on one leg. Most of the simulated activities resulted in frictional torques that were near the previously reported oxide layer depassivation threshold torque. The predicted bending moments were also found at a level believed to contribute to the oxide layer depassivation. The calculated magnitudes and directions of the moments applied directly to the head-neck taper junction provided realistic mechanical loading data for *in vitro* and computational studies on the mechanical behaviour and multiaxial fretting at the head-neck interface. Frictional torques and the moment of normal walking was found to be in a range inclusive of most of the other activities. Considering that normal walking has the highest frequency among other daily activities, this activity's frictional forces and moments were found to be suitable loading profile for further investigation on fretting-corrosion of the head-neck interface. Comparing these results with of the ISO standard, it can be concluded that frictional moments and daily loads are very dynamic and three-dimensional. It can be suggested that for realistic testing arrangement, testing simulators and standards should be improved to impose loads equivalent to real-world conditions of the implants.

Considering the effect of mechanical loads on fretting phenomenon, mechanical responses of the head-neck interface to the loads applied to the interface were studied for a better

understanding of the degradation. Due to the enclosed geometry of the head-neck interface, Finite Element Analysis was found to be the best way to have a perspective of stress, strain and micromotion fields of the head-neck interface. Mechanical response of a modular head-neck interface of hip joint implants under realistic loads of level walking were investigated using a Finite Element model that was developed by another PhD student in the team. The realistic loads of the walking activity consisted of three-dimensional gait forces and the associated frictional moments. A previously reported geometry of a modular CoCr/CoCr head-neck interface with a proximal contact was used in this investigation. To study the level of contribution and also the effect of superposition of the load components, three different scenarios of loading were studied: gait forces only, frictional moments only and combined gait forces and frictional moments. Stress-field, micromotions, shear stresses and fretting work at the contacting nodes of the interface were analysed. Gait forces only were found to significantly influence the mechanical environment of the head-neck interface by temporarily extending the contacting area (8.43% of initially non-contacting surface nodes temporarily came into contact) and therefore, changed the stress-field and resulting micromotions during the gait cycle. The frictional moments only did not cause considerable changes in the mechanical response of the interface (only 0.27% of the non-contacting surface nodes temporarily came into contact). However, when superposed with the gait forces, the mechanical response of the interface, particularly micromotions and fretting work, changed significantly as compared to the case of forces only. The normal contact stresses and micromotions obtained from this realistic load-controlled study were typically in the range of 0-275 MPa and 0-38 µm, respectively. These ranges were found comparable to previous experimental displacement-controlled pin/cylinder-on-disk fretting-corrosion studies. From the results of the Finite Element Analysis, it can be found that superposition of the forces and moments in the head-neck interfaces can lead to complicated mechanical responses of the interface which can't be replicated with the simple unidirectional forces on the implant.

To investigate the contribution of forces and frictional moments in fretting-corrosion of head-neck interface, *in vitro* tests were conducted on the real scale head-neck interface in simulated service conditions. The simulated service condition comprised varying loads on the implant in the presence of Ringer's solution. Ringer's solutionrepresented the corrosive ambient of the body around the interface. Considering that loads of the level walking activity

were found to be inclusive of most of the other activities and also level walking has a significantly higher repeat frequency, load profiles of this activity were applied to the interface. To depict a better view of the interaction of the forces and frictional moments in inducing fretting-corrosion, a range of activity forces of 900 to 1800N (steps of 300N) were combined with a range of frictional moments of 0Nm to 7.5Nm (steps of 1.25Nm). Two different material combinations CoCr/CoCr and CoCr/Ti alloy of head-neck interface were examined to provide an insight into the effects of these material combinations. The results from Open Circuit Potential and post-test surface investigation of the interfaces suggested that CoCr/Ti alloy combination was more vulnerable to fretting-corrosion. Of the causes for this could be the higher vulnerability of different material combinations with higher electronegative difference; additionally, lower surface hardness of Ti alloy material made it more vulnerable to the fretting of its passive protective layer, followed by the corrosion of the active elements' underneath. In both material combinations, increase in the vertical forces significantly increased the intensity of the corrosion. Increase of the frictional moment in combination with lower applied activity loads (e.g. 900N) increased the corrosion at the interface while it had a smaller effect in combination with higher activity loads (e.g. 1800N).

Limitation of the current research: In analytical calculations of frictional moment assumption of a constant friction coefficient (extracted from under the peak load) is of the main limitation of the method. This assumption had a successful while conservatively on a higher margin calculation from the realistic moments of the metal-on-metal bearing couples. However, there wasn't a good agreement for hard-on-soft (metal-on-polyethylene) due to their complicated frictional behaviour (decrease of friction coefficient upon an increase in contact stress). Upon availability of a model for friction behaviour of material combination as a function of effective parameters (e.g. contact stress and relative velocity), the model should be improved to have a more realistic anticipation of the frictional moments.

Regarding Finite Element Analysis of the taper junction under daily activities, considering changes in the geometry and material composition after fretting-corrosion of the interface, the mechanical response of the interface would vary through the fretting-corrosion. Upon availability of material models and fretting wear models for FEA, anticipation from future of the taper junction in service condition can be well improved in early stages of the design and before even first prototyping.

Regarding the *in vitro* investigation of the fretting-corrosion, low number of specimens, low number of cycle of tests limited the results. Using more sophisticated test setups which can apply 3D forces and frictional moments simultaneously can reveal the nature of degradation of the head-neck taper junction more accurately. Also, it is suggested that the effect of stronger junctions (larger contact area due to longer and greater diameter of taper) to experimentally be investigated. This may provide a better vision on parameters which can be improved for.

Future Work Suggestions: Increase the intensity of fretting-corrosion because of increase in the forces and frictional moments applied to interface suggest that implementing the currently common biometals, such as CoCrMo and Ti6Al4V, in the modular interfaces wouldn't be the best practice considering the service condition. Biocompatibility of these biometals is owed to their passive layer which is reliable in interfaces with lower hardness, such as bone in femoral stem-bone interface and polyethylene in head cup interface; however, these passive layers can be easily disrupted in metal-on-metal interfaces and become a source of ions and debris emission and cause metallosis in the surrounding tissues. As a result, the researcher suggests future studies to implement functionally graded materials from current biometals of Ti alloy and CoCr to biocompatible, biodegradable and bioresorbable materials, such as Mg alloys at the modular interfaces of the implant. Upon achieving a viable solution, this implant could benefit from higher hardness and fretting resistance of the CoCr or Ti alloy when interfaced with polyethylene in head-cup interface and bone when interfaced with pelvic and femur and it will emit biodegradable and bioresorbable debris and ions of Mg alloys as opposed to the currently vulnerable metal-on-metal interface, such as modular head-neck interface. Alternatively, due to compromises in the current taper geometry strength due to smaller tapers length and taper diameter, studies can be conducted on improving the mechanical geometry of the taper junction to control the induced mechanical environment on the implant and increase the performance of the taper junction. Development and improvement of test protocols for interfaces in the implant with regard to fretting-corrosion performance is of the needs of the community.

Annex A, MATLAB code to calculate frictional moment

Analytical calculation of frictional moment:

```
clc
clear all
% Forces dimesion= (BW%)
Forcein = xlsread ('Hip98FjohnstonA.xls', 'A2:E202');
Rangles = xlsread ('Hip98FjohnstonA.xls ' , 'F2:H202' );
FEanglein = Rangles ( : ,  1 );
AAanglein = Rangles ( : ,  2 );
IERanglein = Rangles (: ,  3 );
ii= 100;
% LEFT HIP SIMULATIOM
 instance = (0 : 1/(ii) : 1);
FEangleout = interp1(Forcein( : ,1),FEanglein( : ,1),instance,'linear');
 AAangleout = interp1(Forcein( : ,1),AAanglein( : ,1),instance,'linear');
% left hip coordinate positive directions are X=medial,y=anterior,
% z=superior. so flexion, abduction and external rotation are positive and
% in input file internal rotation is positive so the IER angle will be
% timed to -1.
IERangleout = - interp1(Forcein( : ,1),IERanglein( : ,1),instance,'linear');
% Forceout(: ,1)= time instance
Forceout(: ,1)  = instance;
% Forceout(: ,2)= force in FE axis(medial)
Forceout(: ,2)  = interp1(Forcein( : ,1),Forcein( : ,2),instance,'linear');
% Forceout(: ,3)= force in AA axis (anterior)
Forceout(: ,3)  = interp1(Forcein( : ,1),Forcein( : ,3),instance,'linear');
```

```
% Forceout(: ,4)=force in IER axis (superior)

Forceout(: ,4)  = interp1(Forcein( : ,1),Forcein( : ,4),instance,'linear');

% Forceout(: ,5)= resultant force

Forceout(: ,5)  = interp1(Forcein( : ,1),Forcein( : ,5),instance,'linear');

% plot(FEangleout)

% hold on

% plot(AAangleout)

% plot(IERangleout)

% plot(Forceout)

%  DoN is direction of neck in left hip head coordinate x= medial

%  y=anterior z=superior

DoN=[cosd(12);sind(12);cosd(35)];

DoN=DoN/norm(DoN);

% finding the head coordinate direction according to cup coordinate neutral

% position x= medial(FER), y =anterior(AAR) z= superior(IER) for this coordinate


for i = 1:ii+1

   FER = (pi/180).* FEangleout(1 , i);

   AAR = (pi/180).* AAangleout(1 , i);

   IER = (pi/180).* IERangleout(1 , i);

% RotationMC0Ci rotate cup to ith position of head

   RotationMc0Ci = [ cos(AAR)*cos(IER), -cos(AAR)*sin(IER), sin(AAR);

 cos(FER)*sin(IER)  +  cos(IER)*sin(FER)*sin(AAR),  cos(FER)*cos(IER)  -
sin(FER)*sin(AAR)*sin(IER), -cos(AAR)*sin(FER);

 sin(FER)*sin(IER)  -  cos(FER)*cos(IER)*sin(AAR),  cos(IER)*sin(FER)  +
cos(FER)*sin(AAR)*sin(IER), cos(FER)*cos(AAR)];

% CoordDirs(1:3,i)= x direction of rotated hip( coordinate in cup coordinate
```

```
% CoordDirs(4:6,i)= y direction of rotated hip coordinate in cup coordinate
% CoordDirs(7:9,i)= z direction of rotated hip coordinate in cup coordinate


CoordDirs(1:3,i)=RotationMc0Ci (1:3,1);
CoordDirs(4:6,i)=RotationMc0Ci (1:3,2);
CoordDirs(7:9,i)=RotationMc0Ci (1:3,3);
% CoordDirs(10:12,i) is rotated direction of neck
CoordDirs(10:12,i)=RotationMc0Ci*DoN;
% quiver3(0,0,0,(CoordDirs(1,i)),(CoordDirs(2,i)),(CoordDirs(3,i)))
% quiver3(0,0,0,(CoordDirs(4,i)),(CoordDirs(5,i)),(CoordDirs(6,i)))
% quiver3(0,0,0,(CoordDirs(7,i)),(CoordDirs(8,i)),(CoordDirs(9,i)))
% hold on
end



V1=zeros(3,ii);
for i = 1:ii
  X1= CoordDirs(1:3,i);
  Y1= CoordDirs(4:6,i);
  Z1= CoordDirs(7:9,i);
  X2= CoordDirs(1:3,i+1);
  Y2= CoordDirs(4:6,i+1);
  Z2= CoordDirs(7:9,i+1);
%   RmCiCiplus1=[X1(1,1) X1(2,1) X1(3,1);
%       Y1(1,1) Y1(2,1) Y1(3,1);
%       Z1(1,1) Z1(2,1) Z1(3,1)]
```

```
%    RmCiCiplus1= rotaion matrice from Ci to Ci+1
% V1 is rotation vector of coord i+1 from coord i
% det(RmCiCiplus1);
i
RmCiCiplus1=[dot(X2,X1) dot(Y2,X1) dot(Z2, X1);...
dot(X2,Y1) dot(Y2,Y1) dot(Z2, Y1);...
dot(X2,Z1) dot(Y2,Z1) dot(Z2, Z1)];
[A B] = eig(RmCiCiplus1);



Realeigvalue = find(imag(diag(B))==0);
V1(:, i)= A(:, Realeigvalue );
rotangle=asin((dot(X1,Z2)- (V1(3, i)/ V1(2, i))*dot(Y2,X1))/(V1(3,i)^2/V1(2,i)+V1(2,i)));
V1(:, i)=sign(rotangle)* V1(:, i)


end
% % to draw plot of xi xi+1 and rotation vector V1 will be transformed to C0
% % cord as other cord are determined in C0
Estar=200e3;
RHertz=(2/46.437-2/46.601)^-1;
R=46/2;
T=zeros(3);
 for i= 1:ii
Zprime=[Forceout(i ,2);Forceout(i ,3);Forceout(i ,4)];
Zprime=Zprime/norm(Zprime);
Xprime=cross(Zprime,[1;0;0]);
```

```
Xprime=Xprime/norm(Xprime);
Yprime=cross(Zprime,Xprime);
% T is the matrice wich project each component of a vector from first cord
% on a direction of second cord. A(x)* cos(x,xprime)+ A(y)*cos(y.xprime)+
% A(z)*cos(z,xprime= A(xprime)
T= [Xprime'; Yprime'; Zprime'];
V2=T*V1(:,i);
DoNi=T*DoN;

% Force=mean(Forceout(i:i+1 ,5));
Force=(Forceout(i ,5));
a=(3.*Force.*RHertz./(4.*Estar)).^(1/3);
P0=3.*Force./(2.*pi.*a.^2);
P=@(teta) P0.*sqrt((1-(R.*sin(teta)./a).^2));
D=@(teta,phi) R.*sqrt((sin(teta).*sin(phi).*V2(3,1)-cos(teta).*V2(2,1)).^2+...
    (cos(teta).*V2(1,1)-sin(teta).*cos(phi).*V2(3,1)).^2+...
    (sin(teta).*cos(phi).*V2(2,1)-sin(teta).*sin(phi).*V2(1,1)).^2);
da=@(teta) R.^2.*sin(teta);
tetamax= asin(a/R);

fun=@(teta,phi)R.^2.*P0 .*R...
   .*0.16.*sqrt((1-(R.*sin(teta)./a).^2))...
  .*sqrt((sin(teta).*sin(phi).*V2(3,1)-cos(teta).*V2(2,1)).^2+...
    (cos(teta).*V2(1,1)-sin(teta).*cos(phi).*V2(3,1)).^2+...
    (sin(teta).*cos(phi).*V2(2,1)-sin(teta).*sin(phi).*V2(1,1)).^2)...
    .*sin(teta);
```

```
I(i,:)=integral2(fun,0, tetamax, 0 , 2.*pi);

MV2(:,i)=I(i,:).*V2;

MDoNi(:,i)=dot(MV2(:,i),DoNi);

portion(i,:)=dot(V1(:,i),DoN);

MV1(:,i)=I(i,:).*V1(:,i);

end

plot(1:i,I)


hold on

plot(1:i,-MV1)


plot(1:i,-MDoNi(1,1:i))
```

Calculation of frictional moment for different activities

```
 clc;

clear all;

close all;

%% Forces dimesion=  1: Cycle%, 2: -Fx[%BW], 3:-Fy[%BW], 4: -Fz[%BW],

% 5:Fr[%BW], 6: Flexion[deg], 7:Abduction[deg]

% pages : 1:slow walking, 2:normal walking, 3: fast walking, 4: stair up,

% 5: stair down,6:standing up, 7: sitting down, 8: standing, 9: knee H

% heavy L light

% bending

Forceangle=zeros(201,7,9);


for i = 1:27;

Forceangle(:,:,i) = xlsread ('orthoload data.xlsx', i , 'A3:G203');
```

```
end


%% LEFT HIP SIMULATION


ii=200;
DoN=[cosd(9.75);sind(9.75);cosd(45)];
DoN=DoN/norm(DoN);
% difining cord neck: zprime in distal to proximal of neck. yprime: cross
% of z prime and z which will be in postro anterior direction of neck,  x
% prime cross (yprime and z prime)fwei
zn = DoN;
yn = cross(zn, [0,0,1]');
yn = yn/norm(yn);
xn = cross(yn,zn);



%% transfer matrix from head cord to neck cord Thton: Mn= Thton*Mh
Thton=[dot([1;0;0],xn) dot([0;1;0],xn) dot([0;0;1], xn);...
   dot([1;0;0],yn) dot([0;1;0],yn) dot([0;0;1], yn);...
   dot([1;0;0],zn) dot([0;1;0],zn) dot([0;0;1], zn)];


%% finding the head coordinate direction according to cup coordinate nuteral
% position x= medial(FER), y =anterior(AAR) z= superior(IER) for this coordinate



for j = 1:27;
```

```
   for i = 1:ii+1;
      FER = (pi/180).* Forceangle(i , 6, j);
      AAR = (pi/180).* Forceangle(i , 7, j);
      IER = 0;
% RotationMC0Ci rotate cup to ith position of head
   RotationMc0Ci = [ cos(AAR)*cos(IER), -cos(AAR)*sin(IER), sin(AAR);
 cos(FER)*sin(IER) + cos(IER)*sin(FER)*sin(AAR), cos(FER)*cos(IER) -
sin(FER)*sin(AAR)*sin(IER), -cos(AAR)*sin(FER);
 sin(FER)*sin(IER) - cos(FER)*cos(IER)*sin(AAR), cos(IER)*sin(FER) +
cos(FER)*sin(AAR)*sin(IER), cos(FER)*cos(AAR)];
% CoordDirs(1:3,i)= x direction of rotated hip( coordinate in cup coordinate
% CoordDirs(4:6,i)= y direction of rotated hip coordinate in cup coordinate
% CoordDirs(7:9,i)= z direction of rotated hip coordinate in cup coordinate

CoordDirs(1:3,i,j)=RotationMc0Ci (1:3,1);
CoordDirs(4:6,i,j)=RotationMc0Ci (1:3,2);
CoordDirs(7:9,i,j)=RotationMc0Ci (1:3,3);
% CoordDirs(10:12,i) is rotated direction of neck
CoordDirs(10:12,i,j)=RotationMc0Ci*DoN;
   end
end

V1=zeros(3,ii,27);
rotangle=zeros(27,ii);
for j = 1:27;
   for i = 1:ii;
```

```
   X1= CoordDirs(1:3,i,j);

   Y1= CoordDirs(4:6,i,j);

   Z1= CoordDirs(7:9,i,j);

   X2= CoordDirs(1:3,i+1,j);

   Y2= CoordDirs(4:6,i+1,j);

   Z2= CoordDirs(7:9,i+1,j);

    RmCiCiplus1=[dot(X2,X1) dot(Y2,X1) dot(Z2, X1);...

    dot(X2,Y1) dot(Y2,Y1) dot(Z2, Y1);...

    dot(X2,Z1) dot(Y2,Z1) dot(Z2, Z1)];

    [A B] = eig(RmCiCiplus1);


    Realeigvalue = find(imag(diag(B))==0);

    V1(:, i,j)= A(:, Realeigvalue );

    rotangle(j,ii)=asin((dot(X1,Z2)- (V1(3, i,j)/ V1(2,
i,j))*dot(Y2,X1))/(V1(3,i,j)^2/V1(2,i,j)+V1(2,i,j)));

    V1(:, i,j)=sign(rotangle(j,ii))* V1(:, i,j);

    end

end



Estar=200e3;

RHertz=(2/46.437-2/46.601)^-1;

R=46/2;

T=zeros(3);


for j = 1:27;

    for i = 1:ii;
```

```
Zprime=[Forceangle(i ,2,j);Forceangle(i ,3,j);Forceangle(i ,4,j)];
Zprime=Zprime/norm(Zprime);
Xprime=cross(Zprime,[1;0;0]);
Xprime=Xprime/norm(Xprime);
Yprime=cross(Zprime,Xprime);
% T is the matrice which project each component of a vector from first cord
% on a axis of the second cord. A(x)* cos(x,xprime)+ A(y)*cos(y.xprime)+
% A(z)*cos(z,xprime= A(xprime)
T= [Xprime'; Yprime'; Zprime'];
V2=T*V1(:,i,j);
DoNi=T*DoN;

% Force=mean(Forceout(i:i+1 ,5));
Force=(Forceangle(i ,5,j));
a=(3.*Force.*RHertz./(4.*Estar)).^(1/3);
P0=3.*Force./(2.*pi.*a.^2);
P=@(teta) P0.*sqrt((1-(R.*sin(teta)./a).^2));
D=@(teta,phi) R.*sqrt((sin(teta).*sin(phi).*V2(3,1)-cos(teta).*V2(2,1)).^2+...
 (cos(teta).*V2(1,1)-sin(teta).*cos(phi).*V2(3,1)).^2+...
 (sin(teta).*cos(phi).*V2(2,1)-sin(teta).*sin(phi).*V2(1,1)).^2);
da=@(teta) R.^2.*sin(teta);
tetamax= asin(a/R);

fun=@(teta,phi)R.^2.*P0 .*R...
.*0.12.*sqrt((1-(R.*sin(teta)./a).^2))...
.*sqrt((sin(teta).*sin(phi).*V2(3,1)-cos(teta).*V2(2,1)).^2+...
```

```
    (cos(teta).*V2(1,1)-sin(teta).*cos(phi).*V2(3,1)).^2+...
    (sin(teta).*cos(phi).*V2(2,1)-sin(teta).*sin(phi).*V2(1,1)).^2)...
    .*sin(teta);
   I(i,j,:)=0.001*integral2(fun,0, tetamax, 0 , 2.*pi);
   Mfrictioncordi(:,i,j)=I(i,j,:)*V1(:,i,j);
%    Mforcecordi(:,i,j)=0.07.*cross(DoN,Forceangle(i,2:4,j));
   % cord neck: yprime in direction of y in anterior direction, zprime in
   % distal proximal direction of neck, xprime in cross of yprime and zprime
   % the CCD is 135 degree so the angle between z and zprime is 45 degree
   Mtotalcordneck(:,i,j)=Thton*Mfrictioncordi(:,i,j);
   Vcoordneck(:,i,j)=Thton*V1(:,i,j);
  end
  end
fignames=cellstr(['(a) slow walking  '; '(b) medium walking'; '(c) fast walking  '; '(d) stair up
';...
   '(e) stair down    ';'(f) sit-to-stand  '; '(g) stand-to-sit  '; '(h) standing      '; '(i) knee bending
']);


strings = char(fignames);



%% weight (average of activities, high, low)
Weight=[847,836,847,836,847,836,836,920,847,980,980,980,980,980,980,980,...
   980,980,702,702,702,702,702,702,702,702,702];


%% maximum of L/H ratio
% Rmn (1,:)= abs value ratio, Rmn(2,:)=min ratio,
```

```
% Rmn(3,:)=max(max(H,L,ave)),Rmn(4,:)=min(min(H,L,ave)),Rmn(5,:)=range;Rmn(6:8,:)

% slope @ moment of the change of direction for largest range Nm/s

% zint=zero intersecting component of average patient(1:200)

zint=[102,102,100,106,181,70,103,1,92];

Acttime=[1.24 , 1.1 , 0.95 , 1.59 , 1.44 , 2.489 , 3.72 , 6.7 , 4.7 ];

clear Rmnmax

for i=1:9

Rmn(1,i)=max(abs((Weight(i+18)*Mtotalcordneck(3,:,i+18)/100)))/max(abs((Weight(i+9)*Mt
otalcordneck(3,:,i+9)/100)));

Rmn(2,i)=(min(Weight(i+18)*Mtotalcordneck(3,:,i+18)/100))/(min(Weight(i+9)*Mtotalcordn
eck(3,:,i+9)/100));

ma=[max(Weight(i+18)*Mtotalcordneck(3,:,i+18)/100),max(Weight(i+9)*Mtotalcordneck(3,:
,i+9)/100),...

        max(Weight(i)*Mtotalcordneck(3,:,i)/100)];

mi=[min(Weight(i+18)*Mtotalcordneck(3,:,i+18)/100),min(Weight(i+9)*Mtotalcordneck(3,:,i
+9)/100),...

        min(Weight(i)*Mtotalcordneck(3,:,i)/100)];

Rmn(3,i)=max(ma);

Rmn(4,i)=min(mi);

Rmn(5,i)=max(ma)-min(mi);

Rmn(6,i)=Weight(i)*Mtotalcordneck(3,zint(i),i);

Rmn(7,i)=Weight(i)*Mtotalcordneck(3,zint(i)+1,i);

Rmn(8,i)=(Rmn(7,i)-Rmn(6,i))/0.5*Acttime(i);

end



%% resulttable columns1:27=        Activity 1:9

%                       L patient, H patient, Average
```

```
% row 1:8
% 1 MaxMf; 2 MaxMn; 3 MaxF; 4 TMaxMf; 5 TMaxMn; 6 TMaxF; 7 Dir of maxMf;
% 8% #change of directions;
%
% i= activity counter j=patient counter
resulttable=zeros(11,27);
for i=0:8;
   for j=1:3;
%       a=3*i+j
%       b=28-9*j+i
    d=find(I(:,28-9*j+i)==max(I(:,28-9*j+i)));

    resulttable(1,3*i+j)=Weight(:,28-9*j+i)*0.01*max(I(:,28-9*j+i));
    resulttable(4,3*i+j)=d/2;
    resulttable(7:9,3*i+j)=V1(1:3,d,28-9*j+i);
%     find the index of maximum  and using it

    d=find(abs(Mtotalcordneck(3,:,28-9*j+i))==...
       max(abs(Mtotalcordneck(3,:,28-9*j+i))));

    resulttable(2,3*i+j)=Weight(:,28-9*j+i)*0.01*abs(Mtotalcordneck(3,d,28-9*j+i));
    resulttable(5,3*i+j)=d/2;

    d=find(abs(Forceangle(:,5,28-9*j+i))==...
       max(abs(Forceangle(:,5,28-9*j+i))));
```

```
      resulttable(3,3*i+j)=Weight(:,28-9*j+i)*0.01*Forceangle(d,5,28-9*j+i);
      resulttable(6,3*i+j)=d/2;
      h=0
      for k=1:199;
       if Mtotalcordneck(3,k,28-9*j+i)*Mtotalcordneck(3,k+1,28-9*j+i)<=0
        h=h+1;
        end
      end
     resulttable(10,3*i+j)=h;
    end
end

%% MnComponents of X of all activities as fig1 y as fig2 z as fig3
linewidthnumber = 2;
legendfontsize = 20;
labelfontsize = 20;
axisfontsize = 20;
titlefontsize=20;
Yname=cellstr(['Mf(x) in neck coordinate (Nm)';...
   'Mf(y) in neck coordinate (Nm)';...
   'Mf(z) in neck coordinate (Nm)']);
for i= 1:3;
   figure (i);
   plot (1:2:100, 847 * Mtotalcordneck(i,1:4:200,2)/100 ,'k-.d',...
        1:2:100, 847 * Mtotalcordneck(i,1:4:200,4)/100 ,'r-.*', ...
        1:2:100, 847 * Mtotalcordneck(i,1:4:200,5)/100 ,'b--',...
```

```
        1:2:100, 847 * Mtotalcordneck(i,1:4:200,6)/100 ,'k-',...
        1:2:100, 847 * Mtotalcordneck(i,1:4:200,7)/100 ,'r:',...
        1:2:100, 847 * Mtotalcordneck(i,1:4:200,9)/100 ,'b-.o',...
          'LineWidth',linewidthnumber,'MarkerSize',8);


%    tit= strcat(fignames(i));
%    , ' Mf & Mn neck coordinate');
 set(gca, 'FontSize', axisfontsize);


   ax = gca;
   ax.XGrid = 'off';
   ax.YGrid = 'on';
   %create output file
   ylim ([-6 6])
   set(gca,'XTick', 0:25:100);
   set(gca,'YTick', -5:1:5);
   set(xlabel('activity cycle %'),'FontSize', labelfontsize);
   set(ylabel(Yname(i)) , 'FontSize', labelfontsize);
   legend ('normal walking ','stair up ','stair down ','sit-to-stand ', 'stand-to-sit','knee
bending');
   print( '-dtiff', '-r300',num2str(i));
end
% close all
%    set(legend ('Mf Average ','Mf H patient ','Mf L patient ',...
%             'Mn Average ','Mn H patient ','Mn L patient '),...
%              'FontSize', legendfontsize);
%    set(title(tit),'FontSize', titlefontsize);
```

```
%     set(gca, 'FontSize', axisfontsize);
%     refline(0, 3.92+.97);
%     refline(0, -3.92-.97);
%     refline(0, 7.23+.55);
%     refline(0, -7.23-.55);
% % %     adding smaller threshold and greater threshold to plot
% %     text( 75 , 3.6+.97,'L.T ','FontSize', 20,'Color', [1 .5 0])
% %     text( 75 , -3.6-.97,'L.T ','FontSize', 20,'Color', [1 .5 0])
% %     text( 75 , 7.3+.55,'U.T ','FontSize', 20,'Color','r')
% %     text( 75 , -7.3-.55,'U.T ','FontSize', 20,'Color','r')
%
%      text( 75 , 3.6+.5,'L.T ','FontSize', 20,'Color', [1 .5 0])
%     text( 75 , -3.6-.5,'L.T ','FontSize', 20,'Color', [1 .5 0])
%     text( 75 , 7,'U.T ','FontSize', 20,'Color','r')
%     text( 75 , -7,'U.T ','FontSize', 20,'Color','r')
%      print( '-dtiff', '-r300',num2str(7));
%
%      print( '-dtiff', '-r300',num2str(1000*i));


%% figure of force and angle for L patient H patient average
% y1=zeros(201,9);
% y2=zeros(201,6);
% for i= 1:9;
%     y1(:,1:3)=Forceangle(:,2:4,i);
%     y1(:,4:6)=Forceangle(:,2:4,i+9);
%     y1(:,7:9)=Forceangle(:,2:4,i+18);
```

```
%     y2(:,1:2)=Forceangle(:,6:7,i);
%     y2(:,3:4)=Forceangle(:,6:7,i+9);
%     y2(:,5:6)=Forceangle(:,6:7,i+18);
%
%     figure (i);
%     [ax,p1,p2]=plotyy ( 0:0.5:100 , y1(:,1:9), 0:0.5:100,y2(:,1:6));
%     print( '-dtiff', '-r300',num2str(10000*i))
% end
%
linewidthnumber = 2;
legendfontsize = 20;
labelfontsize = 20;
axisfontsize = 20;
titlefontsize=20;
% for i= 1:9;
% %  set(gcf,'Units','inches','Position',[2 2 10 7])
%     figure (100*i);
%     [ax,p1,p2]=plotyy (0:0.5:100, 8.47*Forceangle(:,2:4,i),0:4:100,...
%         Forceangle(1:8:201,6:7,i),'plot','plot');
%     tit= strcat(fignames(i));
% set(ax(1),'Position', [0.13+0.05 0.11+0.05 0.775-0.1 0.815-0.1]);
% set(ax(2),'Position', [0.13+0.05 0.11+0.05 0.775-.1 0.815-0.1]);
%
%     lmarker={'o','d'};
%
% for idx=1:3;
```

```
%     set(p1(idx),'LineWidth',2);
%     set(p1(idx),'linestyle',lstyle{idx});
%     set(p1(idx),'Color',lcolor{1});
% end
% for idx=1:2;
%     set(p2(idx),'LineWidth',2);
%     set(p2(idx),'linestyle',lstyle{idx});
%     set(p2(idx),'Color',lcolor{2});
%     set(p2(idx),'Marker',lmarker{idx});
% end
%
%     title(tit);
%
%     xlabel(ax(1),'activity cycle %');
%     ylabel(ax(1),'Contact force (N)');
%     set(ylabel(ax(2),'Angle (degree)'));
%     set(gca, 'FontSize', 20);
%     set(ax(2),'FontSize',20);
%     set(ax(1),'box','off')
%     set(ax(1),'XTick', 0:25:100);
%     set(ax(1),'YTick', -1000:1000:2500);
%     set (ax(1),'Ylim',[-1000 2500]);
%     set (ax(2),'Ylim',[-10 65]);
%     set(ax(2),'YTick',[-10:10:65]);
%      tit= strcat(fignames(i), ' neck coordinate');
%     %create output file
```

```
% %     legend ('Fx ','Fy ','Fz ','Flexion ', 'Abduction');
%  legend ('Px ','Py ','Pz ','Flexion ', 'Abduction');
% %      print( '-dtiff', '-r300',num2str(100*i));
%
% end


%% Mn for L patient H patient Average
FEMinp(:,1)=(0:0.005:.995)';
for i=2:10
FEMinp(:,i)=( Weight(i-1) *Mtotalcordneck(3,:,i-1)/100);


end
xlswrite('FEaxsyMnsim.xlsx',FEMinp);


%% Forces dimesion=  1: Cycle%, 2: -Fx[%BW], 3:-Fy[%BW], 4: -Fz[%BW],
% 5:Fr[%BW], 6: Flexion[deg], 7:Abduction[deg]
% pages : 1:slow walking, 2:normal walking, 3: fast walking, 4: stair up,
% 5: stair down,6:standing up, 7: sitting down, 8: standing, 9: knee H
% heavy L light
% bending
% Forceangle=zeros(201,7,9);
clear ZZZ;


 ZZZ(:,1)= (847 * Forceangle(1:200,4,2)/100);
 ZZZ(:,3)= (847 * Forceangle(1:200,4,4)/100);
 ZZZ(:,5)= (847 * Forceangle(1:200,4,5)/100);
```

```
ZZZ(:,7)= (847 * Forceangle(1:200,4,6)/100);

ZZZ(:,9)= (847 * Forceangle(1:200,4,7)/100);


ZZZ(:,2)= (sqrt((847 * Mtotalcordneck(2,1:200,2)/100).^2+(847 *
Mtotalcordneck(3,1:200,2)/100).^2))'

ZZZ(:,4)= (sqrt((847 * Mtotalcordneck(2,1:200,4)/100).^2+(847 *
Mtotalcordneck(3,1:200,4)/100).^2))'

ZZZ(:,6)= (sqrt((847 * Mtotalcordneck(2,1:200,5)/100).^2+(847 *
Mtotalcordneck(3,1:200,5)/100).^2))'

ZZZ(:,8)= (sqrt((847 * Mtotalcordneck(2,1:200,6)/100).^2+(847 *
Mtotalcordneck(3,1:200,6)/100).^2))'

ZZZ(:,10)= (sqrt((847 * Mtotalcordneck(2,1:200,7)/100).^2+(847 *
Mtotalcordneck(3,1:200,7)/100).^2))'


xlswrite('Experimentsinput.xlsx',ZZZ);


% for i= 1:9;
%
%    figure (10*i);
%    plot (0.5:0.5:100, Weight(i) *Mtotalcordneck(3,:,i)/100 ,'k-', ...
%        0.5:0.5:100, Weight(i+9)*Mtotalcordneck(3,:,i+9)/100,'k-.',...
%        0.5:0.5:100, Weight(i+18)*Mtotalcordneck(3,:,i+18)/100,'k--',...
%        'LineWidth',linewidthnumber);
%
%    tit= strcat(fignames(i), ' Mn neck coordinate');
%
%    title(tit);
%
```

```
%    ax = gca;
%    ax.XGrid = 'off';
%    ax.YGrid = 'on';
%    %create output file
%    ylim ([-8 10])
%    set(gca,'XTick', 0:25:100);
%    set(gca,'YTick', -8:4:8);
%    set(xlabel('activity cycle %'),'FontSize', labelfontsize);
%    set(ylabel('Nm') , 'FontSize', labelfontsize);
%    set(legend ('Mn Average ','Mn H patient ','Mn L patient '),...
%                'FontSize', legendfontsize);
%    set(title(tit),'FontSize', titlefontsize);
%   set(gca, 'FontSize', axisfontsize);
% print( '-dtiff', '-r300',num2str(10*i));
%
% end
 % Mf for L patient H patient Average
% for i= 1:9;
%
%    figure (100*i);
%    plot (1:4:100, Weight(i) *I(1:8:200,i)/100 ,'k-o', ...
%          1:4:100, Weight(i+9)*I(1:8:200,i+9)/100,'k--o',...
%          1:4:100, Weight(i+18)*I(1:8:200,i+18)/100,'k:o',...
%         'LineWidth',linewidthnumber);
%
%    tit= strcat(fignames(i), ' Mf neck coordinate');
```

```
%   set(gca, 'FontSize', 12);
%
%    ax = gca;
%    ax.XGrid = 'off';
%    ax.YGrid = 'on';
%    %create output file
%    ylim ([-8 10])
%    set(gca,'XTick', 0:25:100);
%    set(gca,'YTick', -8:4:8);
%    set(xlabel('activity cycle %'),'FontSize', labelfontsize);
%    set(ylabel('Nm') , 'FontSize', labelfontsize);
%    set(legend ('Mf Average ','Mf H patient ','Mf L patient '),...
%                'FontSize', legendfontsize);
%
%    set(title(tit),'FontSize', titlefontsize);
%    set(gca, 'FontSize', axisfontsize);
%     print( '-dtiff', '-r300',num2str(100*i));
%
% end
%% Mf and Mn together
% for i= 1:9;
%    figure (1000*i);
%    plot (1:4:100, Weight(i) *I(1:8:200,i)/100 ,'r-o', ...
%          1:4:100, Weight(i+9)*I(1:8:200,i+9)/100,'r--d',...
%          1:4:100, Weight(i+18)*I(1:8:200,i+18)/100,'r:*',...
%          0.5:0.5:100, Weight(i) *Mtotalcordneck(3,:,i)/100 ,'k-', ...
```

```
%         0.5:0.5:100, Weight(i+9)*Mtotalcordneck(3,:,i+9)/100,'k--',...
%         0.5:0.5:100, Weight(i+18)*Mtotalcordneck(3,:,i+18)/100,'k:',...
%         'LineWidth',linewidthnumber,'MarkerSize',8);
%
%    tit= strcat(fignames(i));
% %     , ' Mf & Mn neck coordinate');
%   set(gca, 'FontSize', 12);
%
%    ax = gca;
%    ax.XGrid = 'off';
%    ax.YGrid = 'on';
%    %create output file
%    ylim ([-8 10])
%    set(gca,'XTick', 0:25:100);
%    set(gca,'YTick', -8:4:8);
%    set(xlabel('activity cycle %'),'FontSize', labelfontsize);
%    set(ylabel('Nm') , 'FontSize', labelfontsize);
% %     set(legend ('Mf Average ','Mf H patient ','Mf L patient ',...
% %                 'Mn Average ','Mn H patient ','Mn L patient '),...
% %                  'FontSize', legendfontsize);
%    set(title(tit),'FontSize', titlefontsize);
%    set(gca, 'FontSize', axisfontsize);
%    refline(0, 3.92+.97);
%    refline(0, -3.92-.97);
%    refline(0, 7.23+.55);
%    refline(0, -7.23-.55);
```

```
% % %     adding smaller threshold and greater threshold to plot
% %     text( 75 , 3.6+.97,'L.T ','FontSize', 20,'Color', [1 .5 0])
% %     text( 75 , -3.6-.97,'L.T ','FontSize', 20,'Color', [1 .5 0])
% %     text( 75 , 7.3+.55,'U.T ','FontSize', 20,'Color','r')
% %     text( 75 , -7.3-.55,'U.T ','FontSize', 20,'Color','r')
%
%      text( 75 , 3.6+.5,'L.T ','FontSize', 20,'Color', [1 .5 0])
%     text( 75 , -3.6-.5,'L.T ','FontSize', 20,'Color', [1 .5 0])
%     text( 75 , 7,'U.T ','FontSize', 20,'Color','r')
%     text( 75 , -7,'U.T ','FontSize', 20,'Color','r')
%      print( '-dtiff', '-r300',num2str(7));
%
%      print( '-dtiff', '-r300',num2str(1000*i));
%
% end
```

Finite Element Analysis data interpretation code

```
% Polishedsurfval 1)node ID,2)  Cpress,3)   cshear1,4)  cshear2,5)  mises,...
% 6)s11,7) s22,8)   s33,9)  s12,10) s13,11) s23,12) x abaqus,
% 13)   y abaqus ,14)   z abaqus,
% 15)u1, 16)u2, 17)u3,18)THETA,19)RHO,20)Z
clear all
clc


a=xlsread('nechsurfacenodes.xlsx');
a=a(:);
Polishedsurfval=zeros(1,length(a),20); %make it (4,length(a),20) when had all the activities;
```

```
% Mediumwalkingvalues=zeros(4,96485,17);
for i=1:1 %i is number of the simulation
   Mediumwalkingvalues(1,:,:)=xlsread('Mediumwalkingvalues.xlsx',i);
end
for j=1:1  %j is number of the simulation
   for i= 1:length(a);
      t= find(Mediumwalkingvalues(j,:,1)==a(i));
      %h=length(t);
      %if h==0; %active this part for incompleted inplut files
      %Polishedsurfval(i,:)=zeros(1,20);
      %else
      Polishedsurfval(j,i,1:17)=Mediumwalkingvalues(j,t,:);
      [x,y,z]=cart2pol(Polishedsurfval(j,i,12),Polishedsurfval(j,i,14),Polishedsurfval(j,i,13));
      Polishedsurfval(j,i,18:20)=[x,y,z];
       i
   end
  j
end
b=zeros(1,length(a),16); %make it (4,length(a),16) when had all the activities
b(1,:,1)=Polishedsurfval(1,:,20);% bringing z to the  column 1
b(1,:,2)=Polishedsurfval(1,:,18);% bringing theta to  column 2
%b 1)z 2)theta 3)Cpress,4)cshear1,5)cshear2,6) mises,...
% 7)s11,8)s22,9)s33,10)s12,11)s13,12)s23 13) sqrt(CSHEAR1^2+CSHEAR2^2)
% 14)nu 15)relative displacement (u2) 16)node ID
b(1,:,3:12)=Polishedsurfval(1,:,2:11);
b(1,:,13)=sqrt((Polishedsurfval(1,:,3).^2+Polishedsurfval(1,:,4).^2));
```

```
b(1,:,14)=b(1,:,13)./b(1,:,3);

%
b(1,:,15)=sqrt(Polishedsurfval(1,:,15).^2+Polishedsurfval(1,:,16).^2+Polishedsurfval(1,:,17).^
2);

b(1,:,15)=Polishedsurfval(1,:,17);

b(1,:,16)=Polishedsurfval(1,:,1);

% find the moving nodes

nu=0.3;

tt=find(b(1,:,14)>=nu);%tt=node row number with friction factor greater than nu


b(1,tt(1:length(tt)),16)

b(1,tt(1:length(tt)),4)

b(1,tt(1:length(tt)),5)

b(1,tt(1:length(tt)),13)

ww=find(b(:,:,2)>=pi/2)%moving the nodes over pi/2 to range of -3pi/2- -pi

for ii=1:length(ww)

  b(:,ww(ii),2)=b(:,ww(ii),2)-2*pi;

  ii

end

b(:,:,2)=b(:,:,2)+1.5*pi;


%% plots


% d(activity,

% parameter[1)z 2)theta 3)Cpress,4)cshear1,5)cshear2,6) mises,...

% 7)s11,8)s22,9)s33,10)s12,11)s13,12)s23 13) sqrt(CSHEAR1^2+CSHEAR2^2)

% 14)nu 15)relative disp 16) node ID
```

```
% ,layer,
% agular section)


d=zeros(1,16,201,480);
for k=1:1
   c=sortrows(squeeze(b(k,:,:)));
   for j=1:16
      for i=1:201
         d(k,j,i,1:480)=c((i-1)*480+1:i*480,j)';
      end
   end
end


linewidthnumber = 2;
legendfontsize = 20;
labelfontsize = 20;
axisfontsize = 20;
titlefontsize=20;
figure (10)
  ax = gca;
   ax.XGrid = 'off';
   ax.YGrid = 'on';
   %create output file
%    ylim ([-8 10])
   set(gca,'XTick', 0:2:18);
%    set(gca,'YTick', -8:4:8);
```

```
bb=zeros(1,3,201);%(simulation,cpress chshear nu,z)
for k=1:1;%simulation counter
    for j=1:1;%parameter counter cpress cshear nu
    h=[3 13 14];
   bb(k,j,:)=max(squeeze(d(k,h(j),:,:)),[],2);

   [x y] = ind2sub(size(squeeze(d(k,h(j),:,:))),idx)
    end
end
qq=zeros(3,201);
for i=1:201
   qq=[1:201;x';(squeeze(d(1,3,1:201,x(i))))'];

end

surf(squeeze(d(1,2,1,:)),squeeze(d(1,1,:,1))*1e3,squeeze(d(1,3,:,:))*1e-
6,'edgecolor','none');%rad, mm, Mpa
caxis([1,1000])
alpha(0.4)
view([-135,34])
set(xlabel('Angular position (rad) '),'FontSize', labelfontsize);
set(ylabel('Neck length proximal to distal(mm)'),'FontSize', labelfontsize);
set(zlabel('Contact pressure (MPa)'),'Fontsize', labelfontsize);
xlim([0 2*pi])
ylim([0 18])
zlim([0 900])
```

```
set(get(gca,'xlabel'),'rotation',-15)

set(get(gca,'ylabel'),'rotation',15)

set(gca, 'FontSize', axisfontsize);

hold on

plot3(qq(1,:),qq(2,:),qq(3,:)*1e-6,'ro');

hold off

% print('SurfacePlot','-depsc','-tiff')

size(squeeze(d(1,3,:,:)))

figure (2)

surf(squeeze(d(1,13,:,:)),'edgecolor','none');

alpha(0.4)

figure (3)

surf(squeeze(d(1,14,:,:)),'edgecolor','none');

alpha(0.4)

figure (4)

d(1,15,45,:)=d(1,15,46,:);

d(1,15,80,:)=d(1,15,81,:);

d(1,15,156,:)=d(1,15,157,:);

d(1,15,187,:)=d(1,15,188,:);

surf(-squeeze(d(1,15,:,:))-3.2e-4,'edgecolor','none');

alpha(0.7)

figure (5)

surf(abs(((squeeze(d(1,15,:,:))+3.2e-4).*squeeze(d(1,13,:,:)))),'edgecolor','none');

alpha(.5)

sum(sum(abs((squeeze(d(1,15,:,:))+3.2e-
4).*squeeze(d(1,13,:,:)))*17*pi*13.76/(480*201),2))*1e-6
```

```
linewidthnumber = 2;
legendfontsize = 20;
labelfontsize = 20;
axisfontsize = 20;
titlefontsize=20;
figname1=cellstr(['Force only            ';'Frictional Moment       ';...
   'Force & Frictional Moment';'Frictional Torque       ']);
   length('Contact Shear Stress              ')
figname2=cellstr(['Contact Pressure                ';...
            'Contact Shear Stress             ';...
            'Contact Shear Stress/Contact Pressure']);

for k=1:1;
      aa=3;%aa= first layer
      bbb=401;%bbb= last layer
      cc=2;%cc= steps
      figure (10*k);
      plot(0:(cc/(bbb-aa))*18:18,squeeze(bb(k,3,aa:cc:bbb)),'k-', ...%1e-6 to make as MPa
          0:(cc/(bbb-aa))*18:18,squeeze(bb(k,3,aa:cc:bbb)),'k-.',...
          0:(cc/(bbb-aa))*18:18,squeeze(bb(k,3,aa:cc:bbb)),'k--',...
          0:(cc/(bbb-aa))*18:18,squeeze(bb(k,3,aa:cc:bbb)),'k:',...
          'LineWidth',linewidthnumber);

%     tit= strcat(figname2(i));
%
%     title(tit);
```

```
%
   ax = gca;
   ax.XGrid = 'off';
   ax.YGrid = 'on';
   %create output file
%    ylim ([-8 10])
   set(gca,'XTick', 0:2:18);
%    set(gca,'YTick', -8:4:8);
   set(xlabel('Neck length (mm)'),'FontSize', labelfontsize);
   set(ylabel('Contact Shear Stress/Contact pressure') , 'FontSize', labelfontsize);
   set(legend ('F only','F&M','Mn','Mf'),...
            'FontSize', legendfontsize);
%    set(title(tit),'FontSize', titlefontsize);
  set(gca, 'FontSize', axisfontsize);
print( '-dtiff', '-r300',num2str(k));
end
% dd=10; %dd= divisions in whole of the length
% ll=360; %ll= last layer z
% pn=floor(ll/dd)% pn =number of plot points
% bb=zeros(pn,1);
% for i= 1:pn
%
%    bb(i)=max(d(3,1+i*(ll/pn),:));
% end


% linewidthnumber = 2;
```

```
% legendfontsize = 20;

% labelfontsize = 20;

% axisfontsize = 20;

%  titlefontsize=20;


% ax = gca;

%     ax.XGrid = 'off';

%     ax.YGrid = 'on';

%

%     ylim ([-8 10])

%     set(gca,'XTick', 0:25:100);

%     set(gca,'YTick', -8:4:8);

%     set(gca,'ZTick', -8:4:8);

%     set(xlabel('Z neck length distal to proximal'),'FontSize', labelfontsize);

%     set(ylabel('\phi anterior face is zero ccw about neck axis') , 'FontSize', labelfontsize);

%     set(zlabel(fignames(j)) , 'FontSize', labelfontsize);

% %     set(legend ('Mn Average ','Mn H patient ','Mn L patient '),...

% %                 'FontSize', legendfontsize);

%     set(title(fignames(j)),'FontSize', titlefontsize);

%    set(gca, 'FontSize', axisfontsize);

% print( '-dtiff', '-r300',num2str(10*i));
```

Annex B, Technical drawings the testing systems

Base

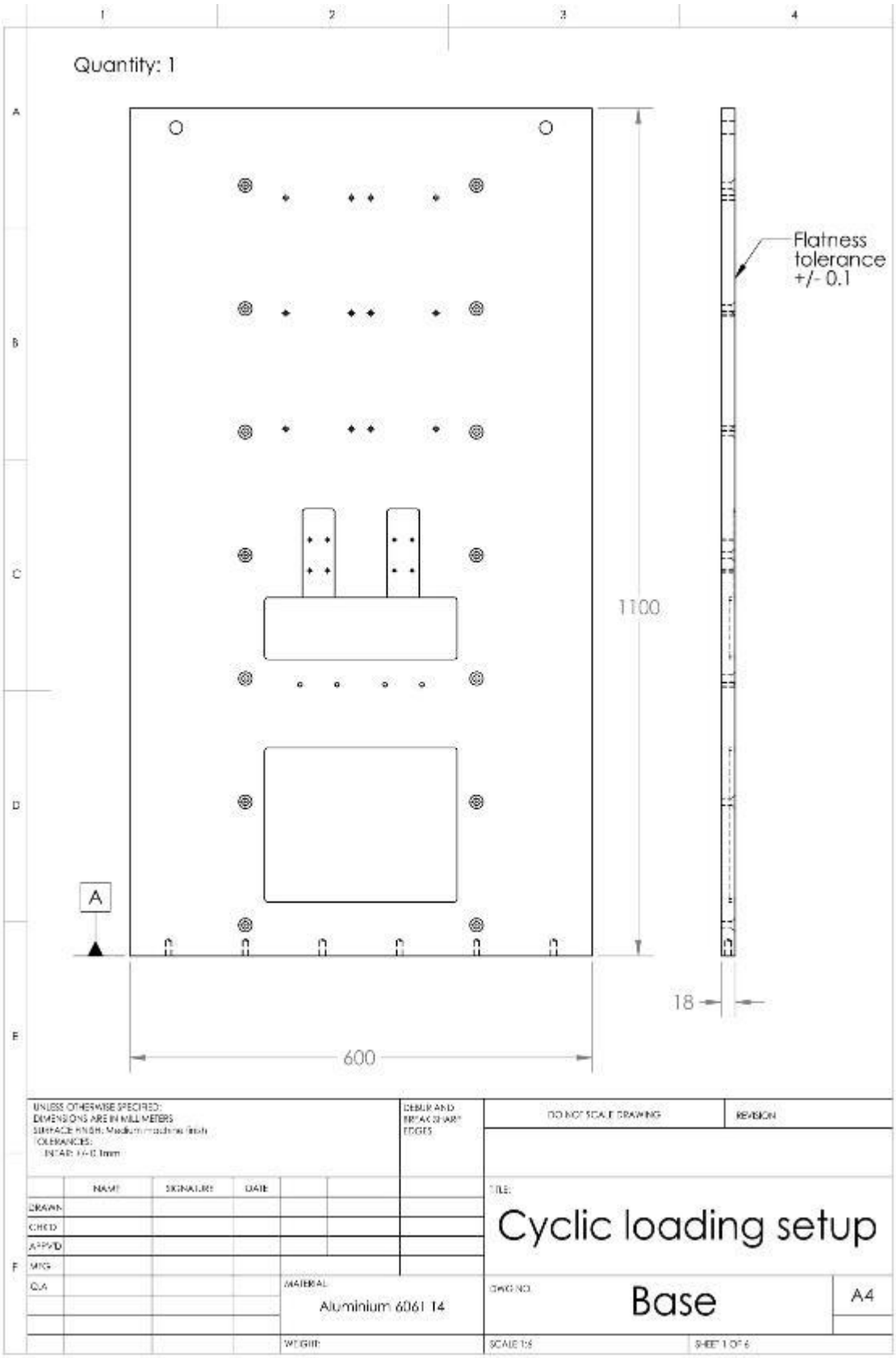

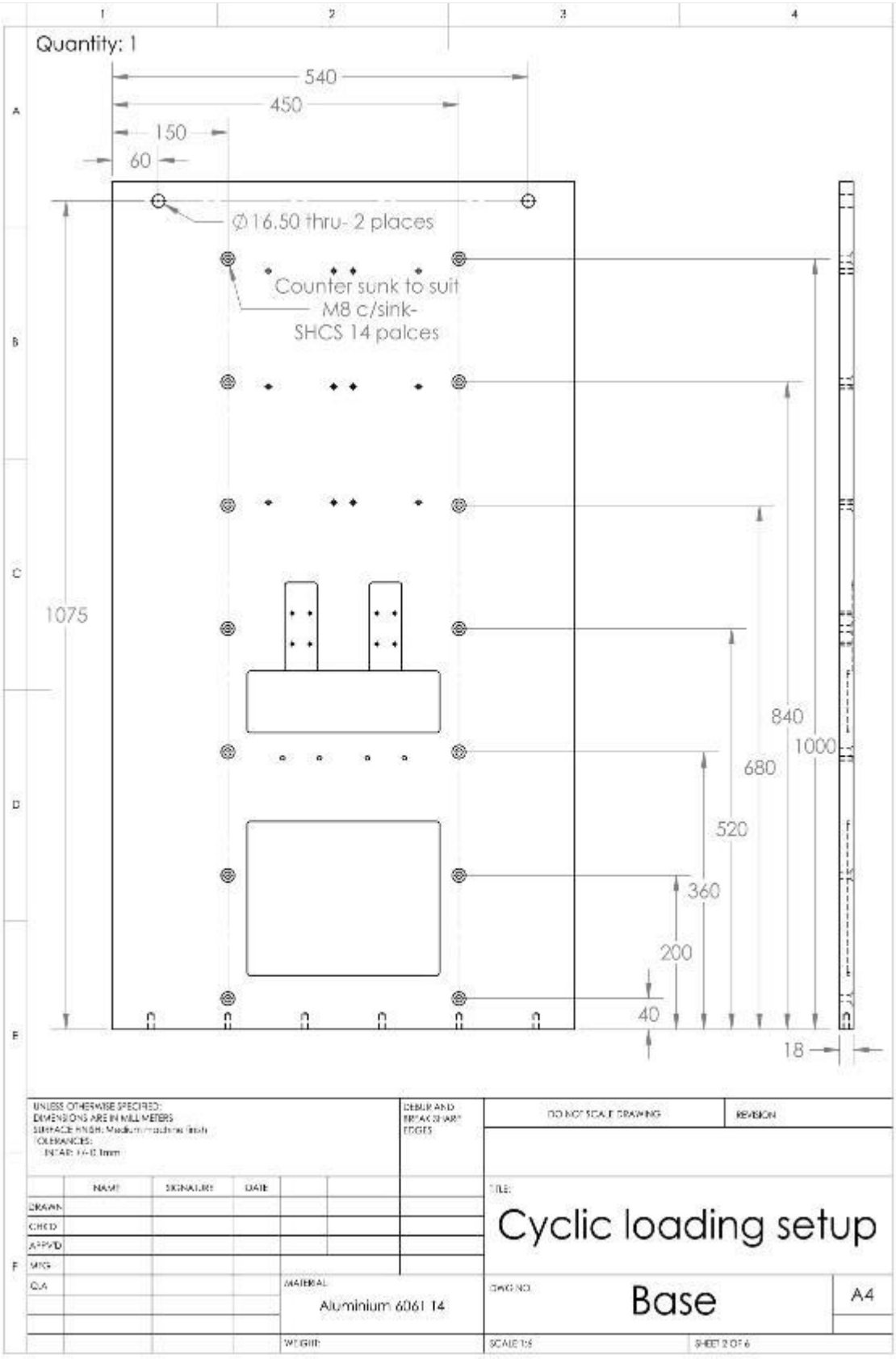
Quantity: 1
540
450
150
60
Ø16.50 thru- 2 places
Counter sunk to suit
M8 c/sink-
SHCS 14 palces
1075
840
1000
680
520
360
200
40
18
DO NOT SCALE DRAWING
REVISION
TITLE:
Cyclic loading setup
Base
A4
Aluminium 6061 T4

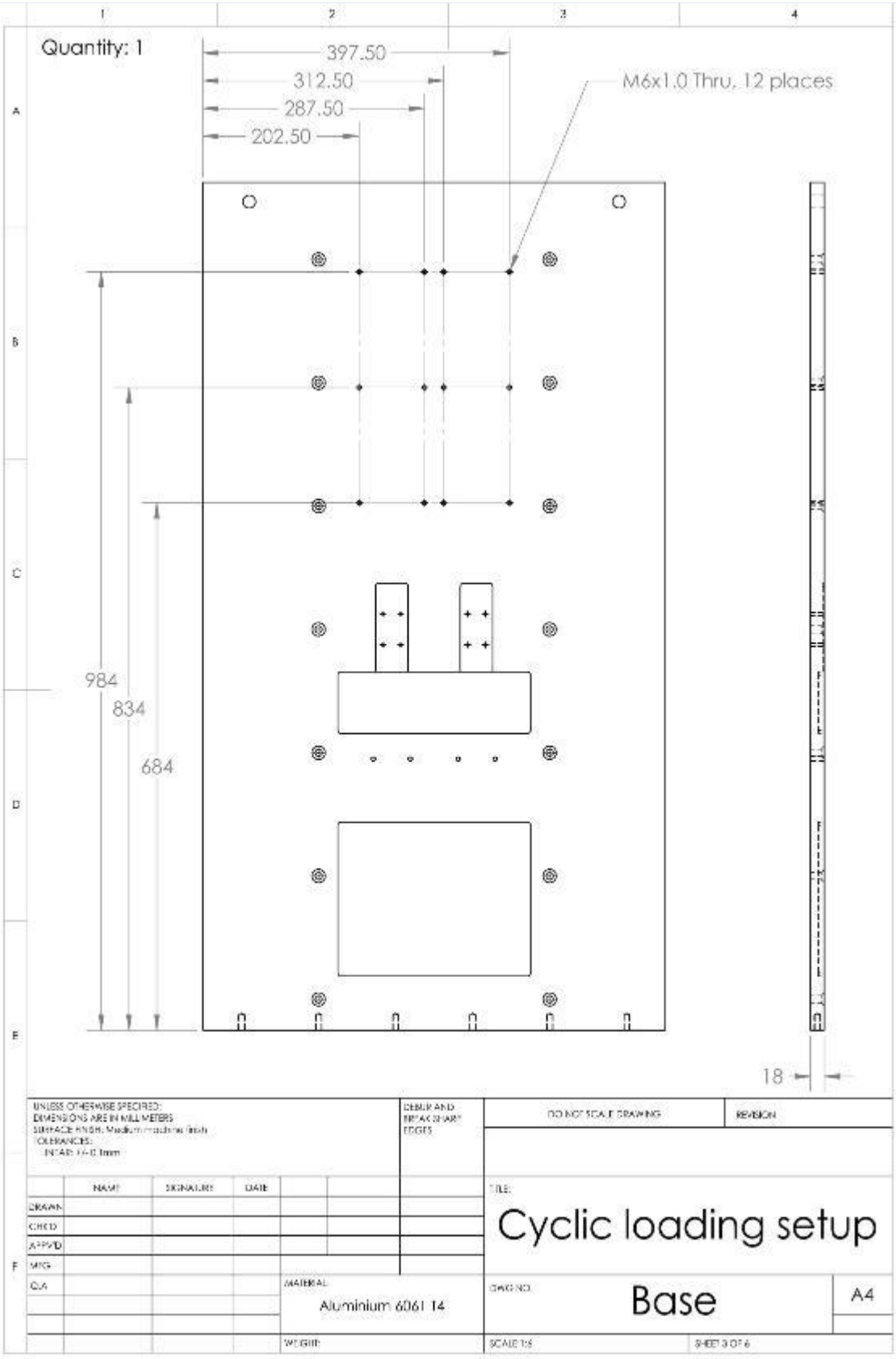
Quantity: 1
397.50
312.50
287.50
202.50
M6x1.0 Thru, 12 places
984
834
684
18
DO NOT SCALE DRAWING
REVISION
Cyclic loading setup
Base
A4
Aluminium 6061 T4

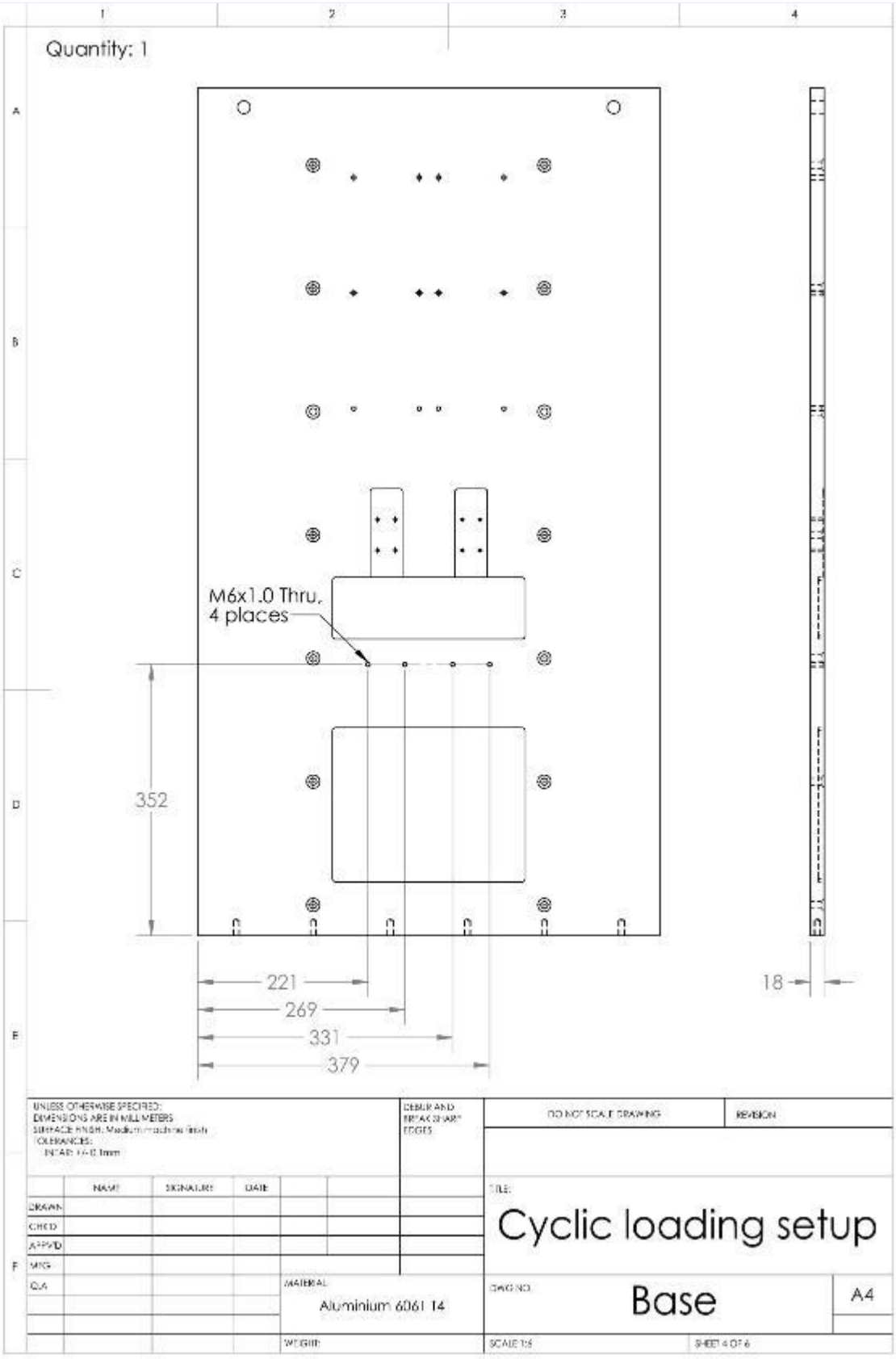
Quantity: 1
M6x1.0 Thru,
4 places
352
221
269
331
379
18
UNLESS OTHERWISE SPECIFIED:
DIMENSIONS ARE IN MILLIMETERS
DEBUR AND BREAK SHARP EDGES
DO NOT SCALE DRAWING
REVISION
NAME
SIGNATURE
DATE
DRAWN
CHKD
APPVD
MFG
QA
MATERIAL
Aluminium 6061 T4
WEIGHT:
TITLE:
Cyclic loading setup
DWG NO.
Base
A4
SCALE:1:5
SHEET 4 OF 6

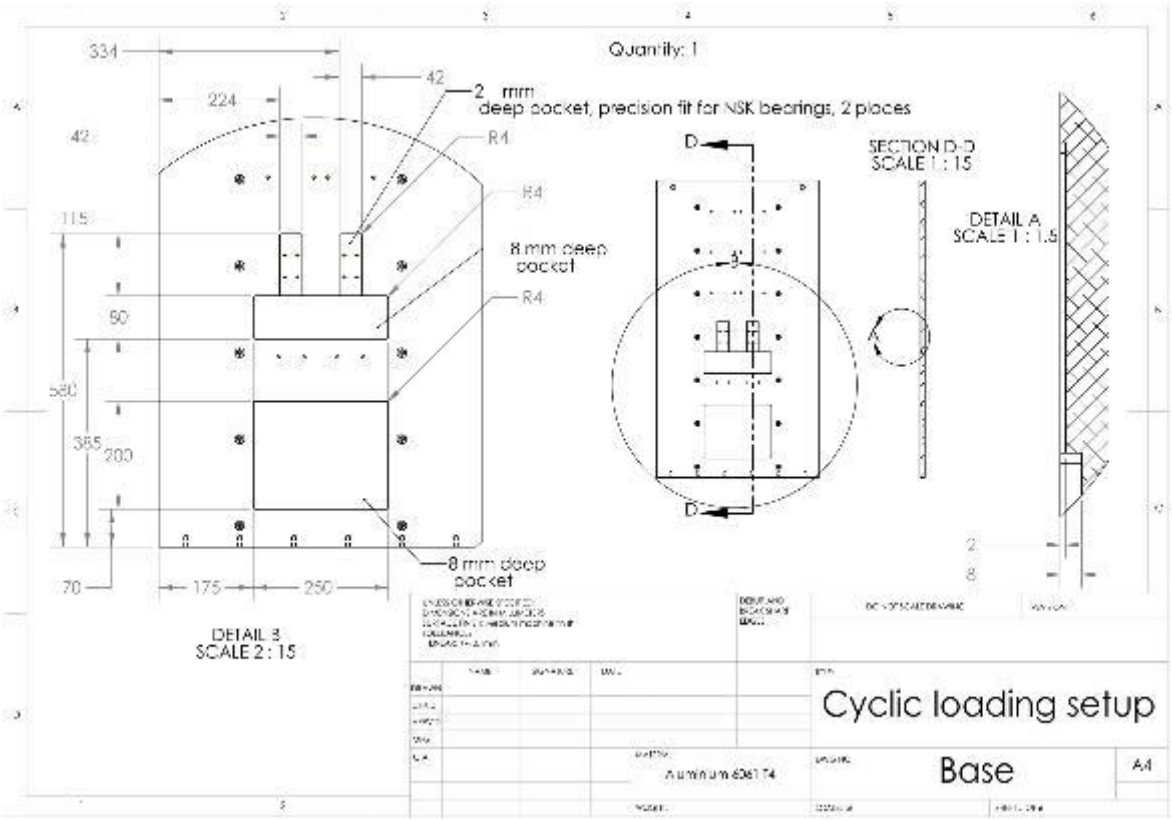
Quantity: 1
334
224
42
42
2 mm deep socket, precision fit for NSK bearings, 2 places
R4
R4
R4
8 mm deep pocket
8 mm deep pocket
115
50
580
385
200
70
175
250
DETAIL B
SCALE 2 : 15
SECTION D-D
SCALE 1 : 15
DETAIL A
SCALE 1 : 1.5
Cyclic loading setup
Base
Aluminum 6061 T4
A4

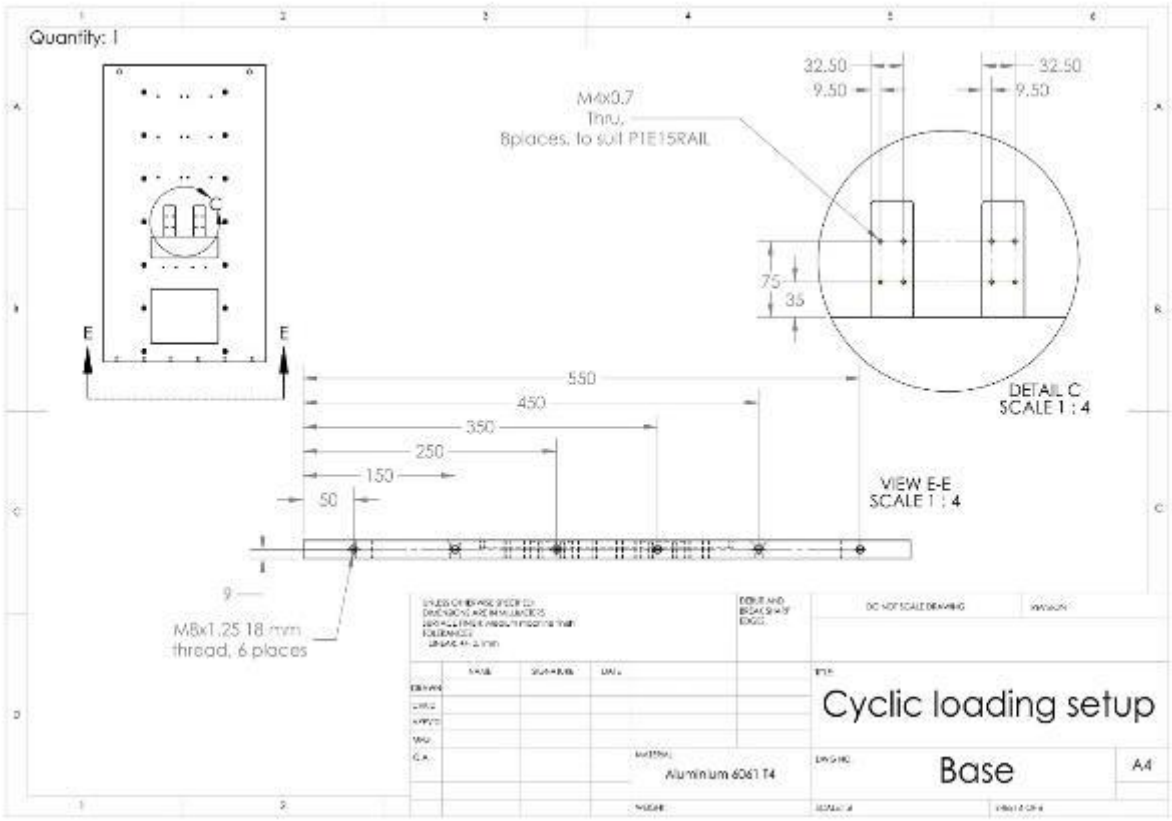
Quantity: 1
M4x0.7
Thru,
8places, to suit P1E15RAIL
32.50
9.50
32.50
9.50
75
35
DETAIL C
SCALE 1 : 4
E
E
550
450
350
250
150
50
VIEW E-E
SCALE 1 : 4
9
M8x1.25 18 mm
thread, 6 places
Cyclic loading setup
Base
Aluminum 6061 T4
A4

Sample base

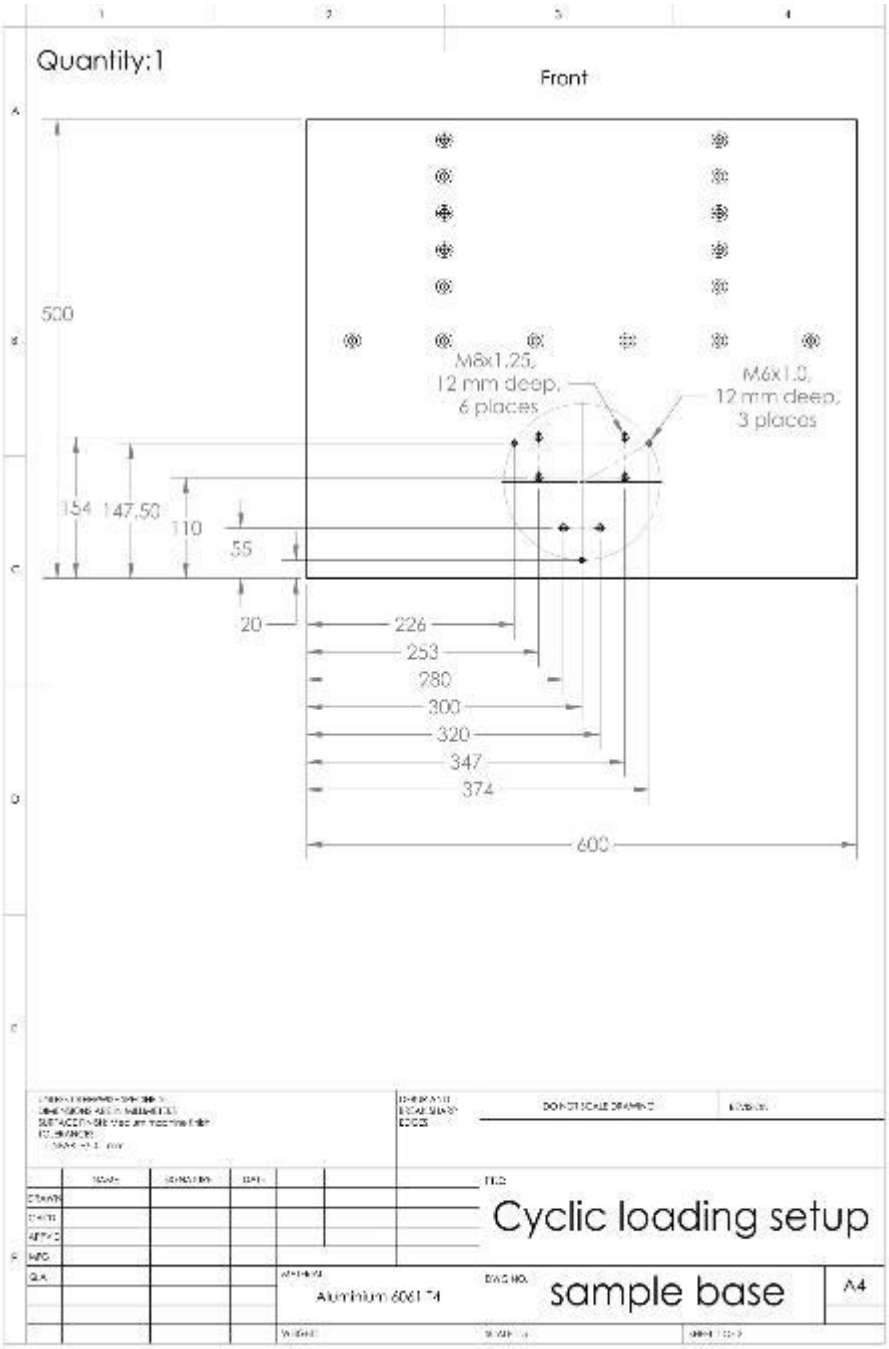
Quantity:1
Front
500
M8x1.25,
12 mm deep,
6 places
M6x1.0,
12 mm deep,
3 places
154
147.50
110
55
20
226
253
280
300
320
347
374
600
Cyclic loading setup
sample base
A4
Aluminium 6061-T4

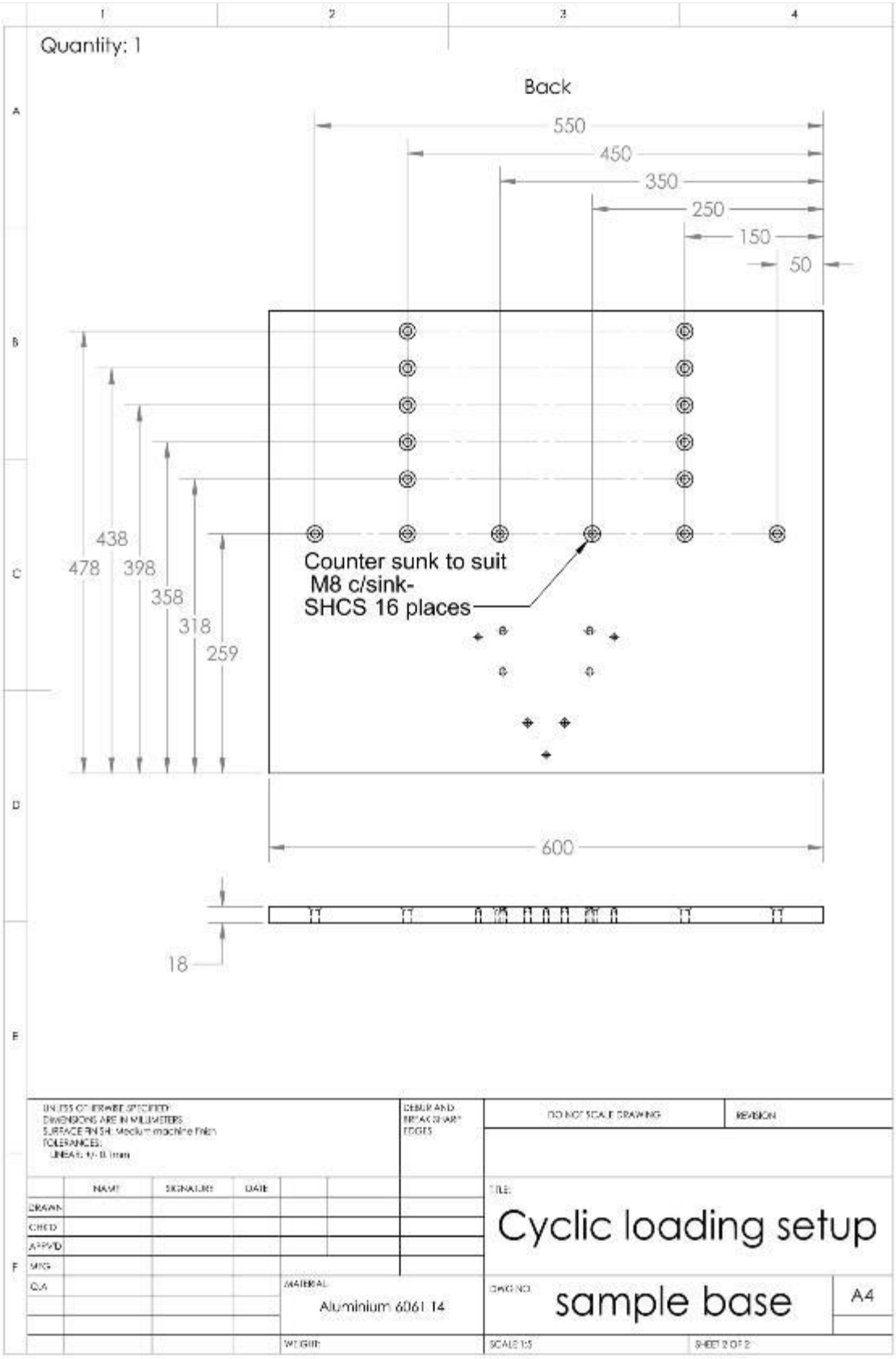
Quantity: 1
Back
550
450
350
250
150
50
438
478
398
358
318
259
Counter sunk to suit
M8 c/sink-
SHCS 16 places
600
18
Cyclic loading setup
sample base
A4
Aluminium 6061 T4

Gusset

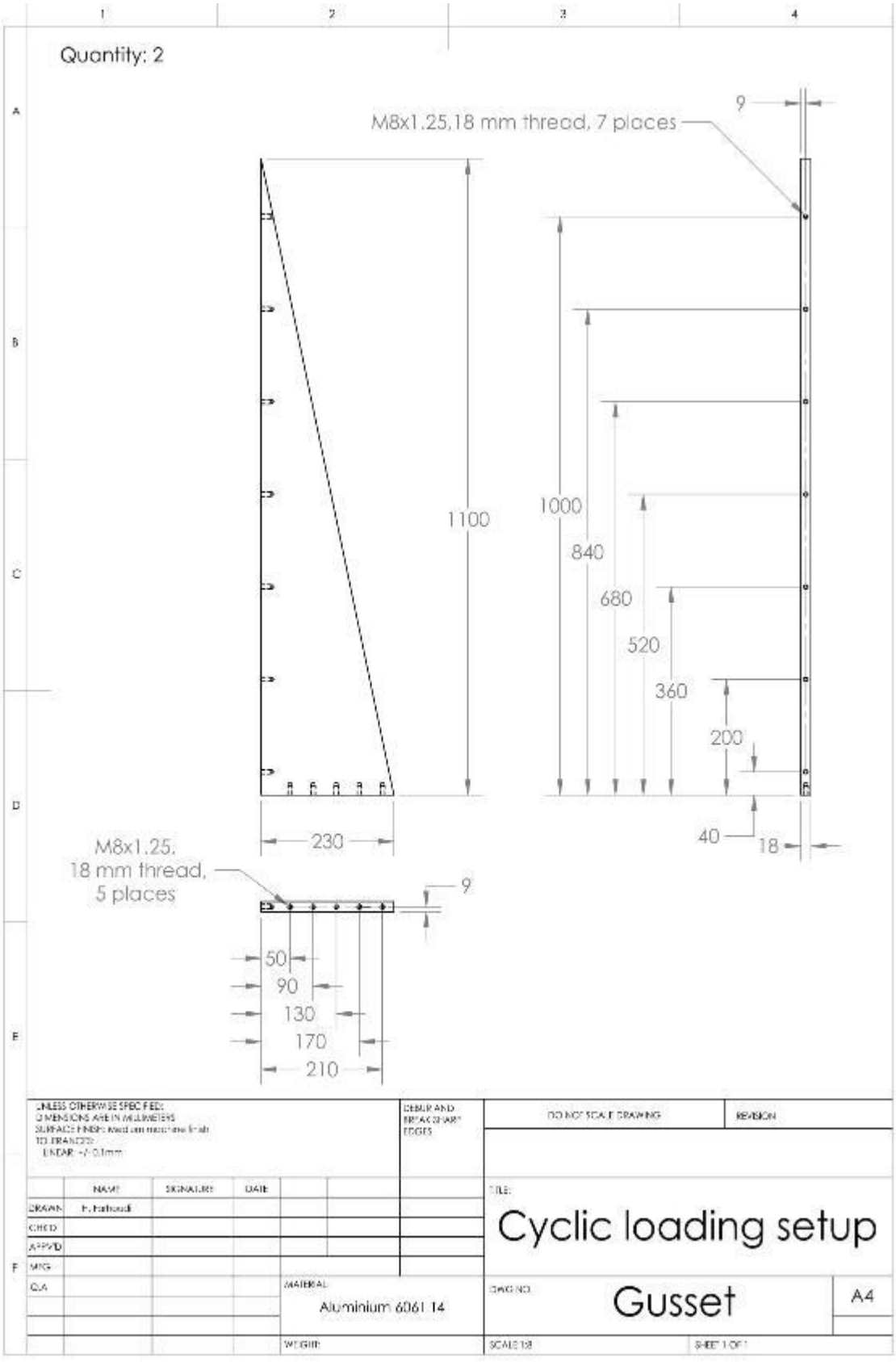
Quantity: 2
M8x1.25,18 mm thread, 7 places
9
1100
1000
840
680
520
360
200
40
18
230
M8x1.25,
18 mm thread,
5 places
9
50
90
130
170
210
UNLESS OTHERWISE SPECIFIED:
DIMENSIONS ARE IN MILLIMETERS
SURFACE FINISH:
TOLERANCES:
LINEAR +/- 0.1mm
DEBUR AND BREAK SHARP EDGES
DO NOT SCALE DRAWING
REVISION
NAME
SIGNATURE
DATE
DRAWN
CHKD
APPVD
MFG
QA
TITLE:
Cyclic loading setup
MATERIAL
Aluminium 6061 T4
DWG NO.
Gusset
A4
WEIGHT:
SCALE:1:8
SHEET 1 OF 1

Top female gripper

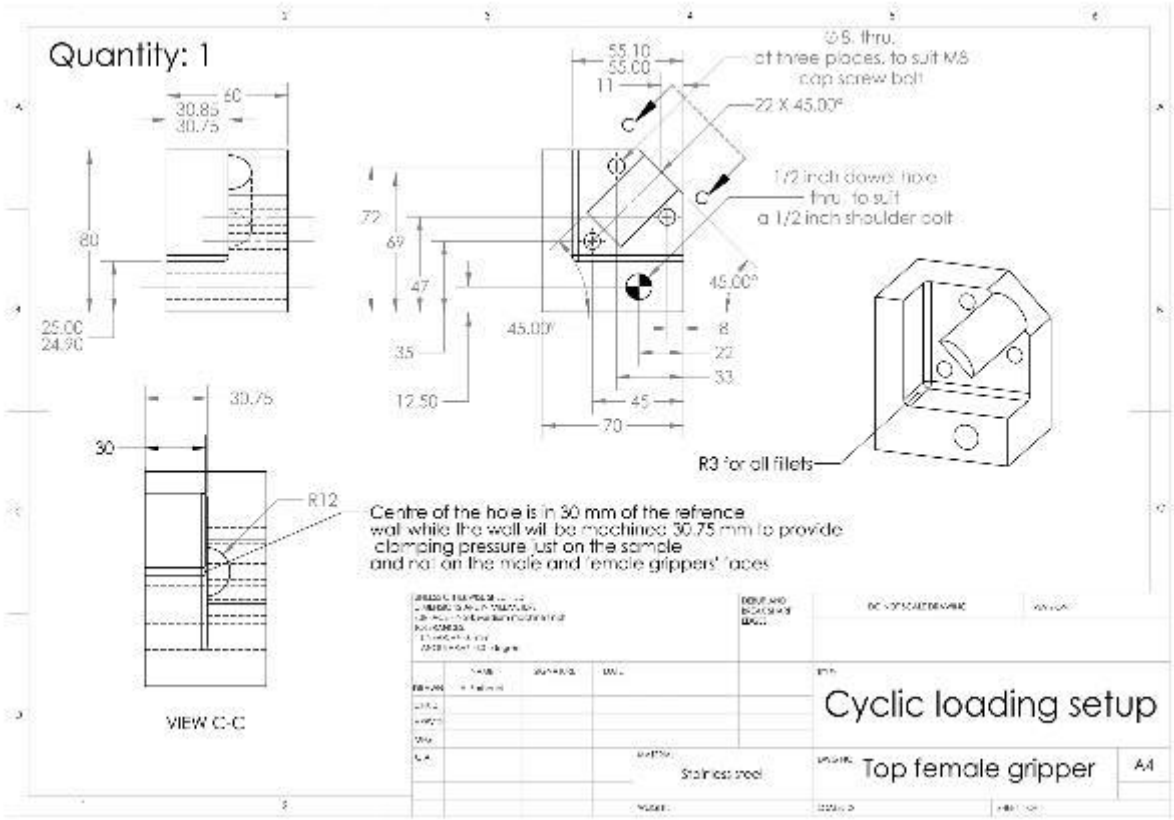

Bottom female gripper

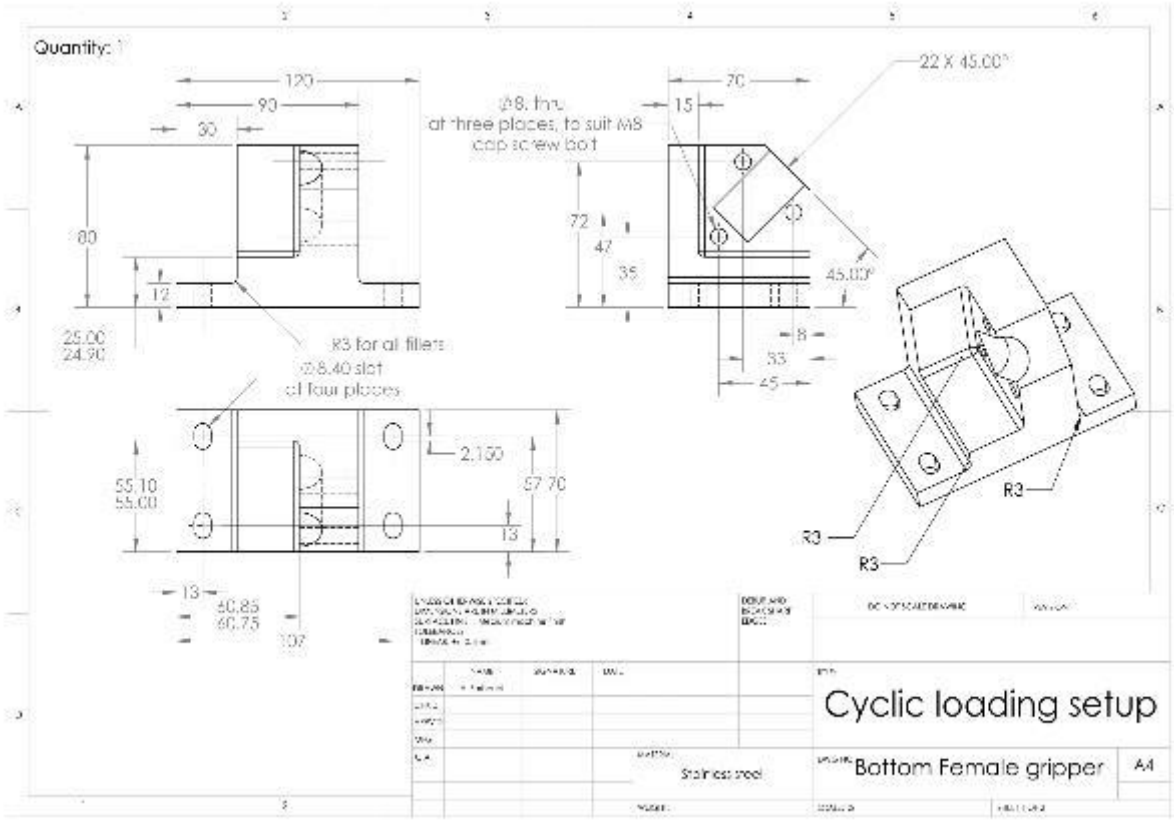

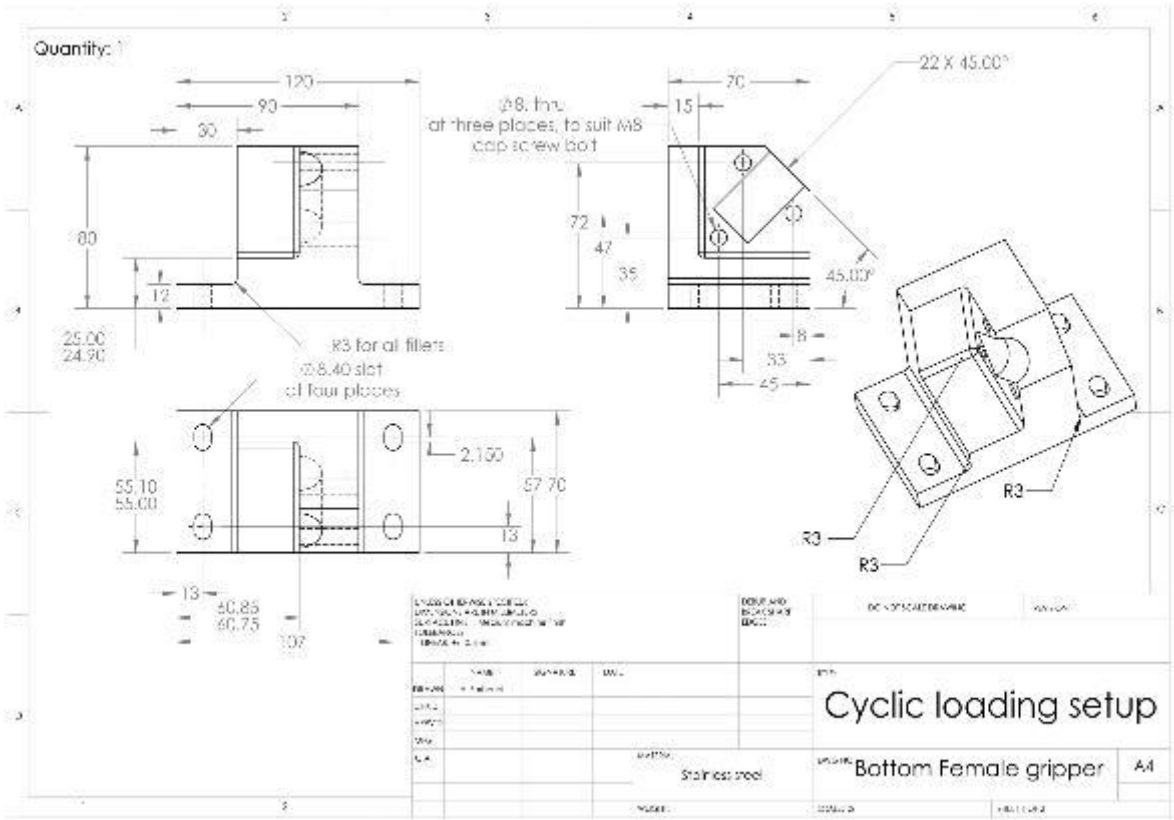

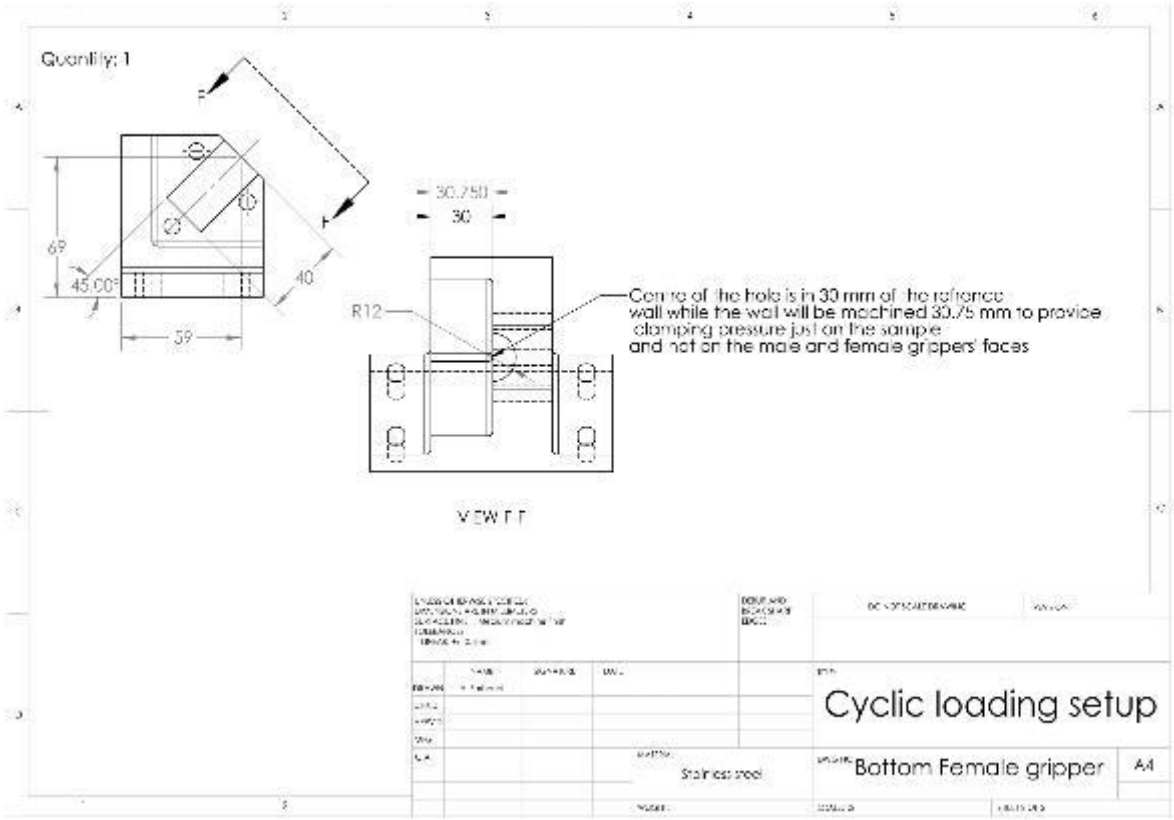
Quantity: 1
69
45.00°
39
40
30.750
30
R12
Centre of the hole is in 30 mm of the reference wall while the wall will be machined 30.75 mm to provide clamping pressure just on the sample and not on the male and female grippers' faces
VIEW F-F
Cyclic loading setup
Stainless steel
Bottom Female gripper
A4

Male round gripper

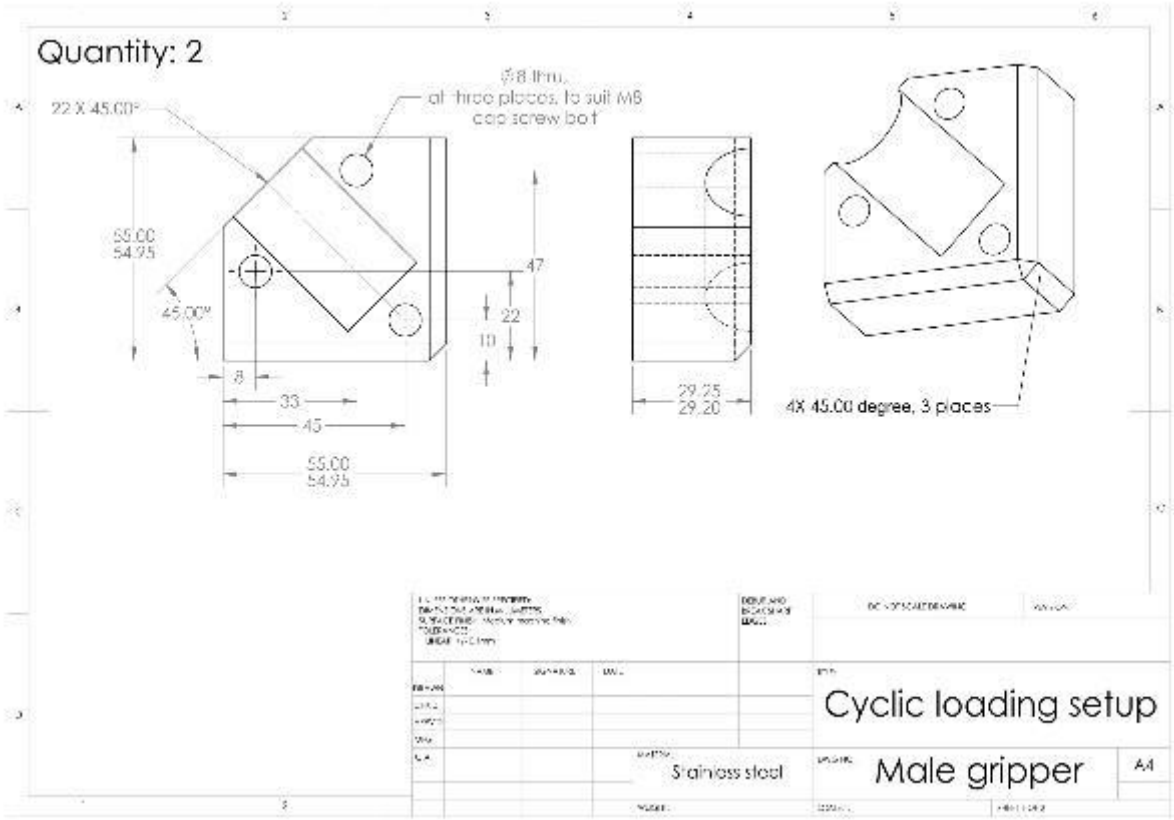

Thrust bearing housing

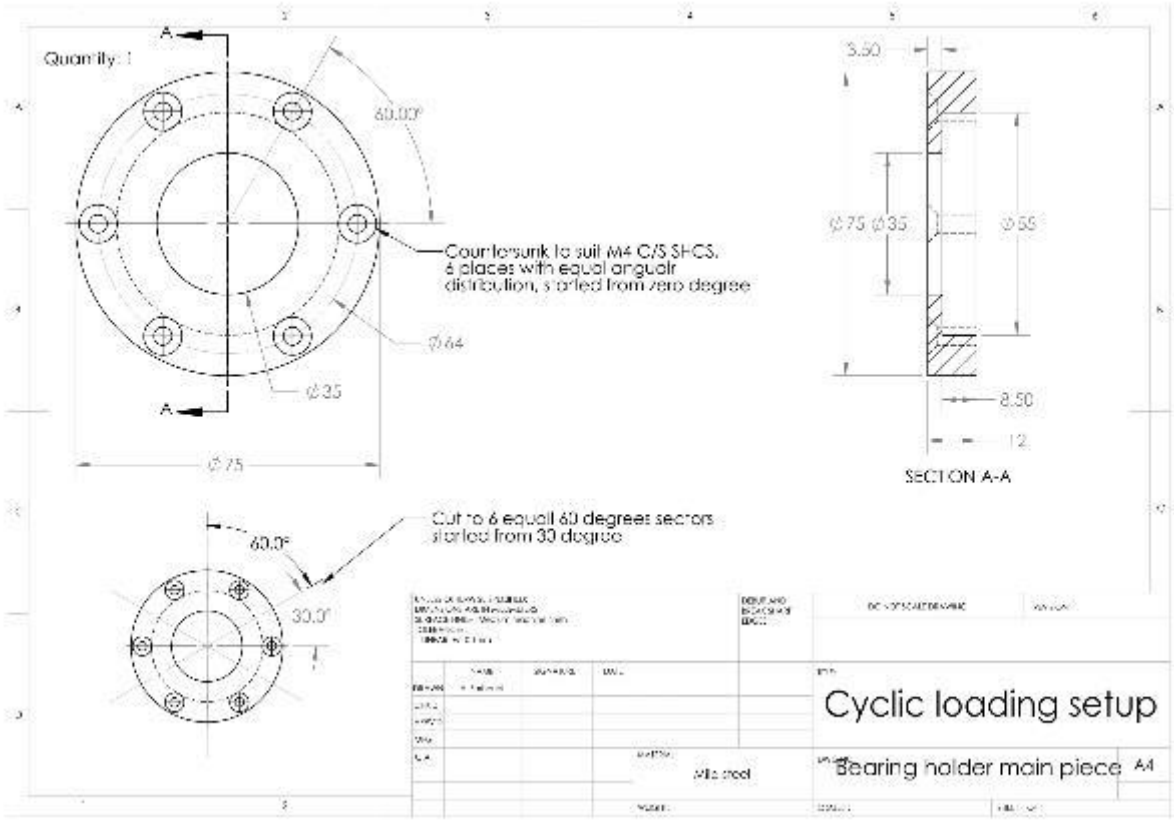

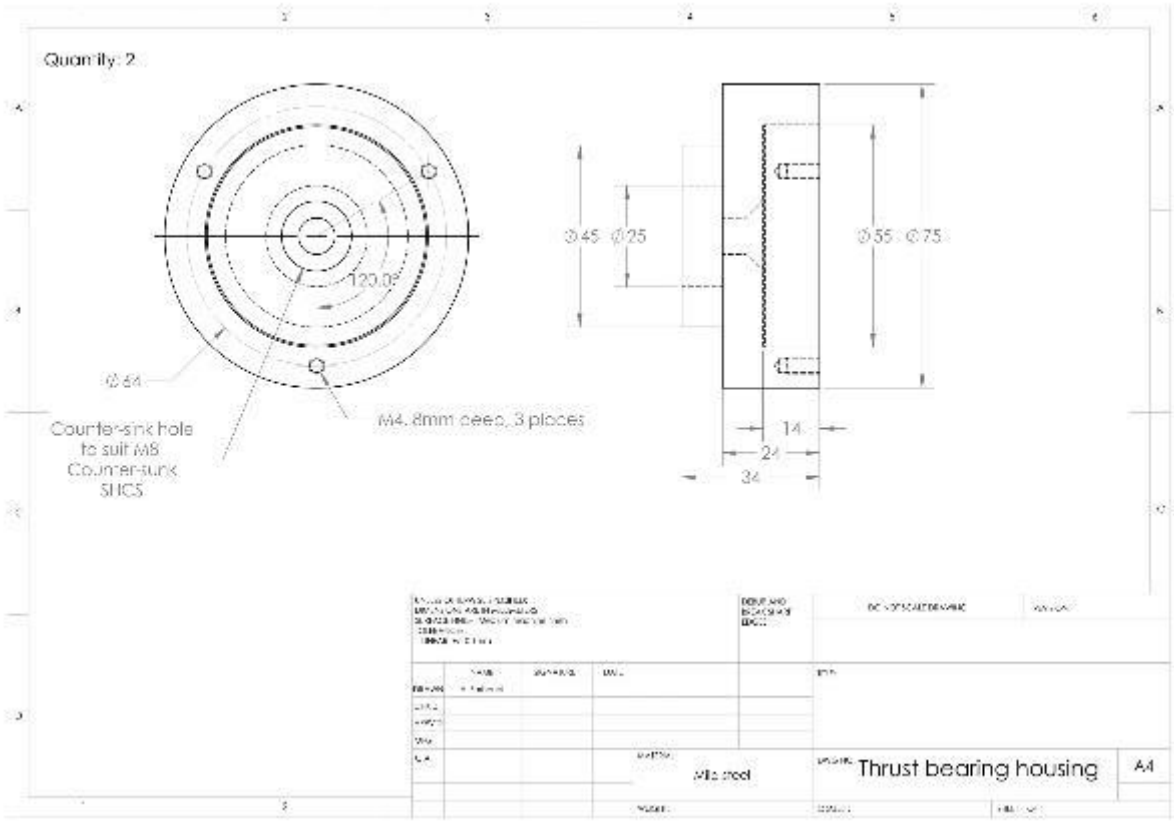

Spherical bearing rod

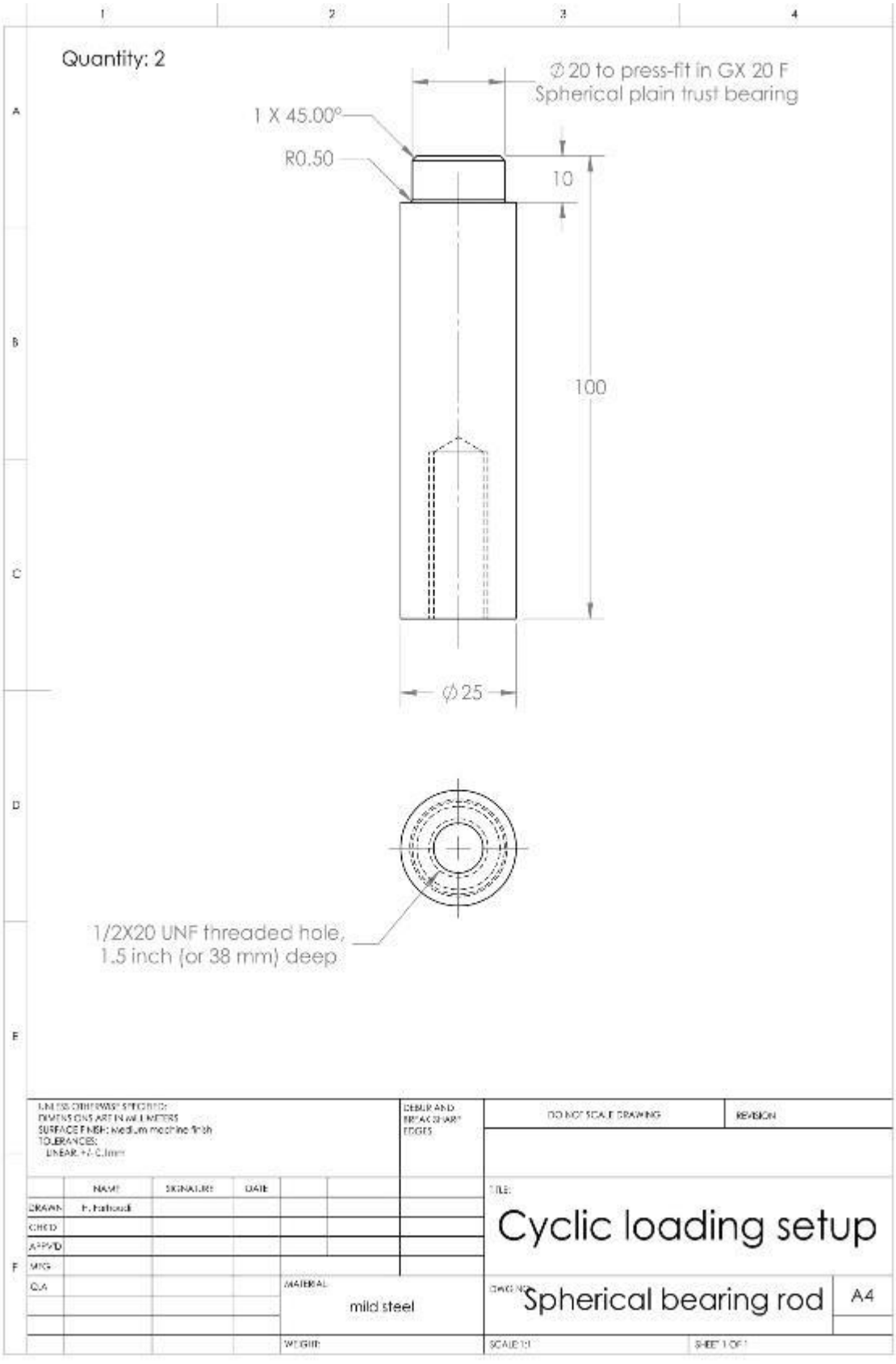

Head specimen

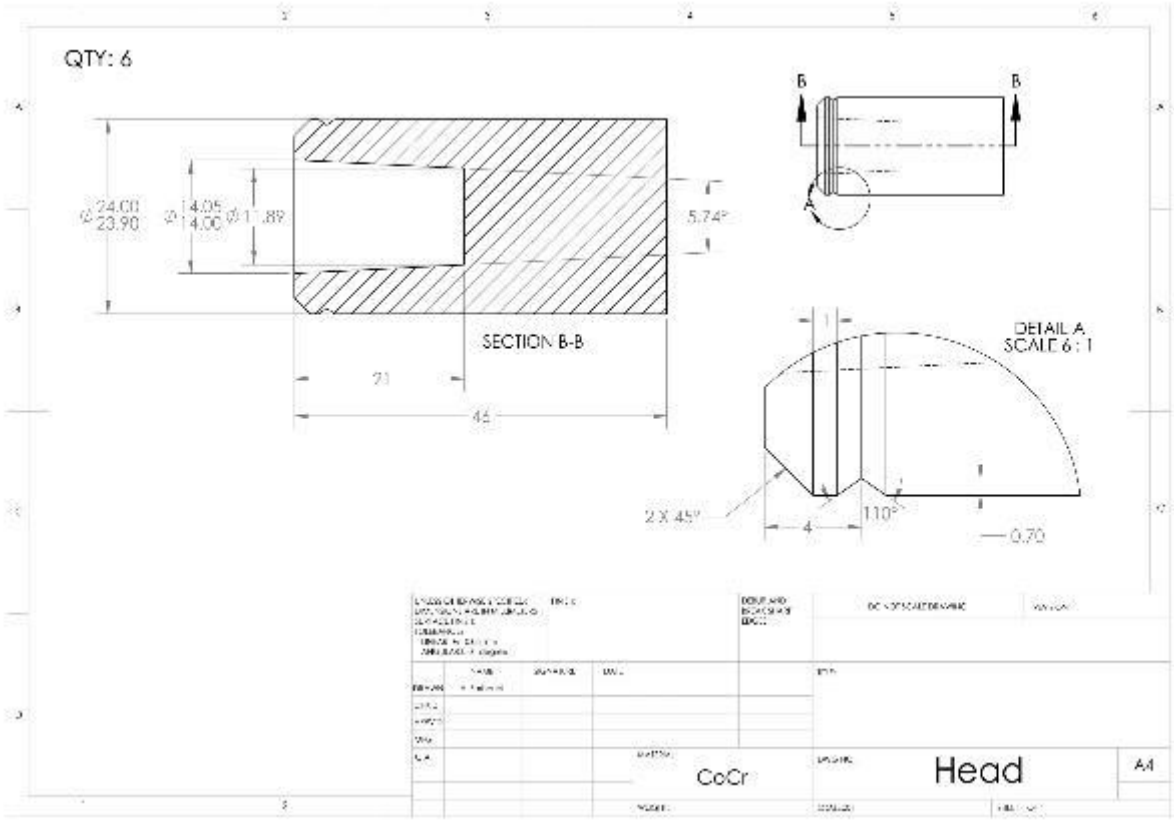

Neck specimen

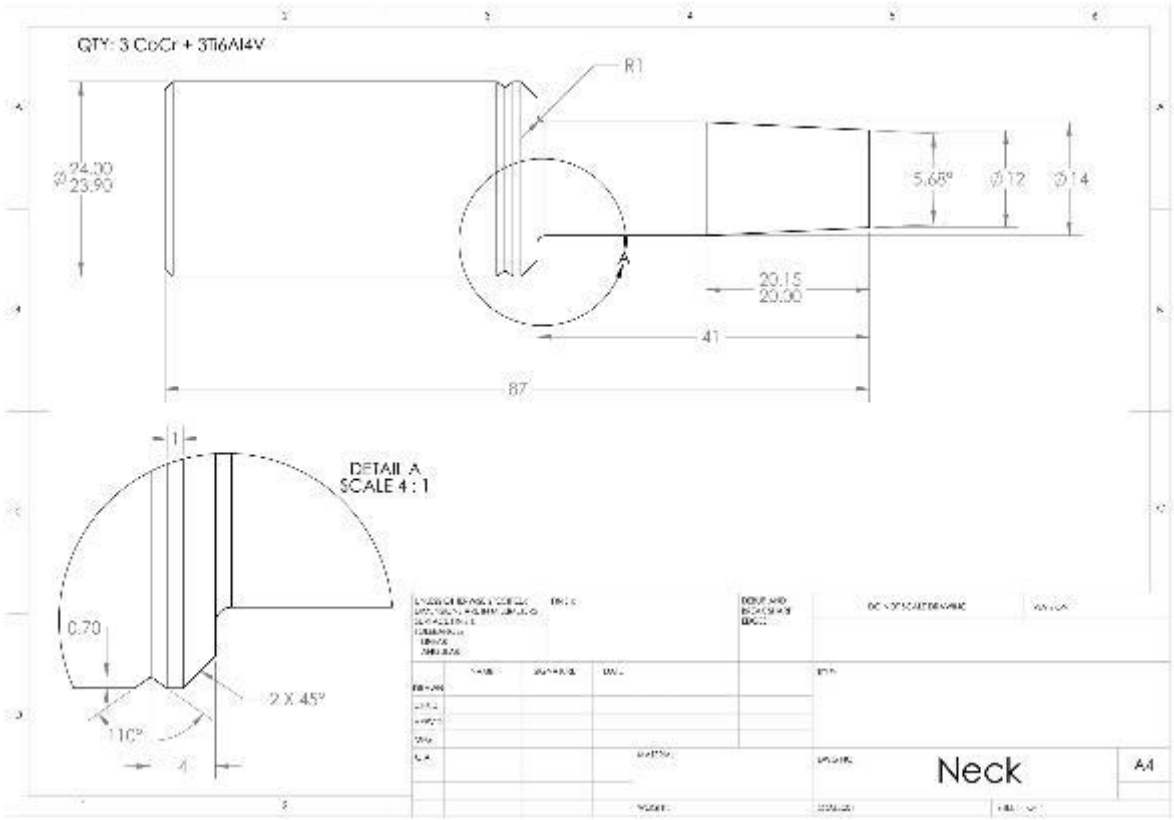

Annex C, LabVIEW code for state machine and data acquisition of the testing system

Force generation_NI9375 B.vi
C:\Users\Hamid\Google Drive\setup (corrosion fatigue)\Labview\Hamid VIS\Fretting-corrosion measurement\Force generation_CD Edit Folder\Fretting-corrosion measurement\Force generation_NI9375 B.vi
Last modified on 3/17/2017 at 5:28 PM
Printed on 2/25/2018 at 3:57 PM

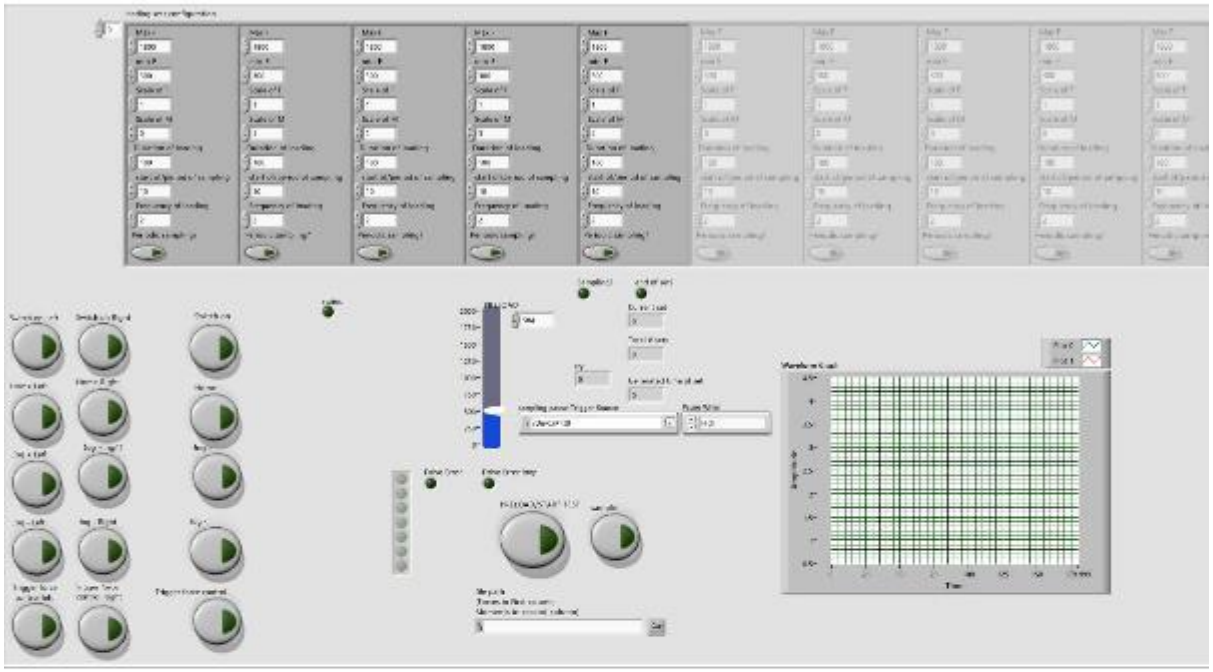

Force generation_NI9375 B.vi
C:\Users\Hamid\Google Drive\setup (corrosion fatigue)\Labview\Hamid VIS\Fretting-corrosion measurement\Force generation_CD Edit Folder\Fretting-corrosion measurement\Force generation_NI9375 B.vi
Last modified on 3/17/2017 at 5:28 PM
Printed on 2/25/2018 at 3:57 PM

Force generation_NI9375 B.vi
C:\Users\Hamid\Google Drive\setup (corrosion fatigue)\Labview\Hamid VIS\Fretting-corrosion measurement\Force generation_CD Edit Folder\Fretting-corrosion measurement\Force generation_NI9375 B.vi
Last modified on 3/17/2017 at 5:28 PM
Printed on 2/25/2018 at 3:57 PM

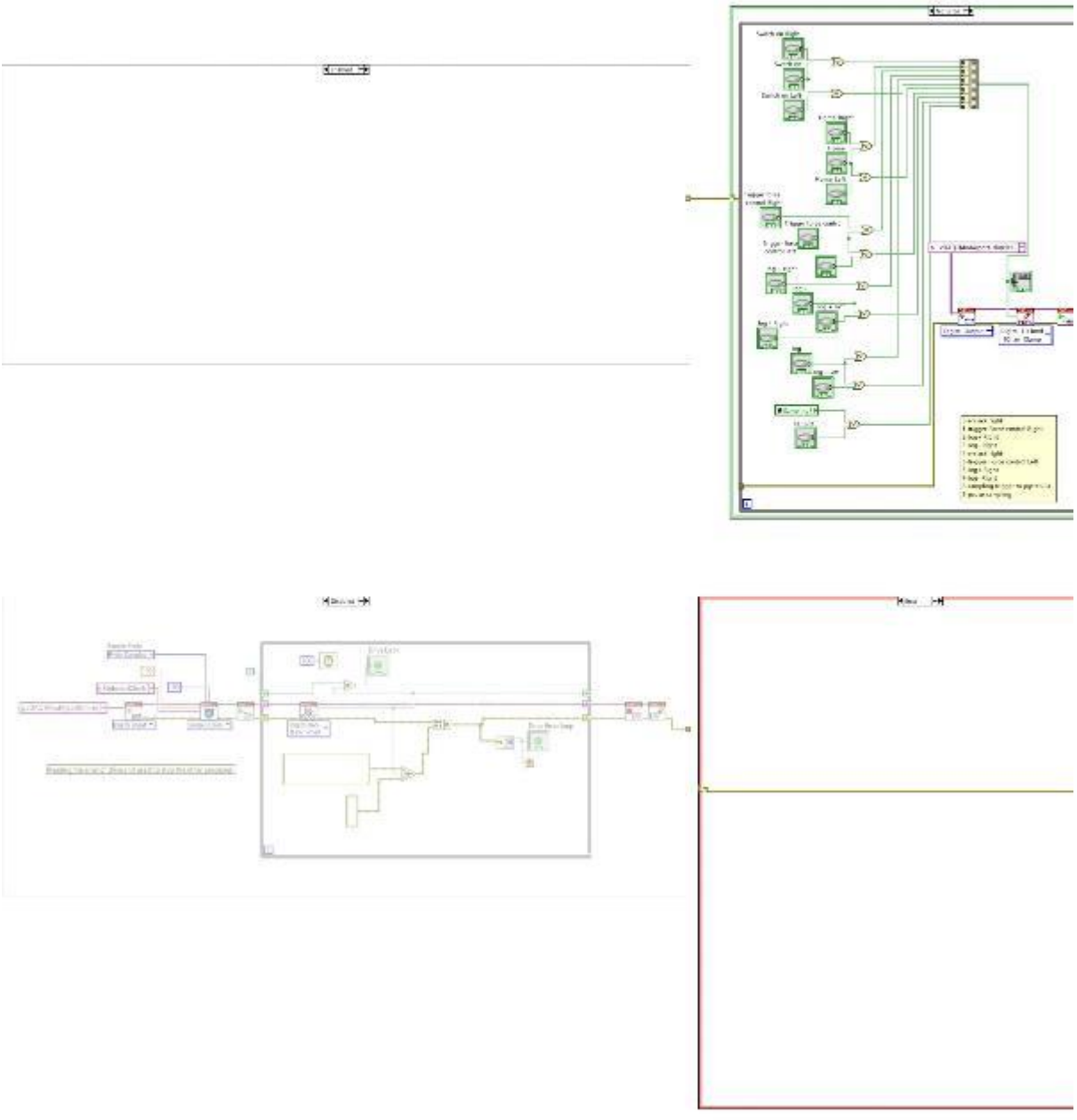

Force generation_NI9375 B.vi
C:\Users\Hamid\Google Drive\setup (corrosion fatigue)\Labview\Hamid VIS\Fretting-corrosion measurement\Force generation_CD Edit Folder\Fretting-corrosion measurement\Force generation_NI9375 B.vi
Last modified on 3/17/2017 at 5:28 PM
Printed on 2/25/2018 at 3:57 PM

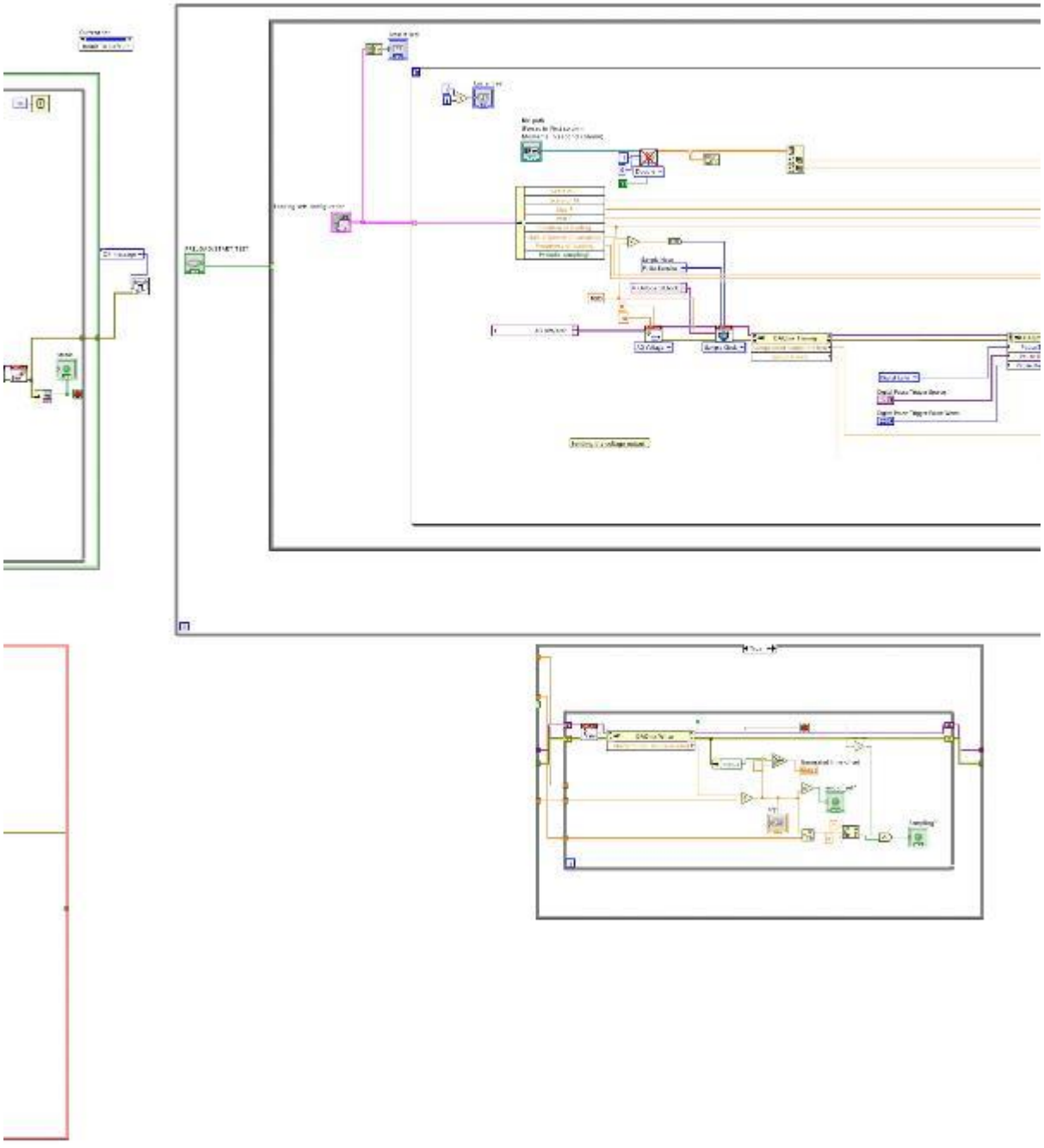

Force generation_NI9375 B.vi
C:\Users\Hamid\Google Drive\setup (corrosion fatigue)\Labview\Hamid VIS\Fretting-corrosion measurement\Force generation_CD Edit Folder\Fretting-corrosion measurement\Force generation_NI9375 B.vi
Last modified on 3/17/2017 at 5:28 PM
Printed on 2/25/2018 at 3:57 PM

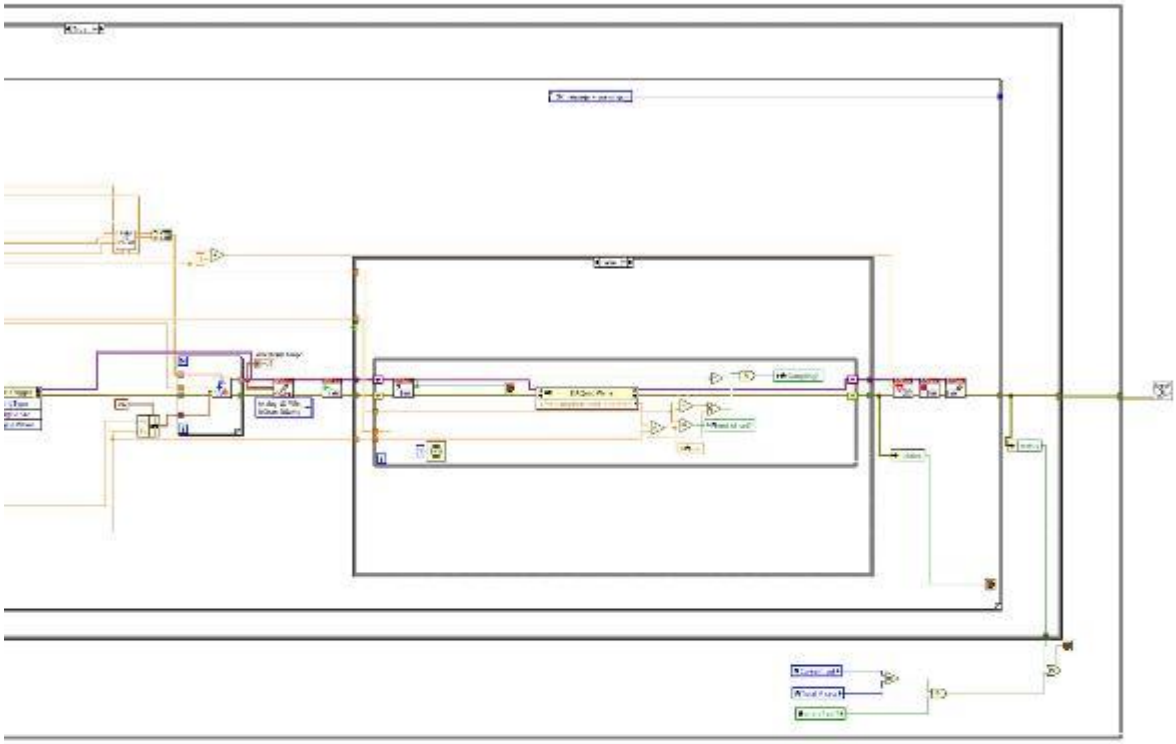

Force generation_NI9375 B.vi
C:\Users\Hamid\Google Drive\setup (corrosion fatigue)\Labview\Hamid VIS\Fretting-corrosion measurement\Force generation_CD Edit Folder\Fretting-corrosion measurement\Force generation_NI9375 B.vi
Last modified on 3/17/2017 at 5:28 PM
Printed on 2/25/2018 at 3:57 PM

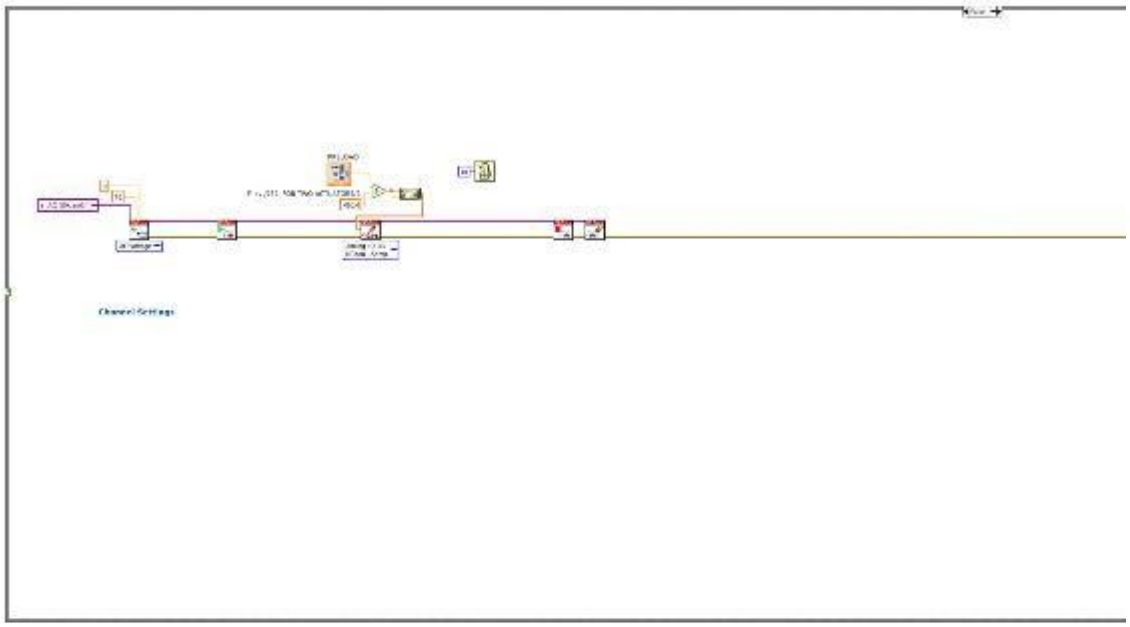

Force generation_NI9375 B.vi
C:\Users\Hamid\Google Drive\setup (corrosion fatigue)\Labview\Hamid VIS\Fretting-corrosion measurement\Force generation_CD Edit Folder\Fretting-corrosion measurement\Force generation_NI9375 B.vi
Last modified on 3/17/2017 at 5:28 PM
Printed on 2/25/2018 at 3:57 PM

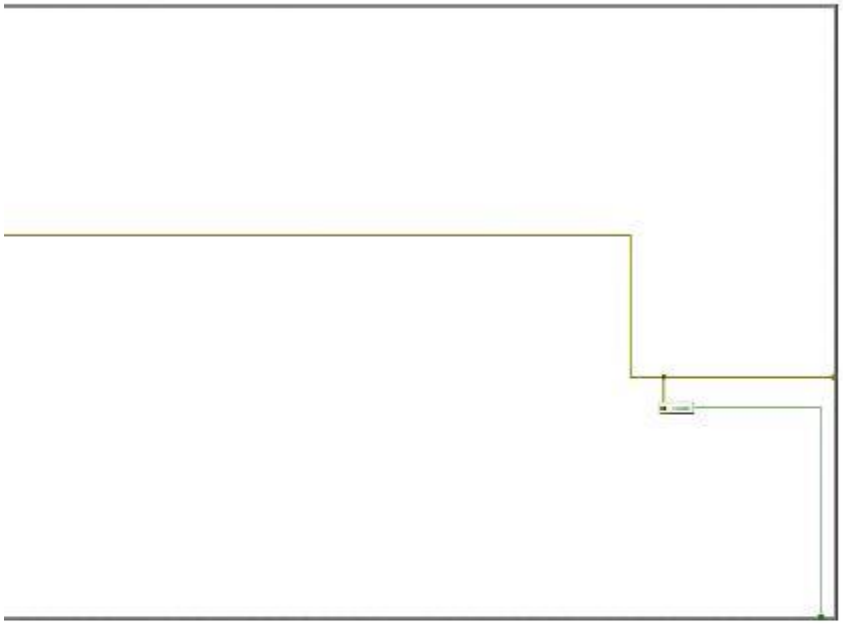

References

(1996). ASM handbook. Materials Park, Ohio :, ASM International.
Adam, P., R. Philippe, M. Ehlinger, O. Roche, F. Bonnomet, D. Molé and M. H. Fessy (2012). "Dual mobility cups hip arthroplasty as a treatment for displaced fracture of the femoral neck in the elderly. A prospective, systematic, multicenter study with specific focus on postoperative dislocation." Orthopaedics & Traumatology: Surgery & Research **98**(3): 296-300.
Ansari, J. S., G. S. Matharu and H. Pandit (2018). "Metal-on-metal hips: current status." Orthopaedics and Trauma **32**(1): 54-60.
ASM-International-Handbook (2005). ASM Handbook, ASM International.
Atwood, S. A., E. W. Patten, K. J. Bozic, L. A. Pruitt and M. D. Ries (2010). "Corrosion-induced fracture of a double-modular hip prosthesis: A case report." Journal of Bone and Joint Surgery - Series A **92**(6): 1522-1525.
Barton, J. (1827). "On the treatment of anchylosis, by the formation of artificial joints." North American Medical and Surgical Journal **3**(279): 400.
Baxmann, M., S. Y. Jauch, C. Schilling, W. Blömer, T. M. Grupp and M. M. Morlock (2013). "The influence of contact conditions and micromotions on the fretting behavior of modular titanium alloy taper connections." Medical Engineering & Physics **35**(5): 676-683.
Bergmann, G., G. Deuretzbacher, M. Heller, F. Graichen, A. Rohlmann, J. Strauss and G. N. Duda (2001). "Hip contact forces and gait patterns from routine activities." Journal of Biomechanics **34**(7): 859-871.
Bergmann, G., F. Graichen and A. Rohlmann (1993). "Hip joint loading during walking and running, measured in two patients." Journal of Biomechanics **26**(8): 969-990.
Bergmann, G., F. Graichen, A. Rohlmann, A. Bender, B. Heinlein, G. N. Duda, M. O. Heller and M. M. Morlock (2010). "Realistic loads for testing hip implants." Bio-Medical Materials and Engineering **20**(2): 65-75.
Berthier, Y., L. Vincent and M. Godet (1989). "Fretting fatigue and fretting wear." Tribology International **22**(4): 235-242.
Bishop, N. E., A. Hothan and M. M. Morlock (2013). "High friction moments in large hard-on-hard hip replacement bearings in conditions of poor lubrication." Journal of Orthopaedic Research **31**(5): 807-813.
Bishop, N. E., F. Waldow and M. M. Morlock (2008). "Friction moments of large metal-on-metal hip joint bearings and other modern designs." Medical Engineering & Physics **30**(8): 1057-1064.
Bobyn, J. D., M. Tanzer, J. J. Krygier, A. R. Dujovne and C. E. Brooks (1994). "Concerns with modularity in total hip arthroplasty." Clinical Orthopaedics and Related Research(298): 27-36.
Bolland, B. J. R. F., D. J. Culliford, D. J. Langton, J. P. S. Millington, N. K. Arden and J. M. Latham (2011). "High failure rates with a large-diameter hybrid metal-on-metal total hip replacement: clinical, radiological and retrieval analysis." Journal of Bone & Joint Surgery, British Volume **93-B**(5): 608-615.
Bowman, K. F., J. Fox and J. K. Sekiya (2010). "A Clinically Relevant Review of Hip Biomechanics." Arthroscopy: The Journal of Arthroscopic & Related Surgery **26**(8): 1118-1129.
Brien, W. W., E. A. Salvati, J. H. Healey, M. Bansal, B. Ghelman and F. Betts (1990). "Osteogenic sarcoma arising in the area of a total hip replacement. A case report." J Bone Joint Surg Am **72**(7): 1097-1099.
Bronzino, J. (2006). Biomedical Engineering Fundamentals, CRC Press.
Bryant, M. (2013). Fretting-crevice corrosion of cemented metal on metal total hip replacements. PhD, The University of Leeds.
Bryant, M., M. Ward, R. Farrar, R. Freeman, K. Brummitt, J. Nolan and A. Neville (2014). "Characterisation of the surface topography, tomography and chemistry of fretting corrosion product found on retrieved polished femoral stems." Journal of the Mechanical Behavior of Biomedical Materials **32**(0): 321-334.
C. Kaddick, M. M. C. B. M. H. M. A. W. (2015). On the Measurement of Three-Dimensional Taper Moments Due to Friction and Contact Load in Total Hip Replacement

Modularity and Tapers in Total Joint Replacement Devices. West Conshohocken, PA, ASTM International.
Campbell, P., E. Ebramzadeh, S. Nelson, K. Takamura, K. De Smet and H. Amstutz (2010). "Histological Features of Pseudotumor-like Tissues From Metal-on-Metal Hips." Clinical Orthopaedics and Related Research® **468**(9): 2321-2327.
Campbell, P., E. Ebramzadeh, S. Nelson, K. Takamura, K. De Smet and H. C. Amstutz (2010). "Histological features of pseudotumor-like tissues from metal-on-metal hips." Clin Orthop Relat Res **468**(9): 2321-2327.
Canham, C. D., P. I. Muradov, J. B. Simpson and S. J. Incavo (2017). "Corrosion and adverse local tissue reaction after total hip arthroplasty with a modular titanium alloy femoral neck." Arthroplast Today **3**(4): 211-214.
Charnley, J. (1961). "Arthroplasty of the hip. A new operation." Lancet **1**(7187): 1129-1132.
Collier, J. P., M. B. Mayor, R. E. Jensen, V. A. Surprenant, H. P. Surprenant, J. L. McNamar and L. Belec (1992). "Mechanisms of failure of modular prostheses." Clin Orthop Relat Res(285): 129-139.
Collier, J. P., M. B. Mayor, I. R. Williams, V. A. Surprenant, H. P. Surprenant and B. H. Currier (1995). "The tradeoffs associated with modular hip prostheses." Clin Orthop Relat Res(311): 91-101.
Collier, J. P., V. A. Surprenant, R. E. Jensen and M. B. Mayor (1991). "Corrosion at the interface of cobalt-alloy heads on titanium-alloy stems." Clin Orthop Relat Res(271): 305-312.
Collier, J. P., V. A. Surprenant, R. E. Jensen, M. B. Mayor and H. P. Surprenant (1992). "Corrosion between the components of modular femoral hip prostheses." Journal of Bone and Joint Surgery - Series B **74**(4): 511-517.
Collier, J. P., V. A. Surprenant, R. E. Jensen, M. B. Mayor and H. P. Surprenant (1992). "Corrosion between the components of modular femoral hip prostheses." J Bone Joint Surg Br **74**(4): 511-517.
Cook, R. B., B. J. R. F. Bolland, J. A. Wharton, S. Tilley, J. M. Latham and R. J. K. Wood (2013). "Pseudotumour Formation Due to Tribocorrosion at the Taper Interface of Large Diameter Metal on Polymer Modular Total Hip Replacements." The Journal of Arthroplasty **28**(8): 1430-1436.
Cook, R. I., M. Render and D. D. Woods (2000). "Gaps in the continuity of care and progress on patient safety." Bmj **320**(7237): 791-794.
Cooper, H. J. (2014). "The local effects of metal corrosion in total hip arthroplasty." Orthopedic Clinics of North America **45**(1): 9-18.
Cooper, H. J., C. J. Della Valle, R. A. Berger, M. Tetreault, W. G. Paprosky, S. M. Sporer and J. J. Jacobs (2012). "Corrosion at the head-neck taper as a cause for adverse local tissue reactions after total hip arthroplasty." J Bone Joint Surg Am **94**(18): 1655-1661.
Cooper, H. J., R. M. Urban, R. L. Wixson, R. M. Meneghini and J. J. Jacobs (2013). "Adverse local tissue reaction arising from corrosion at the femoral neck-body junction in a dual-taper stem with a cobalt-chromium modular neck." J Bone Joint Surg Am **95**(10): 865-872.
Corlett, N., L. E. Eiselstein and N. Budiansky (2010). 2.03 - Crevice Corrosion. Shreir's Corrosion. B. C. G. L. L. R. S. Stott. Oxford, Elsevier**:** 753-771.
Damm, P., A. Bender, G. Duda and G. Bergmann (2017). "In vivo measured joint friction in hip implants during walking after a short rest." PLOS ONE **12**(3): e0174788.
Damm, P., J. Dymke, R. Ackermann, A. Bender, F. Graichen, A. Halder, A. Beier and G. Bergmann (2013). "Friction in Total Hip Joint Prosthesis Measured *In Vivo* during Walking." PLoS ONE **8**(11): e78373.
Damm, P., F. Graichen, A. Rohlmann, A. Bender and G. Bergmann (2010). "Total hip joint prosthesis for in vivo measurement of forces and moments." Medical Engineering & Physics **32**(1): 95-100.
De Martino, I., J. B. Assini, M. E. Elpers, T. M. Wright and G. H. Westrich (2015). "Corrosion and Fretting of a Modular Hip System: A Retrieval Analysis of 60 Rejuvenate Stems." J Arthroplasty **30**(8): 1470-1475.
Del Balso, C., M. G. Teeter, S. C. Tan, J. L. Howard and B. A. Lanting (2016). "Trunnionosis: Does Head Size Affect Fretting and Corrosion in Total Hip Arthroplasty?" The Journal of Arthroplasty **31**(10): 2332-2336.

Donaldson, F. E., J. C. Coburn and K. L. Siegel (2014). "Total hip arthroplasty head–neck contact mechanics: A stochastic investigation of key parameters." Journal of Biomechanics **47**(7): 1634-1641.
Duisabeau, L., P. Combrade and B. Forest (2004). "Environmental effect on fretting of metallic materials for orthopaedic implants." Wear **256**(7–8): 805-816.
Dyrkacz, R. M. R., J. M. Brandt, J. B. Morrison, S. T. O' Brien, O. A. Ojo, T. R. Turgeon and U. P. Wyss (2015). "Finite element analysis of the head–neck taper interface of modular hip prostheses." Tribology International **91**: 206-213.
Elkins, J. M., J. J. Callaghan and T. D. Brown (2014). "Stability and Trunnion Wear Potential in Large-diameter Metal-on-Metal Total Hips: A Finite Element Analysis." Clinical Orthopaedics and Related Research® **472**(2): 529-542.
English, R., A. Ashkanfar and G. Rothwell (2015). "A computational approach to fretting wear prediction at the head–stem taper junction of total hip replacements." Wear **338–339**: 210-220.
English, T. A. and M. Kilvington (1979). "In vivo records of hip loads using a femoral implant with telemetric output (a prelimary report)." Journal of Biomedical Engineering **1**(2): 111-115.
Fabry, C., S. Herrmann, M. Kaehler, E.-D. Klinkenberg, C. Woernle and R. Bader (2013). "Generation of physiological parameter sets for hip joint motions and loads during daily life activities for application in wear simulators of the artificial hip joint." Medical Engineering & Physics **35**(1): 131-139.
Fallahnezhad, K., H. Farhoudi, R. Oskouei and M. Taylor (2016). "Influence of geometry and materials on the axial and torsional strength of the head-neck taper junction in modular hip replacements: A finite element study." Journal of the Mechanical Behavior of Biomedical Materials.
Fallahnezhad, K., H. Farhoudi, R. H. Oskouei and M. Taylor (2016). "Influence of geometry and materials on the axial and torsional strength of the head–neck taper junction in modular hip replacements: A finite element study." Journal of the mechanical behavior of biomedical materials **60**: 118-126.
Farhoudi, H., R. Hashemi Oskouei, C. Jones and M. Taylor (2014). Three-dimensional frictional moment induced from head-cup bearings of hip joint implants. Australian and New Zealand Orthopaedic Research Society (ANZORS), 20th Annual Scientific Meeting.
Farhoudi, H., R. H. Oskouei, C. F. Jones and M. Taylor (2015). "A novel analytical approach for determining the frictional moments and torques acting on modular femoral components in total hip replacements." Journal of Biomechanics **48**(6): 976-983.
Farhoudi, H., R. H. Oskouei, A. A. Pasha Zanoosi, C. F. Jones and M. Taylor (2016). "An Analytical Calculation of Frictional and Bending Moments at the Head-Neck Interface of Hip Joint Implants during Different Physiological Activities." Materials **9**(12): 982.
Flanagan, S., E. Jones and C. Birkinshaw (2010). "In vitro friction and lubrication of large bearing hip prostheses." Proc Inst Mech Eng H **224**(7): 853-864.
Fontana, M. G. (2005). Corrosion Engineering, Tata McGraw-Hill.
Fouvry, S., P. Kapsa and L. Vincent (1995). "Analysis of sliding behaviour for fretting loadings: determination of transition criteria." Wear **185**(1–2): 35-46.
Fridrici, V., S. Fouvry and P. Kapsa (2001). Fretting Wear Behaviour of a Titanium Alloy. Fundamentals of Tribology and Bridging the Gap Between the Macro- and Micro/Nanoscales. B. Bhushan, Springer Netherlands. **10:** 413-421.
Gascoyne, T. C., T. R. Turgeon and C. D. Burnell (2018). "Retrieval Analysis of Large-Head Modular Metal-on-Metal Hip Replacements of a Single Design." The Journal of Arthroplasty.
Gilbert, J. L., C. A. Buckley and J. J. Jacobs (1993). "In vivo corrosion of modular hip prosthesis components in mixed and similar metal combinations. The effect of crevice, stress, motion, and alloy coupling." J Biomed Mater Res **27**(12): 1533-1544.
Gilbert, J. L., S. Mali, R. M. Urban, C. D. Silverton and J. J. Jacobs (2012). "In vivo oxide-induced stress corrosion cracking of Ti-6Al-4V in a neck–stem modular taper: Emergent behavior in a new mechanism of in vivo corrosion." Journal of Biomedical Materials Research Part B: Applied Biomaterials **100B**(2): 584-594.

Gilbert, J. L., M. Mehta and B. Pinder (2009). "Fretting crevice corrosion of stainless steel stem–CoCr femoral head connections: Comparisons of materials, initial moisture, and offset length." Journal of Biomedical Materials Research Part B: Applied Biomaterials **88B**(1): 162-173.
Gill, H. S., J. Alfaro-Adrian, C. Alfaro-Adrian, P. McLardy-Smith and D. W. Murray (2002). "The effect of anteversion on femoral component stability assessed by radiostereometric analysis." J Arthroplasty **17**(8): 997-1005.
Goldberg, J. R. and J. L. Gilbert (2003). "In vitro corrosion testing of modular hip tapers." Journal of Biomedical Materials Research Part B: Applied Biomaterials **64B**(2): 78-93.
Goldberg, J. R., J. L. Gilbert, J. J. Jacobs, T. W. Bauer, W. Paprosky and S. Leurgans (2002). "A multicenter retrieval study of the taper interfaces of modular hip prostheses." Clin Orthop Relat Res(401): 149-161.
Gomez, P. F. and J. A. Morcuende (2005). "Early attempts at hip arthroplasty--1700s to 1950s." Iowa Orthop J **25**: 25-29.
Haider, H., J. N. Weisenburger and K. L. Garvin (2016). "Simultaneous measurement of friction and wear in hip simulators." Proceedings of the Institution of Mechanical Engineers, Part H: Journal of Engineering in Medicine **230**(5): 373-388.
Hamrock, B. J. and D. Dowson (1978). "Elastohydrodynamic Lubrication of Elliptical Contacts for Materials of Low Elastic Modulus I—Fully Flooded Conjunction." Journal of Lubrication Technology **100**(2): 236-245.
Han, A., G. Pillon, A. Nichici, B. Vannes and D. Grevey (2006). "Study and evaluation of fretting critical slip conditions by applying the design of experiments method." Wear **261**(10): 1080-1086.
Heredia, S. and S. Fouvry (2010). "Introduction of a new sliding regime criterion to quantify partial, mixed and gross slip fretting regimes: Correlation with wear and cracking processes." Wear **269**(7–8): 515-524.
Higgs, G. B., J. A. Hanzlik, D. W. MacDonald, J. L. Gilbert, C. M. Rimnac and S. M. Kurtz (2013). "Is increased modularity associated with increased fretting and corrosion damage in metal-on-metal total hip arthroplasty devices?: a retrieval study." J Arthroplasty **28**(8 Suppl): 2-6.
Higgs, G. B., J. A. Hanzlik, D. W. MacDonald, J. L. Gilbert, C. M. Rimnac, S. M. Kurtz and C. the Implant Research Center Writing (2013). "Is Increased Modularity Associated With Increased Fretting and Corrosion Damage in Metal-On-Metal Total Hip Arthroplasty Devices?: A Retrieval Study." The Journal of arthroplasty **28**(8 0): 2-6.
Hussenbocus, S., D. Kosuge, L. B. Solomon, D. W. Howie and R. H. Oskouei (2015). "Head-Neck Taper Corrosion in Hip Arthroplasty." BioMed Research International **2015**: 9.
Ingram, A. J. (1988). "Soft tissue sarcoma associated with aluminum oxide ceramic total hip arthroplasty." Clin Orthop Relat Res(235): 311-312.
Jacobs, J. J., J. L. Gilbert and R. M. Urban (1998). "Corrosion of metal orthopaedic implants." Journal of Bone and Joint Surgery - Series A **80**(2): 268-282.
Jacobs, J. J., J. L. Gilbert and R. M. Urban (1998). "Corrosion of metal orthopaedic implants." J Bone Joint Surg Am **80**(2): 268-282.
Jacobs, J. J., A. K. Skipor, L. M. Patterson, N. J. Hallab, W. G. Paprosky, J. Black and J. O. Galante (1998). "Metal release in patients who have had a primary total hip arthroplasty. A prospective, controlled, longitudinal study." J Bone Joint Surg Am **80**(10): 1447-1458.
Jauch, S. Y., L. G. Coles, L. V. Ng, A. W. Miles and H. S. Gill (2014). "Low torque levels can initiate a removal of the passivation layer and cause fretting in modular hip stems." Medical Engineering & Physics **36**(9): 1140-1146.
Johnson, K. L. (1987). Contact Mechanics, Cambridge University Press.
Johnston, R. C. and G. L. Smidt (1969). "Measurement of Hip-Joint Motion during Walking EVALUATION OF AN ELECTROGONIOMETRIC METHOD." The Journal of Bone & Joint Surgery **51**(6): 1083-1094.
Jones, R. and R. Lovett (1929). RW. Orthopaedic. W. Wood. Baltimore.

Korovessis, P., G. Petsinis, M. Repanti and T. Repantis (2006). "Metallosis after contemporary metal-on-metal total hip arthroplasty: Five to nine-year follow-up." Journal of Bone and Joint Surgery - Series A **88**(6): 1183-1191.
Kretzer, J. P., E. Jakubowitz, M. Krachler, M. Thomsen and C. Heisel (2009). "Metal release and corrosion effects of modular neck total hip arthroplasty." Int Orthop **33**(6): 1531-1536.
Krishnan, H., S. P. Krishnan, G. Blunn, J. A. Skinner and A. J. Hart (2013). "INSTRUCTIONAL REVIEW: HIP Modular neck femoral stems." The bone and joint journal **95**: 1011-1021.
Kurtz, S. M., S. B. Kocagöz, J. A. Hanzlik, R. J. Underwood, J. L. Gilbert, D. W. MacDonald, G.-C. Lee, M. A. Mont, M. J. Kraay, G. R. Klein, J. Parvizi and C. M. Rimnac (2013). "Do Ceramic Femoral Heads Reduce Taper Fretting Corrosion in Hip Arthroplasty? A Retrieval Study." Clinical Orthopaedics and Related Research **471**(10): 3270-3282.
Langkamer, V. G., C. P. Case, C. Collins, I. Watt, J. Dixon, A. J. Kemp and R. M. Atkins (1997). "Tumors around implants." J Arthroplasty **12**(7): 812-818.
Langton, D. J., R. Sidaginamale, J. K. Lord, A. V. F. Nargol and T. J. Joyce (2012). "Taper junction failure in large-diameter metal-on-metal bearings." Bone & Joint Research **1**(4): 56-63.
Lanting, B. A., M. G. Teeter, E. M. Vasarhelyi, T. G. Ivanov, J. L. Howard and D. D. Naudie (2015). "Correlation of corrosion and biomechanics in the retrieval of a single modular neck total hip arthroplasty design: modular neck total hip arthroplasty system." J Arthroplasty **30**(1): 135-140.
Learmonth, I. D., C. Young and C. Rorabeck (2007). "The operation of the century: total hip replacement." Lancet **370**(9597): 1508-1519.
Liu, F., Z. M. Jin, F. Hirt, C. Rieker, P. Roberts and P. Grigoris (2006). "Transient elastohydrodynamic lubrication analysis of metal-on-metal hip implant under simulated walking conditions." Journal of Biomechanics **39**(5): 905-914.
Liu, X., P. K. Chu and C. Ding (2004). "Surface modification of titanium, titanium alloys, and related materials for biomedical applications." Materials Science and Engineering: R: Reports **47**(3–4): 49-121.
Mahmood, S. S., S. S. Mukka, S. Crnalic and A. S. Sayed-Noor (2015). "The Influence of Leg Length Discrepancy after Total Hip Arthroplasty on Function and Quality of Life: A Prospective Cohort Study." The Journal of Arthroplasty **30**(9): 1638-1642.
Mathew, M. T., T. Uth, N. J. Hallab, R. Pourzal, A. Fischer and M. A. Wimmer (2011). "Construction of a tribocorrosion test apparatus for the hip joint: Validation, test methodology and analysis." Wear **271**(9–10): 2651-2659.
Mathiesen, E. B., J. U. Lindgren, G. G. Blomgren and F. P. Reinholt (1991). "Corrosion of modular hip prostheses." J Bone Joint Surg Br **73**(4): 569-575.
McDougall, A. (1956). "Malignant tumour at site of bone plating." J Bone Joint Surg Br **38-b**(3): 709-713.
McKee, G. K. and J. Watson-Farrar (1966). "REPLACEMENT OF ARTHRITIC HIPS BY THE McKEE-FARRAR PROSTHESIS." Journal of Bone & Joint Surgery, British Volume **48-B**(2): 245-259.
Mencière, M. L., T. Amouyel, J. Taviaux, M. Bayle, C. Laterza and P. Mertl (2014). "Fracture of the cobalt-chromium modular femoral neck component in total hip arthroplasty." Orthopaedics & Traumatology: Surgery & Research **100**(5): 565-568.
Meng, Q., F. Liu, J. Fisher and Z. Jin (2013). "Contact mechanics and lubrication analyses of ceramic-on-metal total hip replacements." Tribology International **63**(0): 51-60.
Meng, Q., J. Wang, P. Yang, Z. Jin and J. Fisher (2015). "The lubrication performance of the ceramic-on-ceramic hip implant under starved conditions." Journal of the Mechanical Behavior of Biomedical Materials **50**: 70-76.
Meng, Q. E., F. Liu, J. Fisher and Z. M. Jin (2011). "Transient elastohydrodynamic lubrication analysis of a novel metal-on-metal hip prosthesis with a non-spherical femoral bearing surface." Proc Inst Mech Eng H **225**(1): 25-37.
Mohrbacher, H., J. P. Celis and J. R. Roos (1995). "Laboratory testing of displacement and load induced fretting." Tribology International **28**(5): 269-278.

Moore, B. F. and P. F. Lachiewicz (2017). "Corrosion and adverse tissue reaction after modular unipolar hip hemiarthroplasty." Arthroplast Today **3**(4): 207-210.
Morlock, M., E. Schneider, A. Bluhm, M. Vollmer, G. Bergmann, V. Müller and M. Honl (2001). "Duration and frequency of every day activities in total hip patients." Journal of Biomechanics **34**(7): 873-881.
Morlock, M. M. (2015). "The Taper Disaster - How Could it Happen?" HIP International **25**(4): 339-346.
Nassif, N. A., D. H. Nawabi, K. Stoner, M. Elpers, T. Wright and D. E. Padgett (2013). "Taper Design Affects Failure of Large-head Metal-on-metal Total Hip Replacements." Clin Orthop Relat Res.
Nassutt, R., M. A. Wimmer, E. Schneider and M. M. Morlock (2003). "The influence of resting periods on friction in the artificial hip." Clin Orthop Relat Res(407): 127-138.
Neu, R. W. (2011). "Progress in standardization of fretting fatigue terminology and testing." Tribology International **44**(11): 1371-1377.
O'Reilly, O. M. (2008). Intermediate Dynamics for Engineers: A Unified Treatment of Newton-Euler and Lagrangian Mechanics, Cambridge University Press.
Oldfield, J. W. and W. H. Sutton (1978). "Crevice Corrosion of Stainless Steels: I. A Mathematical Model." British Corrosion Journal **13**(1): 13-22.
Oldfield, J. W. and W. H. Sutton (1980). "New Technique for Predicting the Performance of Stainless Steels in Sea Water and other Chloride-containing Environments." British Corrosion Journal **15**(1): 31-34.
Panagiotidou, A., B. Bolland, J. Meswania, J. Skinner, F. Haddad, A. Hart and G. Blunn (2013). "Effect of Increased Frictional Torque on the Fretting Corrosion Behaviour of the Large Diameter Femoral Head." Bone & Joint Journal Orthopaedic Proceedings Supplement **95-B**(SUPP 34): 473.
Panagiotidou, A., J. Meswania, K. Osman, B. Bolland, J. Latham, J. Skinner, F. S. Haddad, A. Hart and G. Blunn (2015). "The effect of frictional torque and bending moment on corrosion at the taper interface : an in vitro study." Bone Joint J **97-b**(4): 463-472.
Pandit, H., S. Glyn-Jones, P. McLardy-Smith, R. Gundle, D. Whitwell, C. L. M. Gibbons, S. Ostlere, N. Athanasou, H. S. Gill and D. W. Murray (2008). "Pseudotumours associated with metal-on-metal hip resurfacings." Journal of Bone and Joint Surgery - Series B **90**(7): 847-851.
Park, H. (1783). An account of a new method of treating diseases of the joints of the knee and elbow [electronic resource] : in a letter to Mr. Percival Pott / By H. Park. London, printed for J. Johnson.
Penman, H. G. and P. A. Ring (1984). "Osteosarcoma in association with total hip replacement." J Bone Joint Surg Br **66**(5): 632-634.
Picard, F., E. Montbarbon, Y. Tourne, J. M. Leroy and D. Saragaglia (1997). "[Pseudotumor manifestation of metallosis in a hip prosthesis]." Int Orthop **21**(5): 352-354.
Pillar, R. M. (2009). Metallic Biomaterials. Biomedical Materials. R. Narvan, Springer**:** 41-81.
Pivec, R., A. J. Johnson, S. C. Mears and M. A. Mont (2012). "Hip arthroplasty." Lancet **380**(9855): 1768-1777.
Preuss, R., K. Lars Haeussler, M. Flohr and R. M. Streicher (2012). "Fretting Corrosion and Trunnion Wear—Is it Also a Problem for Sleeved Ceramic Heads?" Seminars in Arthroplasty **23**(4): 251-257.
Radha, R. and D. Sreekanth (2017). "Insight of magnesium alloys and composites for orthopedic implant applications – a review." Journal of Magnesium and Alloys **5**(3): 286-312.
Rayan, F., M. Dodd and F. S. Haddad (2008). "European validation of the Vancouver classification of periprosthetic proximal femoral fractures." J Bone Joint Surg Br **90**(12): 1576-1579.
Rehmer, A., N. E. Bishop and M. M. Morlock (2012). "Influence of assembly procedure and material combination on the strength of the taper connection at the head–neck junction of modular hip endoprostheses." Clinical Biomechanics **27**(1): 77-83.
Resende, R. A., R. N. Kirkwood, J. F. Rudan and K. J. Deluzio (2017). "How symmetric are metal-on-metal hip resurfacing patients during gait? Insights for the rehabilitation." Journal of Biomechanics **58**: 37-44.

Rodrigues, D. C., R. M. Urban, J. J. Jacobs and J. L. Gilbert (2009). "In vivo severe corrosion and hydrogen embrittlement of retrieved modular body titanium alloy hip-implants." J Biomed Mater Res B Appl Biomater **88**(1): 206-219.
Royhman, D., M. Patel, J. J. Jacobs, M. A. Wimmer, N. J. Hallab and M. T. Mathew (2017). "In vitro simulation of fretting-corrosion in hip implant modular junctions: The influence of pH." Medical Engineering & Physics.
Ryu, R. K., E. G. Bovill, H. B. Skinner and W. R. Murray (1987). "Soft tissue sarcoma associated with aluminum oxide ceramic total hip arthroplasty. A case report." Clinical orthopaedics and related research(216): 207-212.
Saikko, V. (2006). "Effect of contact pressure on wear and friction of ultra-high molecular weight polyethylene in multidirectional sliding." Proc Inst Mech Eng H **220**(7): 723-731.
Saikko, V. and O. Calonius (2002). "Slide track analysis of the relative motion between femoral head and acetabular cup in walking and in hip simulators." Journal of Biomechanics **35**(4): 455-464.
Salvati, E. A., J. R. Lieberman, O. L. Huk and B. G. Evans (1995). "Complications of femoral and acetabular modularity." Clin Orthop Relat Res(319): 85-93.
Savarino, L., D. Granchi, G. Ciapetti, E. Cenni, A. Nardi Pantoli, R. Rotini, C. A. Veronesi, N. Baldini and A. Giunti (2002). "Ion release in patients with metal-on-metal hip bearings in total joint replacement: a comparison with metal-on-polyethylene bearings." J Biomed Mater Res **63**(5): 467-474.
SchÄfer, R., U. SoltÉsz and P. f. Bernard (1998). "Friction in hip-joint prostheses and its influence on the fixation of the artificial head." Journal of Materials Science : Materials in Medicine **9**(12): 687-690.
Scholes, S. C. and A. Unsworth (2000). "Comparison of friction and lubrication of different hip prostheses." Proceedings of the Institution of Mechanical Engineers, Part H: Journal of Engineering in Medicine **214**(1): 49-57.
Scholes, S. C., A. Unsworth, R. M. Hall and R. Scott (2000). "The effects of material combination and lubricant on the friction of total hip prostheses." Wear **241**(2): 209-213.
Schramm, M., D. C. Wirtz, U. Holzwarth and R. P. Pitto (2000). "The Morse taper junction in modular revision hip replacement - A biomechanical and retrieval analysis." Biomedizinische Technik **45**(4): 105-109.
Shan, X. and J. H. Payer (2007). "Comparison of Ceramic and Polymer Crevice Formers on the Crevice Corrosion Behavior of Ni-Cr-Mo Alloy C-22." CORROSION 2007.
Smith, A. J., P. Dieppe, P. W. Howard and A. W. Blom (2012). "Failure rates of metal-on-metal hip resurfacings: analysis of data from the National Joint Registry for England and Wales." Lancet **380**(9855): 1759-1766.
Sonntag, R., S. Braun, L. Al-Salehi, J. Reinders, U. Mueller and J. P. Kretzer (2017). "Three-dimensional friction measurement during hip simulation." PLOS ONE **12**(9): e0184043.
St. John, K. R., L. D. Zardiackas and R. A. Poggie (2004). "Wear evaluation of cobalt–chromium alloy for use in a metal-on-metal hip prosthesis." Journal of Biomedical Materials Research Part B: Applied Biomaterials **68B**(1): 1-14.
Swaminathan, V. and J. L. Gilbert (2012). "Fretting corrosion of CoCrMo and Ti6Al4V interfaces." Biomaterials **33**(22): 5487-5503.
Swaminathan, V. and J. L. Gilbert (2013). "Potential and frequency effects on fretting corrosion of Ti6Al4V and CoCrMo surfaces." Journal of Biomedical Materials Research Part A **101A**(9): 2602-2612.
Swann, M. (1984). "Malignant soft-tissue tumour at the site of a total hip replacement." J Bone Joint Surg Br **66**(5): 629-631.
Tetreault, M. W., J. J. Jacobs, W. Mahmud and D. Nam (2018). "Adverse Local Tissue Reaction After a Metal-on-Metal Total Hip Prosthesis Without Elevated Serum Metal Ion Levels." Orthopedics **41**(3): e438-e441.
Thom, B., K. Imran, M. Tim, L. Elaine, V. Nico and J. Dennis (2017). "A combined experimental and finite element approach to analyse the fretting mechanism of the head–stem taper junction in total hip replacement." Proceedings of the Institution of Mechanical Engineers, Part H: Journal of Engineering in Medicine **231**(9): 862-870.

Ulrich, S. D., T. M. Seyler, D. Bennett, R. E. Delanois, K. J. Saleh, I. Thongtrangan, M. Kuskowski, E. Y. Cheng, P. F. Sharkey, J. Parvizi, J. B. Stiehl and M. A. Mont (2008). "Total hip arthroplasties: what are the reasons for revision?" Int Orthop **32**(5): 597-604.
Ulrich, S. D., T. M. Seyler, D. Bennett, R. E. Delanois, K. J. Saleh, I. Thongtrangan, M. Kuskowski, E. Y. Cheng, P. F. Sharkey, J. Parvizi, J. B. Stiehl and M. A. Mont (2008). "Total hip arthroplasties: What are the reasons for revision?" International Orthopaedics **32**(5): 597-604.
Urban, R. M., J. L. Gilbert and J. J. Jacobs (2006). Corrosion of modular titanium alloy stems in cementless hip replacement. ASTM Special Technical Publication.
Viceconti, M., O. Ruggeri, A. Toni and A. Giunti (1996). "Design-related fretting wear in modular neck hip prosthesis." Journal of Biomedical Materials Research **30**(2): 181-186.
Wang, A., A. Essner and R. Klein (2001). "Effect of contact stress on friction and wear of ultra-high molecular weight polyethylene in total hip replacement." Proceedings of the Institution of Mechanical Engineers, Part H: Journal of Engineering in Medicine **215**(2): 133-139.
Wang, F. C., C. Brockett, S. Williams, I. Udofia, J. Fisher and Z. M. Jin (2008). "Lubrication and friction prediction in metal-on-metal hip implants." Phys Med Biol **53**(5): 1277-1293.
White, S. P., G. J. Weir and N. J. Laycock (2000). "Calculating chemical concentrations during the initiation of crevice corrosion." Corrosion Science **42**(4): 605-629.
Wiles, P. (1958). "The surgery of the osteo-arthritic hip." British Journal of Surgery **45**(193): 488-497.
Williams, S., D. Jalali-Vahid, C. Brockett, Z. Jin, M. H. Stone, E. Ingham and J. Fisher (2006). "Effect of swing phase load on metal-on-metal hip lubrication, friction and wear." J Biomech **39**(12): 2274-2281.
Williams, S., T. D. Stewart, E. Ingham, M. H. Stone and J. Fisher (2004). "Metal-on-metal bearing wear with different swing phase loads." J Biomed Mater Res B Appl Biomater **70**(2): 233-239.
Zhang, T., N. M. Harrison, P. F. McDonnell, P. E. McHugh and S. B. Leen (2013). "A finite element methodology for wear–fatigue analysis for modular hip implants." Tribology International **65**(0): 113-127.
Zhou, Z. R., S. Fayeulle and L. Vincent (1992). "Cracking behaviour of various aluminium alloys during fretting wear." Wear **155**(2): 317-330.